Study on the morphological effect of metal oxide based electrode materials for energy storage applications

THESIS SUBMITTED FOR THE DEGREE OF
DOCTOR OF PHILOSOPHY (SCIENCE)
OF
JADAVPUR UNIVERSITY

By

SAMIK SAHA, M.Sc.

DEPARTMENT OF PHYSICS
&
DEPARTMENT OF INSTRUMENTATION SCIENCE

JADAVPUR UNIVERSITY
Kolkata – 700032
INDIA

April-2022

অধ্যাপকবাসুদেবঘোষ
পদার্থবিদ্যাবিভাগ
যাদবপুরবিশ্ববিদ্যালয়
কলকাতা - ৭০০০৩২ , ভারত

Prof. Basudev Ghosh
Department of Physics
Jadavpur University
Kolkata – 700 032, INDIA

Certificate from Supervisor

This is to certify that the thesis entitled **"Study on the morphological effect of metal oxide based electrode materials for energy storage applications"** submitted by **Sri Samik Saha,** who got his name registered on 20/09/2018 (**Index No: 185/18/Phys./26)** for the award of Ph. D. (Science) degree of Jadavpur University, is absolutely based upon his own work under the joint supervision of Dr. Sachindranath Das, Department of Instrumentation Science, Jadavpur University and myself and that neither this thesis nor any part of it has been submitted for either any degree/ diploma or any other academic award anywhere before.

01.04.2022
Dr. Basudev Ghosh.
Professor
Department of Physics
Jadavpur University
Kolkata-700032

Email : bsdvghosh@gmail.com

Date :- 31·03·2022

Certificate from Supervisor

This is to certify that the thesis entitled **"Study on the morphological effect of metal oxide based electrode materials for energy storage applications"** submitted by **Sri Samik Saha,** who got his name registered on 20/09/2018 (**Index No: 185/18/Phys./26**) for the award of Ph. D. (Science) degree of Jadavpur University, is absolutely based upon his own work under the joint supervision of Dr. Basudev Ghosh, Department of Physics, Jadavpur University and myself and that neither this thesis nor any part of it has been submitted for either any degree/ diploma or any other academic award anywhere before.

Das.
31·03·2022

Dr. Sachindranath Das
Assistant Professor
Dept. of Instrumentation Science
Jadavpur University
Kolkata-700032

Dr. Sachindranath Das
Assistant Professor
Dept. of Instrumentation Science
Jadavpur University, Raja S. C. Mallick Road, Kol-32

E-mail : sachindas15@gmail.com
sachindran.das@jadavpuruniversity.in
Mob. : +91-9432181532
Ph. : 033-2457-2965 (Off.)

Declaration of the Scholar

I, **Samik Saha**, hereby declare that I have carried out the work contained in this thesis in the Department of Physics, Jadavpur University and in the Department of Instrumentation Science, Jadavpur University under the joint supervision of **Dr. Basudev Ghosh**, Department of Physics, Jadavpur University and **Dr. Sachindranath Das**, Department of Instrumentation Science, Jadavpur University, Kolkata- 700032. Neither this thesis nor any part of this thesis has been submitted for any degree/ diploma or other academic awards anywhere before.

Date: 1/04/2022

SAMIK SAHA

Index No: 185/18/Phys./ 26

Jadavpur University

Kolkata-700032

JADAVPUR UNIVERSITY

KOLKATA-700 032
MARK SHEET

NO.: CW/16052/ 000786

(For Ph.D/M. Phil. Course Work)

Results of the	PH.D. COURSE WORK EXAMINATION, 2020
In SCIENCE	held in DECEMBER, 2019 – JANUARY, 2020
Name SAMIK SAHA	Class Roll No. 201920706015
Examination Roll No. PHDPHY20115	Registration No. of

Subject Code / Name	Credit Hr.(c_i)	Marks
COMPULSORY UNITS:: EX/PHY/PHD/A & B RESEARCH METHODOLOGY & REVIEW OF RESEARCH WORK	8	84
ELECTIVE UNITS ::	8	78
EX/PHY/PHD/01 :: MATERIAL CHARACTERIZATION TECHNIQUES EX/PHY/PHD/09 :: ADVANCED X-RAY CRYSTALLOGRAPHY		

Total Marks : 162 (out of 200)   Remarks: P

Prepared by :   Checked by :

Date of issue : 16 / 09 / 2020   Controller of Examinations

v

Dedicated to my family

Acknowledgments

The thesis entitled ***"Study on the morphological effect of metal oxide based electrode materials for energy storage applications"*** is a result of broad literature reviewing and extensive experimental work performed in the Department of Physics and Department of Instrumentation Science, Jadavpur University, Jadavpur, Kolkata-700032, under the joint guidance of Prof. Basudev Ghosh, Department of Physics and Dr. Sachindranath Das, Department of Instrumentation Science, Jadavpur University.

It is an honest pleasure to express my immense appreciation and boundless love to the people involved in completing this thesis.

First and foremost, I would like to express my most sincere gratitude to both my supervisors, Prof. Basudev Ghosh and Dr. Sachindranath Das, for their patience and invaluable guidance, help, support, and encouragement during these years. The joy and enthusiasm they have for the research were contagious and motivated me to push forward even during challenging times in the Ph.D. pursuit. I owe them my profound admiration and respect.

I also want to thank the Dept. of Physics and Dept. of Instrumentation Science, Jadavpur University, for providing all kinds of support for pursuing my doctoral degree. I want to thank the Dean of Science, Head of the Department of Physics, and Head of Instrumentation Science for providing me with laboratory and other essential facilities during my research work.

I am also grateful to Prof. Chittaranjan Sinha, Prof. Swapan Kumar Bhattacharya, Department of Chemistry, Jadavpur University, Prof. Satyaranjan Bhattacharyya, SINP, Kolkata, and Dr. Mahasweta Nandi, Visva-Bharati, India for their support regarding different characterizations.

I am very much thankful to my colleagues in my laboratory Dr. Apurba Ray, Dr. Atanu Roy, Dr. Priyabrata Sadhukhan, Dr. Prasenjit Maji, Dr. Subhasish Patra, Mithun Halder, Souvik Mal, Swagatalakhmi Pujaru, Adwaita Kundu, for their constant help and support towards the completion of my thesis.

I am very much grateful to the Council of Industrial Research (CSIR), India, for providing me junior and senior research fellowships to carry out the research (Fellowship Award no. 09/096(0898)/2017-EMR-I).

I would also like to express my sincere thanks to Government General Degree College, Dantan-II, West-Midnapore, West-Bengal, India, and Dept. of Higher Education, Science and Technology and Biotechnology, Government of West Bengal to allow me to continue my research alongside the assigned teaching and administrative work in the college.

In addition, I would like to acknowledge my teammates of We The BOHEMIANS, with whom I got the pleasure of spending quality time trekking in the mighty Himalaya. I am also grateful to my friends Abhijit, Arnab, Rit, Rup, Sayan, Jeet, Koushik, Avik for their love and support during different situations. I would also like to thank Pinaki Moitra (Pinaki Kaka) for his constant motivation during my entire academic year.

Last but not least; I would like to express my gratitude, especially to my parents (Late Soumitra Saha and Neena Saha), my sister (Senjuti Saha), my brother-in-law (Hrishikesh Das), and my fiancée Ashmita for their enthusiasm, inspiration, and help in different situations of my life and during the tenure of the research.

Table of content

List of Figures

magenta and O atoms are shown in red.

List of Tables

List of Publications

A. Journal publications included in this thesis

1. Effect of Morphological Ordering on the Electrochemical Performance of MnO_2-GO composite, **S. Saha**, P. Maji, D. A. Pethsangave, A. Roy, A. Ray, S. Some, S. Das, *Electrochimica Acta* 317 (2019) 199-210.

2. Rotary-Jet spin assisted fabrication of MnO_2 microfiber for supercapacitor electrode application, **S. Saha**, P. Sadhukhan, S. R. Chowdhury, S. Das, *Materials Letters*, (2020) 128342.

3. Effect of particle morphology on the electrochemical performance of hydrothermally synthesized $NiMn_2O_4$, **S. Saha**, A. Roy, A. Ray, T. Das, M. Nandi, B. Ghosh, S. Das, *Electrochimica Acta*, 353 (2020) 136515.

4. Study of morphological effect on the electrochemical charge storage performance of rotary-jet spin synthesized $NiMn_2O_4$/carbon fiber, **S. Saha**, A. Roy, S. Das, *(to be communicated soon).*

B. Book chapter included in this thesis

1. "Nanomaterials in thin-film form for new generation energy storage device applications", **S. Saha** and S. Das, *Chemical Solution Synthesis for Materials Design and Thin Film Device Applications, Elsevier*, 2021.

C. Conference presentations

1. Electrochemical studies of MnO_2-CNT composite in ordered structure, *4th International conference on Nanoscience and Nanotechnology*, (ICON-2017), 9-11 August, 2017, SRM University, Kattankulathur-603203.

2. Hydrothermal synthesis of $NiMn_2O_4$ and investigation of its electrochemical performance for supercapacitor, 2nd National Symposium on Shaping the Energy Future: Challenges and Opportunities, (SEFCO-2018), 11-12 May, 2018, CSIR-Indian Institute of Petroleum, Dehradun, India.

3. Effect of different surfactants on the pseudocapacitive properties of $NiMn_2O_4$, International conference on Supercapacitors, Energy Storage and Applications (ICSEA-2019), 8-10 March, 2019, CMET, Thrissur, Kerala, 680581.

4. Electrochemical studies of MnO_2-GO composite in ordered structure, National Conference on Science, Technology and Emerging Applications of Microscopy, (STEAM-2019), 11-12 November, 2019, Dept. of Chemistry, Dr. Bhimrao Ambedkar University, Agra.

D. List of journal publications not included in this thesis

1. A Cu(II) Metal Organic Framework with a Tetranuclear Core: Structure, Magnetism, and Supercapacitor Activity, S. Jana, *S. Saha*, A. Chandra, S. El Fallah, S. Das, C. Sinha, Cryst. Growth Des. 2022, doi: 10.1021/acs.cgd.1c01109

2. MWCNT incorporated wool-ball-like CuO@ NiO hybrid nanostructures for high-performance energy storage device, M. Chatterjee, *S. Saha*, S. Das, S. Bhattacharyya, S. K. Pradhan, *Journal of Alloys and Compounds*, 886 (2021) 161313.

3. Influence of electrochemical active surface area on the oxygen evolution reaction and energy storage performance of MnO_2-multiwalled carbon nanotube composite, A. Roy, A. Ray, *S. Saha*, M. Ghosh, T. Das, M. Nandi, G. Lal, S. Das, *International Journal of Energy Research*, 11 (2021) 45.

4. Performance of asymmetric supercapacitor fabricated with perovskite‑type $Sr2^+$ incorporated $LaMnO_3$ ($La_{0.7}$ $Sr_{0.3}MnO_3$) nanostructures in neutral 1M Na_2SO_4 aqueous electrolyte, A. Roy, F. E. C. Gordillo, *S. Saha*, U. Pal, S. Das, *International Journal of Energy Research*, 9 (2021) 45.

5. Temperature and frequency dependent dielectric relaxation of Ni-Fe-Oxide nanocomposites" A. Ray, P. Maji, A. Roy, *S. Saha*, P. Sadhukhan, S. Pujaru, P. Sengupta, Yasnur Sk. and S. Das, *Material Research Express*, 6 (2020) 12

6. Advanced asymmetric supercapacitor with $NiCo_2O_4$ nanoparticles and nanowires electrodes: A comparative morphological hierarchy, M. Chatterjee, *S. Saha*, S. Das, S. K. Pradhan, *Journal of Alloys and Compounds*, 821 (2020) 153503

7. Temperature and frequency dependent dielectric relaxation of Ni–Fe–Oxide nanocomposites, A. Ray, P. Maji, A. Roy, *S. Saha*, P. Sadhukhan, S. Das, *Materials Research Express* 6 (12), 1250h4

8. Electrochemical Energy Storage Properties of Ni-Mn-Oxide Electrodes for Advance Asymmetric Supercapacitor Application: A. Ray, A. Roy, *S. Saha*, M. Ghosh, S. R. Chowdhury, T. Maiyalagan, S. K. Bhattacharya, and S. Das, *Langmuir* 35 (2019), 8257−8267

9. Study on charge storage mechanism in working electrodes fabricated by sol-gel derived spinel $NiMn_2O_4$ nanoparticles for supercapacitor application; A. Ray, A. Roy, M. Ghosh, J. A. Ramos-Ramón, *S. Saha*, U. Pal, S. K. Bhattachrya, S. Das, *Applied Surface Science* 463 (2019) 513-525

10. NiO-CNT composite for high performance supercapacitor electrode and oxygen evolution reaction, A. Roy, A. Ray, *S. Saha*, M. Ghosh, T. Das, B. Satpati, M. Nandi, S. Das, *Electrochimica Acta*, 283 (2018) 327-337.

11. Investigation on energy storage and conversion properties of multifunctional PANI-MWCNT composite, A. Roy, A. Ray, *S. Saha*, S. Das, *International Journal of Hydrogen Energy*, 43 (2018) 7128-7139.

12. Investigation on energy storage and conversion properties of multifunctional PANI-MWCNT composite, A. Roy, A. Ray, *S. Saha*, S. Das, *International Journal of Hydrogen Energy*, 43 (2018) 7128-7139.

13. Morphological behaviour, electronic bond formation and electrochemical performance study of V_2O_5-Polyaniline composite and its application in asymmetric supercapacitor, A. Roy, A. Ray, P. Sadhukhan, *S. Saha* and S. Das, *Materials Research Bulletin* 107 (2018) 379-390.

E. *List of book chapter not included in the thesis*

1. "Ni-Based Electrocatalyst for Full Water Splitting" A. Roy, *S. Saha*, A. Ray, S. Das, Electrochemical Water Splitting, *Materials Research Foundations*, Vol. 59, pp 125-140, 2019.

2. "Transition Metal Oxide-Based Nano-materials for Energy Storage Application" A. Ray, A. Roy, *S. Saha*, S. Das, Science, Technology and Advanced Application of Supercapacitors, *InTechOpen*, 2018, Nov 5.

ABSTRACT

Title: "Study on the morphological effect of metal oxide based electrode materials for energy storage applications."
Index No: 185 / 18 / PHYS / 26

As an intermediate energy storage device between dielectric capacitors and batteries, supercapacitors have attracted much attention due to their high power densities relative to secondary batteries and high energy density compared to traditional electric double-layer capacitors. Commercial supercapacitor utilizes high surface area carbon as an electrode to store charges. Unfortunately, these devices with carbon electrodes cannot demonstrate high energy density due to the physical storage mechanism. On the other hand, different transition metal oxides and few conducting polymer-based electrodes can store charges via fast and reversible faradic reaction with suitable electrolytes and demonstrate very high energy density. Ideal material for supercapacitor should have a high surface area, good electrical conductivity, optimum porosity, high specific capacitance, and excellent thermal and chemical stability. Apart from these parameters, morphology of the electrode material influences all these mentioned parameters and thus plays a vital role in determining the overall performance. An ordered morphology of the electrode material can enhance the surface area and can offer optimum porosity. A morphology where all the redox-active sites of the electrode material are electrically connected via some conductive pathways provides additional benefits of good conductivity and stability. In this thesis work, we have observed the effect of morphology on the electrochemical charge storage performance of the electrode material.

MnO_2 has been chosen for our first work as an electrode material. To stabilize against the volumetric strain during the repetitive charge discharge process, graphene oxide has been added to MnO_2 to form a composite. To study the effect of morphology, electrospinning technique has been used to fabricate fiber-like morphology of this composite. This morphology was chosen because of the fact that different redox-active sites can be electrically connected through the carbonized fiber structure. Detailed electrochemical performance testing showed that this ordered and well-connected morphology enhances the performance of this composite compared to the bulk sample having negligible interconnection between the redox-active sites. A high specific capacitance of ~893 F g^{-1} was obtained for this fibrous composite, whereas the bulk disordered sample offered 546 F g^{-1}. Using the fibrous sample as a positive electrode and activated carbon as a negative electrode, we fabricated an asymmetric two-electrode device which demonstrated a high specific capacitance of

212 F g^{-1} and a peak power density of 2.8 kW kg^{-1} and a peak energy density of 96.75 Wh kg^{-1}.

But electrospinning is a shallow yield process and is not suitable for mass production. To speed up the process of fiber production, we devised a simple Rotary Jet Spin (RJ-Spin) setup, which is identical to a candy floss machine. MnO_2/C fiber was fabricated using the RJ-Spin setup, and its electrochemical performances were evaluated to find the effect of fibrous morphology. A three-electrode-specific capacitance of 663 F g^{-1} was obtained for this sample. The two-electrode asymmetric device showed a specific capacitance of 136 F g^{-1}, a high power density of 3.2 kW kg-1, and a high energy density of 56.7 Wh kg^{-1}.

To reduce the resistance of MnO_2 based electrodes and enhance the charge storage performance, a bimetal oxide of Ni and Mn ($NiMn_2O_4$) was synthesized on nickel foam via a hydrothermal route. During the synthesis, different surfactants and mineralizer were used to tune the morphology of the synthesized $NiMn_2O_4$. By studying the detailed electrochemical performance, the effect of morphology of these samples was studied. It was seen that the addition of sodium dodecyl sulfate (SDS) as a surfactant resulted in an accumulation of spherical nanoparticles of $NiMn_2O_4$ with good interconnection between them. A specific capacitance of 1937 F g^{-1} was obtained for this sample coated on nickel foam. A two-electrode asymmetric device has been fabricated using the SDS-assisted hydrothermally synthesized powder sample as a positive electrode and activated carbon as a negative electrode. The device offers a specific capacitance of 270 F g^{-1} with excellent cyclic stability and good power and energy density.

As the conducting pathways provided by the nickel foam enhance the electrochemical performance, we tried to form $NiMn_2O_4$/Carbon fiber using the RJ-spin technique. For this purpose, the same SDS-assisted hydrothermally synthesized powder of $NiMn_2O_4$ was taken and was arranged in fiber form through RJ-spinning. Its electrochemical charge storage performance was compared to the powder sample to correlate the effect of morphology with the electrochemical performance. We have seen that the fibrous sample offered a specific capacitance of 460 F g^{-1} compared to the specific capacitance value of 405 F g^{-1} provided by the powder sample. It was also seen that the fibrous sample offered good rate capability and less resistance to current flow.

Chapter 1

Introduction

1.1 Introduction

At the dawn of human civilization, energy in the form of fire was the prima facie requirement for society to sustain. We have come along a long way with the blessing of our constructive scientific thinking. Today we have learned to utilize the different natural resources to generate the energy we need. Non-renewable resources such as coal, petroleum, and nuclear fuel are at the heart of energy production today. Presently, the world's 74% energy requirement is mitigated by these non-renewable sources (figure 1.1.1) [1]. The utilization of these energy sources has brought the industrial revolution, and our society has seen colossal growth in terms of living quality and economic prospects. However, an uncontrolled utilization of these limited natural resources has brought a few problems which are needed to be addressed. Firstly, these natural resources take millions of years to form, and hence they are limited for usage for the very long term. The present rate at which coal is being mined can sustain us for 100 more years or less, and the same is even worse with petroleum, with a time limit of only 40 years [2]. Secondly, these energy sources emit many different greenhouse gases as a by-product, increasing the pollution level in the atmosphere risking the health of all the living creatures on this planet [3-5]. Nuclear energy also belongs to a class of non-renewable energy sources. However, like other non-renewable sources, it is clean and carbon-free. The fuel for generating nuclear
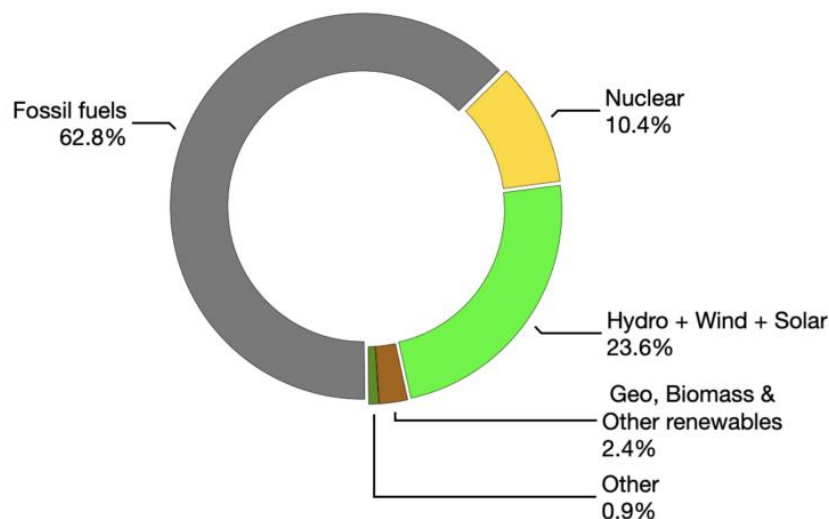
Figure 1.1.1: World's energy generation% from different sources

energy is also very cheap. But fuel price is only a minor fraction of the high total cost, which includes the cost of infrastructure building, radioactive waste management, and radiation safety. As the initial investment requires a lump sum amount of capital,

nuclear energy generation has not seen a high growth as it was expected during the early stage of development. For example, in India, the total electrical energy generated in 2020-2021 was 43 TWh. This was only 3.11% of the total electricity generation during that year, and it is very much less than the global average of 10%. Different renewable energy sources like solar, wind, tidal, etc., produce clean and endless energy. Considering only solar, the total amount of energy received by earth is around 7000 to 8000 times the annual global requirement [6-7]. Thus, these sources have the capability to meet the world's demand for energy. Different countries are adopting various policies to use these renewable sources efficiently. This has led to billions of dollars in the research of efficient utilization of these renewable energy sources. Tremendous research effort during the last few decades has revolutionized this field. However, there is a crucial drawback for energy generation from these renewable sources. When it is cloudy or night, the solar cell cannot generate power. It is the same story with wind power. No wind means no wind power. Tidal power, on the other hand, can provide uninterrupted energy. However, tidal power stations require a high initial investment to make the whole assembly corrosion-proof also affects the marine lives in the local water body. India had initiated two tidal power projects of 3.75 megawatts and 50 megawatts in West Bengal (2007) and Gujarat (2011), respectively. However, both these projects were cancelled because of inflated costs. Till date, there is no commercial tidal energy generation plant in our country. Because of this high initial cost, tidal energy is still not a popular renewable energy source. For the other renewable sources, the intermittent nature of energy production is the leading cause of the lack of popularity. Recently, grid-connected solar systems have seen an upsurge. Different countries, including India, have tried to motivate their citizens to install roof-top grid-connected solar systems equipped with the net-metering facility. This type of system generates power during the day, and part of this is used to meet the demand of the building, and the rest is fed to the grid system to be used in other places. This reduces the electricity bill of the building, and thus it was thought it would bring revolution to the energy sector. However, these grid-connected systems have a serious drawback. During the peak generation time of the day, the energy fed to the grid is high, whereas, during the night, when there is no generation, energy is taken from the grid to meet the electricity requirement of the building during the night. To maintain the grid balancing correspondingly during day, the power generated from different thermal plants has to be reduced, and during the night, it has

to be again increased. As thermal plants are a high inertial system, a change in their capacity during a day is not possible. Thus national grid policy limits a certain percentage of renewable electrical energy to be connected to the grid. This percentage varies in different countries and depends on the demands and available solar energy.

Apart from the pollution generated from different electrical power plants, the transportation sector also contributes to air pollution significantly. Figure 1.1.2 (a) shows the worldwide percentage of air pollution from a different mode of transportation for the year 2020. It can be seen; passenger cars contribute to the most pollution. To reduce this part, electric vehicles (EVs) are being developed and are

(a)

- Rail 3%
- Two/three–wheelers 3%
- Light commercial vehicles 5%
- Buses and minibuses 7%
- Aviation 8%
- Shipping 11%
- Passenger cars 41%
- Medium and heavy trucks 22%

(b)
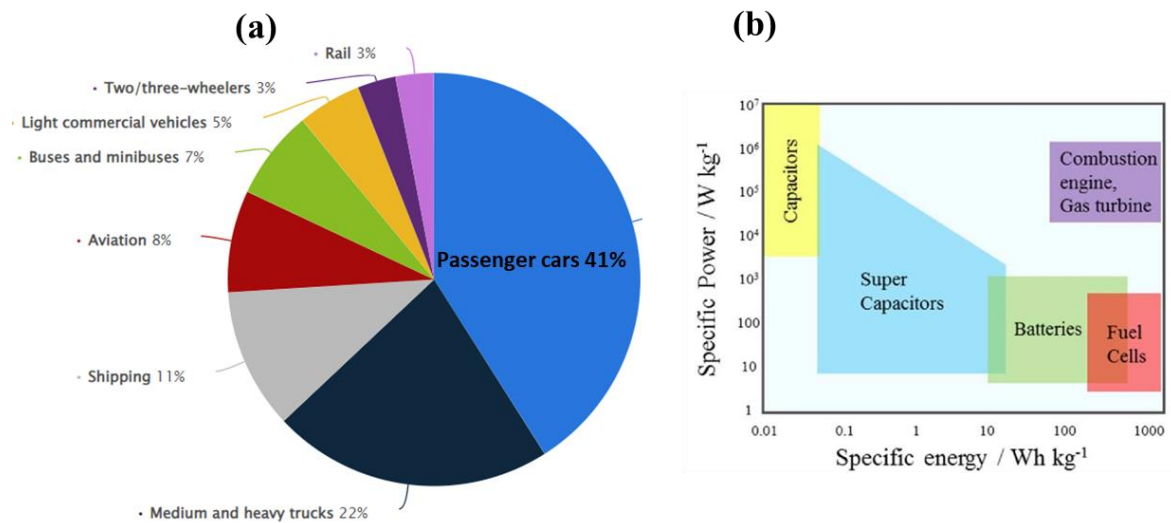
Figure 1.1.2: (a) Worldwide percentage of air pollution from transportation sector (a) Ragone plot for different energy storage devices

already running on the road. To popularize these EVs, suitable and cost-effective energy storage systems are required to replace polluting combustion engines. However, it must have to be ensured to charge these EVs via renewable energy sources. Otherwise, there will be indirect pollution from these EVs if they are charged from non-renewable sources.

The problems of the intermittent nature of energy production from renewable energy sources as well as the pollution from the transport sector can be addressed by developing suitable energy storage systems. At present, there are different energy storage systems like electrolytic capacitors, batteries, fuel cells, etc. [8-13]. Capacitors can store a very small amount of energy and can deliver it within a very short period of time. On the other hand, batteries and fuel cells can store a huge amount of energy

but they cannot deliver it quickly like a capacitor. Figure 1.1.2 (b) shows the typical power density vs. energy density plot (also known as the Ragone plot) for different energy storage devices [14, 15]. As can be seen from figure 1.1.2, capacitor possesses very high power density and very less energy density, whereas batteries and fuel cells possess high energy density but low power density. Combustion engine based on non-renewable petroleum source offers very high energy density and moderate power density. The supercapacitor is a relatively new energy storage technology that bridges
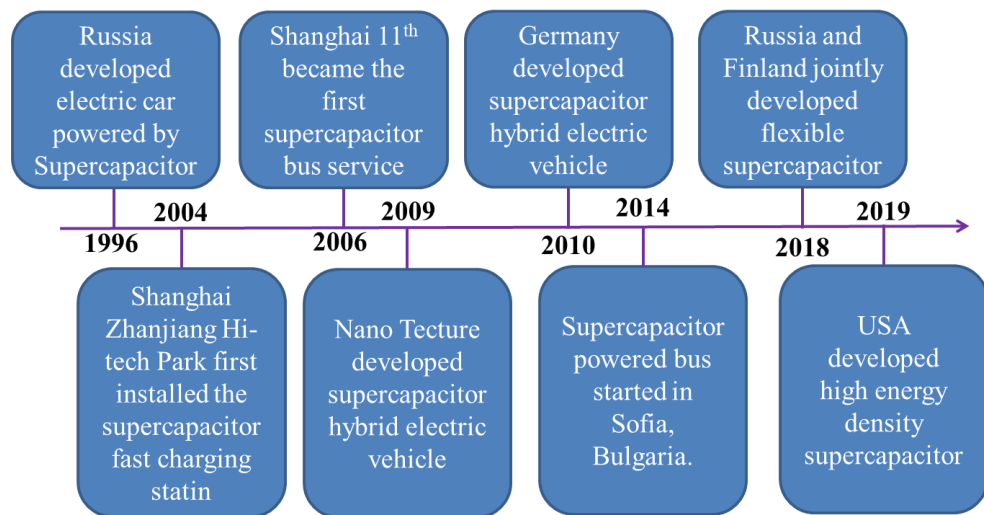
Figure 1.1.3: Development of Supercapacitor in different countries

the gap between batteries and capacitors [16-20]. These devices can deliver higher power density than the batteries and possess energy density higher than the conventional electrolytic capacitors. There are several advantages of supercapacitors over batteries. Supercapacitor takes very little time to charge. In some cases, they are nearly 1,000 times faster than the charge time for a similar-capacity battery [21, 22]. Owing to the quick charging time, supercapacitors are used to harvest energy from the regenerative brakes of hybrid cars. The operating temperature of the supercapacitor is much higher than the batteries. With proper insulation packages, the operating temperature can range between -40° and 85 °C [23, 24]. In terms of repeated use, the supercapacitor is much safer than the battery. It being smaller in size than a battery of similar capacity, supercapacitor takes little space in a contemporary device. Different countries have already developed supercapacitors of different storage capacities, and these have been used to power various devices. Figure 1.1.3 shows the development of supercapacitors in different countries.
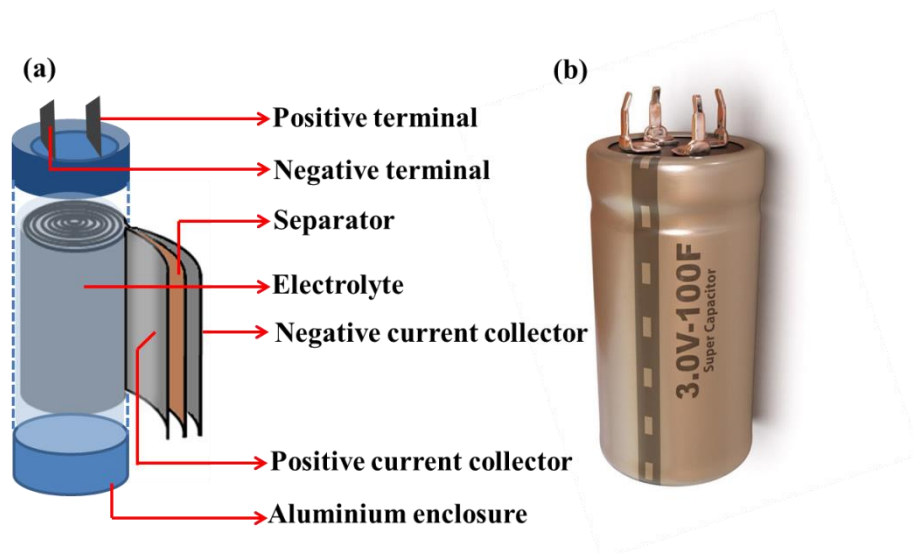
Figure 1.1.4: (a) Schematic of a commercial supercapacitor device. (b) Image of a commercial supercapacitor device

Presently the majority of the commercially available supercapacitors are manufactured from carbon-based film material where the presynthesized activated carbon is hot pressed on conducting steel or on aluminum foils. Here, steel or aluminum foils act as current collectors. The choice of the current collector is crucial. It should possess high electrical conductivity and the ability to bind the electrode material. For some applications, as in the wearable industry, the current collector has to be flexible enough to allow mechanical bending of the devices. Two such carbon-coated steel or aluminum foils are placed in close proximity separated by a separator, as shown in figure 1.1.4 (a). The separator is soaked in a suitable electrolyte. A cylindrical roll is kept inside a cylindrical aluminum enclosure. Carbon has a higher surface area which aids in the storage of a huge quantity of charges on the surface. Figure 1.1.4 (b) shows the image of a commercial supercapacitor device. However, as the storage mechanism, in this case, is purely based on the formation of double layer of charges (Electric Double Layer) [25], the energy density obtained from such a device is not very high.

As an alternative to the carbon-based electrodes, researchers around the globe are working with various transitional metal oxides based, or conducting polymer-based electrodes, such as ruthenium(IV) oxide(RuO_2), manganese(IV) oxide (MnO_2), vanadium pentoxide (V_2O_5), titanium dioxide (TiO_2), iron(III) oxide (Fe_2O_3), polyaniline(PANI), polypyrrole, PEDOT: PSS, etc. [26-28].   These electrodes can

6

store a large quantity of charges via fast and reversible redox reaction with an appropriate electrolyte and provide higher capacitance than that of the EDLC counterpart. However, the problems with these electrodes are that they offer very high resistance to charge flow. This increases the resistance of the device and impedes power delivery. Alongside, as the charge storage mechanism involves repeated redox reaction cycles, these electrodes get degraded over time. To address these issues, researchers have combined different carbon-based materials with a metal oxide to form composite [29-31]. Different carbonaceous materials not only provide the conducting paths for the electron through the redox-active sites but also provide structural support to the redox-active material to prevent large volumetric strain during repeated charge-discharge cycles. Thus ideal electrode material for supercapacitor should pose the following properties:

- Good electronic conductivity
- High surface area
- Optimum porosity
- Excellent chemical stability
- Ability to perform fast and reversible redox reactions
- High specific capacitance
- Low cost
- Environmental friendly

All these properties cannot be found in a single electrode material. Thus a large volume of research is necessary to tune these properties for particular electrode material. Presently, supercapacitor suffers from the drawback of relatively low energy density and high self-discharge rate. To address the issue of low energy density, researchers around the globe are trying to develop a new type of energy storage device, which is a hybrid of supercapacitor and battery and is known as Supercapattery [32], where a battery-type electrode is assembled with a capacitive type electrode. Thus both high power density and energy density can be obtained from such devices. To address the issue of high self-discharge of supercapacitor, different engineered separators are used with different combinations of electrolytes. Thus the field of supercapacitor research is very vast and wide open. Researchers around the

globe are constantly trying to find a suitable combination of materials and also trying different material engineering techniques to address the drawbacks of these devices.

1.2 Motivation behind the thesis

Sustainable development of human civilization requires efficient utilization of all-natural resources. From the previous discussions, it is pretty much clear that renewable energy is the future, and it is the most important requirement for sustainability. Guided by this fact, researchers from different countries, including India, have invested efforts in the research of energy generation from renewable sources. This has naturally led to the extension of research in the field of energy storage.

Among the different energy storage devices, the supercapacitor is a relatively new addition. It possesses moderate energy density, which is higher than the conventional capacitors, and moderate power density, which is higher than the batteries and fuel cells. Presently, the global market for supercapacitors is growing very fast. The main driving force behind this growth is the increasing demand for efficient and compact energy storage devices across various segments like electric vehicle, consumer electronics, power electronics, etc. According to the research conducted by the Allied Market Research, the supercapacitor market generated approximately $ 3.27 billion in 2019 worldwide. It is estimated that this market will reach a value of $ 16.95 billion in 2027, recording an astounding compound annual growth rate (CAGR) of 23% from 2020 to 2027. At present, the consumer electronics and electric vehicle industries are the two major segments where the demand for supercapacitors is highest. The rapid popularity of wearable electronics, mobile electronics, electric vehicles, etc., has accelerated this demand. To keep up with this pace of demand and need for more advanced energy storage solutions, extensive research is required to improve the performance of these storage devices.

Although having many advantages, commercial supercapacitors have a few disadvantages [33]. The major drawback is the low energy density. The Li-ion batteries used in cell phones generally have a specific energy of 100-200 Wh/kg. On the other hand, the supercapacitor of similar size can typically store 5 Wh/kg. To address this issue, as already mentioned, different transition metal oxides and

conducting polymers are being explored as an alternative to carbon-based electrodes. These alternative electrodes can store vast quantities of charges via reversible redox reaction with a suitable electrolyte. Presently, RuO_2 is the most promising electrode material for supercapacitors [34]. However, because of its high cost and poor impact on the environment, different alternatives are under investigation. MnO_2 is one such popular alternative because of its high theoretical capacitance, low cost, and environmental friendliness [35]. However, being a metal oxide, MnO_2 show very high resistance to current flow, which can hamper the performance of the electrode. This resistive nature of this single metal oxide can be addressed by forming double metal oxides such as $NiMn_2O_4$ [36]. Double metal oxides usually show much lower resistance compared to their single metal oxide counterpart [37]. Also, the presence of multiple valence states enhances their redox activity. A great deal of work is necessary to tune the synthesis scheme of these metal oxides to get the optimum result from the fabricated electrodes.

The overall performance of the metal oxide-based electrodes strongly depends on the morphology [38-40]. By optimizing the same, a connected network of redox-active sites can be formed within the electrode. The choice of proper morphology can even reduce the resistance of the electrode material and can also provide structural support to the electrodes. This structural support is beneficial for the long life of these electrodes. In a few recent works, the morphological effect of these metal oxides has been shown to improve the performance of the electrodes. But still, a good amount of research is necessary in this direction to fully utilize the potential of these oxide-based electrodes.

Hence, the motivation of this thesis work lies in the development of morphologically ordered oxide-based electrode materials for supercapacitor electrode application.

1.3 Objective of the Thesis

This thesis work is an attempt to find out the relationship between particle morphology and its electrochemical storage performance. Transition metal oxide-based electrodes can store huge charges, but because of their high resistive nature, these electrodes are of no practical use. By tuning the particle morphology, it is possible to tune the resistance of these metal oxides, which can be beneficial for

storage applications. Also, morphology tuning can allow us to increase the surface area of these materials, which is an added benefit for electrochemical charge storage. Among the different transition metal oxides, MnO_2 has been chosen as an alternative to RuO_2 for the reasons stated earlier. The electrospinning technique has been used to tune the morphology of MnO_2 in the form of fiber. The fiber type morphology was chosen because of the fact that different redox-active sites can be electrically connected through the carbonized fiber structure. Detailed electrochemical performance testing was carried out to establish the relation to the particle morphology with the electrochemical performance. However, electrospinning is a very low-yield process that requires very high voltage. We devised a simple Rotary Jet Spin (RJ-Spin) setup which is identical to the candy floss machine, to increase the yield of metal oxide fiber. MnO_2/C fiber was fabricated using the RJ-Spin setup, and its electrochemical performances were evaluated to find the effect of fibrous morphology. In an attempt to reduce the resistance of MnO_2 based electrodes and to enhance the charge storage performance, a bimetal oxide of Ni and Mn ($NiMn_2O_4$) was synthesized via a hydrothermal route. During the synthesis, different surfactants and mineralizer were used to tune the morphology of the synthesized $NiMn_2O_4$. By studying the detailed electrochemical performance, the effect of morphology of these different chemically equivalent samples was studied. Finally, to improve the electrochemical performance further, a fiber-like morphology of the $NiMn_2O_4$ was prepared using the RJ-spin technique and its electrochemical performance was compared to the powder sample to correlate the effect of morphology with the electrochemical performance.

1.4 Organization of the Thesis

The whole thesis work is divided into different chapters, and the content of each can be summarised as follows

Chapter 2 contains detailed discussions regarding the different parts of a supercapacitor device. The different charge storage mechanisms are also discussed elaborately. In the second part, a comprehensive literature review regarding a few recent research works on different electrode materials for supercapacitor has been included. Special emphasis has been given to MnO_2 and $NiMn_2O_4$. This chapter also includes a detailed discussion on the two-electrode supercapacitor device and its

different parts. As already mentioned, the morphology of the electrode materials plays a vital role in determining the overall charge storage performance. Hence, the later part of this chapter has been dedicated to discussing the different researches where the morphologies of the electrode materials have been tuned to get the optimum storage performance.

Chapter 3 discusses the details of different characterization facilities which have been used to pursue the thesis work. A brief working mechanism along with the schematic has been provided for the different facilities like XRD, SEM, TEM, BET, XPS, and FTIR. The working of the electrochemical characterization setup has been discussed in detail, along with the comprehensive procedure for electrochemical performance testing of an electrode material using both the three and two-electrode systems.

Chapter 4 describes the experimental section of the thesis work. In section 4.1, we have described the detailed synthesis scheme of ordered and disordered samples of MnO_2-GO. Section 4.2 discusses the synthesis of MnO_2 fiber using the RJ-Spin technique. The problem of high resistivity of MnO_2 has been addressed by synthesizing a bimetal oxide, namely $NiMn_2O_4$ using the hydrothermal technique. Different surfactants and mineralizers have been incorporated separately during the synthesis to obtain different morphologies of $NiMn_2O_4$ with an aim to tune the charge storage performance. The experimental details are provided in section 4.3. Finally, the RJ-Spin technique has again been utilized to fabricate the fiber structure of $NiMn_2O_4$, with an aim to reduce the resistance further down. This has been discussed in section 4.4.

Chapter 5 discusses the results of the different characterizations and experimental findings for the different synthesized materials, which have already been discussed in the previous chapter. This chapter follows the same sequence as that of the previous chapter. Section 5.1 discusses the XRD, XPS, SEM of ordered and disordered samples of MnO_2-GO. The electrochemical charge storage properties in a three-electrode system and in a two-electrode system have also been discussed. The different experimental results, including the three-electrode and two-electrode electrochemical characterization of RJ-Spin, synthesized MnO_2 fiber, have been included in section 5.2. In section 5.3, physical, compositional, and electrochemical charge storage properties of hydrothermally synthesized $NiMn_2O_4$ have been

discussed. Detailed discussions on the formation mechanism of different morphological variants have been included. Finally, section 5.4 has been devoted to discussing the experimental results of RJ-Spin synthesized $NiMn_2O_4$ fiber. Its electrochemical storage performance has been compared with the powder $NiMn_2O_4$ sample to find out the morphological effect on the electrochemical performance.

Chapter 6 summarizes all the experimental results and concludes the thesis with all the major findings. Finally, the later part of this chapter is devoted to the discussion on further future scope of work.

1.4 References

[1] Statistical Review of World Energy, 2020, 69th edition, BP (British Petroleum).

[2] Statistical Review of World Energy, 2016, BP (British Petroleum).

[3] F. Perera, Pollution from Fossil-Fuel Combustion is the Leading Environmental Threat to Global Pediatric Health and Equity: Solutions Exist. *Int J Environ Res Public Health*. 15 (2017) 1 doi:10.3390/ijerph15010016

[4] J. Lelieveld, K. Klingmüller, A. Pozzer, R. T. Burnett, A. Haines, V. Ramanathan, Effects of fossil fuel and total anthropogenic emission removal on public health and climate. *Proceedings of the National Academy of Sciences* 116 (2019) 7192-7197 doi: 10.1073/pnas.1819989116

[5] F. Johnsson, J. Kjärstad & J. Rootzén, The threat to climate change mitigation posed by the abundance of fossil fuels, *Climate Policy*, 19 (2019) 258-274 doi: 10.1080/14693062.2018.1483885

[6] L. Hammarström, Overview: capturing the sun for energy production. *Ambio*. 41 (2012) 103-107 doi:10.1007/s13280-012-0263-8

[7] M. I. Sohail, A. A. Waris, M. A. Ayub, M. Usman, M. Z. Rehman, M. Sabir, T. Faiz, Chapter One - Environmental application of nanomaterials: A promise to sustainable future. *Comprehensive Analytical Chemistry*, Elsevier, 87 (2019) 1-54, ISSN 0166-526X, ISBN 9780128213209 doi: 10.1016/bs.coac.2019.10.002.

[8] R. Elliman, C. Gould and M. Al-Tai, Review of current and future electrical energy storage devices. *50th International Universities Power Engineering Conference (UPEC)*, (2015) 1-5 doi: 10.1109/UPEC.2015.7339795.

[9] A. Zayed, A. L. Shaqsi, K. Sopian, A. Al-Hinai, Review of energy storage services, applications, limitations, and benefits. *Energy Reports*, 6 (2020) 288-306 doi: 10.1016/j.egyr.2020.07.028.

[10] J. B. Goodenough, Rechargeable batteries: challenges old and new. *J Solid State Electrochem* 16 (2012) 2019–2029 https://doi.org/10.1007/s10008-012-1751-2

[11] J. B. Goodenough, Evolution of Strategies for Modern Rechargeable Batteries. *Accounts of Chemical Research,* 46 (2013) 1053-1061 doi: 10.1021/ar2002705

[12] A. Kirubakaran, S. Jain, R. K. Nema, A review on fuel cell technologies and power electronic interface, *Renewable and Sustainable Energy Reviews*, 13 (2009) 2430-2440 doi: 10.1016/j.rser.2009.04.004

[13] A. Choudhury, H. Chandra, A. Arora, Application of solid oxide fuel cell technology for power generation—A review. *Renewable and Sustainable Energy Reviews*, 20 (2013) 430-442 doi: 10.1016/j.rser.2012.11.031.

[14] P. J. Hall, E. J. Bain, Energy-storage technologies and electricity generation, *Energy Policy*, 36 (2008) 4352-4355 doi: 10.1016/j.enpol.2008.09.037.

[15] B. D. McCloskey, Expanding the Ragone Plot: Pushing the Limits of Energy Storage. *The Journal of Physical Chemistry Letters,* 6 (2015) 3592-3593 doi: 10.1021/acs.jpclett.5b01813

[16] A. González, E. Goikolea, J. A. Barrena, & R. Mysyk, Review on supercapacitors: Technologies and materials. *Renewable and Sustainable Energy Reviews*, 58 (2016) 1189-1206 doi: 10.1016/j.rser.2015.12.249

[17] K. Sharma, A. Arora, & S. K. Tripathi,. Review of supercapacitors: Materials and devices, *Journal of Energy Storage*, 21 (2019) 801-825 doi: 10.1016/j.est.2019.01.010

[18] K. V. G Raghavendra, R. Vinoth, K. Zeb, C. V. M. Gopi, S. Sambasivam, M. R. Kummara, & H. J. Kim, An intuitive review of supercapacitors with recent progress and novel device applications. *Journal of energy storage*, 31 (2020) 101652 doi: 10.1016/j.est.2020.101652

[19] J. Zhao, & A. F. Burke, Review on supercapacitors: Technologies and performance evaluation. *Journal of Energy Chemistry*, 59 (2021) 276-291 doi: 10.1016/j.jechem.2020.11.013.

[20] A. Muzaffar, M. B. Ahamed, K. Deshmukh, & J. Thirumalai, A review on recent advances in hybrid supercapacitors: Design, fabrication and applications. *Renewable and sustainable energy reviews*, 101 (2019) 123-145 doi: 10.1016/j.rser.2018.10.026

[21] A. G. Pandolfo, A. F. Hollenkamp, Carbon properties and their role in supercapacitors, *Journal of Power Sources*, 157 (2006) 11-27 doi: 10.1016/j.jpowsour.2006.02.065

[22] A. Pasquier, I. Plitz, S. Menocal, G. Amatucci, A comparative study of Li-ion battery, supercapacitor and non-aqueous asymmetric hybrid devices for automotive applications, *Journal of Power Sources*, 115 (2003) 171-178 doi: 10.1016/S0378-7753(02)00718-8

[23] E. Iwama, P. L. Taberna, P. Azais, L. Brégeon, P. Simon, Characterization of commercial supercapacitors for low temperature applications, *Journal of Power Sources,* 219 (2012) 235-239 doi: 10.1016/j.jpowsour.2012.07.029

[24] K. Hung, C. Masarapu, T. Ko, B. Wei, Wide-temperature range operation supercapacitors from nanostructured activated carbon fabric, *Journal of Power Sources,* 193 (2009) 944-949 doi: 10.1016/j.jpowsour.2009.01.083

[25] P. Sharma, T. S. Bhatti, A review on electrochemical double-layer capacitors, *Energy Conversion and Management*, 51 (2010) 2901-2912 doi: 10.1016/j.enconman.2010.06.031

[26] Y. Jiang, & J. Liu,. Definitions of pseudocapacitive materials: a brief review. *Energy & Environmental Materials*, 2 (2019) 30-37 doi: 10.1002/eem2.12028

[27] R. Chen, M. Yu, R. P. Sahu, I. K. Puri, I. Zhitomirsky, The Development of Pseudocapacitor Electrodes and Devices with High Active Mass Loading. *Adv. Energy Mater*, 10 (2020) 1903848 doi:10.1002/aenm.201903848

[28] N. R. Chodankar, H. D. Pham, A. K. Nanjundan, J. F. S. Fernando, K. Jayaramulu, D. Golberg, Y. K. Han, D. P. Dubal, True Meaning of Pseudocapacitors and Their Performance Metrics: Asymmetric versus Hybrid Supercapacitors. *Small*, 16 (2020) 2002806 doi:10.1002/smll.202002806

[29] S. Kumar, G. Saeed, L. Zhu, K. N. Hui, N. H. Kim, & J. H. Lee, 0D to 3D carbon-based networks combined with pseudocapacitive electrode material for high energy density supercapacitor: A review. *Chemical Engineering Journal*, 403 (2021)126352 doi: 10.1016/j.cej.2020.126352

[30] R. A. Fisher, M. R. Watt, & W. J. Ready, Functionalized carbon nanotube supercapacitor electrodes: a review on pseudocapacitive materials. *ECS Journal of Solid State Science and Technology*, 2 ((2013)) M3170 doi: 10.1149/2.017310jss

[31] A. Ehsani, A. A. Heidari, & H. M. Shiri, Electrochemical pseudocapacitors based on ternary nanocomposite of conductive polymer/graphene/metal oxide: an introduction and review to it in recent studies. *The Chemical Record*, 19 (2019) 908-926 doi: 10.1002/tcr.201800112

[32] L. Yu, G. Z. Chen, Supercapatteries as High-Performance Electrochemical Energy Storage Devices. *Electrochem. Energ. Rev*. 3, (2020) 271–285. https://doi.org/10.1007/s41918-020-00063-6

[33] S. Huang, X. Zhu, S. Sarkar, and Y. Zhao, Challenges and opportunities for supercapacitors. *APL Materials* 7 (2019)100901 doi: 10.1063/1.5116146

[34] D. Majumdar, T. Maiyalagan, Z. Jiang, Recent Progress in Ruthenium Oxide-Based Composites for Supercapacitor Applications. *ChemElectroChem* 6 (2019) 4343 doi: 10.1002/celc.201900668

[35] D. Majumdar, Review on Current Progress of MnO_2-Based Ternary Nanocomposites for Supercapacitor Applications. *ChemElectroChem*, 8 (2021) 291-336 doi: 10.1002/celc.202001371

[36] S. D. Dhas, P. S. Maldar, M. D. Patil, M. R. Waikar, R. G. Sonkawade, S. K. Chakarvarti, & A. V. Moholkar. Probing the electrochemical properties of $NiMn_2O_4$ nanoparticles as prominent electrode materials for supercapacitor applications. *Materials Science and Engineering: B*, 271 (2021) 115298 doi: 10.1016/j.mseb.2021.115298

[37] A. Ray, A. Roy, S. Saha, M. Ghosh, S.R. Chowdhury, T. Maiyalagan, S.K. Bhattacharya, S. Das, Electrochemical energy storage properties of Ni-Mn-Oxide electrodes for advance asymmetric supercapacitor application, *Langmuir*, 35 (2019) 8257–8267 doi:10.1021/acs.langmuir.9b00955.

[38] S. Chen, W. Xing, J. Duan, X. Huc and S. Z. Qiao, Nanostructured morphology control for efficient supercapacitor electrodes, *J. Mater. Chem. A*, 1 (2013) 2941-2954 doi: 10.1039/C2TA00627H

[39] S. Kim, J. Lee, H. Ahn, H. Song, and J. Jang, Facile Route to an Efficient NiO Supercapacitor with a ThreeDimensional Nanonetwork Morphology, *ACS Appl. Mater. Interfaces,* 5 (2013) 1596−1603 doi: 10.1021/am3021894

[40] Z. Ye, T. Li, G. Ma, X. Peng, J. Zhao, Morphology controlled MnO_2 electrodeposited on carbon fiber paper for high-performance supercapacitors, *Journal of Power Sources*, 351 (2017) 51-57 doi: 10.1016/j.jpowsour.2017.03.104

Originality Report for Chapter 1

(*Generated using Ithenticate Software excluding the first author publications of Mr. Samik Saha)

Chapter 1

ORIGINALITY REPORT

1%
SIMILARITY INDEX

PRIMARY SOURCES

1. ebin.pub
   Internet
   11 words — < 1%

2. S.A. Hashmi, Ashok Kumar, S.K. Tripathi. "Investigations on electrochemical supercapacitors using polypyrrole redox electrodes and PMMA based gel electrolytes", European Polymer Journal, 2005
   Crossref
   9 words — < 1%

3. www.eecs.ucf.edu
   Internet
   9 words — < 1%

4. Mitsuie Matsumura, Chika Hirai. "Transport Mechanism of Electrolyte Vapor to Reforming Catalyst", Industrial & Engineering Chemistry Research, 1998
   Crossref
   8 words — < 1%

5. X. Y. Zhou, A. Pramuanjaroenkij, S. Kakaç. "Chapter 21 A Review on Miniaturization of Solid Oxide Fuel Cell Power Sources-I: State-of-The-Art Systems", Springer Science and Business Media LLC, 2008
   Crossref
   6 words — < 1%

EXCLUDE QUOTES   OFF   EXCLUDE MATCHES   OFF
EXCLUDE BIBLIOGRAPHY   OFF

Chapter 2

Literature Review

2.1 Introduction

A capacitor can temporarily store electric charge. The conventional capacitor can be charged and discharged very quickly. The Leyden jar (Figure 2.1.1 (a)) is believed to be the first capacitor invented by Pieter van Musschenbroek at the University of Leyden in Netherland back in the year 1746. A glass jar was wrapped inside and outside using a thin metal foil [1,2]. The foil in the inner side was connected to a potential source, while the foil in the outer side was connected to the ground. It was seen that this arrangement of metal foils could store electric charge even after the device was disconnected from the source of electricity. However, the mechanism of such charge storage phenomena was unknown at that time.

Figure 2.1.1 (a) Leyden jar (b) From left: ceramic capacitor, ceramic (disc shaped), polyester film capacitor, tubular ceramic capacitor, polystyrene, metalized polyester film, aluminium electrolytic capacitor

Fast forward to the 21st century, today, commercial capacitors are available in many different types, forms, and shapes with varying capacities. These capacitors contain two conducting plates kept in close proximity separated by an insulating spacer. The incorporation of such insulating film enhances the permittivity of free space and increases the charge storage capability. When a potential is applied across its two terminals, the positive and negative charges move towards the plates of opposite polarity and thus, an electrostatic field is established. Now the capacitor is said to be charged. This charged capacitor, when connected via an external circuit, can drive a load by utilizing the electrostatic energy stored in the electric field. At the end of this operation, the capacitor is said to be discharged when it no longer contains any charge. The capacitance of a capacitor which is the measure of how much charge can be stored on a particular device, is the ratio of electric charge to the potential difference between the terminals. Its SI unit is farad (F) and given by the equation (2.1.1).

$$Farad = \frac{Coulomb}{Volt} \qquad\qquad (2.1.1)$$

At the earlier stage of development, a paper was used as the insulating spacer. Those devices could store charges at high voltages. But paper-based capacitor was not suitable for a humid environment as it can absorb moister and can short circuit the two conducting plates. Nowadays, different spacers are used, including plastic films, different ceramic materials (a mixture of ferroelectric or paraelectric substances), glass, mica, etc. Ceramic capacitors are small in size and hence suitable for on-chip applications. Another type of capacitor is the electrolytic capacitor which contains a metal plate (made of aluminum or tantalum) coated with an oxide insulating layer. This metal plate acts as a positive electrode, whereas the negative electrode in such capacitors is made of a liquid electrolyte. These types of capacitors offer very high capacitance because of the ultra-thin spacer and large anode surface. However, electrolyte capacitors suffer from the drawback of poor stability and high leakage current [3–5].

The different form of conventional capacitors as discussed, all store charges via the formation of electrostatic field. Hence these are all passive devices. Supercapacitors are relatively new energy storage devices that can store large amounts of energy than conventional capacitors and demonstrate higher power density than rechargeable batteries. General Electric company first patented the commercial-grade supercapacitor in 1957, which was based on the formation of electric double layer in lamp black-based electrode [6]. Electrodes that are made of activated carbon, carbon aerogel, carbon nanotubes (CNT), graphene etc., offer extremely high capacitance (~ 12 kF as of 2020) and are finding different applications replacing the use of Li-ion batteries in some cases [7].

2.2 Different classes of supercapacitors

According to the charge storage mechanism, supercapacitors can be categorized into two main groups, namely, electric double layer capacitor (EDLC) and pseudocapacitor (Figure 2.2.1) [8–11]. As the name suggests, EDLC mainly store charges electrostatically. The charge storage capacity of such capacitors is significantly governed by the surface area of the material composing the electrode. Different carbonaceous materials like porous carbon, activated carbon, graphene,
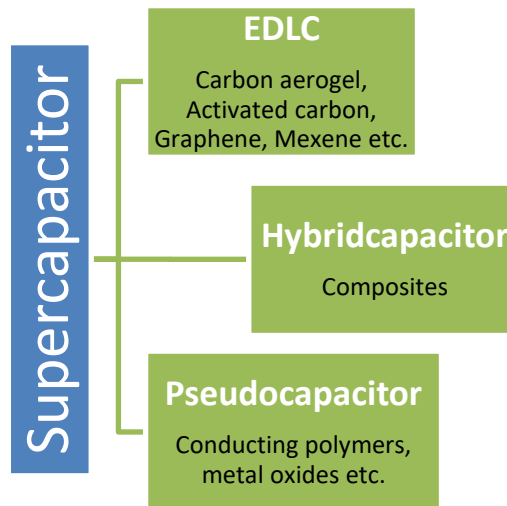
Figure 2.2.1 Classification of supercapacitor

carbon nanotube (CNT), carbon aerogel, etc., are utilized as supercapacitor electrode materials because they offer a very high ratio of surface to volume. On the contrary, different oxides of different transition metals and few conducting polymer-based electrodes constitute the class of pseudocapacitor [12,13]. These electrodes store charges faradically, i.e., by performing reversible redox reactions with the electrolyte. However, redox-active material in nano form can store charges both electrostatically and faradically due to a rise in the surface-to-volume ratio. In this case, these supercapacitors are called hybrid capacitors and yield a very high capacity value owing to the contribution from both these mechanisms. In the following section, we will briefly discuss different mechanisms responsible for charge storing in the supercapacitor.

2.2.1 Electric double layer capacitor (EDLC)

Various carbonaceous materials are coated on suitable current collectors such as steel plates, aluminum foil, etc., to fabricate the electrodes for EDLCs. Two such electrodes are kept in close proximity, separated by a separator soaked in a suitable electrolyte. In this process, no transfer of charge occurs between electrodes and electrolytes. The principle mechanism of energy storage by EDLCs is the formation of an electrochemical double layer. When a potential difference is established between the electrodes, charges are accumulated on electrode surfaces. Owing to the attraction of opposite charges, the respective ions from the electrolyte diffuse over the separator onto the pores of the oppositely charged electrodes. The double layer of

21
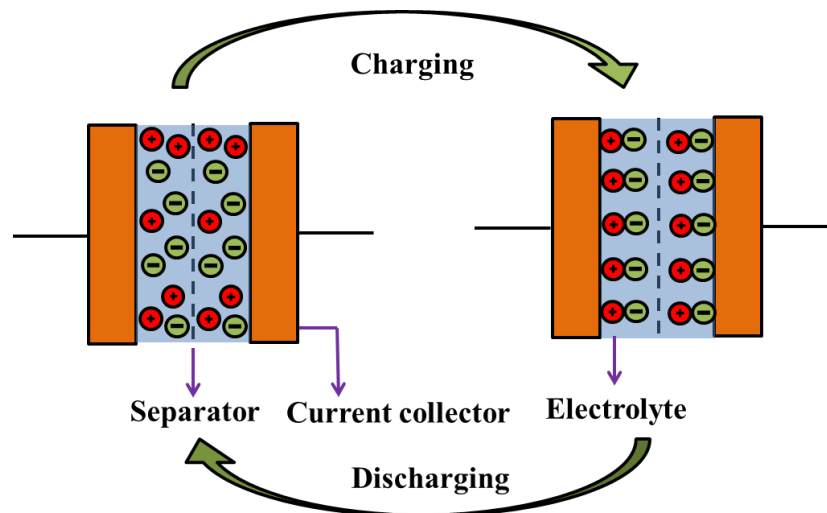
Figure 2.2.2 Simplified model of charge storage in EDLC

charge, thus formed, prevent further recombination of ions at the electrodes. The length of a typical double layer can be of the order of a few angstroms. Figure 2.2.2 shows the charging and discharging state of an EDLC device. As the storage mechanism is purely physical, EDLCs allow very fast energy delivery implying high power density. Additionally, the physical mechanism eliminates the swelling, usually observed in batteries, which is mainly due to the recurrent faradic charge-discharge cycles. Thus, the lifetime of EDLCs can be very long. However, due to the physical mechanism of charge storage, EDLCs provide very little energy density, and hence further research is necessary to improve the same [14].

Detailed storage mechanism: Formation of double layer

When charged using an external power source, surfaces immersed in an electrolyte solution attract ions of similar charge and repeal the counter ions. Thus, two layers of charge are formed. One layer contains the charge on the surface, and the other layer contains the counter ions. These two layers are separated by an atomic distance; *d*. Helmholtz first theoretically modelled this structure which is recognized as electric double layer. This model assumes the electric potential has a maximum value of Ψ_0 on the surface and gradually falls to zero value in the electrolyte solution. This variation of potential from a maximum value to zero is observed on the atomic dimension *d*. This variation has been shown in figure 2.2.3 (a). Thus Helmholtz assumed that the layers of opposite kinds of charges are immobilized on the surface due to electrostatic attraction. Later, Gouy and Chapman suggested that ions near the
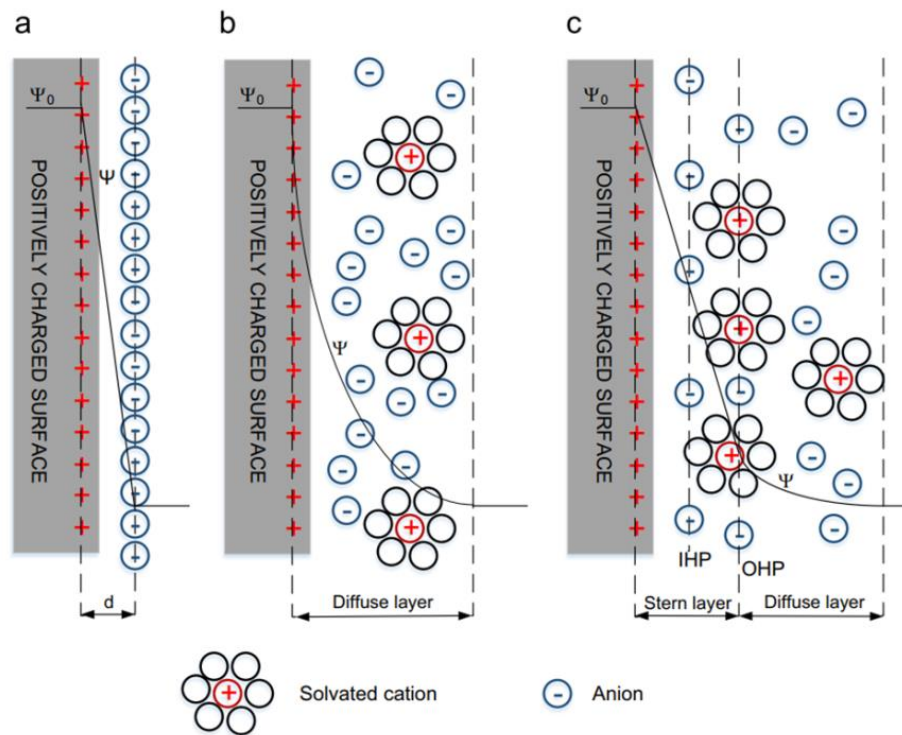
Figure 2.2.3 Schematics of double layer formation at a charged surface. (a) Helmholtz model (b) Gouy-Chapman and (c) Stern model

surface of the surface are in continuous random thermal motion; thus, they cannot remain fixed rather, the ions diffuse into the solution and form a relatively thick layer called a diffuse double layer. Gouy and Chapman modified the Helmholtz model by assuming the potential to decay more slowly, as shown in figure 2.2.3 (b). But this model overestimates the value of double layer capacitance. Thus, these two models do not provide a proper description of the double layer formed. Stern combined both these two models. It was assumed in Stern's model that there are two layers of ionic charge distribution. The layer close to the surface is known as the Stern layer, and the other layer is known as the diffuse layer, as shown in figure 2.2.3 (c). The Stern layer resembles the layer which was assumed to form in the Helmholtz model. Thus the ions in this layer are strongly adsorbed by the electrode and are immobile. The outer Helmholtz plane (OHP) and inner Helmholtz plane (IHP) are two imaginary planes that are used to distinguish the two types of adsorbed ions. The outer layer or the diffuse layer is much similar to that assumed in the Gouy-Chapman model. In the Stern model, the total double layer capacitance (C_{dl}) can be estimated from the capacitances arising out of the Stern layer (C_H) and the outer diffusion layer (C_{diff}) using the equation (2.2.1) [15, 16]:

$$\frac{1}{C_{dl}} = \frac{1}{C_H} + \frac{1}{C_{diff}}$$

<div align="right">(2.2.1)</div>

The capacitance due to double layer depends on many factors like surface area and the porosity of the electrode material, size of electrolyte ions and its ionic conductivity, accessibility of these electrolyte ions in the electrode surface, chemical affinity of the electrode surface to the electrolyte ions, etc. In summary, EDLCs store charges via the formation of an electric double layer at the interface of the high surface area carbon electrode and the electrolyte. Its storage capacity can be very high (from a few farads to thousands of farads) compared to the conventional capacitor (from few μF to few mF) because of the large surface area electrode [17].

2.2.2 Pseudocapacitor

The mechanism of charge storage in the pseudocapacitor electrode is different from EDLC. When a potential is applied externally to the electrode, the active materials undertake a reversible and fast redox reaction (or faradic reaction), which involves the movement of charges across the double layer through the electrolyte. This kind of redox reaction is also responsible for energy storage in a battery. However, in the case of pseudocapacitor, this redox reaction is very fast, which results in a relatively high power density compared to batteries [18]. Different transition metal oxides like RuO_2, MnO_2, V_2O_5, etc., along with a few conducting polymers like PANI, PEDOT: PSS, polypyrrole, etc., are currently under consideration to be used as electrode materials [19–23]. These electrode materials can perform a fast redox reaction with suitable electrolytes. The storage mechanism is slow in the case of pseudocapacitor because of the chemical reaction involved. For this reason, the pseudocapacitor usually shows less power density compared to the EDLC.

Detailed storage mechanism

Different faradaic mechanisms can lead to pseudocapacitive charge storage phenomena. This mainly depends on the type of active material. These mechanisms are [24, 25]:

a) Underpotential Deposition: Underpotential deposition or adsorption pseudocapacitance arises when metal ions from the electrolyte solution are adsorbed on the current collector forming a monolayer [26, 27]. This occurs when a potential is

<div align="center">24</div>

less negative than the equilibrium or Nernst potential for the reduction of the metal. Deposition of lead on the gold surface is an example of such deposition as shown via the reversible chemical reaction (2.2.2).

$$2e + xPb^{2+} + Au \leftrightarrow Au.xPb \tag{2.2.2}$$

During the charging, Pb^{2+} ions from the electrolyte solution get deposited on the gold surface by accepting or storing two electrons. As the process is reversible, the opposite phenomenon occurs during the discharging, resulting in two electrons' release. Figure 2.2.4 (a) shows such a mechanism of charge storing.
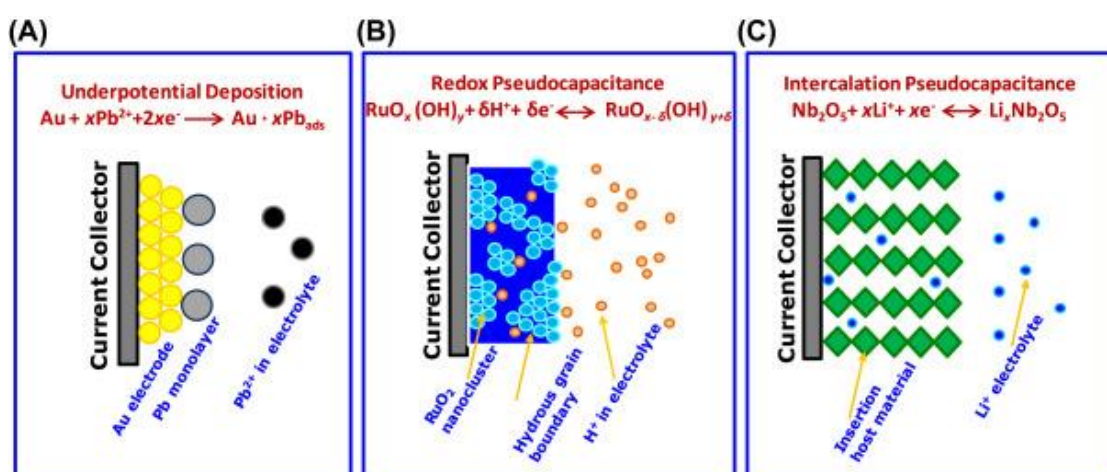
Figure 2.2.4 Different mechanisms of pseudocapacitive charge storage. (a)Underpotential deposition (b) redox pseudocapacitance (c) intercalation pseudocapacitance.

b) Redox Pseudocapacitance: Redox pseudocapacitance occurs when the ions from the electrolyte surface are adsorbed near the surface of the active material via a fast and reversible faradic charge transfer. Hydrous RuO_2 shows this type of pseudocapacitance. While charging, the RuO_2 accepts protons from the electrolyte and releases them back during the discharge process. Protons from the electrolyte solution interact only with the surface (within 10 nm of the surface) of the active material, and this faradic process does not involve phase change of the active material [28]. Figure 2.2.4 (b) shows the redox pseudocapacitance mechanism.

c) Intercalation Pseudocapacitance: Pseudocapacitive charge storage via intercalation of ions in the bulk of the active materials occurs when the ions from the electrolyte solution penetrate deep into the active material and perform reversible redox reactions. Intercalation pseudocapacitance is possible only when the active material has a tunnel or layer-like structure. For this reason, only a few materials show this

type of charge storage like $t\text{-}Nb_2O_5$, $\delta\text{-}MnO_2$, etc. [29, 30]. Battery-type materials also show this type of storage mechanism. However, in the battery, the electrode suffers phase change, whereas in intercalation pseudocapacitance, no phase change occurs for the active material [31]. Figure 2.2.4 (c) shows the charge storage mechanism due to intercalation pseudocapacitance.

2.2.3 Hybrid supercapacitor

Electrode materials for hybrid supercapacitor store charges via both the physical and pseudocapacitive charge storage mechanisms [13]. Because of the contribution from both these two mechanisms, energy density and power density become very high for these types of materials. Composites of different carbonaceous materials with different redox-active materials constitute this class of hybrid electrode material. In these composites, carbon-based materials store charges via double layer formation, whereas the redox-active material stores charges via reversible faradic reactions with the electrolyte. Carbon-based elements also stabilize the redox-active material against the large volumetric strain suffered during the redox reaction by providing a backbone. Alongside, carbon-based elements provide a high way to the electrons, and thus conductivity of the sample increases. Usually, the carbon-based material is responsible for enhancing the power density, and redox-active material is responsible for enhancing the energy density of the composite. Composite of NiO-CNT, MnO_2-Graphene, PANI-CNT, etc., are examples of hybrid supercapacitor electrode materials [32–34].

2.3 Electrochemical characterizations to differentiate between the storing mechanisms

After synthesizing an electrode material, generally, three main characterizations are performed to test the charge storage performance of the material. These characterizations are performed in a three-electrode setup, as shown in figure 2.3.1 (a). Here 'CE' and 'WE' are the counter and working electrodes, respectively. The material under investigation is coated in a thin film form on the working electrode, which undergoes the redox reaction. The resulting current is measured between these two electrodes. The third one is the reference electrode which generates a constant reference potential with respect to which the potential of the working electrode can be measured. A few popular reference electrodes are the Calomel electrode
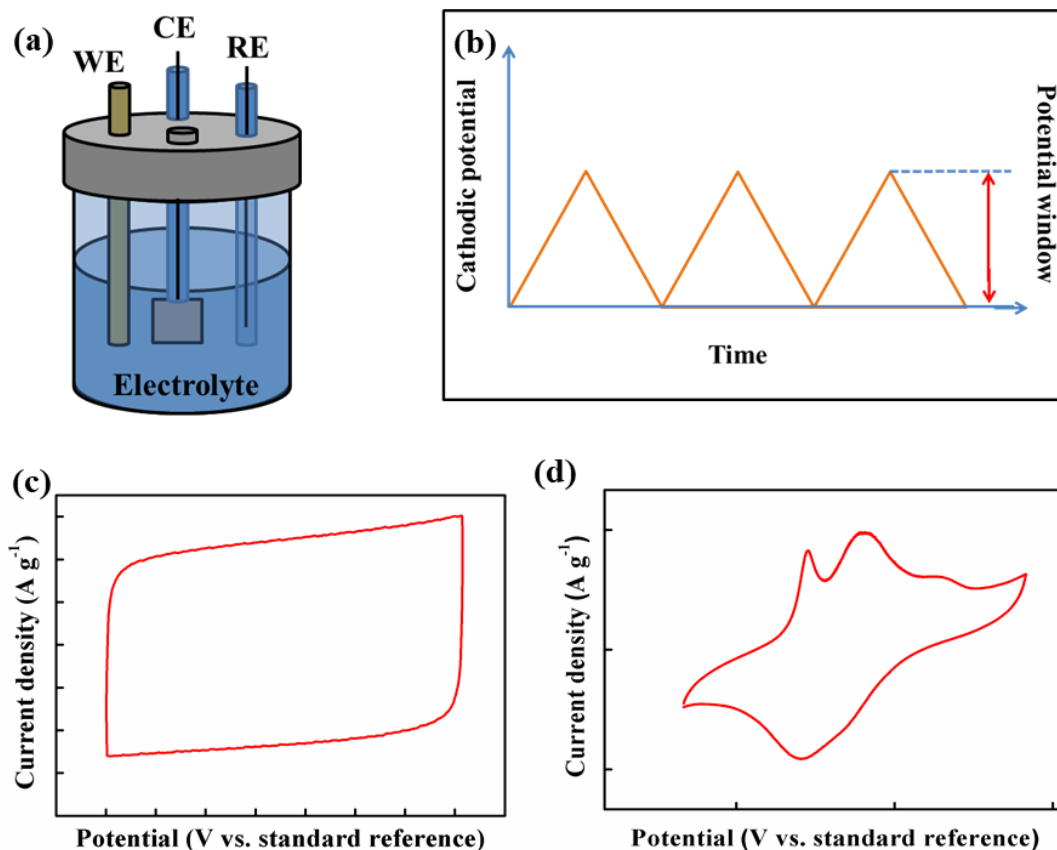
Figure 2.3.1 (a) Three-electrode setup for electrochemical characterization. (b) Potential waveform for the CV measurement. CV diagram for (c) EDLC and (d) Pseudocapacitor

(Hg/HgCl/KCl) or the silver-silver chloride electrode (Ag/AgCl/4M KCl). These three electrodes are kept submerged in a suitable electrolyte. Cyclic voltammetry (CV) is one of the three characterization techniques which is performed in this similar three-electrode setup [35, 36]. CV study provides information on the oxidation and reduction processes of molecular species coated on the working electrode. A triangular potential (figure (2.3.1 (b))) is applied between the RE and WE and the resulting current is measured between CE and WE. To investigate the material property for supercapacitive application, a suitable potential window is chosen. CV scan is performed at different scan rates. Scan rate controls the rate of change of the potential, or more generally, it controls the slope of the applied triangular potential waveform. A high scan rate decreases the width of the diffusion layer formed at the working electrode, which results in a higher current. Figure 2.3.1 (c) shows the typical CV diagram for an EDLC, which offers a rectangular CV diagram. On the other hand, CV diagram for a pseudocapacitor (figure 2.3.1 (d)) deviates significantly from the rectangular shape, which sometimes contains prominent oxidation or reduction peaks.
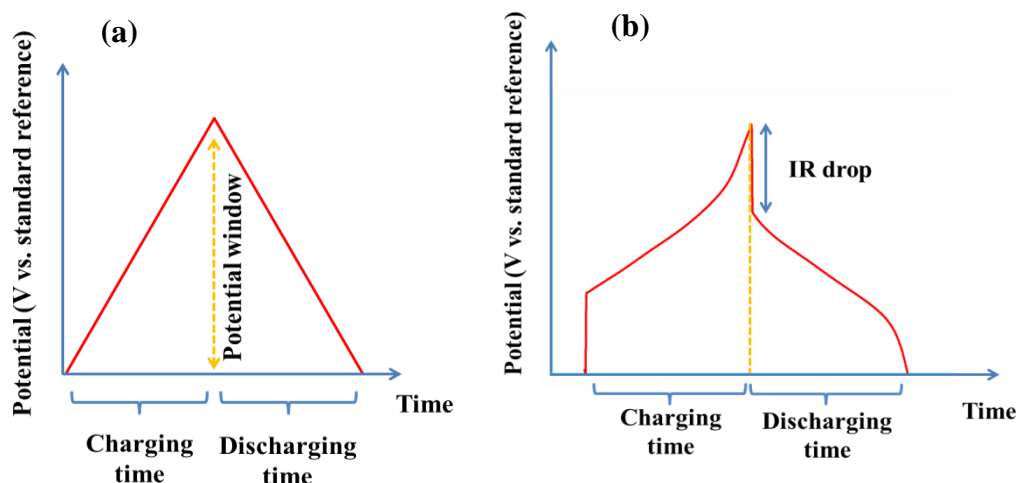
Figure 2.3.2 GCD profile for (a) EDLC and (b) Pseudocapacitor

The specific capacitance for the material under investigation at a particular scan rate can be obtained from the area under the CV curve using the equation (2.3.1)

$$C_m = \frac{i}{2mv} \tag{2.3.1}$$

Where, v and m are the potential sweeping rate and mass of the active material, respectively. Here i is the area under the CV curve which can be calculated from equation (2.3.2) [37].

$$i = \frac{\int_{v_a}^{v_c} i(v)dv}{(v_c - v_a)} \tag{2.3.2}$$

Where v_c and v_a are the highest and lowest points of the potential range, respectively. Galvanostatic charge discharge (GCD) is another electrochemical characterization technique that is performed to observe the charging and discharging behavior of WE. A constant current is applied between the CE and WE, and the potential of the WE is measured over time with respect to the RE. Figure 2.3.2 (a) shows the typical GCD pattern for an EDLC. The triangular shape of the GCD pattern resembles the EDLC nature; on the other hand, pseudocapacitor electrode material displays non-triangular GCD curves, as evident from figure 2.3.2 (b).One more interesting point that can be observed from the GCD plot of figure 2.3.2 (b) is that during the beginning of the discharge, a sharp fall is noticed. This sharp fall is mainly due to the internal resistance as well as the contact resistance of the electrode material with the current

collector [38]. Usually, the GCD is performed within the same potential window as the CV. The rising half of the GCD curve is the charging curve. Once the higher potential is reached, the charging current is reversed to the negative value, and hence the discharging curve is obtained. Equation (2.3.3) can also be used to calculate specific capacitance from the GCD measurements for a particular current density.

$$C_m = \frac{i}{(-\frac{dV}{dt})}$$

(2.3.3)
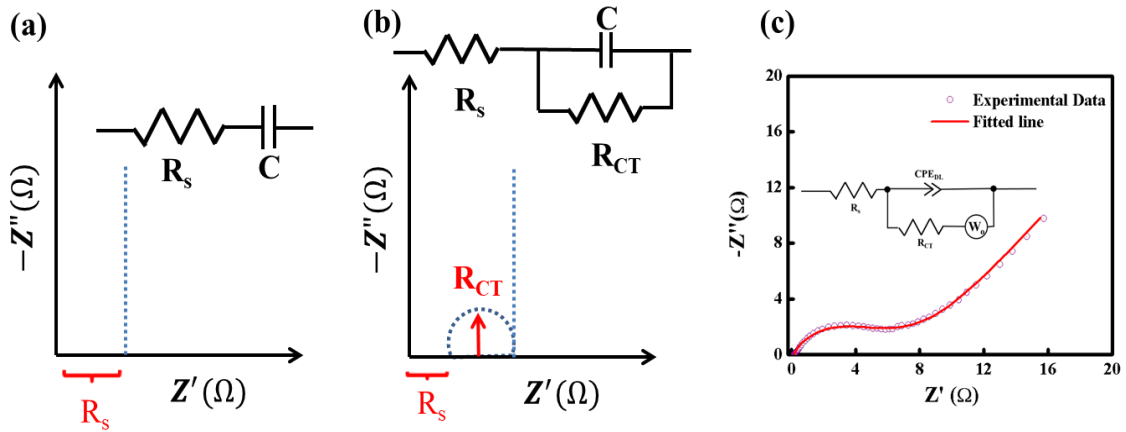
Figure 2.3.3 Nyquist plot for (a) ideal capacitor with a series resistance (b) capacitor with a leakage resistance in parallel (c) an actual supercapacitor electrode.

Here, i is the current density applied externally, and dV/dt is the average slope of the discharging part of the GCD curve.

The third characterization is the electrochemical impedance spectroscopy (EIS) which provides different dynamical processes occurring at the WE and the electrolyte. EIS can be used to determine the resistive and capacitive properties of an electrode material by applying a perturbation to the electrode in the form of a sinusoidal AC signal of magnitude 2–10 mV. The frequency of the perturbation signal is varied, and thus an impedance spectrum is obtained. We consider a circuit where an ideal capacitor C and a resistor R are connected in series. For this circuit, the complex impedance Z is given by equation (2.3.4)

$$Z(\omega) = R - \frac{i}{\omega C}$$

(2.3.4)

Here, ω is the frequency of the applied perturbation and i is the usual imaginary unit. The real part Z_r and the imaginary part Z_{im} of the complex impedance are given by:

(2.3.5)

$$Z_r = R$$

$$Z_{im} = -\frac{1}{\omega C} \hspace{6cm} (2.3.6)$$

When the frequency of the applied perturbation is varied, the Z_r remains fixed; as for the present circuit, it is independent of frequency. Hence, the plot of -Z_{im} vs. Z_r becomes a straight line parallel to the -Z_{im}-axis, as shown in Figure 2.3.3 (a). From this plot value of the series resistance (R_s) can be calculated as shown in the same figure. This method of demonstrating the EIS spectra is called the Nyquist plot. Another method of demonstrating the EIS data is the Bode plot, where the logarithm of modulus of impedance (log Z) is plotted against the logarithm of applied frequency (log f). However, in reality, an ideal capacitor cannot be realized in practice. A more realistic approach to model a capacitor is to consider a high resistance parallel to that capacitor, which takes into account the leakage of charge over time. In such a case, the Nyquist plot becomes circular in the higher frequency region along with a spike parallel to the –Z_{im} axis, as shown in figure 2.3.3 (b). From the same plot value of the leakage, resistance can be calculated from the radius of the semicircle. However, in reality, a much more complex Nyquist plot is obtained for a practical capacitor, especially for a supercapacitor, owing to much more complex charge dynamics at the electrode-electrolyte interface. In such a case, the Nyquist plot has to be fitted with different circuit elements to obtain different information like contact resistance, charge transfer resistance, Warburg impedance, etc. For example, the Nyquist plot of figure 2.3.3 (c) shows such a typical complex nature. This is a plot for a supercapacitor electrode material. This Nyquist plot has been fitted using the model circuit shown in figure 2.3.3 (c) (inset). Here, CPE_{DL} is the constant phase element that takes into account the double layer effect at the interface of the electrode, and W_o is the Warburg element which is due to the frequency-dependent diffusion [39].

Thus different parameters determine the overall charge storage performance of electrode material. Table 2.3.1 summarizes these different parameters and their meaning.

Table 2.3.1: Different parameters related to the charge storage performance of the electrode material.

Parameters	Significance
Specific capacitance	Charge storing capability per unit mass of the electrode material.

Areal specific capacitance	Charge storing capability per unit area of the electrode material.
Volumetric specific capacitance	Charge storing capability per unit volume of the active material.
Specific energy	Electrical energy stored per unit mass of the active material.
Specific power	Stored electrical power per unit mass of the electrode material.
Electrochemical reversibility	Determines the reversibility of the redox reaction.
Potential window	Signifies the operating voltage window within which the active material can perform reversible redox reaction with the electrolyte.
Rate capability	Determines the capacitance response at various potential scan rates or current densities. It is related to the power generating efficiency at a high current with minimum loss of voltage.
Long cyclic life	Charge storage capability for the electrode usually degrades over repeated charging and discharging cycles. This parameter determines the long life performance of the electrode material.
Columbic efficiency	Signifies the efficiency of charge transfer through electrochemical reaction. It is the ratio of charging time and discharging time for an electrode material in GCD experiment, where the charging and discharging currents are the same.
Equivalent Series Resistance (ESR)	It determines the resistance of the different components in the whole electrochemical cell. This resistance includes material resistance, electrolyte resistance, etc. It can be found out from the EIS studies.

2.4 Different electrode materials

At present different research groups around the world are investigating different types of materials for supercapacitor electrodes. Different EDLC based materials offer extraordinary power density as well as excellent long-life, whereas different pseudocapacitive materials offer high storage capacity with excellent energy density. Hence efforts have been made to prepare composites of these two types of materials to enhance the overall storage performance. Here we discuss a few such materials and their charge storage performances.

2.4.1 Porous Carbon

Carbons derived from different sources have been used to fabricate supercapacitor electrodes. These electrodes store charges via the formation of double layer, and no redox process is involved in the storage mechanism. Hence this type of material can extend the lifetime of the electrode owing to the physical charge storage mechanism. Porous carbon is low cost, environmentally friendly, and offers the agility to tune its surface area. Activated carbon (AC), a type of porous carbon, has been successfully commercialized because of its large surface area, micro-porosity, and relatively low cost. Different waste products like rice husks, waste of tea, waste of coffee beans, etc., have been used to synthesize AC to fabricate EDLC type supercapacitor electrodes [40]. The charge storage properties of these electrodes depend on the carbonization and activation steps during the synthesis. Inal et al. prepared AC from the waste of tea using carbonization and chemical activation using zinc chloride ($ZnCl_2$). The heat-treated sample showed a good specific surface area of 923 m^2 g^{-1}. They measured the electrochemical charge storage performance in a two-electrode configuration which exhibited the highest specific capacitance of 140 F g^{-1} at a current density of 1 A g^{-1}. The device retained 98% of its initial value of specific capacitance after 10000 GCD cycles [41].

2.4.2 Carbon nanotube (CNT)

Carbon nanotubes (CNTs) have remained in the center of material science research since their discovery because of their attractive structural, mechanical, and electrical properties [42]. CNTs are fabricated when a graphite sheet is rolled to form a cylindrical shape, as shown in figure 2.4.1. Thus we have a carbon nanotube with
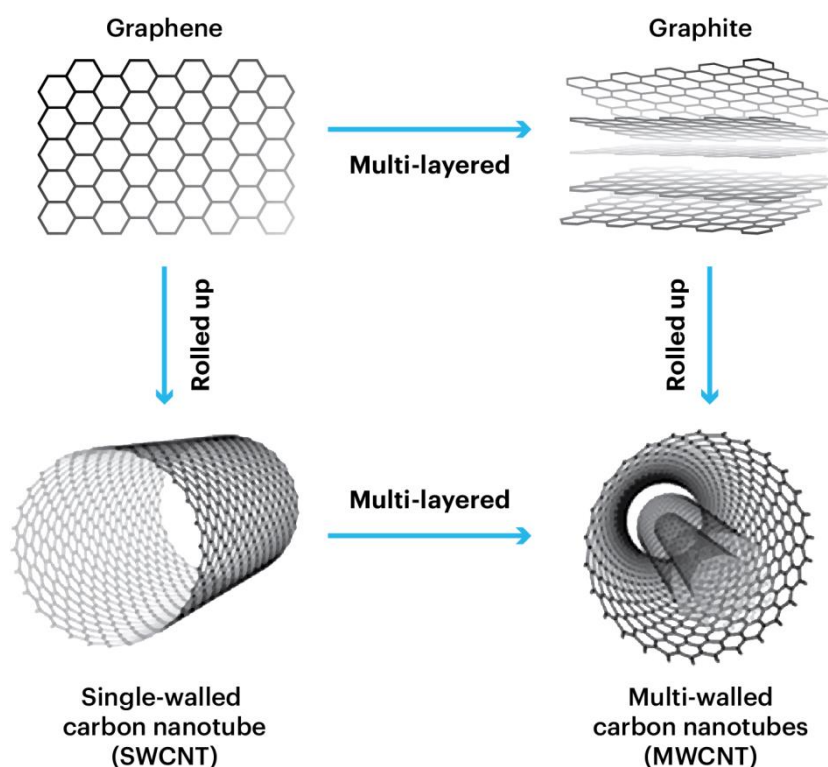
Figure 2.4.1 Different types of CNTs

only one layer of rolled up layer of graphite sheet known as single walled carbon nanotube (SWCNT). On the other hand, multiwalled carbon nanotube (MWCNT) contains more than one layer of graphite layer. CNTs can have a diameter of the order of 1 nm while their length can be of the order of a few microns, offering very high surface area and low resistivity, which is beneficial for electrochemical charge storage applications. Niu et al., in 1997, first demonstrated the supercapacitive properties of CNTs [43]. Catalytically grown carbon nanotubes having an average diameter of 80 Å were used for fabricating the electrodes. Initially, the CNTs were treated with nitric acid to disassemble the CNT cluster and functionalize the surface with oxygenated groups. These acid-treated CNTs were dispersed in water and filtered, which resulted in a carbon nanotube sheet after drying. A test device was assembled using two such sheets as electrodes separated by polymer separator. 38 wt% H_2SO_4 was used as electrolyte. A maximum specific capacitance of 104 F g^{-1} was attained from the test cell. Yu et al. reported a stretchable supercapacitor based on SWCNT microfilm. To fabricate the stretchable substrate, surface treated poly(dimethylsiloxane) (PDMS) was used. SWCNT was deposited on this elastic substrate. The device demonstrated a specific capacitance of 54 F g^{-1} when no strain was applied and 52 F g^{-1} when a 30% strain was applied [44].

2.4.3 Graphene

Graphene has attracted tremendous research interest soon after its first synthesis in 2004 [45]. It is the two-dimensional single-layer carbons in of sp^2-hybridized state (figure 2.4.2). Very low electrical resistivity and high thermal conductivity, ultra-high surface area (~2700 m^2 g^{-1}), chemical stability, and excellent
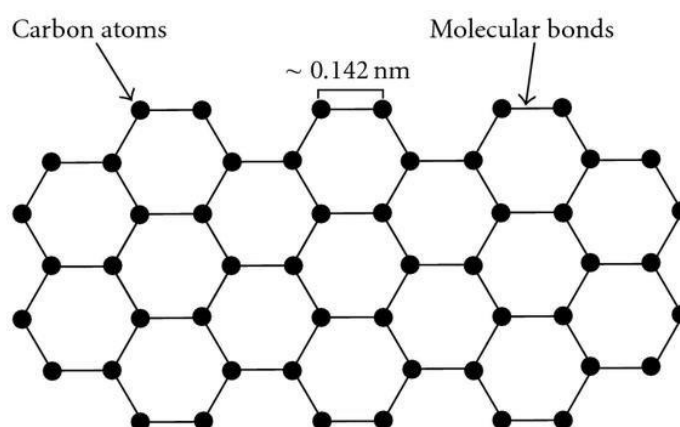
Figure 2.4.2 Structure of graphene

mechanical strength (~1 TPa) make it suitable for application in supercapacitor electrodes. Liu et al. in 2010 reported a supercapacitor device with graphene-based electrode [46]. Graphene oxide (GO) was produced via the modified hummers method. In this process, natural graphite is oxidized using a mixture of sulphuric acid, sodium nitrate, and potassium permanganate. The obtained GO was treated with hydrazine to remove the oxygen-containing groups. Finally, the obtained graphene powder was coated on the aluminium foil to fabricate coin sized supercapacitor cell. A rectangular CV profile was obtained within a wide potential window of 4 V. This suggests excellent double layer charge storage mechanism. The coin cell displayed a specific energy density of 85.6 Wh kg^{-1} at 25 °C. Zhang et al. used a novel vacuum filtration deposition method to deposit graphene in the pore of nickel foam [47]. In this process, commercially available graphene nanoplatelets were refluxed using an acidic solution of concentrated nitric acid. This refluxed graphene, along with PVDF binder, was dissolved in absolute ethanol. The mixture was then forced through the nickel foam using a vacuum filtration deposition process. After the deposition, the deposited nickel foams were dried at 100 °C in a vacuum. A specific capacitance of 152 F g^{-1} was acquired at 10 mV s^{-1} scan rate using an aqueous 6 M KOH electrolyte medium in a two-electrode setup using as-deposited nickel foams as the positive and

negative electrode. The electrodes retained 95% of their initial capacitance after 2000 cycles. However, graphene nanosheets tend to aggregate during the electrode fabrication, which hampers the electrochemical performance by reducing the practical surface area [48].

2.4.4 Ruthenium oxide and its composites

Among different transitional metal oxides, RuO_2 is the most promising pseudocapacitive electrode material because of its fast charge dynamics, high theoretical specific capacitance, high electrical conductivity (~105 S cm^{-1}), chemical and thermal stability in the electrolyte. The charge storage mechanism of RuO_2 was first proposed by Trasatti et al. [49], which is due to the electronic protonic "double insertion" mechanism as shown in equation (2.4.1):

$$RuO_x(OH)_y + \delta H^+ + \delta e^- \leftrightarrow RuO_{x-\delta}(OH)_{y+\delta} \qquad (2.4.1)$$
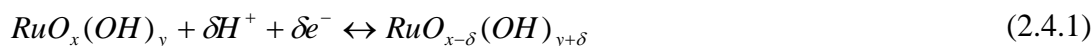
The oxidation state of ruthenium varies among Ru^{4+}, Ru^{3+}, and Ru^{2+}. These redox reactions mainly occur at the surface or nearer to the surface of the RuO_2 coated electrode. Hence the surface area of the active material composing the electrode, in this case, is a vital parameter to obtain higher specific capacitance. The anhydrous crystalline form of RuO_2 shows a very low specific capacitance (~30 F g^{-1}) value,
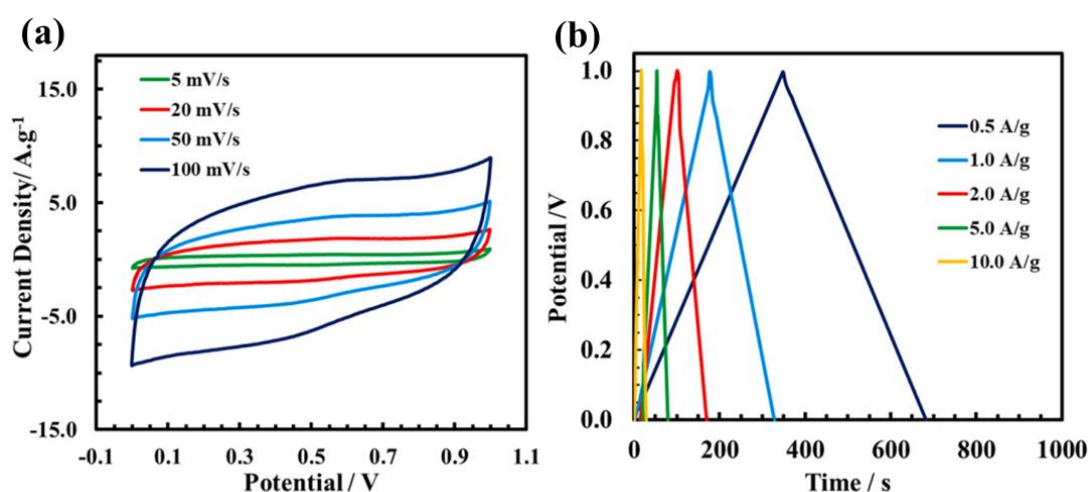
Figure 2.4.3 (a) CV and (b) GCD for the rGO/RuO$_2$ aerogel

whereas the hydrous form of RuO_2 offers higher specific capacitance [50]. Patil et al. synthesized hydrous RuO_2 thin film on different substrates like glass and stainless steel using chemical bath deposition. Being in hydrous form, the thin film of RuO_2 showed a higher specific capacitance of 73 F g^{-1} at 2 mV s^{-1} scan rate in 0.5 M H$_2$SO$_4$

electrolyte [51]. Korkmaz et al. synthesized a composite of rGO and RuO_2 in the form of an aerogel mixture. The electrochemical study revealed that this composite did not show any redox peak at the higher side of the scan rate. The CV curves thus resembled almost ideal reversible capacitive behavior, and the GCD curves showed triangular type nature as shown in figure 2.4.3 (a) and (b), respectively. The highest specific capacitance of 328.6 F g^{-1} was obtained for this sample at 5 mV s^{-1} scan rate [52]. Table 2.4.1 summarises the different results concerning the charge storage capability of RuO_2 and its composites.

Table 2.4.1: Results from different reports on RuO_2 and its different composites.

Sample Name	Measurement Configuration	Specific capacitance value	Ref.
Anhydrous RuO_2	3-electrode. Electrolyte: Aqueous 0.5 M H_2SO_4	58 F g^{-1} @ 2 mV s^{-1}	[19]
Hydrous nanotubular array of RuO_2	3-electrode. Electrolyte: Aqueous 1 M H_2SO_4	1300 F g^{-1} @ 10 mV s^{-1}	[53]
Spray deposited RuO_2 film	3-electrode. Electrolyte: Aqueous 0.5 M H_2SO_4	551 F g^{-1} @ 5 mV s^{-1}	[54]
Pulse electrodeposited RuO_2	3-electrode. Electrolyte: Aqueous 0.5 M H_2SO_4	1724 F g^{-1} @ 5 A g^{-1}	[55]
RuO_2/Carbon nanofiber	3-electrode. Electrolyte: Aqueous 2 M H_2SO_4	220 F g^{-1} @ 5 mV s^{-1}	[56]
Flexible RuO_2/Graphene Thin film	3-electrode. Electrolyte: Aqueous 0.5 M H_2SO_4	1561 F g^{-1} @ 5 mV s^{-1}	[57]
SnO_2-RuO_2 composite film	3-electrode. Electrolyte: Aqueous 0.5 M H_2SO_4	150 F g^{-1}	[58]
RuO_2/CNT	3-electrode. Electrolyte: Aqueous 1M L^{-1} H_2SO_4	900 F g^{-1}	[59]
RuO_2/electrospun carbon fiber	3-electrode. Electrolyte: Aqueous 2 M H_2SO_4	544 F g^{-1}	[60]
RuO_2-Fe_2O_3 embedded mesoporous carbon	3-electrode. Electrolyte: Aqueous 0.5 M H_2SO_4	1668 F g^{-1} @ 1 A g^{-1}	[61]

2.4.5 Manganese dioxide and its composites

Although RuO_2 is popular in lab-grade devices and different military-based applications because of its high cost and toxicity, it is not commercially popular. As an alternative to RuO_2, Manganese dioxide (MnO_2) has gained popularity because of its ultrahigh theoretical value of specific capacitance (~1370 F g^{-1}), environment friendliness, and abundance [62]. In 1999, Lee and Nobel Laureate Goodenough first
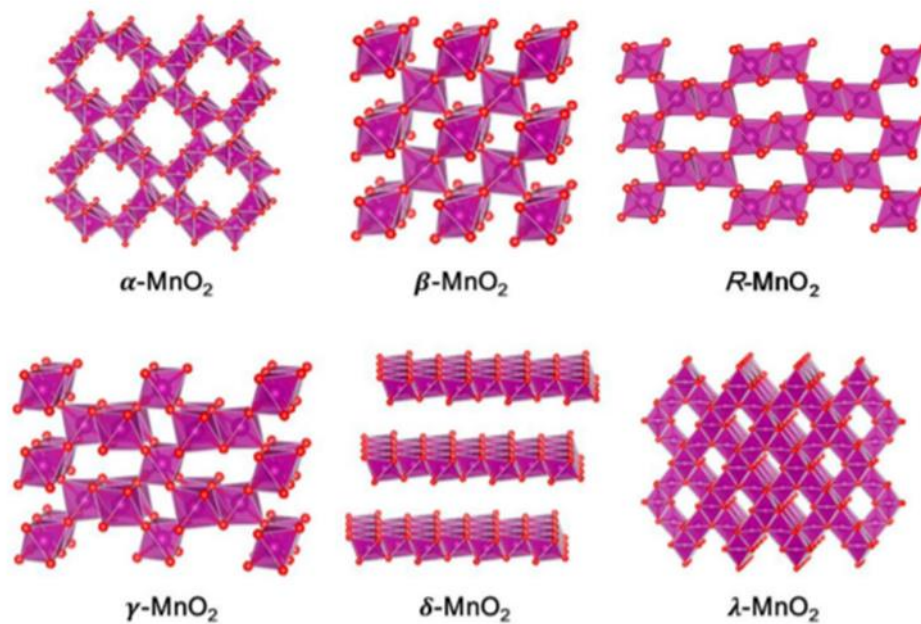
Figure 2.4.4 Different polymorphs of MnO₂. Mn atoms are shown in magenta and O atoms are shown in red.

reported the supercapacitor behavior of amorphous $MnO_2.nH_2O$ in an aqueous KCl electrolyte medium. A specific capacitance value of 200 F g^{-1} was reported [63]. MnO_2 generally shows six different types of polymorphic forms, as shown in figure 2.4.4 [64]. Different atomic positions in these different polymorphs result in the variation of surface characteristics, pore size, and channel or tunnel size. These variations lead to significant variations in the charge storage performance of these different polymorphs. For example, Zhang et al. studied the electrochemical charge storage performance of these different polymorph phases. It was found that the specific capacitance values varied in the order: β-MnO_2< γ-MnO_2 < δ-MnO_2 < α-MnO_2 [65]. The charge storage by MnO_2 electrode in the aqueous electrolyte is due to the pseudocapacitive mechanism. Two different mechanisms are usually proposed to explain the charge storage phenomena [66]. The first one is based on the

intercalation of protons (H^+) or metal cations (C^+) in the bulk of the material during the reduction process. On the other hand, during the oxidation process, the deintercalation of H^+ or C^+ occurs. Equation (2.4.2) and (2.4.3) shows the charge storage phenomena by MnO_2 through the first mechanism.

$$MnO_2 + H^+ + e^- \leftrightarrow MnOOH \qquad\qquad (2.4.2)$$

$$MnO_2 + C^+ + e^- \leftrightarrow MnOOC \qquad\qquad (2.4.3)$$

In the second mechanism, the surface adsorptions of the electrolyte ions on MnO_2 electrode surface are taken into consideration and are shown via the equation (2.4.4).

$$(MnO_2)_{surface} + C^+ + e^- \leftrightarrow (MnO_2^- C^+)_{surface} \qquad\qquad (2.4.4)$$
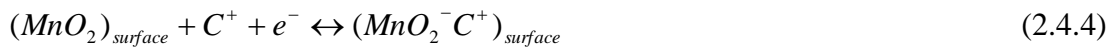
This adsorption and desorption of ions occur very near the electrode's surface, and bulk of the sample remains inactive in this case. Although having many advantages, pristine MnO_2 possesses few serious drawbacks as an electrode material for supercapacitors. MnO2 demonstrates low electrical conductivity in pristine form, which hampers the charge transport rate. It also tends to dissolve in different aqueous electrolytes, reducing the material's stability. Further, through the repeated charge/ discharge cycles, the crystal structure of MnO_2 suffers irreversible volume expansion, which causes swelling in the electrode. To address these problems, different researchers across the world developed a composite of MnO_2 with different materials like CNTs, graphenes, activated carbon, carbon fiber, other metal oxides, sulfides, etc. For example, Vangapally et al. synthesized carbon/MnO_2 composite using table sugar as a source for carbon. The hydrothermal reaction was used to prepare the composite, which showed a nanorod-like morphology. This composite showed a specific capacitance of 416 F g^{-1} at 1 A g^{-1}. Because of the presence of carbon in the composite, its conductivity and electrochemical stability increase, which causes the electrode to retain a specific capacitance of 90% of the primary value after being charged and discharged for 5000 cycles [67]. A lot of work has been performed using MnO_2 and its composites to be used as electrode material for supercapacitors. Table 2.4.2 shows a summary of a few of the published results.

Table 2.4.2: Results from different reports on MnO_2 and its different composites.

Sample Name	Measurement Configuration	Specific capacitance value	Ref.
Porous MnO_2	3-electrode. Electrolyte: Aqueous 0.5 M Na_2SO_4	222 F g^{-1} @ 2 mV s^{-1}	[68]
MnO_2 nanopillars	3-electrode. Electrolyte: Aqueous 1 M Na_2SO_4	603 F g^{-1} @ 5 mV s^{-1}	[69]
MnO_2 nanorod	3-electrode. Electrolyte: Aqueous 0.1 M Na_2SO_4	166.2 F g^{-1}	[70]
Hollow MnO_2 nanofiber	3-electrode. Electrolyte: Aqueous 1 M Na_2SO_4	291 F g^{-1} @ 1 A g^{-1}	[71]
GO-MnO_2	3-electrode. Electrolyte: Aqueous 1 M Na_2SO_4	216 F g^{-1} @ 150 mA g^{-1}	[72]
MnO_2-CNT	3-electrode. Electrolyte: Aqueous 1 M Na_2SO_4	201 F g^{-1} @ 1 A g^{-1}	[73]
MnO_2 on Ni-foam	3-electrode. Electrolyte: Aqueous 1 M Na_2SO_4	241 F g^{-1} @ 1A g^{-1}	[74]
Polypyrrole-covered MnO_2	3-electrode. Electrolyte: Aqueous 1 M L^{-1} Na_2SO_4	141 F g^{-1} @ 2 mA cm^{-2}	[75]
MWCNTs/ MnO_2/PPy composite	3-electrode. Electrolyte: Aqueous 1 M L^{-1} Na_2SO_4	806 F g^{-1}@ 1 A g^{-1}	[76]
Carbon@MnO_2 core-shell nanospheres	3-electrode. Electrolyte: Aqueous 1 M L^{-1} Na_2SO_4	252 F g^{-1} @ 2 mV s^{-1}	[77]

2.4.6 Other metal oxides

Among the different oxides of transition metals, cobalt oxide (Co_3O_4), nickel oxide (NiO), titanium dioxide (TiO_2), vanadium pentoxide (V_2O_5), iron oxide (Fe_3O_4), etc. have been explored for their potential charge storage applications. For example, Vijayakumar et al. synthesized NiO nanomaterial via microwave method. From the SEM image, it was seen that the sample annealed at 300 °C temperature shows a nanoflake-like structure. These nanoflakes of NiO showed a specific capacitance of
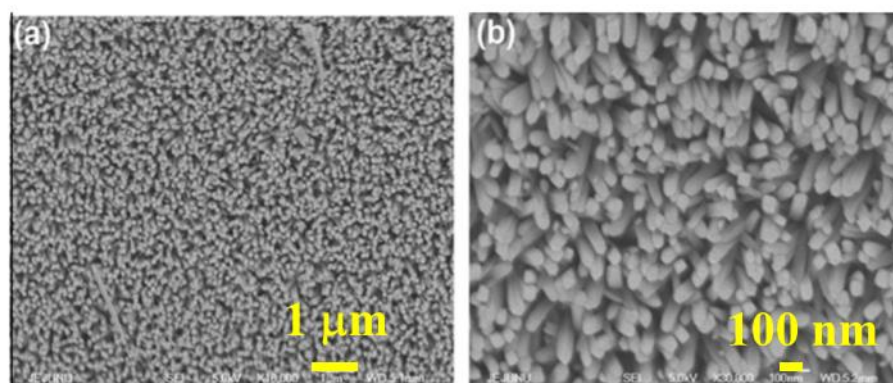
Figure 2.4.5 FESEM image of TiO$_2$ nanotube arrays on FTO substrate (a) in low magnification and (b) in high magnification

~400 F g^{-1} at 0.5 mA cm^{-2} current density [78]. Cobalt oxide, although being a battery-type material, has been explored as a potential candidate for supercapacitor electrodes. Co_3O_4 displays good electrochemical activity. Its size and shape can be controlled relatively easily. Meher et al. layered and porous Co_3O_4 structure through the hydrothermal method. Through the electrochemical characterizations, it was seen that Co_3O_4 displayed a reversible redox reaction. A high specific capacitance of 548 F g^{-1} was obtained at 8 A g^{-1} in a 1 M aqueous KOH electrolyte [79]. TiO_2 is another transition-metal oxide that is very cheap and environmentally friendly. Ramdoss et al. fabricated TiO_2 nanorods on fluorine-doped tin oxide (FTO) substrates using the hydrothermal method and studied its electrochemical performance. FESEM images of the coated substrate showed uniform distribution of TiO_2 nanorods (figure 2.4.5) with an average diameter of 60-70 nm. These vertically aligned nanorods were used as an electrode to study its charge storage performance. An aerial specific capacitance of 85 μF cm^{-2} was obtained at 5 mV s^{-1} in a 1 M aqueous Na_2SO_4 electrolyte [80]. V_2O_5 possesses multiple oxidation states and thus can offer good pseudocapacitive charge storage performance. Balamuralitharan et al. synthesized V_2O_5 nanorods through

hydrothermal technique. For the electrochemical characterization, the nanorods were dropcasted on a stainless steel substrate which acted as the working electrode. A remarkably high specific capacitance of 417.5 mF cm^{-2} was obtained at 5 mV s^{-1} scan rate. The electrodes were shown to retain 80% of their primary specific capacitance after being charged and discharged for 5000 cycles performed at 0.5 mA cm^{-2} [81]. Fe_2O_3 is another cheap and environmentally friendly material that offers easy redox reaction with the electrolyte. Mitchell et al. synthesized mono-disperse nanocrystal of Fe_3O_4 with an average particle size of 8 nm. The electrochemical study revealed that these nanocrystals offered a specific capacitance of 185 F g^{-1} with good cyclic stability [82]. These different single metal oxides can be used as electrodes in future energy storage devices. However, these single metal oxides show very high resistance to current flow, which hampers the power delivery and reduces the long-term stability. On the other hand, bimetallic oxides show relatively good conductivity and superior electrochemical activity compared to their mono-metallic oxide counterparts. The superior electrochemical activity arises mainly due to the presence of multi-oxidation states in such oxides. It is also possible to improve the power density and the energy density of the electrode made of these bimetallic oxides through the synergistic effect of both two metal ions. Hence researchers around the globe are experimenting with different bimetallic oxides to improve the performance of a supercapacitor device.

2.4.7 Bimetallic oxide of Ni and Mn (NiMn$_2$O$_4$)

$NiMn_2O_4$ offers high conductivity, high theoretical specific capacitance, and excellent stability among the different bimetallic oxides. Hence it has been investigated by different researchers for its potential applications in supercapacitors, catalysis, electrochemical sensors, etc. Dhas et al. synthesized $NiMn_2O_4$ powder using a simple sol-gel route. They studied the effect of annealing temperature and the electrolyte concentration on the electrochemical performance of the electrode made of this powder. All the electrochemical performances were reported in a three-electrode arrangement in aqueous KOH electrolyte with variable concentrations ranging from 1 M to 6 M. The sample annealed at 500 °C (NMO1) showed better electrochemical charge storage performance compared to the same sample annealed at 600 °C (NMO2) and 700 °C (NMO3). Next, the effect of electrolyte concentration was studied using the NMO1 sample. It was seen that with the increasing the KOH

41

concentration, the charge storage performance increases. In 1 M KOH electrolyte, it offered 571 F g^{-1}, and in 6 M KOH electrolyte, it offered a specific capacitance of 762 F g^{-1} (value measured from CV at 5 mV s^{-1} scan rate). It was concluded that the improvement of specific capacitance is due to the increment of electrolyte ions which increases the electrochemical activity [83]. Umar et al. synthesized $NiMn_2O_4$ nanodisk on reduced graphene oxide (rGO) using a low-temperature colloidal solution method and studied it for both the electrochemical sensor and supercapacitor. The sensor was used to sense acetylacetone. The electrochemical charge storage capability was measured in a three-electrode arrangement using 1 M aqueous Na_2SO_4 electrolyte within a wide potential window of 1 V. $NiMn_2O_4$ nanodisk decorated on rGO demonstrated a highest specific capacitance of 356 F g^{-1} at 0.5 A g^{-1} current density.
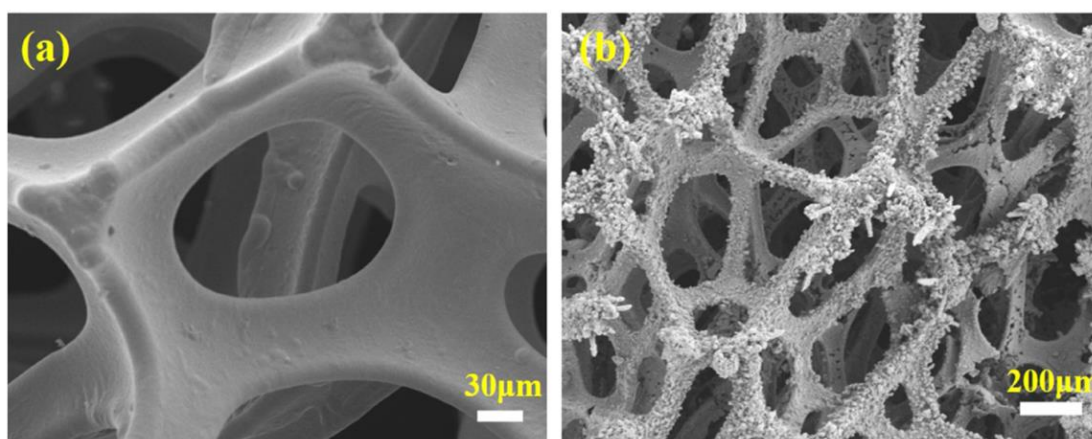
Figure 2.4.6 SEM image of NiMn$_2$O$_4$ coated on Ni-foam at (a) low resolution (b) high resolution

On the other hand, only $NiMn_2O_4$ shows a specific capacitance of 199 F g^{-1} at the same current density. This improvement of specific capacitance is mainly due to rGO, which increases the specific surface area of the sample, and thus the charge storage performance improves [84]. Choice of the current collector is an important parameter to obtain the best performance from a supercapacitor electrode. Wei et al. synthesized ultrathin $NiMn_2O_4$ arrays on Ni-foam current collector using hydrothermal reaction. Through the reaction, the coating of $NiMn_2O_4$ was formed directly on the Ni-foam. Because of this, no binder was required to fabricate the electrode. As it is well known, most of the binders are nonconductive and deteriorates the performance of the electrode. This kind of microstructure provides large number of active sites for the electrolyte ions and the conductive channel of Ni-foam effectively connects the different redox active sites electronically. Figure 2.4.6 shows the $NiMn_2O_4$ coated Ni-

foam used by Wei et al. The electrochemical performance measured in 6 M KOH electrolyte displayed a specific capacitance value of 662.5 F g^{-1} at current density of 1 A g^{-1} current density [85]. Table 2.4.3 summarises the different results regarding the supercapacitive charge storage performance obtained with $NiMn_2O_4$ and its different composites.

Table 2.4.3: Results from recent reports on $NiMn_2O_4$ and its different composites

Sample Name	Measurement Configuration	Specific capacitance value	Ref.
rGO/NiMn$_2$O$_4$	3-electrode. Electrolyte: Aqueous 1 M Na$_2$SO$_4$	693 F g^{-1} @ 1 A g^{-1}	[86]
Spherical carbon decorated with NiMn$_2$O$_4$	3-electrode. Electrolyte: Aqueous 2 M KOH	470.7 F g^{-1} @ 1 A g^{-1}	[87]
CNT/ NiMn$_2$O$_4$ core-shell nanocomposite	3-electrode. Electrolyte: Aqueous 6 M KOH	915.6 F g^{-1} @ 1 A g^{-1}	[88]
NiMn$_2$O$_4$ on Ni-foam	3-electrode. Electrolyte: Aqueous 6 M KOH	802 F g^{-1} @ 1 A g^{-1}	[89]
NiMn$_2$O$_4$ supported on N$_2$ dopped graphene	3-electrode. Electrolyte: Aqueous 6 M KOH	1308.2 F g^{-1} @ 1 A g^{-1}	[90]
Co^{2+} and Zn^{2+} dopped NiMn$_2$O$_4$ supported on rGO	3-electrode. Electrolyte: Aqueous 3.5 M KOH	710 F g^{-1} @ 1 A g^{-1}	[91]

2.4.8 Other bimetallic oxides

Among the different bimetallic oxides, Ni-Co-oxide, Mn-Co-oxide, Zn-Co-oxide, Ni-Zn-oxide, etc., have been investigated as the electrode material for supercapacitive charge storage application. Nickel cobaltite ($NiCo_2O_4$), a transition bimetallic oxide, generally shows a cubic spinel structure. The electronic conductivity of $NiCo_2O_4$ is higher than both NiO and Co_3O_4 by at least two orders of magnitude, which can

improve the charge storage performance of these bimetallic oxides [92]. It shows high theoretical specific capacitance because of richer faradic reactions by both the Ni and Co ions in alkaline electrolytes. Lei et al. synthesized flower-shaped microsphere of $NiCo_2O_4$ using microwave-assisted heating technique. The electrochemical property of the synthesized sample was carried out in a 6 M aqueous KOH solution, which showed a maximum specific capacitance of 1006 F g^{-1} at 1 A g^{-1} current density. The long cycle performance was tested by performing 1000 GCD cycles, at the end of which the sample retained 93% of its initial specific capacitance. Thus although this bimetal oxide shows ultrahigh specific capacitance, its degradation over a long cycle is relatively high, and thus much work is necessary to improve its storage performance [93]. Like Ni-Co-oxide, Mn-Co-oxide also shows good potential to be used as an electrode material for supercapacitor application. Mn-Co-oxide displays high specific capacitance due to multiple redox reactions with the electrolyte. However, due to very small specific surface area, relatively less conductivity, and structural stability, Mn-Co-oxide still possesses technical challenges to be used as an electrode material. Gaire et al. addressed these issues with Mn-Co-oxides by incorporating reduced graphitic oxide (rGO) in Mn-Co-oxide. To eliminate the need of binder, the precursor solution was spray coated directly on a highly conducting Pt-Si substrate. A highly porous structure was seen from the morphological characterization of the substrate. The coated substrates were used as the working electrode for electrochemical characterizations. An ultrahigh areal specific capacitance of 11 mF cm^{-2} was obtained in 1 M aqueous KOH solution at 0.4 mA cm^{-2} current density. Most importantly, the composite electrode showed ultrahigh-specific capacitance retention of 95% after 80000 cycles. This remarkable charge storage performance was attributed to the synergistic effect of the rGO and the Mn-Co-oxide [94]. Bimetal oxide of zinc and cobalt has also drawn considerable attention in the field of research [95, 96]. For example, in the work of Xu et al., porous $ZnCo_2O_4$ was synthesized through hydrothermal reaction, which showed a high specific capacitance of 776.2 F g^{-1} at 1 A g^{-1} current density and good capacitive retention of 84.3% at 3 A g^{-1} [97].

Thus bimetal oxides show good potential to be used as a supercapacitor electrode material. However, these materials are still not commercially viable as there are various issues with these electrode materials which are required to be addressed. Deep

research in this avenue is required for the enhancement of the overall storage performance.

2.5 Two-electrode supercapacitor device
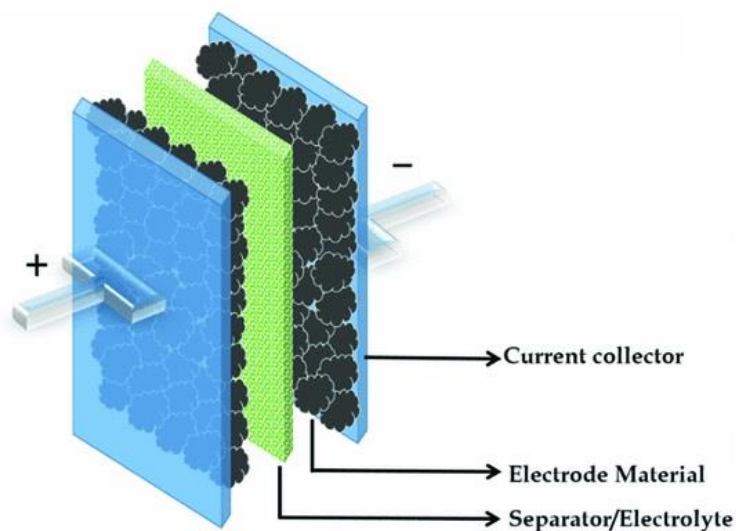
Figure 2.5.1 Schematic of a two-electrode supercapacitor device

A symmetric two-electrode supercapacitor device is fabricated by utilizing the coating of the same electrode material in both electrodes. On the other hand, if two different electrode materials are used, it is termed an asymmetric supercapacitor device. Usually, in such a device the redox-active material is coated on the positive electrode, and carbonaceous material is coated on the negative electrode.

The energy density (E, in the unit of Wh kg^{-1}) and the power density (P, in the unit of W kg^{-1}) of the device can be calculated from the equations (2.5.1) and (2.5.2) [98].

$$E = \frac{1}{2}\left[\frac{C(\Delta V)^2}{3.6}\right]$$
(2.5.1)

$$P = \frac{3600 \times E}{\Delta T}$$
(2.5.2)

Here, C is the device's specific capacitances (in the unit of F g^{-1}) at different current densities as obtained from the GCD, ΔV is the working potential window, and ΔT is the different discharge times corresponding to different current densities. For the best performance of the device, the active materials should be carefully chosen, and mass

deposition of the active materials should be optimized. Apart from the active materials, we need to focus on its other important parts to obtain the optimum performance from the two-electrode devices. These parts are the current collector, separator, and electrolyte.

2.5.1 Current collector

The current collector serves two main purposes. Firstly, it collects/sends electrons from/to electrodes during discharging/charging. Secondly, it provides the necessary mechanical support to the electrode material. A good current collector should have very less contact resistance and good bonding with the electrode material [99, 100]. It should also have high electric conductivity to carry or deliver power with minimum loss. To stick the electrode material more efficiently to the current collector,
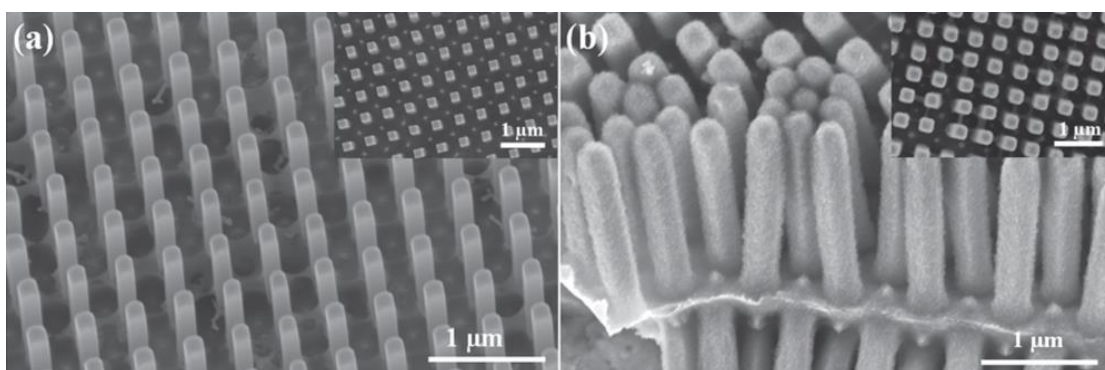
Figure 2.5.2 (a) Pt Nanotube array (b) MnO$_2$ deposited nanotube array

different surface treatments are performed. This increases the bonding capacity of the current collector. Wen et al. used the atomic layer deposition (ALD) technique to fabricate platinum nanotube arrays using anodic alumina (AAO) template. They successfully fabricated a current collector of the size of 1 cm x 1 cm, free of any structural defect. Next, to deposit MnO$_2$ on the nanotube array electrodeposition method was used, which acted as the electrode for the supercapacitor. Figure 2.5.2 (a) shows the SEM image of the Pt-nanotube array, and figure 2.5.2 (b) shows the same array after MnO$_2$ deposition. This structure of the current collector maximizes the surface area for MnO$_2$ deposition. A good charge storage capability along with excellent stability was reported for this structure [101]. Both commercially and in lab-grade devices, different materials like copper, nickel, aluminum etc., are used as current collectors. In a typical supercapacitor device, the current collector does not

participate in any reaction. Hence the choice of the current collector should be such that it does not react with the electrolyte. Also, with the rise in popularity of wearable electronics, the current collector should be flexible. Thus a good amount of research is required to improve the material composition and architecture of the current collector to meet the global requirements.

2.5.2 Separator

The separator in a supercapacitor device is kept between two electrodes. It serves three main purposes. Firstly and most importantly, it prevents short-circuiting the device by providing electrical insulation between the two electrodes. Secondly, it acts as a storage reservoir for the liquid electrolyte, and thirdly during the charging-discharging process, it allows the passage of electrolyte ions [102, 103]. In commercial devices, a cellulose-based separator is used along with organic electrolyte because of its good wettability. The choice of the separator is defined by the properties of the electrolyte. The separator material must be thermally stable at the working temperature range, and it must be chemically/electrochemically inert. Besides, its thickness must be as thin as possible to enhance the charge storage capacity. To use in the flexible supercapacitor, the separator should also be flexible enough to accommodate the change in the shape of the overall device. Among the major disadvantages of a supercapacitor, the principal one is the high self-discharge rate. Proper design strategies of the separator can suppress the self-discharge rate. Peng et al. synthesized polyacrylonitrile coated sodium dodecyl benzene sulfonate (PAN@SDBS) nanofiber membrane through coaxial electrospinning method. This membrane was used as a separator for the supercapacitor. The device showed a slow self-discharge rate because of the constrained ion diffusion due to the concentration gradient through the engineered membrane [104]. The field of separator engineering receives relatively less research interest compared to that of electrode materials and electrolytes. However, a few major drawbacks can be resolved through the proper engineering of the separator. Hence more research is necessary to advance the general performance of the supercapacitor device.

2.5.3 Electrolyte

The electrolyte is another important part of the supercapacitor device. It is an important detrimental component that controls other important parameters like operating potential window, self-discharge, rate performance, internal resistance, cycle life, operating temperature, etc. [105]. Among the different types, electrolytes can broadly be classified into two different categories, liquid electrolytes and solid-state electrolytes. Liquid electrolytes can be further classified into two groups:

```
                        ┌──────────────┐
                        │  Electrolyte │
                        └──────────────┘
                   ┌───────────┴───────────┐
            ┌──────────────┐        ┌──────────────┐
            │    Liquid    │        │  Solid-state │
            │  electrolyte │        │  electrolyte │
            └──────────────┘        └──────────────┘
          ┌────────┴────────┐
   ┌──────────────┐  ┌──────────────┐
   │   Aqueous    │  │ Non-aqueous  │
   │  electrolyte │  │  electrolyte │
   └──────────────┘  └──────────────┘
```
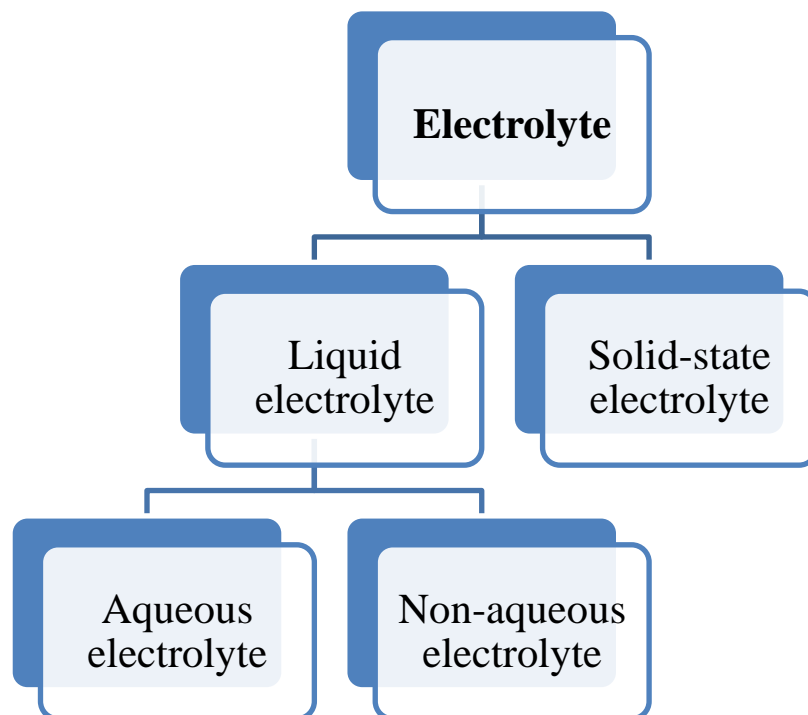
<p align="center"><strong style="color:blue">Figure 2.5.3 Classification of electrolytes</p>

aqueous electrolytes and non-aqueous electrolytes [106]. The broad classification of electrolytes has been shown in figure 2.5.3. Aqueous electrolyte-based supercapacitors usually offer high capacitance because of the high ionic conductivity of the electrolyte. But operating potential window, in this case, becomes very narrow owing to the small decomposition potential of the electrolyte. Because of this small potential window, the energy density offered by the device becomes less. On the other hand, supercapacitor with non-aqueous electrolyte can offer higher potential window and thus a much higher energy density can be obtained. Solid electrolytes also offer high potential window, with an added benefit that in a device with solid electrolyte there is no leakage problem. Thus there is no single electrolyte which can satisfy all the requirements for supercapacitor.

Aqueous electrolytes are extensively used in the laboratory because of their low cost and ease of handle-ability. To date, no commercial device has been fabricated with aqueous electrolytes because of low energy density. Aqueous electrolytes have higher ionic conductivity than organic and ionic liquid electrolytes [107]. H_2SO_4 is the most popular acidic type of aqueous electrolyte because of the ultrahigh ionic conductivity of 0.8 S cm^{-1} (at room temperature) [108]. Because of this high ionic conductivity, device resistance can be reduced, and power density can be increased. Different alkaline type aqueous electrolytes are also frequently used for device fabrication. Aqueous KOH electrolyte is a commonly used alkaline electrolyte that also offers high ionic conductivity of 0.6 S cm^{-1} (at 25 °C). NaOH and LiOH are also used in supercapacitor device fabrication among the other alkaline electrolytes. Alongside acidic and alkaline electrolytes, neutral electrolytes are also popular in the research field. Aqueous solutions of Na_2SO_4, KCl, NaCl, etc., have been widely used because they can provide a relatively higher potential window compared to alkaline and acidic electrolytes. Also, these types of neutral electrolytes result in less corrosion of the current collector.

Among the non-aqueous type electrolytes, organic electrolytes are mainly used in the commercial market because of their high operating potential window of 2.5 to 2.8 V. However; they are costly offer low ionic conductivity and low specific capacitance. They are also highly flammable and toxic. Tetraethyl ammonium tetrafluoroborate (TEABF$_4$) in acetonitrile (AC) solvent or propylene carbonate (PC) are examples of organic type electrolytes [109,110].

Ionic liquids also belong to the non-aqueous type electrolyte. They are basically salts having melting points under 100 °C and comprise of inorganic or organic anions and organic cations [111]. Because of the weak interactions between the ions, they tend to have a low melting point. By varying the combinations of cations and anions, the properties of ionic liquids can be tuned easily. Ionic liquids are non-flammable, thermally, and electrochemically more stable. A relatively high potential window (> 3 V) can be achieved with this type of electrolyte. Combinations of ammonium, sulfonium, pyrrolidinium, imidazolium, and phosphonium cations and hexafluorophosphate (PF$_6$), tetrafluoroborate (BF$_4$), bis(fluorosulfonyl)imide (FSI), bis(trifluoromethanesulfonyl) imide (TFSI), and dicyanamide (DCA) anions are useally used as ionic liquid electrolytes in supercapacitor application [112, 113].

Recently, electrochemical energy storage devices containing solid-state electrolytes have gained research attention due to the rapidly increasing demand for portable electronics, wearable electronics, etc. The solid-state electrolytes serve two different purposes. Firstly, it acts as an electrolyte to conduct the ions, and secondly, it acts as the separator for the two electrodes [114]. Among the different types of solid-state electrolytes, polymer electrolytes are most often used for supercapacitors. Polymer-based electrolytes can be classified into three different categories: solid polymer electrolyte (SPE), gel polymer electrolyte (GPE), and polyelectrolyte. Among these three types, gel polymer electrolyte is most extensively used in supercapacitor application due to its highest ionic conductivity among the other solid-state electrolytes. A gel polymer contains a host polymer like polyethylene oxides (PEO), polyvinyl alcohol (PVA), etc., and an aqueous electrolyte like Na_2SO_4, KOH, H_2SO_4, etc. [115].

2.6 Properties of ideal electrode material

Although electrolyte, separator, and current collector play a major role in determining the overall performance of the supercapacitor, the major contribution in charge storage capability and overall device stability is mainly determined by the choice of electrode material. Supercapacitor electrode material must have high surface area, good electrical conductivity, good thermal and chemical stability, corrosion resistivity and good surface wettability in the electrolyte used. Apart from these, the electrode materials should be of low cost, easy to process, and environmentally friendly with good recyclability. The pseudocapacitive materials require additional criteria which are to easily transfer the faradic charge. This is essential to enhance the overall performance [116]. The specific capacitance value of typical electrode material is dependent on many essential parameters like its surface area, morphology, distribution of pore size, and pore shape. It is seen that the material with reduced pore sizes offers high capacitance and high energy density. However, the reduced pore size increases the resistive nature of the electrode material, which reduces the power density [117].

Thus, the most important requirements for fabricating an efficient supercapacitor electrode include improving the number of available electrochemically active sites by enhancing specific surface area of the electrode material, tuning the pore size and

pore shape of the electrode material and increasing the connection between individual redox active sites by tuning the morphology [118–120]. Different researchers have tried to tune the morphology of the electrode material to improve the electrochemical charge storage performance.

2.7 Morphological effect on the performance of electrode materials

Kim and co-workers synthesized nickel oxide (NiO) nano structures with different morphologies through the sol-gel method [121]. The morphologies of the synthesized samples were varied by changing the basicity of the precursor solution. Under weak basic conditions (using hexamethylene tetramine (HMTA)), flower-like nanostructure, as shown in figure 2.7.1 (a) was obtained. The medium basic precursor prepared by ammonium hydroxide (NH$_4$OH) resulted in the formation of nanoslice of NiO and is shown in figure 2.7.1 (b). On the other hand, much smaller nano particles of NiO having a diameter ~ 50 nm were obtained under strong basic condition
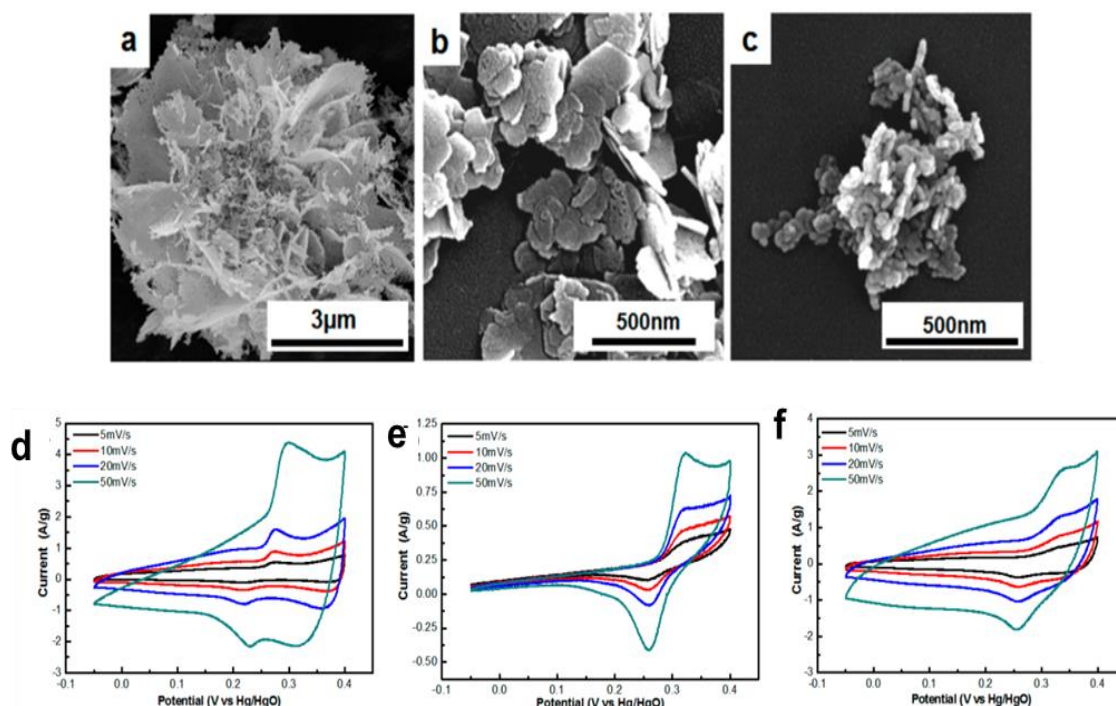
Figure 2.7.1 SEM images of (a) nanoflower (b) nanoslice (c) nanoparticles of NiO. CV diagram of (d) nanoflower (e) nanoslice (f) nanoparticles of NiO

obtained by adding lithium hydroxide (LiOH) in the precursor. From the BET specific surface area measurement, it was estimated that the nanoflower-like structure had a specific surface area of 159 m^2 g^{-1} with a pore volume of 0.66 cc g^{-1}. Whereas the

same value for the other two samples was 193 m^2 g^{-1} for nanoslice (pore volume 0.3 cc g^{-1}) and 233 m^2 g^{-1} (pore volume 0.51 cc g^{-1}) for the nanoparticles of NiO. Hence, at first glance, it may seem that the sample with a larger specific surface area should offer better electrochemical storage performance. However, electrochemical characterizations revealed that the morphology with minimum surface area (nanoflower of NiO) demonstrated the highest specific capacitance of 480 F g^{-1} at a current density of 0.5 A g^{-1} in 2 M aqueous KOH solution. Figure 2.7.1 (d), (e), and (f) show the CV diagrams within the same potential window for the sample nanoflower, nanoslice, and nanoparticles, respectively. These diagrams revealed that the nanoflower offered the highest loop area at any particular scan rate compared to the other two samples. The associated XPS study revealed that the nanoflower type sample is more hydrous than the other two samples, which could be due to the higher pore volume of the sample. This hydrous nature of the sample and the well-connected redox-active sites can provide easy paths to the OH$^-$ ions which enhance the redox activity. Thus it was concluded that the electrochemical storage performance depends strongly on the connectivity of the crystallites and the type of pore present in the sample. A similar type of observation was reported by Sun et al. with the binary metal oxide of nickel and cobalt [122]. The morphology of the Ni-Co binary oxide was varied by varying the Co: Ni ratio during the synthesis procedure, which resulted in nanoplate, nanorod and nanoparticles of the binary oxide. It was seen that the sample with Ni: Co = 1:1 showed the highest surface area of 156.4 m^2 g^{-1} with a discreet nanosheet morphology. On the other hand, the sample with Ni: Co = 1:2 demonstrate a comparatively low surface area of ~135 m^2 g^{-1} with a morphology which consists of well-connected porous nanospheres encapsulated in nanosheet Electrochemical study revealed that the sample with Ni: Co = 1:2, although having low surface area compared to the sample with Ni: Co = 1:1 offered highest specific capacitance of 1147 F g^{-1} at a current density of 3 A g^{-1}. However, when the discharge current density was increased to 15 A g^{-1}, it was seen that the sample with Ni: Co = 1:4 outperformed the sample with Ni: Co = 1:2 in terms of specific capacitance value. At this high current density, the sample with Ni: Co = 1:4 offered a specific capacitance of 755 F g^{-1}, whereas the sample with Ni: Co = 1:2 offered 695 F g^{-1}. This is particularly because of the nanorod type morphology of the sample with Ni: Co = 1:4. This reduces the resistance between the individual active sites by providing electronic pathways. At a high discharge current, the storage performance is dominated by the

mass transfer and electron conductivity of the sample, and thus the 1D geometry of the nanorod showed advantages. Several pieces of research have also explored the morphological effect on the electrochemical charge storage performance of MnO_2. Wei et al. synthesized different nanostructures of MnO_2 on gold-coated glass substrate through electrodeposition [123]. Different parameters like solution composition, pH value, deposition current density, etc., were varied to obtain different morphologies. Figure 2.7.2 (a) shows the continuous coating of MnO_2 on the gold substrate, which was obtained at a neutral pH value and at a relatively high deposition current density of 20 mA cm^{-2}. When the current density and pH value are reduced to 0.1 mA cm^{-2} and 5.0, respectively, the columnar structure of MnO_2 was obtained, and an SEM image of the same has been shown in figure 2.7.2 (b). The inset of figure
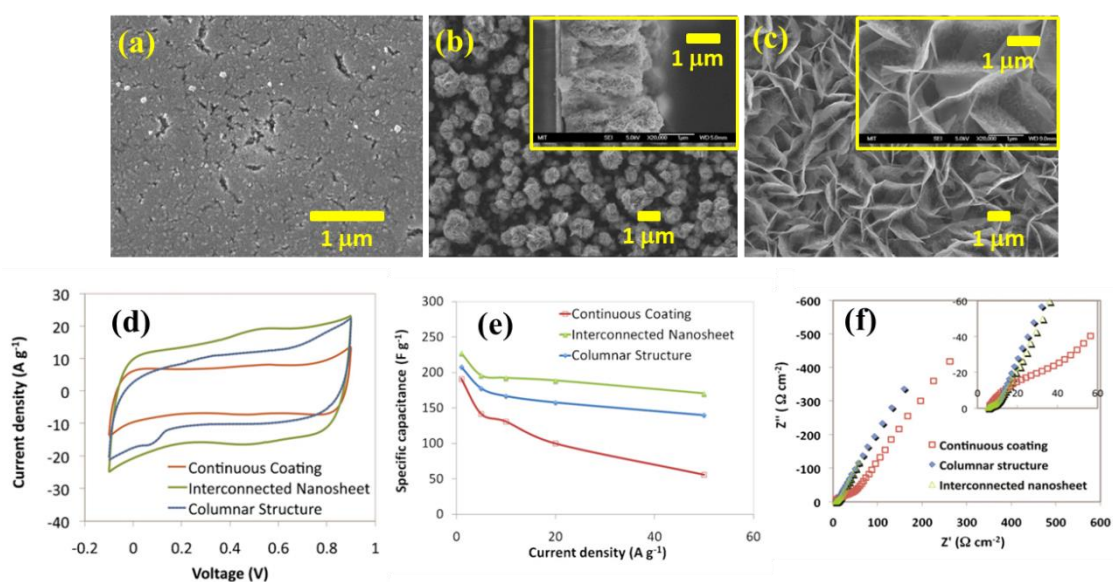
Figure 2.7.2 SEM images of (a) continuous coating (b) columnar structure (inset) cross-sectional SEM (c) interconnected nanosheet (inset) high magnification image of MnO$_2$ (d) comparison of CV diagrams of the MnO$_2$ with different morphologies (e) specific capacitance vs. current density plot for the different morphologies (f) comparison of EIS for deposited MnO$_2$ with different morphologies

2.7.2 (b) shows the cross-sectional view of the columnar structure. If the current density is further reduced, interconnected nanosheet architecture was formed by keeping the pH value constant at 5.0. Figure 2.7.2 (c) and inset show the interconnected architecture in low and high magnifications, respectively. CV study at 100 mV s^{-1} (figure 2.7.2 (d)) revealed that all these samples showed nearly rectangular loops, which suggest excellent capacitive behavior. However, the areas of

these loops are not the same. It is maximum for the sample with interconnected nanosheet architecture and minimum for the continuously coated sample. Thus storage capacity is higher in interconnected nanosheet and it is minimum for continuously coated sample. Figure 2.7.2 (e) shows the specific capacitance vs. current density plot for the different samples. At higher current densities, the aligned morphologies (i.e. nanosheet and columnar structure of MnO_2) retained higher specific capacitances whereas for the continuously coated structure the fall of capacitance with increasing current density is significant. As already explained this is due to the reduced resistance for these samples with interconnected morphology. EIS study shown in figure 2.7.2 (f) predicted the same variation of diffusive resistance for
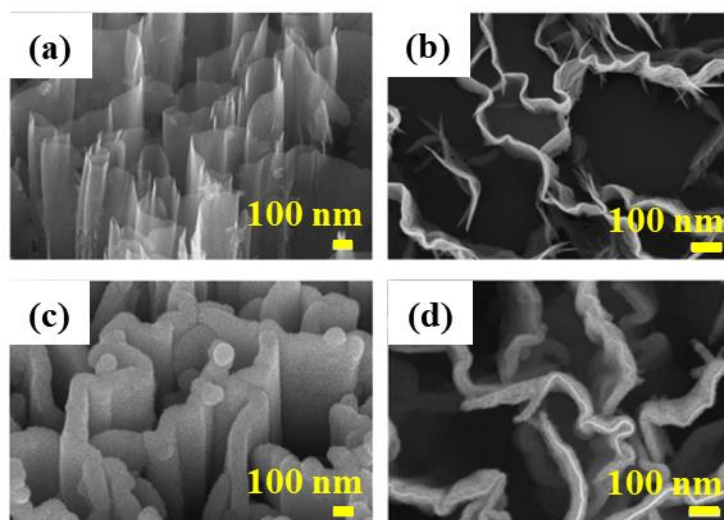
Figure 2.7.3 (a) Tilt view (b) top view of the vertical graphene sheets (c) tilt view and (d) top view of the graphene/MnO_2 sheets

the electrolyte ions i.e. it is minimum for nanosheet architecture and maximum for the continuously coated MnO_2. Thus it can be concluded that the aligned morphologies are better candidate electrochemical charge storage applications as they can provide large number of electrochemically active sites from top of the sample to the bottom layer close to the gold current collector. Also they provide short paths for electron transport which lead to low charge transfer resistances. Charge storage by hybrid mechanism (EDLC + pseudocapacitive) also shows morphological effect. This has been shown by synthesizing vertical graphene sheets coated with MnO_2 and by studying their electrochemical charge storage performance by Zang et al. [124]. Vertical graphene sheets were grown using microwave plasma-assisted chemical vapor deposition on graphite paper. The grown vertical sheets showed a thickness of

less than 1 nm and a height of several tens of microns. Figure 2.7.3 (a) and (b) show the SEM images of the tilt view and the top view of the grown vertical graphene sheets. To improve the charge storage performance of these graphene sheets, a coating of MnO_2 was applied using chemical bath deposition. Figure 2.7.3 (c) and (d) show the SEM images of the tilt view and top view of the MnO_2/graphene hybrid sheets. To compare the electrochemical charge storage performances two other geometries of MnO_2/graphene sheets were fabricated. The lateral and planar structures were fabricated by squeezing the vertical MnO_2/graphene sheets under different pressures. Figure 2.7.4 (b) and (c) show the tilt view of the SEM images of the lateral and planar
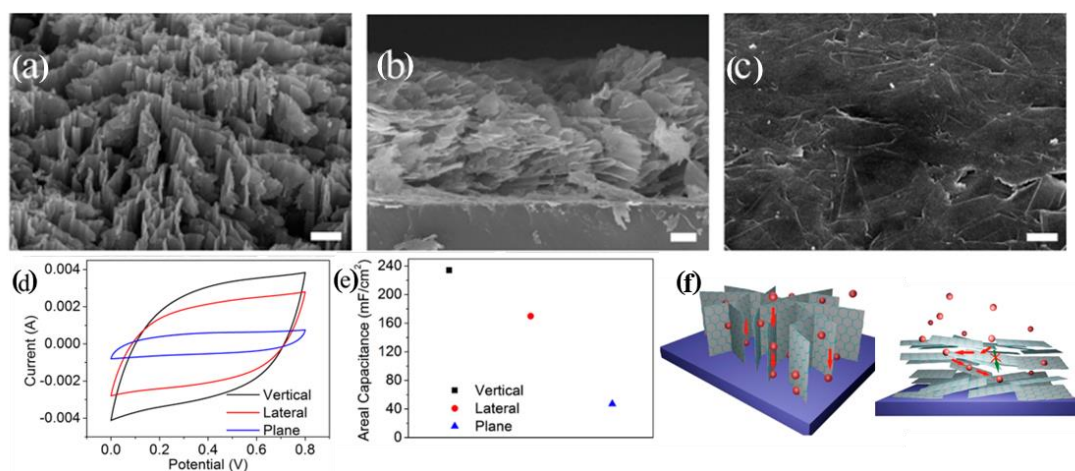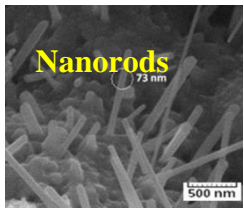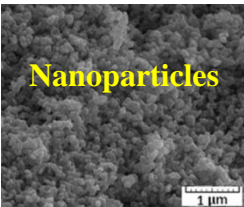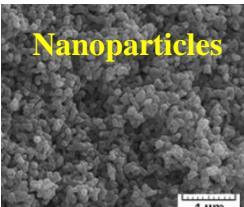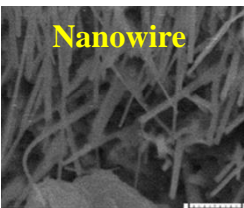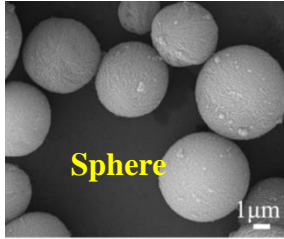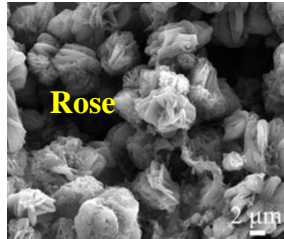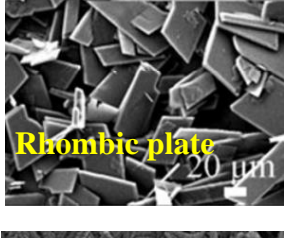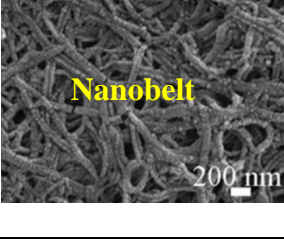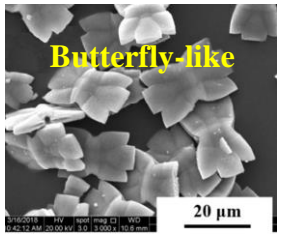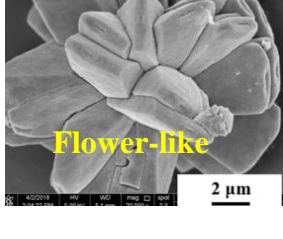
Figure 2.7.4 Tilt view of the SEM images of (a) vertical graphene sheets (b) lateral graphene sheets and (c) planar graphene sheets. (d) CV diagrams for different geometries of MnO_2/graphene sheets. (e) Comparison of areal specific capacitances for these different geometries. (f) Schematic of ion diffusion in the two geometries of the electrodes

MnO_2/graphene sheets. Electrochemical performance testing showed that, the vertical MnO_2/graphene electrode offered the highest CV loop area, and the planar MnO_2/graphene showed the lowest CV loop area (figure 2.7.4 (d)). Thus the areal-specific capacitance for the vertical sheet sample was $\sim$ 240 mF cm^{-2}, which was around six times higher than the planar sheet geometry. Figure 2.7.4 (e) compares the areal-specific capacitances for different geometries. EIS measurement also showed that the vertical graphene sheets offered low contact resistance and low ion diffusion resistance compared to the other geometries. Thus vertically oriented graphene sheets on electrode surfaces are an excellent candidate for the supercapacitor electrodes. Because of the large distance between each sheet ($\sim$ 10 - 100 nm), the electrolyte ions can reach the bottom of graphene sheets in a relatively straight path. This serves two purposes firstly, the electrode material utilization increases as the whole of the electrode material is now accessible to the ions. Secondly, ion diffusion resistance

decreases because of the relatively straight paths. However, in the lateral geometry, the ions cannot reach the bottom of the electrode, and thus material utilization decreases. Figure 2.7.4 (f) shows the schematic for ion diffusion in vertical and lateral geometries of the graphene sheets. However, vertical stack of graphene sheets are not commercially viable as they are prone to change their geometry under slightest of pressure which can cause the degradation of the supercapacitor device. Table 2.7.1 lists a few results regarding the morphological effect on the electrochemical performances of different electrode materials. This thesis work explores the possibility of fabrication of different morphologies of the electrode materials through different methods and then to study the effect of morphology on their respective electrochemical performances.

Table 2.7.1: Results from recent reports on the morphological effect on the electrochemical performance

Sample	Morphologies	Specific capacitances	Ref
Copper oxide (CuO)	Nanorods	86.7 F g^{-1}	[133]
	Nanoparticles	113.5 F g^{-1}	
	Nanoparticles	83.2 F g^{-1}	
	Nanowire	56.3 F g^{-1}	

Polyaniline (PANI)	**Sphere** 1μm	→ 144 F g^{-1}	[134]
	Rose 2 μm	→ 146 F g^{-1}	
	Rhombic plate 20 μm	→ 75 F g^{-1}	
	Nanobelt 200 nm	→ 248 F g^{-1}	
Vanadium pentoxide (V$_2$O$_5$)	**Butterfly-like** 20 μm	→ 483 F g^{-1}	[135]
	Rhombohedral 5 μm	→ 608 F g^{-1}	
	Flower-like 2 μm	→ 544 F g^{-1}	

2.8 Challenges for supercapacitor

The field of supercapacitor research is very vast and is always evolving. Improvements are being made on a daily basis to enhance the performance of this device. Supercapacitors are already finding applications in different fields requiring many charge-discharge cycles. In cars, buses, trains, cranes, and elevators, they have been used as a device to store energy in very little time generated via braking. This technology is known as regenerative braking, which has prolonged the mileage of an electric vehicle. Supercapacitors with a relatively small value of less than 10 F are finding applications in different consumer electronics in parallel to a battery as a power backup module. On the other hand, supercapacitors with a high storage value of greater than 100 F are now being used in hybrid electric vehicles, different portable power tools, etc. [7]. Different manufacturers are now developing supercapacitors with different capacities because of the bright future in different commercial sectors. Table 2.8.1 lists different supercapacitors manufactured by different companies and their properties [8,125].

Table 2.8.1: Properties of commercial supercapacitors

Manufacturer	Window potential (V)	Capacitance (F)	Energy density (Wh kg^{-1})	Power density (W kg^{-1})
Maxwell	2.7	2800	4.45	900
Maxwell	3	3000	4.25	30000
Apowercap	2.7	590	5	2618
Asahi Glass	2.7	1375	4.9	390
Panasonic	2.5	1200	2.3	514
Nesscap	2.7	5085	4.3	958
LS Cable	2.8	3200	3.7	1400
Power Sys	2.7	1350	4.9	650

Although having many advantages like fast charging speed, wide operating temperature, and long service life (around 10 to 15 years), certain problems are needed to be overcome.

- Low energy density

Supercapacitors offer a very small energy density (about 5 Wh kg^{-1}) compared to batteries (>50 Wh kg^{-1}). Thus except for delivering a short burst of energy, it can not

provide the same for a longer duration. To address this problem, a new kind of supercapacitor device are being developed where the positrode is made of a battery type material and the negatrode is made of conventional supercapacitive material. This type of device is now termed as supercapattery, which combines the merits of both battery and supercapacitor [126,127]. Because of the presence of the battery-type material, the energy density of such devices increases.

- High self-discharging rate

Spontaneous decrease of the voltage of a supercapacitor in an open circuit is known as self-discharge. Supercapacitors show a high self-discharging rate of more than 40% per 12 hours. There are three main mechanisms that are responsible for self-discharge. The first one is the faradic side reactions that occur due to impurities or unwanted functional groups on the electrode surface. Overcharging of a supercapacitor also decomposes the electrolyte, which also contributes to the faradic side reaction. The second one is due to the ohomic leakage, which refers to the formation of internal short paths due to incomplete sealing of the two electrodes. The final one is due to the charge redistribution, which arises due to the presence of charge concentration gradient, which causes the flow of charge through the device, causing the loss of voltage [128, 129]. Self-discharge of a supercapacitor limits its usage as a device to store energy for the long term. Different breakthroughs have been made to limit the self-discharge rate. These breakthroughs mainly include modifying the separator, electrolyte, or both [130]. However, these improvements are still yet to be implemented in the commercial field.

- High cost

Finally, the cost of supercapacitor plays a major role in successful commercialization. The principal component of the cost for supercapacitor manufacturing comes from the cost of its electrode materials [131]. The commercially most popular electrode material is high surface area carbon which is moderately expensive. For pseudocapacitive type material like RuO_2, which is very expensive and is only used in military applications. Different researchers are researching to synthesize high surface area carbon from different bio-waste, which could reduce the electrode cost [132]. Apart from electrode material, an electrolyte for supercapacitor is also expensive and adds additional challenges for manufacturing. In fact, presently researched engineered

electrolyte and separators which could reduce the possibility of self-discharge are even more costly. Upscaling the fabrication process can be a way to reduce the cost per device. Researchers from different fields are needed to collaborate for the creation of assembly lines for efficient and cost-effective production.

2.9 References

[1]   J. Ho, T. R. Jow, S. Boggs, Historical introduction to capacitor technology, *IEEE Electr. Insul. Mag.* 26 (2010) 20–25. doi:10.1109/MEI.2010.5383924.

[2]   D. P. Dubal, Y. P. Wu, R. Holze, Supercapacitors: from the Leyden jar to electric busses, *ChemTexts.* 2 (2016). doi:10.1007/s40828-016-0032-6.

[3]   K. Y. Chan, B. Jia, H. Lin, N. Hameed, J.H. Lee, K.T. Lau, A critical review on multifunctional composites as structural capacitors for energy storage, *Compos. Struct.* 188 (2018) 126–142. doi:10.1016/j.compstruct.2017.12.072.

[4]   A. Nishino, Capacitors: Operating principles, current market and technical trends, *J. Power Sources.* 60 (1996) 137–147. doi:10.1016/S0378-7753(96)80003-6.

[5]   L. Qi, L. Petersson, T. Liu, Review of Recent Activities on Dielectric Films for Capacitor Applications, *J. Int. Counc. Electr. Eng.* 4 (2014) 1–6. doi:10.5370/jicee.2014.4.1.001.

[6]   H. I. Becker, Low voltage electrolytic capacitor, U.S. Pat. 2 (1957) 616.

[7]   S. Huang, X. Zhu, S. Sarkar, Y. Zhao, Challenges and opportunities for supercapacitors, *APL Mater.* 7 (2019) 100901. doi:10.1063/1.5116146.

[8]   A. González, E. Goikolea, J. A. Barrena, R. Mysyk, Review on supercapacitors: Technologies and materials, *Renew. Sustain. Energy Rev.* 58 (2016) 1189–1206. doi:10.1016/j.rser.2015.12.249.

[9]   Y. M. Volfkovich, Electrochemical Supercapacitors (a Review), *Russ. J. Electrochem.* 57 (2021) 311–347. doi:10.1134/S1023193521040108.

[10]   R. Kötz, M. Carlen, Principles and applications of electrochemical capacitors, *Electrochim. Acta.* 45 (2000) 2483–2498. doi:10.1016/S0013-4686(00)00354-6.

[11]   G. Wang, L. Zhang, J. Zhang, A review of electrode materials for electrochemical supercapacitors, *Chem. Soc. Rev.* 41 (2012) 797–828. doi:10.1039/c1cs15060j.

[12]   N. R. Chodankar, H. D. Pham, A. K. Nanjundan, J. F. S. Fernando, K. Jayaramulu, D. Golberg, Y. K. Han, D. P. Dubal, True Meaning of Pseudocapacitors and Their Performance Metrics: Asymmetric versus Hybrid Supercapacitors, *Small.* 16 (2020) 1–35. doi:10.1002/smll.202002806.

[13]   A. Muzaffar, M. B. Ahamed, K. Deshmukh, J. Thirumalai, A review on recent advances in hybrid supercapacitors : Design, fabrication and applications, *Renewable and Sustainable Energy Reviews.* 101 (2019) 123–145. doi:10.1016/j.rser.2018.10.026.

[14]   P. Sharma, T. S. Bhatti, A review on electrochemical double-layer capacitors, *Energy Convers.*

Manag. 51 (2010) 2901–2912. doi:10.1016/j.enconman.2010.06.031.

[15]   R. Burt, G. Birkett, X. S. Zhao, A review of molecular modeling of electric double layer capacitors, *Phys. Chem. Chem. Phys.* (2014) 6519–6538. doi:10.1039/c3cp55186e.

[16]   G. H. Bolt, Analysis of the validity of the Gouy-Chapman theory of the electric double layer, *J. Colloid Sci.* 10 (1955) 206–218. doi:10.1016/0095-8522(55)90027-1.

[17]   B. E. Conway, Electrochemical Supercapacitors Scientific Fundamentals and Technological Applications, *Springer.* 25 (1988) 907–915. doi:10.1016/0306-4522(88)90044-9.

[18]   Y. Jiang, J. Liu, Definitions of Pseudocapacitive Materials: A Brief Review, *Energy Environ. Mater.* 2 (2019) 30–37. doi:10.1002/eem2.12028.

[19]   V. Subramanian, S. C. Hall, P. H. Smith, B. Rambabu, Mesoporous anhydrous RuO_2as a supercapacitor electrode material, *Solid State Ionics*. 175 (2004) 511–515. doi:10.1016/j.ssi.2004.01.070.

[20]   X. Li, X. Li, G. Wang, X. Wang, J. Ji, Flexible supercapacitor based on MnO_2 nanoparticles via electrospinning, *J. Mater. Chem. A*. 1 (2013) 10103–10106. doi:10.1039/c3ta11727h.

[21]   A. Ray, A. Roy, P. Sadhukhan, S. R. Chowdhury, P. Maji, S. K. Bhattachrya, S. Das, Electrochemical properties of TiO_2-V_2O_5nanocomposites as a high performance supercapacitors electrode material, *Appl. Surf. Sci*. 443 (2018) 581–591. doi:10.1016/j.apsusc.2018.02.277.

[22]   A. Roy, A. Ray, S. Saha, S. Das, Investigation on energy storage and conversion properties of multifunctional PANI-MWCNT composite, *Int. J. Hydrogen Energy*. 43 (2018) 7128–7139. doi:10.1016/j.ijhydene.2018.02.153.

[23]   J. S. Lee, D. H. Shin, J. Jang, Polypyrrole-coated manganese dioxide with multiscale architectures for ultrahigh capacity energy storage, *Energy Environ. Sci*. 8 (2015) 3030–3039. doi:10.1039/c5ee02076j.

[24]   B. E. Conway, V. Birss, J. Wojtowicz, The role and utilization of pseudocapacitance for energy storage by supercapacitors, *Journal of Power Sources.* 66 (1997) 1–14.

[25]   V. Augustyn, P. Simon, B. Dunn, Pseudocapacitive oxide materials for high-rate electrochemical energy storage, *Energy Environ. Sci*. 7 (2014) 1597–1614. doi:10.1039/c3ee44164d.

[26]   V. Sudha, M. V Sangaranarayanan, Underpotential Deposition of Metals : Structural and Thermodynamic Considerations, *J. Phys. Chem. B.* (2002) 2699–2707.

[27]   E. Herrero, L. J. Buller, H. D. Abruña, Underpotential deposition at single crystal surfaces of Au, Pt, Ag and other materials, *Chem. Rev*. 101 (2001) 1897–1930. doi:10.1021/cr9600363.

[28] H. Xia, S. Meng, G. Yuan, C. Cui, L. Lu, A Symmetric RuO_2 / RuO_2 Supercapacitor Operating at 1 . 6 V by Using a Neutral Aqueous Electrolyte, *Electrochem. Solid-State Lett.*15 (2012) 2012–2015. doi:10.1149/2.023204esl.

[29] S. P. Gupta, B. A. Kakade, B. R. Sathe, Q. Qiao, D. J. Late, P. S. Walke, Thermally driven high-rate intercalated pseudocapacitance of flower-like architecture of ultrathin few layered δ-MnO_2 nanosheets on carbon nano-onions, *ACS Appl. Energy Mater.* 3 (2020) 11398–11409. doi:10.1021/acsaem.0c02325.

[30] A. A. Lubimtsev, P. R. C. Kent, B. G. Sumpter, P. Ganesh, Understanding the origin of high-rate intercalation pseudocapacitance in Nb_2O_5 crystals, *J. Mater. Chem. A.* 1 (2013) 14951–14956. doi:10.1039/c3ta13316h.

[31] Y. Liu, S. P. Jiang, Z. Shao, Intercalation pseudocapacitance in electrochemical energy storage: recent advances in fundamental understanding and materials development, *Mater. Today Adv.* 7 (2020) 100072. doi:10.1016/j.mtadv.2020.100072.

[32] A. Roy, A. Ray, S. Saha, M. Ghosh, T. Das, B. Satpati, M. Nandi, S. Das, NiO-CNT composite for high performance supercapacitor electrode and oxygen evolution reaction, *Electrochim. Acta.* 283 (2018) 327–337. doi:10.1016/j.electacta.2018.06.154.

[33] X. Dong, X. Wang, J. Wang, H. Song, X. Li, L. Wang, M. B. Chan-park, C. Ming, P. Chen, Synthesis of a MnO_2–graphene foam hybrid with controlled MnO_2 particle shape and its use as a supercapacitor electrode, *Carbon* .50 (2012) 4865–4870. doi:10.1016/j.carbon.2012.06.014.

[34] B. Che, H. Li, D. Zhou, Y. Zhang, Z. Zeng, C. Zhao, C. He, E. Liu, X. Lu, Porous polyaniline/carbon nanotube composite electrode for supercapacitors with outstanding rate capability and cyclic stability, *Compos. Part B Eng.* 165 (2019) 671–678. doi:10.1016/j.compositesb.2019.02.026.

[35] P. T. Kissinger, W. Lafayette, W. R. Heineman, Cyclic Voltammetry, *J. Chem. Educ.* 9 (1983) 702–706. doi: 10.1021/ed060p702

[36] J. J. Van Benschoten, J. Y. Lewis, W. R. Heineman, D. A. Roston, P. T. Kissinger, Cyclic Voltammetry Experiment, *J. Chem. Educ.* 9 (1983) 772–776. doi:10.1021/ed060p772.

[37] A. Ray, A. Roy, S. Saha, Transition Metal Oxide-Based Nano-materials for Energy Storage Application, *Intech Open* (2018) 1–17. doi: 10.5772/intechopen.80298

[38] M. Sufyan, S. Dai, M. Wang, D. Guo, L. Chen, X. Wang, C. Hu, Y. Xi, High performance solid state fl exible supercapacitor based on molybdenum sulfide hierarchical nanospheres, *Journal of Power Sources*. 285 (2015) 63–69. doi:10.1016/j.jpowsour.2015.03.079.

[39] W. Wang, S. Guo, I. Lee, K. Ahmed, J. Zhong, Z. Favors, F. Zaera, M. Ozkan, C.S. Ozkan, Hydrous ruthenium oxide nanoparticles anchored to graphene and carbon nanotube hybrid

foam for supercapacitors, *Sci. Rep*. 4 (2014) 9–14. doi:10.1038/srep04452.

[40]   L. Miao, Z. Song, D. Zhu, L. Li, L. Gan, M. Liu, Recent advances in carbon-based supercapacitors, *Mater. Adv*. 1 (2020) 945–966. doi:10.1039/d0ma00384k.

[41]   I. I. Gurten Inal, Z. Aktas, Enhancing the performance of activated carbon based scalable supercapacitors by heat treatment, *Appl. Surf. Sci*. 514 (2020) 145895. doi:10.1016/j.apsusc.2020.145895.

[42]   S. Lijima, Helical microtubules of graphitic carbon, *Nature*. 354 (1991) 56-58. doi: 10.1038/354056a0.

[43]   C. Niu, E. K. Sichel, R. Hoch, D. Moy, and H. Tennent, High power electrochemical capacitors based on carbon nanotube electrodes electrodes, *Appl. Phys. Lett.*1480 (2012) 21–24. doi: 10.1063/1.118568

[44]   C. Yu, C. Masarapu, J. Rong, B. Wei, H. Jiang, Stretchable Supercapacitors Based on Buckled Single-Walled Carbon-Nanotube Macrofilms, *Adv. Mater*. 21 (2009) 4793–4797. doi:10.1002/adma.200901775.

[45]   X. J. Lee, B. Y. Z. Hiew, K. C. Lai, L. Y. Lee, S. Gan, S. Thangalazhy-Gopakumar, S. Rigby, Review on graphene and its derivatives: Synthesis methods and potential industrial implementation, *J. Taiwan Inst. Chem. Eng*. 98 (2019) 163–180. doi:10.1016/j.jtice.2018.10.028.

[46]   C. Liu, Z. Yu, D. Neff, A. Zhamu, B. Z. Jang, Graphene-Based Supercapacitor with an Ultrahigh Energy Density, *Nano Lett*. 10 (2010) 4863–4868. doi:10.1021/nl102661q.

[47]   S. Zhang, Y. Li, N. Pan, Graphene based supercapacitor fabricated by vacuum filtration deposition, *J. Power Sources*. 206 (2012) 476–482. doi:10.1016/j.jpowsour.2012.01.124.

[48]   M. D. Stoller, S. Park, Y. Zhu, J. An, R. S. Ruoff, Graphene-Based Ultracapacitors, *Nano Lett*. 8 (2008) 3498–3502. doi:10.1021/nl802558y.

[49]   S. Trasatti, Physical electrochemistry of ceramic oxides, *Electrochim. Acta*. 36 (1991) 225–241. doi:10.1016/0013-4686(91)85244-2.

[50]   Y. Liu, F. Zhou, V. Ozolins, Ab Initio Study of the Charge-Storage Mechanisms in RuO_2 - Based Electrochemical Ultracapacitors, *J. Phys. Chem. C*. 116 (2012) 1450–1457. doi:10.1021/jp207616s.

[51]   U. M. Patil, S. B. Kulkarni, V. S. Jamadade, C.D. Lokhande, Chemically synthesized hydrous RuO_2 thin films for supercapacitor application, *J. Alloys Compd*. 509 (2011) 1677–1682. doi:10.1016/j.jallcom.2010.09.133.

[52]   S. Korkmaz, A. Kariper, O. Karaman, C. Karaman, The production of rGO/ RuO_2 aerogel

supercapacitor and analysis of its electrochemical performances, *Ceram. Int.* 47 (2021) 34514–34520. doi:10.1016/j.ceramint.2021.08.366.

[53] C. C. Hu, K. H. Chang, M. C. Lin, Y. T. Wu, Design and tailoring of the nanotubular arrayed architecture of hydrous RuO_2 for next generation supercapacitors, *Nano Lett.* 6 (2006) 2690–2695. doi:10.1021/nl061576a.

[54] T. P. Gujar, V. R. Shinde, C. D. Lokhande, W.Y. Kim, K.D. Jung, O.S. Joo, Spray deposited amorphous RuO_2 for an effective use in electrochemical supercapacitor, *Electrochem. Commun.* 9 (2007) 504–510. doi:10.1016/j.elecom.2006.10.017.

[55] R. Arunachalam, R. K. V. Prataap, R. Pavul Raj, S. Mohan, J. Vijayakumar, L. Péter, M. Al Ahmad, Pulse electrodeposited RuO_2 electrodes for high-performance supercapacitor applications, Surf. Eng. 35 (2019) 103–109. doi:10.1080/02670844.2018.1426408.

[56] C. M. Chuang, C. W. Huang, H. Teng, J. M. Ting, Hydrothermally synthesized RuO_2/Carbon nanofibers composites for use in high-rate supercapacitor electrodes, *Compos. Sci. Technol.* 72 (2012) 1524–1529. doi:10.1016/j.compscitech.2012.05.024.

[57] S. Cho, J. Kim, Y. Jo, A. T. A. Ahmed, H. S. Chavan, H. Woo, A. I. Inamdar, J. L. Gunjakar, S. M. Pawar, Y. Park, H. Kim, H. Im, Bendable RuO_2/graphene thin film for fully flexible supercapacitor electrodes with superior stability, *J. Alloys Compd.* 725 (2017) 108–114. doi:10.1016/j.jallcom.2017.07.135.

[58] S. N. Pusawale, P. R. Deshmukh, J. L. Gunjakar, C. D. Lokhande, SnO_2-RuO_2 composite films by chemical deposition for supercapacitor application, *Mater. Chem. Phys.* 139 (2013) 416–422. doi:10.1016/j.matchemphys.2012.12.059.

[59] J. H. Park, J. M. Ko, O. Ok Park, Carbon Nanotube/RuO_2 Nanocomposite Electrodes for Supercapacitors, *J. Electrochem. Soc.* 150 (2003) A864. doi:10.1149/1.1576222.

[60] M. Y. Chung, C. T. Lo, High-performance binder-free RuO_2/electrospun carbon fiber for supercapacitor electrodes, *Electrochim. Acta.* 364 (2020) 137324. doi:10.1016/j.electacta.2020.137324.

[61] D. Xiang, L. Yin, C. Wang, L. Zhang, High electrochemical performance of RuO_2-Fe_2O_3 nanoparticles embedded ordered mesoporous carbon as a supercapacitor electrode material, *Energy.* 106 (2016) 103–111. doi:10.1016/j.energy.2016.02.141.

[62] D. Majumdar, Review on Current Progress of MnO_2-Based Ternary Nanocomposites for Supercapacitor Applications, *ChemElectroChem.* 8 (2021) 291–336. doi:10.1002/celc.202001371.

[63] H. Y. Lee, J. B. Goodenough, Supercapacitor Behavior with KCl Electrolyte, *J. Solid State Chem.* 144 (1999) 220–223. doi:10.1006/jssc.1998.8128.

[64] J. Shin, J. K. Seo, R. Yaylian, A. Huang, Y. S. Meng, A review on mechanistic understanding of MnO_2 in aqueous electrolyte for electrical energy storage systems, *Int. Mater. Rev*. 65 (2020) 356–387. doi:10.1080/09506608.2019.1653520.

[65] Y. Zhang, C. Sun, P. Lu, K. Li, S. Song, D. Xue, Crystallization design of MnO_2 towards better supercapacitance, *CrystEngComm*. 14 (2012) 5892–5897. doi:10.1039/c2ce25610j.

[66] M. Toupin, T. Brousse, D. Bélanger, Charge storage mechanism of MnO_2 electrode used in aqueous electrochemical capacitor, *Chem. Mater*. 16 (2004) 3184–3190. doi:10.1021/cm049649j.

[67] N. Vangapally, K. K. V., A. Kumar, S. K. Martha, Charge storage behavior of sugar derived carbon/MnO_2 composite electrode material for high-performance supercapacitors, *J. Alloys Compd*. 893 (2022) 162232. doi:10.1016/j.jallcom.2021.162232.

[68] P. Wang, Y. Zhao, L. Wen, J. Chen, Z. Lei, Ultrasound − Microwave-Assisted Synthesis of MnO_2 Supercapacitor Electrode Materials, *Ind. Eng. Chem. Res*. 53 (2014) 20116-20123. doi:10.1021/ie5025485.

[69] Z. Yu, B. Duong, D. Abbitt, J. Thomas, Highly ordered MnO_2 nanopillars for enhanced supercapacitor performance, *Adv. Mater*. 25 (2013) 3302–3306. doi:10.1002/adma.201300572.

[70] Y. Li, H. Xie, J. Wang, L. Chen, Preparation and electrochemical performances of α-MnO_2 nanorod for supercapacitor, *Mater. Lett*. 65 (2011) 403–405. doi:10.1016/j.matlet2010.10.048.

[71] K. Xu, S. Li, J. Yang, J. Hu, Hierarchical hollow MnO_2 nanofibers with enhanced supercapacitor performance, *J. Colloid Interface Sci*. 513 (2018) 448–454. doi:10.1016/j.jcis.2017.11.052.

[72] S. Chen, J. Zhu, X. Wu, Q. Han, X. Wang, Graphene Oxide-MnO_2 Nanocomposites for Supercapacitors, *ACS Nano*. 4 (2010) 2822–2830. doi: 10.1021/nn901311t

[73] L. Li, Z. A. Hu, N. An, Y.Y. Yang, Z. M. Li, H.Y. Wu, Facile synthesis of MnO_2/CNTs composite for supercapacitor electrodes with long cycle stability, *J. Phys. Chem. C*. 118 (2014) 22865–22872. doi:10.1021/jp505744p.

[74] D. Yan, Z. Guo, G. Zhu, Z. Yu, H. Xu, A. Yu, MnO_2 film with three-dimensional structure prepared by hydrothermal process for supercapacitor, *J. Power Sources*. 199 (2012) 409–412. doi:10.1016/j.jpowsour.2011.10.051.

[75] A. Bahloul, B. Nessark, E. Briot, H. Groult, A. Mauger, K. Zaghib, C. M. Julien, Polypyrrole-covered MnO_2 as electrode material for supercapacitor, *J. Power Sources*. 240 (2013) 267–272. doi:10.1016/j.jpowsour.2013.04.013.

[76] Y. Chen, X. Zhang, C. Xu, H. Xu, The fabrication of asymmetry supercapacitor based on

MWCNTs/MnO$_2$ /PPy composites, *Electrochim. Acta.* 309 (2019) 424–431. doi:10.1016/j.electacta.2019.04.072.

[77] Y. Zhao, Y. Meng, P. Jiang, Carbon@MnO$_2$ core-shell nanospheres for flexible high-performance supercapacitor electrode materials, *J. Power Sources.* 259 (2014) 219–226. doi:10.1016/j.jpowsour.2014.02.086.

[78] S. Vijayakumar, S. Nagamuthu, G. Muralidharan, Supercapacitor studies on NiO nanoflakes synthesized through a microwave route, *ACS Appl. Mater. Interfaces.* 5 (2013) 2188–2196. doi:10.1021/am400012h.

[79] S. K. Meher, G. R. Rao, Ultralayered Co$_3$O$_4$ for High-Performance Supercapacitor Applications, J. Phys. Chem. C. 115 (2012) 15646. doi: 10.1021/jp201200e.

[80] A. Ramadoss, S. J. Kim, Vertically aligned TiO$_2$ nanorod arrays for electrochemical supercapacitor, *J. Alloys Compd.* 561 (2013) 262–267. doi:10.1016/j.jallcom.2013.02.015.

[81] B. Balamuralitharan, I. H. Cho, J. S. Bak, H. J. Kim, V$_2$O$_5$ nanorod electrode material for enhanced electrochemical properties by facile hydrothermal method for supercapacitor applications, *New J. Chem.* 42 (2018) 11862–11868. doi:10.1039/c8nj02377h.

[82] E. Mitchell, R.K. Gupta, K. Mensah-Darkwa, D. Kumar, K. Ramasamy, B. K. Gupta, P. Kahol, Facile synthesis and morphogenesis of superparamagnetic iron oxide nanoparticles for high-performance supercapacitor applications, *New J. Chem.* 38 (2014) 4344–4350. doi:10.1039/c4nj00741g.

[83] S. D. Dhas, P. S. Maldar, M. D. Patil, M. R. Waikar, R. G. Sonkawade, S. K. Chakarvarti, S. K. Shinde, D.Y. Kim, A. V. Moholkar, Probing the electrochemical properties of NiMn$_2$O$_4$ nanoparticles as prominent electrode materials for supercapacitor applications, *Mater. Sci. Eng. B Solid-State Mater. Adv. Technol.* 271 (2021) 115298. doi:10.1016/j.mseb.2021.115298.

[84] A. Umar, M. S. Akhtar, S. Ameen, M. Imran, R. Kumar, Y. Wang, A. A. Ibrahim, H. Albargi, M. Jalalah, M. A. Alsaiari, M. S. Al-Assiri, Colloidal synthesis of NiMn$_2$O$_4$ nanodisks decorated reduced graphene oxide for electrochemical applications, *Microchem. J.* 160 (2021) 105630. doi:10.1016/j.microc.2020.105630.

[85] H. Wei, J. Wang, L. Yu, Y. Zhang, D. Hou, T. Li, Facile synthesis of NiMn$_2$O$_4$ nanosheet arrays grown on nickel foam as novel electrode materials for high-performance supercapacitors, *Ceram. Int.* 42 (2016) 14963–14969. doi:10.1016/j.ceramint.2016.06.140.

[86] Z. Wang, Z. Zhu, C. Zhang, C. Xu, C. Chen, Facile synthesis of reduced graphene oxide/NiMn$_2$O$_4$ nanorods hybrid materials for high-performance supercapacitors, *Electrochim. Acta.* 230 (2017) 438–444. doi:10.1016/j.electacta.2017.02.023.

[87] M. R. Kim, M. Naidukalla, S. Kim, M. Kim, I. Kim, NiMn$_2$O$_4$ Nanosheet-Decorated

Hierarchically Porous Polyaromatic Carbon Spheres for High-Performance Supercapacitors, *ChemElectroChem*. 4 (2017) 1214–1221. doi:10.1002/celc.201700023.

[88]   Y. Sun, X. Du, J. Zhang, N. Huang, L. Yang, X. Sun, Microwave-assisted preparation and improvement mechanism of carbon nanotube@NiMn$_2$O$_4$ core-shell nanocomposite for high performance asymmetric supercapacitors, *J. Power Sources*. 473 (2020) 228609. doi:10.1016/j.jpowsour.2020.228609.

[89]   X. Du, L. Yang, Y. Fu, S. Liu, N. Huang, S. Wang, Microwave-Assisted Synthesis of NiMn$_2$O$_4$ Grown on Nickel Foam as Electrode Material for High-Performance Supercapacitors, *ChemistrySelect*. 6 (2021) 5567–5574. doi:10.1002/slct.202100895.

[90]   M. Zhang, Z. Song, H. Liu, T. Ma, Biomass-derived highly porous nitrogen-doped graphene orderly supported NiMn$_2$O$_4$ nanocrystals as efficient electrode materials for asymmetric supercapacitors, *Appl. Surf. Sci*. 507 (2020) 145065. doi:10.1016/j.apsusc.2019.145065.

[91]   M. Sandhiya, K. Subramani, M. Sathish, Augmenting the electrochemical performance of NiMn$_2$O$_4$ by doping of transition metal ions and compositing with rGO, *J. Colloid Interface Sci*. 598 (2021) 409–418. doi:10.1016/j.jcis.2021.04.023.

[92]   C. Wang, E. Zhou, W. He, X. Deng, J. Huang, M. Ding, X. Wei, X. Liu, X. Xu, NiCo$_2$O$_4$-based supercapacitor nanomaterials, *Nanomaterials*. 7 (2017) 1–23. doi:10.3390/nano7020041.

[93]   Y. Lei, J. Li, Y. Wang, L. Gu, Y. Chang, H. Yuan, D. Xiao, Rapid microwave-assisted green synthesis of 3D hierarchical flower-shaped NiCo$_2$O$_4$ microsphere for high-performance supercapacitor, *ACS Appl. Mater. Interfaces*. 6 (2014) 1773–1780. doi:10.1021/am404765y.

[94]   M. Gaire, B. Subedi, S. Adireddy, D. Chrisey, Ultra-long cycle life and binder-free manganese-cobalt oxide supercapacitor electrodes through photonic nanostructuring, *RSC Adv*. 10 (2020) 40234–40243. doi:10.1039/d0ra08510c.

[95]   H. Wu, Z. Lou, H. Yang, G. Shen, A flexible spiral-type supercapacitor based on ZnCo$_2$O$_4$ nanorod electrodes, *Nanoscale*. 7 (2015) 1921–1926. doi:10.1039/C4NR06336H.

[96]   L. Hu, B. Qu, C. Li, Y. Chen, L. Mei, D. Lei, L. Chen, Q. Li, T. Wang, Facile synthesis of uniform mesoporous ZnCo$_2$O$_4$ microspheres as a high-performance anode material for Li-ion batteries, *J. Mater. Chem. A*. 1 (2013) 5596. doi:10.1039/c3ta00085k.

[97]   L. Xu, Y. Zhao, J. Lian, Y. Xu, J. Bao, J. Qiu, L. Xu, H. Xu, M. Hua, H. Li, Morphology controlled preparation of ZnCo$_2$O$_4$ nanostructures for asymmetric supercapacitor with ultrahigh energy density, *Energy*. 123 (2017) 296–304. doi:10.1016/j.energy.2017.02.018.

[98]   A. Roy, A. Ray, S. Saha, M. Ghosh, T. Das, B. Satpati, M. Nandi, S. Das, NiO-CNT composite for high performance supercapacitor electrode and oxygen evolution reaction, *Electrochim. Acta*. 283 (2018) 327–337. doi:10.1016/j.electacta.2018.06.154.

[99] S. Park, Y. Lee, G. An, The rational design and interface engineering of an electrolyte and current collector for a stable and high-performance aqueous supercapacitor, *Int. J. Energy Res.* 45 (2021) 16027–16037. doi:10.1002/er.6830.

[100] L. Liu, H. Zhao, Y. Lei, Review on Nanoarchitectured Current Collectors for Pseudocapacitors, *Small Methods.* 3 (2019) 1800341. doi:10.1002/smtd.201800341.

[101] L. Wen, Y. Mi, C. Wang, Y. Fang, F. Grote, H. Zhao, M. Zhou, Y. Lei, Cost-effective Atomic Layer Deposition Synthesis of Pt Nanotube Arrays: Application for High Performance Supercapacitor, *Small.* 10 (2014) 3162–3168. doi:10.1002/smll.201400436.

[102] B. Szubzda, A. Szmaja, M. Ozimek, S. Mazurkiewicz, Polymer membranes as separators for supercapacitors, *Appl. Phys. A.* 117 (2014) 1801–1809. doi:10.1007/s00339-014-8674-y.

[103] S. Xian-Zhong, Z. Xiong, H. Bo, M. Yan-Wei, Effects of Separator on the Electrochemical Performance of Electrical Double-Layer Capacitor and Hybrid Battery-Supercapacitor, *Acta Physico-Chimica.* 30 (2014) 485–491. doi:10.3866/PKU.WHXB201401131.

[104] H. Peng, L. Xiao, K. Sun, G. Ma, G. Wei, Z. Lei, Preparation of a cheap and environmentally friendly separator by coaxial electrospinning toward suppressing self-discharge of supercapacitors, *J. Power Sources.* 435 (2019) 226800. doi:10.1016/j.jpowsour.2019.226800.

[105] C. Zhong, Y. Deng, W. Hu, J. Qiao, L. Zhang, J. Zhang, A review of electrolyte materials and compositions for electrochemical supercapacitors, *Chem. Soc. Rev.* 44 (2015). doi:10.1039/c5cs00303b.

[106] B. Pal, S. Yang, S. Ramesh, V. Thangadurai, R. Jose, Electrolyte selection for supercapacitive devices: a critical review, *Nanoscale Adv.* 1 (2019) 3807–3835. doi:10.1039/C9NA00374F.

[107] C. Zhao, W. Zheng, A Review for Aqueous Electrochemical Supercapacitors, *Front. Energy Res.* 3 (2015) 23. doi:10.3389/fenrg.2015.00023.

[108] M. Toupin, T. Brousse, D. Bélanger, Charge Storage Mechanism of MnO_2 Electrode Used in Aqueous Electrochemical Capacitor, *Chem. Mater.* 16 (2004) 3184–3190. doi:10.1021/cm049649j.

[109] J. Krummacher, C. Schütter, L.H. Hess, A. Balducci, Non-aqueous electrolytes for electrochemical capacitors, *Curr. Opin. Electrochem.* 9 (2018) 64–69. doi:10.1016/j.coelec.2018.03.036.

[110] J. Park, Y.-E. Yoo, L. Mai, W. Kim, Rational Design of a Redox-Active Nonaqueous Electrolyte for a High-Energy-Density Supercapacitor Based on Carbon Nanotubes, *ACS Sustain. Chem. Eng.* 7 (2019) 7728–7735. doi:10.1021/acssuschemeng.8b06486.

[111] L. Miao, Z. Song, D. Zhu, L. Li, L. Gan, M. Liu, Ionic Liquids for Supercapacitive Energy

Storage: A Mini-Review, *Energy & Fuels*. 35 (2021) 8443–8455. doi:10.1021/acs.energyfuels.1c00321.

[112] K. Karuppasamy, J. Theerthagiri, D. Vikraman, C.-J. Yim, S. Hussain, R. Sharma, T. Maiyalagan, J. Qin, H.-S. Kim, Ionic Liquid-Based Electrolytes for Energy Storage Devices: A Brief Review on Their Limits and Applications, *Polymers* . 12 (2020) 918. doi:10.3390/polym12040918.

[113] L. Yu, G. Z. Chen, Ionic Liquid-Based Electrolytes for Supercapacitor and Supercapattery, *Front. Chem.* 7 (2019) 272. doi:10.3389/fchem.2019.00272.

[114] L. Ainiya, The recent advances on potential solid electrolytes for all-solid-state supercapacitors: A short review, *J. Phys. Conf. Ser.* 1417 (2019) 012031. doi:10.1088/1742-6596/1417/1/012031.

[115] H. Yu, J. Wu, L. Fan, K. Xu, X. Zhong, Y. Lin, J. Lin, Improvement of the performance for quasi-solid-state supercapacitor by using PVA–KOH–KI polymer gel electrolyte, *Electrochim. Acta.* 56 (2011) 6881–6886. doi:10.1016/j.electacta.2011.06.039.

[116] P. Forouzandeh, V. Kumaravel, S. C. Pillai, Electrode Materials for Supercapacitors: A Review of Recent Advances, *Catalysts.* 10 (2020) 969. doi:10.3390/catal10090969.

[117] S. Kondrat, P. Wu, R. Qiao, A. A. Kornyshev, Accelerating charging dynamics in subnanometre pores, *Nat. Mater.* 13 (2014) 387–393. doi:10.1038/nmat3916.

[118] Q. Lu, J. G. Chen, J. Q. Xiao, Nanostructured Electrodes for High-Performance Pseudocapacitors, Angew. *Chemie Int. Ed.* 52 (2013) 1882–1889. doi:10.1002/anie.201203201.

[119] C.-C. Hu, K.-H. Chang, M.-C. Lin, Y.-T. Wu, Design and Tailoring of the Nanotubular Arrayed Architecture of Hydrous RuO_2 for Next Generation Supercapacitors, *Nano Lett.* 6 (2006) 2690–2695. doi:10.1021/nl061576a.

[120] L. Mao, K. Zhang, H. S. On Chan, J. Wu, Nanostructured MnO_2/graphene composites for supercapacitor electrodes: The effect of morphology, crystallinity and composition, *J. Mater. Chem.* 22 (2012) 1845–1851. doi:10.1039/C1JM14503G.

[121] S.-I. Kim, J.-S. Lee, H.-J. Ahn, H.-K. Song, J.-H. Jang, Facile Route to an Efficient NiO Supercapacitor with a Three-Dimensional Nanonetwork Morphology, *ACS Appl. Mater. Interfaces.* 5 (2013) 1596–1603. doi:10.1021/am3021894.

[122] X. Sun, G. Wang, H. Sun, F. Lu, M. Yu, J. Lian, Morphology controlled high performance supercapacitor behaviour of the Ni–Co binary hydroxide system, *J. Power Sources.* 238 (2013) 150–156. doi:10.1016/j.jpowsour.2013.03.069.

[123] W. Wei, X. Cui, X. Mao, W. Chen, D. G. Ivey, Morphology evolution in anodically

electrodeposited manganese oxide nanostructures for electrochemical supercapacitor applications—Effect of supersaturation ratio, *Electrochim. Acta*. 56 (2011) 1619–1628. doi:10.1016/j.electacta.2010.10.044.

[124] Y. Zhang, Q. Zou, H. S. Hsu, S. Raina, Y. Xu, J. B. Kang, J. Chen, S. Deng, N. Xu, W. P. Kang, Morphology Effect of Vertical Graphene on the High Performance of Supercapacitor Electrode, *ACS Appl. Mater. Interfaces*. 8 (2016) 7363–7369. doi:10.1021/acsami.5b12652.

[125] M. Mellincovsky, A. Kuperman, C. Lerman, I. Aharon, N. Reichbach, G. Geula, R. Nakash, Performance assessment of a power loaded supercapacitor based on manufacturer data, Energy Convers. *Manag.* 76 (2013) 137–144. doi:10.1016/j.enconman.2013.07.042.

[126] L. Yu, G. Z. Chen, Supercapatteries as High-Performance Electrochemical Energy Storage Devices, *Electrochem. Energy Rev*. 3 (2020) 271–285. doi:10.1007/s41918-020-00063-6.

[127] S. Balasubramaniam, A. Mohanty, S. K. Balasingam, S. J. Kim, A. Ramadoss, Comprehensive Insight into the Mechanism, Material Selection and Performance Evaluation of Supercapatteries, *Nano-Micro Lett*. 12 (2020) 85. doi:10.1007/s40820-020-0413-7.

[128] Z. Wang, X. Chu, Z. Xu, H. Su, C. Yan, F. Liu, B. Gu, H. Huang, D. Xiong, H. Zhang, W. Deng, H. Zhang, W. Yang, Extremely low self-discharge solid-state supercapacitors via the confinement effect of ion transfer, *J. Mater. Chem. A*. 7 (2019) 8633–8640. doi:10.1039/C9TA01028A.

[129] J. Kowal, E. Avaroglu, F. Chamekh, A. Šenfelds, T. Thien, D. Wijaya, D.U. Sauer, Detailed analysis of the self-discharge of supercapacitors, *J. Power Sources*. 196 (2011) 573–579. doi:10.1016/j.jpowsour.2009.12.028.

[130] K. Liu, C. Yu, W. Guo, L. Ni, J. Yu, Y. Xie, Z. Wang, Y. Ren, J. Qiu, Recent research advances of self-discharge in supercapacitors: Mechanisms and suppressing strategies, *J. Energy Chem*. 58 (2021) 94–109. doi:10.1016/j.jechem.2020.09.041.

[131] H. Dura, J. Perry, T. Lecacou, F. Markoulidis, C. Lei, S. Khalil, M. Decker, M. Weil, Cost analysis of supercapacitor cell production, *Int. Conf. Clean Electr. Powe*r, IEEE, (2013) 516–523. doi:10.1109/ICCEP.2013.6586902.

[132] S. Goswami, G. R. Dillip, S. Nandy, A. N. Banerjee, A. Pimentel, S. W. Joo, R. Martins, E. Fortunato, Biowaste-derived carbon black applied to polyaniline-based high-performance supercapacitor microelectrodes: Sustainable materials for renewable energy applications, *Electrochim. Acta*. 316 (2019) 202–218. doi:10.1016/j.electacta.2019.05.133.

[133] B. Ameri, S. S. H. Davarani, R. Roshani, H. R. Moazami, A. Tadjarodi, A flexible mechanochemical route for the synthesis of copper oxide nanorods/nanoparticles/nanowires for supercapacitor applications: The effect of morphology on the charge storage ability, *Journal of*

Alloys and Compounds, 695 (2017) 114. doi: 10.1016/j.jallcom.2016.10.144

[134] Y. Ma, C. Hou, H. Zhang, M. Qiao, Y. Chen, H. Zhang, Q. Zhang, Z. Guo, Morphology-dependent electrochemical supercapacitors in multi-dimensional polyaniline nanostructures, *J. Mater. Chem. A,* 5 (2017) 14041-14052. doi: 10.1039/C7TA03279J

[135] J. Zheng, Y. Zhang, T. Hu, T. Lv, and C. Meng, New strategy for the morphology-controlled synthesis of V_2O_5 microcrystals with enhanced capacitance as battery-type supercapacitor electrodes, *Cryst. Growth Des.* 9 (2018) 5365–5376. doi: 10.1021/acs.cgd.8b00776

Originality Report for Chapter 2

(*Generated using Ithenticate Software excluding the first author publications of Mr. Samik Saha)

Chapter 2

ORIGINALITY REPORT

9%
SIMILARITY INDEX

PRIMARY SOURCES

1	dokumen.pub Internet	147 words — 1%
2	www.science.gov Internet	105 words — 1%
3	pubs.rsc.org Internet	84 words — 1%
4	onlinelibrary.wiley.com Internet	56 words — < 1%
5	Yu Zhang, Qionghui Zou, Hua Shao Hsu, Supil Raina, Yuxi Xu, Joyce B. Kang, Jun Chen, Shaozhi Deng, Ningsheng Xu, Weng P. Kang. "Morphology Effect of Vertical Graphene on the High Performance of Supercapacitor Electrode", ACS Applied Materials & Interfaces, 2016 Crossref	55 words — < 1%
6	Samik Saha, Atanu Roy, Apurba Ray, Trisha Das, Mahasweta Nandi, Basudev Ghosh, Sachindranath Das. "Effect of particle morphology on the electrochemical performance of hydrothermally synthesized NiMn2O4", Electrochimica Acta, 2020 Crossref	44 words — < 1%
7	iopscience.iop.org Internet	42 words — < 1%

Chapter 3

Different characterization

facilities used

3. Different characterization techniques

The thesis work comprises the analysis and discussions of the results obtained from different characterization facilities. These characterization techniques mainly include the structural, compositional, and morphological studies of the different electrode materials under consideration. Once the desired material is synthesized, and the formation of the same is confirmed by the structural, compositional, and morphological analyses, electrochemical characterization techniques are used to access its charge storage performance. This chapter deals with all the different tools and techniques used to investigate a particular electrode material.

3.1 X-ray Diffraction (XRD)

Figure 3.1.1 Rigaku Miniflex-600 diffractometer

X-ray diffraction is an analytical technique that is used to identify the crystalline structure and the composition of the materials [1-3]. A crystalline solid has a periodic structure with a repeated arrangement of atoms. A beam of monochromatic X-ray, when incident on such periodic crystalline material, diffraction of rays occurs. These monochromatic X-rays are produced using a cathode ray tube having a wavelength comparable to the lattice constant of the material. Keeping the direction of the incident X-ray beam fixed, the sample and detector are rotated using an arrangement known as a goniometer. The detector records the intensity of the reflected X-rays as a function of the angle between the directions of the incident beam and diffracted beam. At some certain angles, when the geometry of the goniometer satisfies Bragg's equation consistent with the sample's lattice spacing, a peak in the intensity is observed. By studying such peaks, different properties regarding the sample can be

obtained. We have used the Rigaku Miniflex-600 diffractometer in this thesis work, as shown in figure 3.1.1. The diffractometer has a CuK_α source which generates a monochromatic ray having $\lambda = 1.542$ Å and a D/teX Ultra 1D silicon detector.

3.2 Fourier transform infrared Spectroscopy (FTIR)

Fourier transform infrared spectroscopy (FTIR spectroscopy) is the preferred method of spectroscopy in the infrared (IR) regime of electromagnetic waves [4, 5]. When infrared radiation is incident on a sample, a part of the intensity is absorbed by

Figure 3.2.1 Perkin-Elmer RX1 spectrometer

the sample, and the other part gets transmitted. An infrared spectrum contains absorptions peaks at different wavelengths (hence at different photon energies of the radiation) for a sample. The position of these absorption peaks represents the vibrational frequencies for the vibrations between the bonds of the molecules and atoms constituting the material. As every different material is composed of different atoms and molecules, each different material produces a different IR spectrum. An IR spectrum is like a fingerprint for a particular sample, and no two samples can have the exact same infrared pattern. Thus different organic and inorganic compounds can be positively identified using this technique. Apart from this, the amount of material present in a sample can be estimated from the size of the peaks in the spectrum.

Older IR instruments utilized different dispersive elements like (IR prisms, gratings etc.) to separate the individual wavelengths from the IR source. A detector measured the transmittance or absorbance of a sample at an individual wavelength. However, this method was very slow, and FTIR resolves this problem by incorporating an optical interferometer [6]. An interferometer produces an IR signal

containing all the different wavelengths encoded in it. Thus the transmittance or absorbance can be measured very quickly. The absorption data at individual wavelengths can be decoded by performing a Fourier transform of the signal, which is accomplished by a digital computer present in the instrument itself. Figure 3.2.1 shows the Perkin-Elmer RX1 spectrometer, which we have used in this thesis work. This spectrometer offers a working range of 250-4000 cm^{-1} and has a deuterated triglycine sulfate (DTGS) detector.

3.3 X-Ray photoelectron spectroscopy (XPS)
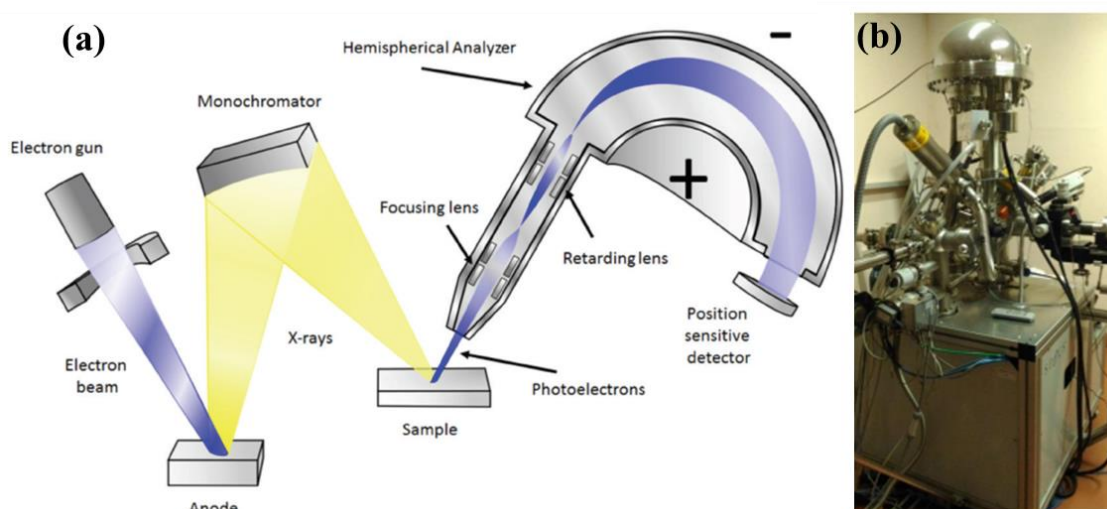
Figure 3.3.1 (a) Schematic of the XPS set-up (b) Photo of the actual XPS instrument

X-ray photoelectron spectroscopy (XPS) is a vital spectroscopic measurement for the study of the chemical composition of the surface of a sample [7, 8]. Thus, this spectroscopy is also recognized as Electron Spectroscopy for Chemical Analysis (ESCA). XPS is a fast and sensitive analysis technique with applications spanning a broad range of organic and inorganic materials. It can detect the spectrum of elements from lithium to uranium. When low-energy X-ray photons bombard a sample, electrons escape from the material surface, resembling the photoelectric effect. XPS is based on the measurement of the kinetic energies of these emitted electrons. The electrons' kinetic energy data ($E_{kinetic}$) provide information about the binding energy ($E_{binding}$) of the atomic orbital from which the electron has escaped. This can simply be calculated from the equation (3.1)

$$E_{binding} = E_{photon} - E_{kinetic} - \phi \qquad (3.1)$$

where E_{photon} is the energy of the incident X-ray photon, which is known with high accuracy and ϕ is a constant for the spectrometer. Each element has a unique set of binding energy. Thus, the concentration of elements at the surface can be identified by measuring the different sets of binding energies of a sample. The binding energy of elements can vary because of differences in the chemical potential, formation of chemical bonds, polarizability of compounds, etc. These variations lead to the identification of the chemical state of the sample [9].

Figure 3.3.1 (a) shows the schematic for a typical XPS setup. An electron gun generates electrons which, upon impinging on an anode, generates an X-ray. A monochromator is used to create a mono-energetic X-ray. This mono-energetic X-ray interacts with the sample, which excites the near-surface electrons, and photoelectron emission takes place. The detector records these emitted electrons, and the intensity in any particular energy is proportional to the number of emissions. XPS requires an ultra-high vacuum (less than 10^{-9} mbar) which assists the photoelectrons in reaching the analyzer. We have performed the XPS measurement using SPECS GmbH spectrometer (Phoibos 100MCD Analyzer) with Al K_α radiation having photon energy of 1.4866 keV. Figure 3.3.1 (b) displays the photo of the actual instrument.

3.4 Scanning electron microscopy (SEM)

Scanning electron microscopy (SEM) is used to examine the morphology of the sample surface [10-12]. When the sample surface is hit by a collimated electron beam, secondary electrons are released from the sample surface. The topography of the sample surface can be reconstructed digitally by two-dimensional scanning of the collimated beam on the sample surface and collecting the secondary electrons. Figure 3.4.1 (a) shows the schematic of an SEM. The instrument contains many different parts. Electron gun produces electron beam via thermionic emission. The thermally excited electrons are emitted from the cathode, usually made of thin tungsten wire. This wire is heated to a very high temperature (2800 K) which results in the ejection of electrons. A positive potential is applied to a specially made anode to produce an electron beam. In some other instruments, LaB_6 crystal is used instead of tungsten cathode as an electron emitter. In a more advanced set-up field emission electron gun is used to produce electron beam current. These types of SEMs are known as Field Emission Scanning Electron Microscope (FESEM) [13]. Apart from the electron gun,
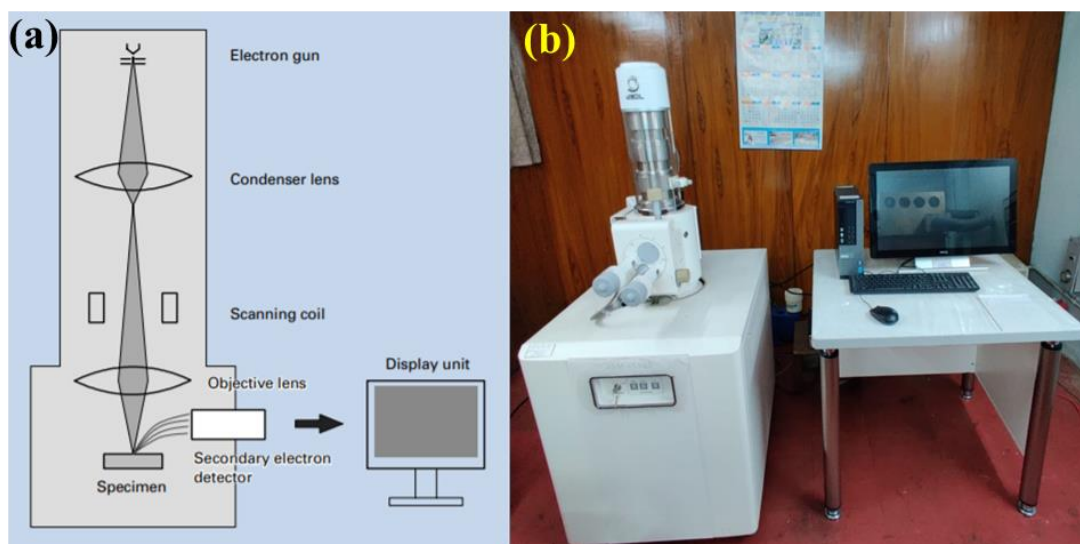
Figure 3.4.1 (a) Schematic of SEM (b) Photo of the actual SEM instrument

different combinations of magnetic lenses are used, which tune the electron beam size, and ultimately, the magnification of the image can be controlled. The secondary electron detector contains a scintillator, a photomultiplier tube, and a high voltage setup to attract the secondary electrons. This type of detector is known as Everhart-Thornley detector (ET-detector). The output from the detector is fed to the digital computer, which produces the magnified image of the sample. As the whole working of the microscope revolves around the controlled use of the electron beam current, a high vacuum environment (10^{-3}-10^{-4} Pa) is necessary for proper working.

The resolving power of any microscope is the minimum separation that can be seen by it and is inversely proportional to the wavelength of the probe used. Thus smaller the wavelength, the greater the resolving power. For an optical microscope, the resolution is about 0.2 μm or 200 nm. In SEM, as the probe used is the stream of electrons, hence its wavelength can be very small compared to the visible light, and thus for most SEM, the resolution can be as small as 10 nm. High magnification of 2,000,000 times can be obtained in a typical SEM instrument.

Sample preparation for SEM is also relatively easy. But it has to be ensured that the surface of the sample to be seen is electronically conductive. Otherwise, the charging of the sample takes place, which distorts the image. To image a non-conductive or relatively less conductive material, it has to be coated with a very thin layer of gold. Figure 3.4.1 (b) shows the actual image of an SEM instrument (JSM-IT100, JEOL).

3.5 Transmission electron microscopy (TEM)
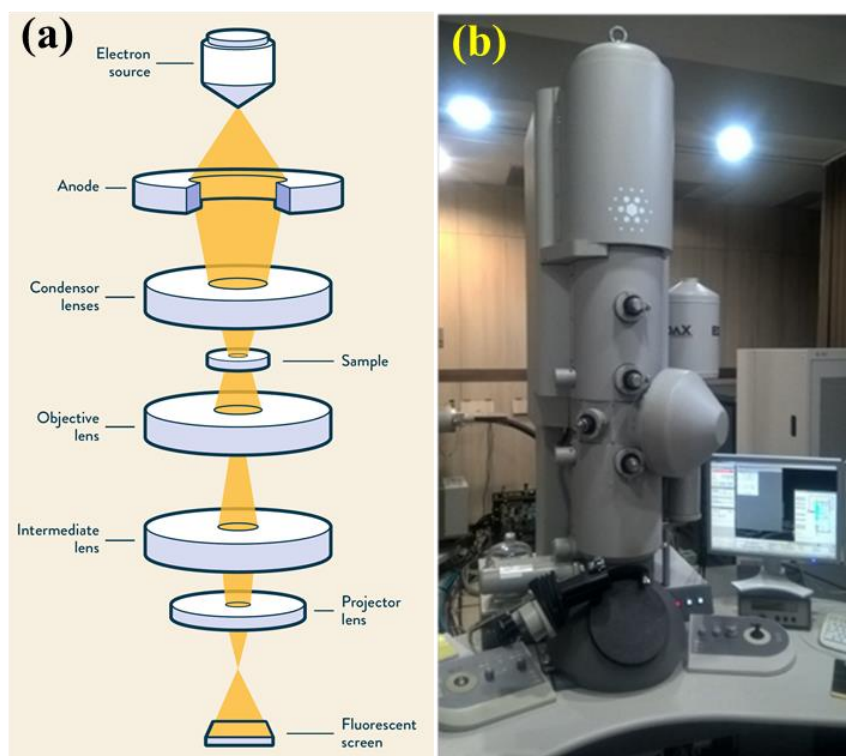
Figure 3.5.1 (a) Schematic of the TEM (b) Photo of the actual TEM instrument

Transmission electron microscopy (TEM) works on the same principle as the transmission light microscope. However, instead of light, a stream of electrons is used in this case. TEM is widely used to study morphology and internal structure of a sample with ultra-high resolution. Figure 3.5.1 (a) shows the schematic of a TEM setup. Like SEM, TEM also requires an electron gun to produce a beam of electrons. Different combinations of magnetic lenses are used to focus and collimate the electron beam. A high potential difference (100 keV – 400 keV) is applied between the cathode and anode to accelerate the electron to very high energy. These high-energy electrons have very small wavelength, and hence very high resolving power can be obtained in TEM. Sample preparation for TEM analysis is relatively complex compared to SEM sample preparation. To allow the passage of electron beam through the sample, it must be less than 150 nm thick. After transmission of electron through the sample, the electron reaches the projector lens, which projects the magnified image of the sample on a phosphorescent screen. A CCD camera digitizes the acquired image for further analysis. Like SEM, a high vacuum environment is also required in TEM. Figure 3.5.1 (b) shows the actual image of the transmission electron microscope (FEI, TF30-ST), which we have used during this thesis work.

3.6 BET

Nitrogen sorption isotherm measurement coupled with BET theory is a powerful technique to estimate the specific surface area and porosity of porous materials [14]. Brunauer–Emmett–Teller theory or the BET theory is n modification over the Langmuir theory [15]. The latter is valid for monolayer adsorption of gas molecules on a surface. On the other hand, the BET theory is applicable to multilayer adsorption
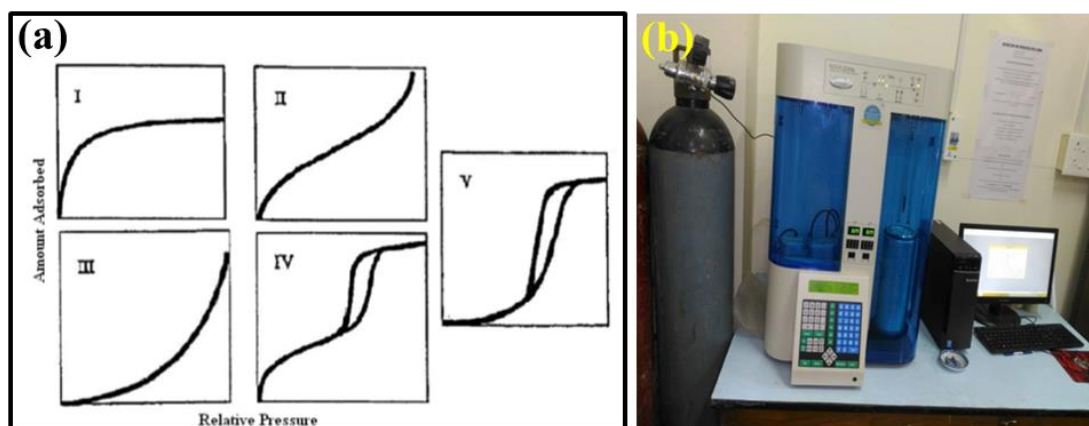
Figure 3.6.1 (a) Different types of isotherms (b) Photo of BET set-up

of gas molecules. Among the different gases, N_2 at temperature 77 K is extensively used as a probe to measure the specific surface area of a material. Isotherms for a particular material are measured during N_2 adsorption and de-adsorption. The isotherms can be classified into five different categories, as shown in figure 3.6.1 (a). Type-I isotherms are seen for microporous materials. A microporous material has pores, sizes of which are less than 2 nm. For such materials, the pore sizes are not much larger than the diameter of the adsorbate. Unlike the type-I isotherm, the type-II isotherm does not show a saturation limit. This means that adsorbate forms multilayer after forming a monolayer of gas. Type-III isotherm indicates vapor adsorption. Type IV and V display a hysteresis loop. This suggests the presence of capillary condensation of adsorbate on the mesoporous materials. Thus the nature of isotherm can reveal the pore distribution in a material. Using isotherms, the specific surface area can be calculated with the help of the Brunauer -Emmet-Teller (BET) theory.

We have measured the nitrogen sorption isotherm of different samples using Quantachrome NOVA 2200e BET Surface Area Analyzer at 77 K (figure 3.6.1 (b)). Before performing the measurements, the samples were degassed for 8–12 h at a relatively high temperature of 423 K. Multipoint BET method was used to estimate

the surface areas of the samples. The pore size distributions were calculated using Non-local density functional theory (NLDFT).

3.7 Electrochemical characterizations

To evaluate an electrode material for its electrochemical charge storage performance, different electrochemical characterizations are. Cyclic Voltammetry (CV), Galvanostatic Charge Discharge (GCD), and Electrochemical Impedance Spectroscopy (EIS) are principal among them. A detailed discussion regarding these
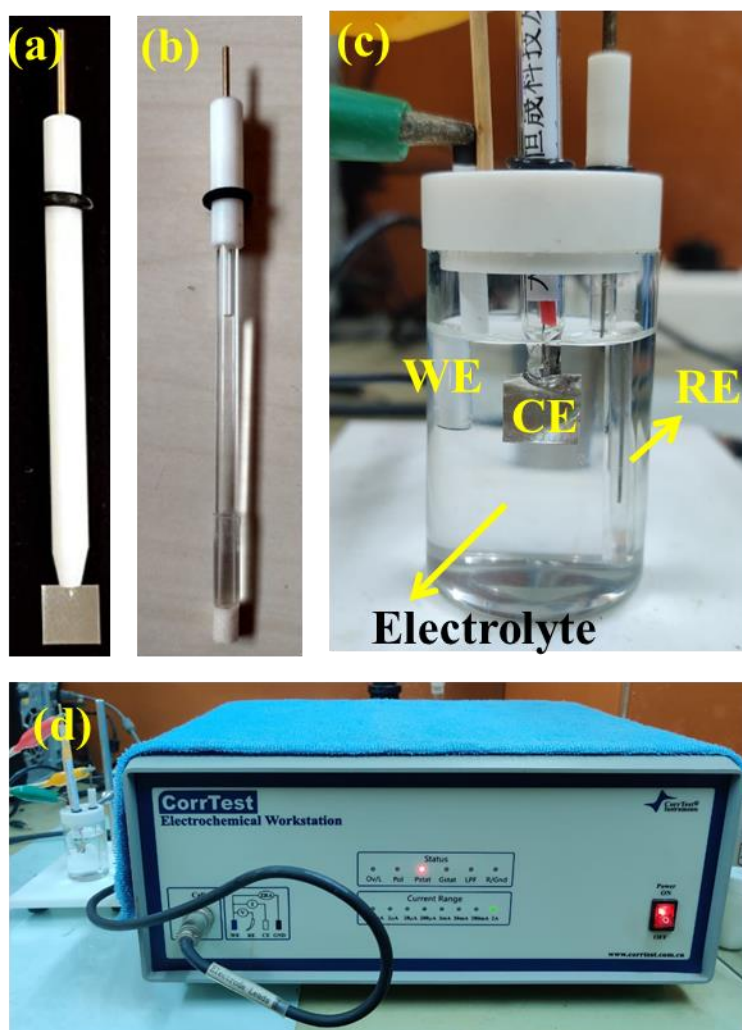
Figure 3.7.1 Photo of the (a) CE (b) RE (c) electrochemical cell and (d) Corrtest CSC-313 electrochemical work station

measurements has already been included in chapter 2. Here we discuss the different technical and practical aspects behind these characterization techniques. These three characterizations can be performed both in 3-electrode and 2-electrode modes. 3-electrode mode is used to evaluate the performance of electrochemical charge storage

capability of particular electrode material. On the other hand, the 2-electrode mode is used to characterize the performance of a two-electrode supercapacitor device. Both 3-electrode and 2-electrode characterizations can be performed using an electrochemical workstation equipped with hardware to precisely control and measure potential and current. In addition to that, to perform EIS, the workstation must be equipped with hardware to control the frequency of an AC signal over a wide range (0.01 Hz to 10^5 Hz).

In 3-electrode mode, as the name suggests, there are three electrodes. The Working Electrode (WE) is the electrode where the potential is applied with respect to the reference electrode (RE), and the current is measured with respect to the counter electrode (CE). The WE is made of inert material such as gold, platinum, or glassy carbon, which does not participate in the electrochemical reaction. The material whose electrochemical performance has to be tested (active material) is coated on the surface of WE. In these cases, the coated surface of the WE serves as an active area where the electrochemical reaction takes place. In most of our experiments, we have taken glassy carbon rods as our WE. Before coating the active material, the circular flat end of the rod is polished using fine emery paper and washed several times. Then the rods are dried in a vacuum. The dried rods are then wrapped with Teflon tape, keeping the circular flat end open. Teflon tape acts as an encapsulation for the sidewall of the rod. Next, the active material is dropcasted on the circular flat end. For this purpose, a slurry of the active material is prepared using 85 wt% active material, 10 wt% carbon black, and 5 wt% polyvinylidene fluoride (PVDF), all mixed in N-Methyl-2-pyrrolidone (NMP) solvent. This slurry is used for dropcasting. Here the carbon black is used as a conductive additive, and PVDF is used as a binder [16]. Following the dropcasting, the rods are kept in a vacuum at 65^0 C for 3 h to dry the coated slurry. This results in the formation of a thin coating of the active material on the flat end of the rod. The rods were weighed before and after deposition. The difference in mass gives the mass of the deposited material. While measuring the electrochemical performance of hydrothermally synthesized $NiMn_2O_4$, we have used Ni-foam as a working electrode. The active material was coated on the Ni-foam during the hydrothermal reaction; thus, the use of a binder was avoided. The counter electrode (CE) is an inert conductor usually made of platinum. The current flows between CE and WE. In our study, we have used a platinum counter electrode of

dimension 1 cm x 1 cm, which is shown in figure 3.7.1 (a). The reference electrode (RE) is the third and final electrode that is used to measure the potential of the WE. RE should be able to maintain a constant potential during the electrochemical reaction and must be chemically stable. There are various REs like Saturated Calomel Electrode (SCE), Standard Hydrogen Electrode (SHE), etc. We have used Ag/AgCl electrodes in saturated KCl as our RE for all the electrochemical measurements (figure 3.7.1 (b)). It maintains a constant potential of 0.197 V with respect to SHE. The high stability in the potential value is reached by a redox reaction in the RE, as given in equation (3.2)

$$AgCl(s) + e^- \leftrightarrow Ag(s) + Cl^- \tag{3.2}$$

All these three electrodes are connected to the respective terminals of the electrochemical workstation and then kept submerged under an electrolyte solution to conduct the experiments, as shown in figure 3.7.1 (c) [17]. We have used Corrtest CS-313 electrochemical workstation for the purpose of all the electrochemical measurements. The photo of the workstation is shown in figure 3.7.1 (d). While performing the 2-electrode measurement, the WE is connected to the positive terminal of the device, and CE and RE are connected together to the negative terminal of the device.

After obtaining the data, the specific capacitance of the device can be calculated both from the CV and GCD experiments using equations (2.3.1) and (2.3.3). Information concerning the different dynamic processes which occur at the electrode-electrolyte interface during the charging-discharging can be obtained from the EIS experiment, which has already been discussed in chapter 2.

3.8 References

[1] L. D. Whittig, & W. R. Allardice, X-ray diffraction techniques. Methods of Soil Analysis: Part 1 *Physical and Mineralogical Methods*, 5 (1986) 331-362. doi: 10.2136/sssabookser5.1.2ed.c12

[2] B. E. Warren, X-ray diffraction methods. *Journal of applied physics*, 12 (1941) 375-384. doi: 10.1063/1.1712915

[3] H. Stanjek, & W. J. H. I. Häusler, Basics of X-ray Diffraction. *Hyperfine interactions*, 154 (2004) 107-119.

[4] C. Berthomieu, & R. Hienerwadel, Fourier transform infrared (FTIR) spectroscopy. *Photosynthesis research*, 101 (2009)157-170. doi: 10.1007/s11120-009-9439-x

[5] C. M. Parler, J. A. Ritter, & M. D. Amiridis Infrared spectroscopic study of sol–gel derived mixed-metal oxides. *Journal of non-crystalline solids,* 279 (2001) 119-125. doi: 10.1016/S0022-3093(00)00401-4

[6] W. D. Perkins, Fourier transform infrared spectroscopy. Part II. Advantages of FT-IR. *Journal of Chemical Education*, 64 (1987) A269. doi: 10.1021/ed064pA269

[7] C. S. Fadley, X-ray photoelectron spectroscopy: Progress and perspectives. *Journal of Electron Spectroscopy and Related Phenomena*, 178 (2010) 2-32. doi: 10.1016/j.elspec.2010.01.006

[8] F. A. Stevie, & C. L. Donley, Introduction to x-ray photoelectron spectroscopy. *Journal of Vacuum Science & Technology A: Vacuum, Surfaces, and Films*, 38 (2020) 063204. doi: 10.1116/6.0000412

[9] E. S. Ilton, J. E. Post, P. J. Heaney, F. T. Ling, & S. N. Kerisit, XPS determination of Mn oxidation states in Mn (hydr) oxides. *Applied Surface Science*, 366 (2016) 475-485. 10.1016/j.apsusc.2015.12.159

[10] K. C. A. Smith, & C. W. Oatley, The scanning electron microscope and its fields of application. *British Journal of Applied Physics*, 6 (1955) 391.

[11] H. Seiler, Secondary electron emission in the scanning electron microscope. *Journal of Applied Physics*, 54 (1983) R1-R18. doi: 10.1063/1.332840

[12] M. Dunlap, & J. E. Adaskaveg, Introduction to the scanning electron microscope. Theory, practice, & procedures. *Facility for Advance Instrumentation. UC Davis*, 52 (1997).

[13] S. L. Erlandsen, C. Frethem, & Y. Chen, Field emission scanning electron microscopy (FESEM) entering the 21st century: nanometer resolution and molecular topography of cell structure. *Journal of Histotechnology*, 23 (2000) 249-259. doi: 10.1179/his.2000.23.3.249

[14] N. Hwang, & A. R. Barron, BET surface area analysis of nanoparticles. *The Connexions project*, (2011) 1-11.

[15] R. Bardestani, G. S. Patience, & S. Kaliaguine, Experimental methods in chemical engineering: specific surface area and pore size distribution measurements—BET, BJH, and DFT. *The Canadian Journal of Chemical Engineering*, 97 (2019) 2781-2791. doi.org/10.1002/cjce.23632

[16] M. Arunkumar and A. Paul, Importance of Electrode Preparation Methodologies in Supercapacitor Applications, *ACS Omega,* 2 (2017) 8039-8050 doi: 10.1021/acsomega.7b01275

[17] N. Elgrishi, K. J. Rountree, B. D. McCarthy, E. S. Rountree, T. T. Eisenhart, and J. L. Dempsey, A Practical Beginner's Guide to Cyclic Voltammetry, *J. Chem. Educ.* 95 (2018) 197–206. doi: 10.1021/acs.jchemed.7b00361

Originality Report for Chapter 3

(*Generated using Ithenticate Software excluding the first author publications of Mr. Samik Saha)

Chapter 3

ORIGINALITY REPORT

10%
SIMILARITY INDEX

PRIMARY SOURCES

1	studentsrepo.um.edu.my Internet	28 words — 1%
2	Jie Xiao, Praveen Meduri, Honghao Chen, Zhiguo Wang et al. "Energetics of Defects on Graphene through Fluorination", ChemSusChem, 2014 Crossref	22 words — 1%
3	orca.cardiff.ac.uk Internet	22 words — 1%
4	jast-journal.springeropen.com Internet	19 words — 1%
5	Atanu Roy, Apurba Ray, Samik Saha, Monalisa Ghosh, Trisha Das, Biswarup Satpati, Mahasweta Nandi, Sachindranath Das. "NiO-CNT composite for high performance supercapacitor electrode and oxygen evolution reaction", Electrochimica Acta, 2018 Crossref	18 words — 1%
6	sutir.sut.ac.th:8080 Internet	17 words — 1%
7	Yifeng Zhang, Yixin Liu, Rongxia Li, Malik Saddam Khan, Picheng Gao, Yong Zhang, Qin Wei. "Visible-light driven Photoelectrochemical Immunosensor Based on	16 words — 1%

87

Chapter 4

Experimental Section

4. Introduction

This chapter discusses the different techniques used to synthesize the different morphologically ordered or disordered samples. In the beginning, we will discuss the synthesis technique for ordered and disordered sample of MnO_2-Graphene Oxide (MnO_2-GO). The ordered sample was prepared using the electrospin technique [1], which offered superior electrochemical charge storage capability compared to the disordered counterpart. Technical aspects of the electrospinning technique have been discussed in the chapter-2.

However, the electrospin technique is a slow yield process; hence to speed up the fiber production, we have indigenously developed a Rotary-Jet Spin device (RJ-Spin) which could be used to produce different types of fibers [2]. We have used this device to produce MnO_2 based fiber and measured its electrochemical charge storage capability.

Bimetal oxides offer good electrochemical charge storage performance compared to mono-metal oxides [3]. Hence, we have chosen a popular bimetallic oxide, namely $NiMn_2O_4$, to study its charge storage capability and effect of particle morphology on electrochemical performance. Ni-based oxides are popular battery-type materials and possess high energy density [4]. On the other hand, electrodes based on Mn-based oxides show a pseudocapacitive charge storage mechanism offering high power density [5]. Hence in $NiMn_2O_4$, the advantage of high energy density and power density can be obtained. Here, we have described the scheme to synthesize $NiMn_2O_4$ using the hydrothermal technique. To study the effect of morphology on the electrochemical performance, different morphological variants of $NiMn_2O_4$ were prepared using different additives during the synthesis.

Finally, we have again utilized the RJ-Spin device to fabricate the morphologically ordered $NiMn_2O_4$ fiber in an attempt to reduce the internal resistance further and to increase the electrochemical charge storage performance.

All the physical, morphological, and electrochemical characterizations of these samples have been discussed in the next chapter (chapter 5), maintaining the same order.

4.1 Synthesis of ordered and disordered sample of MnO$_2$-GO
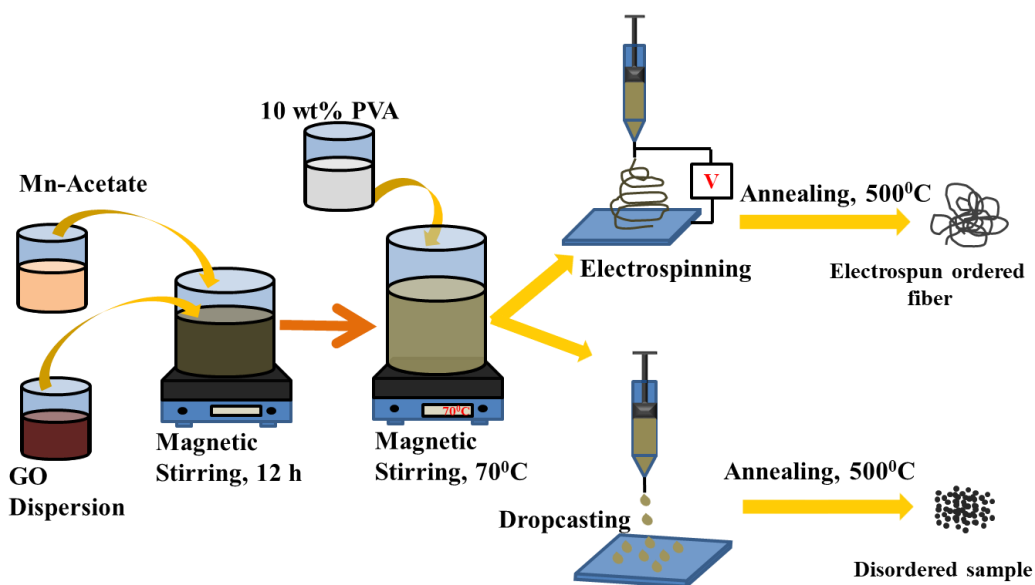
Figure 4.1.1: Scheme to synthesize ordered and disordered samples of MnO$_2$-GO

Manganese (II) acetate tetra hydrate ((CH$_3$COO)$_2$Mn.4H$_2$O) and Polyvinylalcohol (PVA) were obtained from LOBA Chemie. All the chemicals were of analytical grade and were used without any further purification. Graphene Oxide (GO) was prepared from natural graphite powder by using the modified Hummer's method [6]. 27 ml of sulphuric acid (H$_2$SO$_4$) and 3 ml of phosphoric acid (H$_3$PO$_4$) were mixed in a volumetric ratio of 1:9. 0.23 g of graphite powder was added into the acidic mixture under vigorous stirring. Next, 1.3 g of potassium permanganate (KMnO$_4$) was slowly added to the mixture. This mixture was kept under moderate stirring overnight until the color changed to dark green. After that, 0.7 ml hydrogen peroxide (H$_2$O$_2$) was added drop-wise to remove excess KMnO$_4$ from the mixture. Next, an aqueous solution of hydrochloric acid (10 ml acid in 30 ml de-ionized water) was added to the mixture and centrifuged at 5000 rpm for 5 minutes. The residuals were collected and washed using de-ionized water several times. Finally, the GO solution was dried in an oven at 90 ^{o}C for 24 hours to obtain the GO powder. The electrospinning solution of MnO$_2$-GO composite was synthesized by an easy three-step process. At first, 20 mg of GO was dispersed in 5 mL ethanol-water solution (3:7 by volume) using a probe-sonicator for 1 h. In another beaker, 0.1 g of (CH$_3$COO)$_2$ Mn. 4H$_2$O was added to 5 mL distilled water and was kept under continuous stirring for 1 hour. These two solutions were then mixed under continuous magnetic stirring

for 12 h. Finally, 10 wt% PVA was added to the earlier solution and kept under magnetic stirring at temperature 70 °C until a homogeneous viscous mixture was obtained. This polymer solution was divided into two parts. One part was used to perform the electrospinning process, and the other part was used to synthesize dropcasted disordered samples.
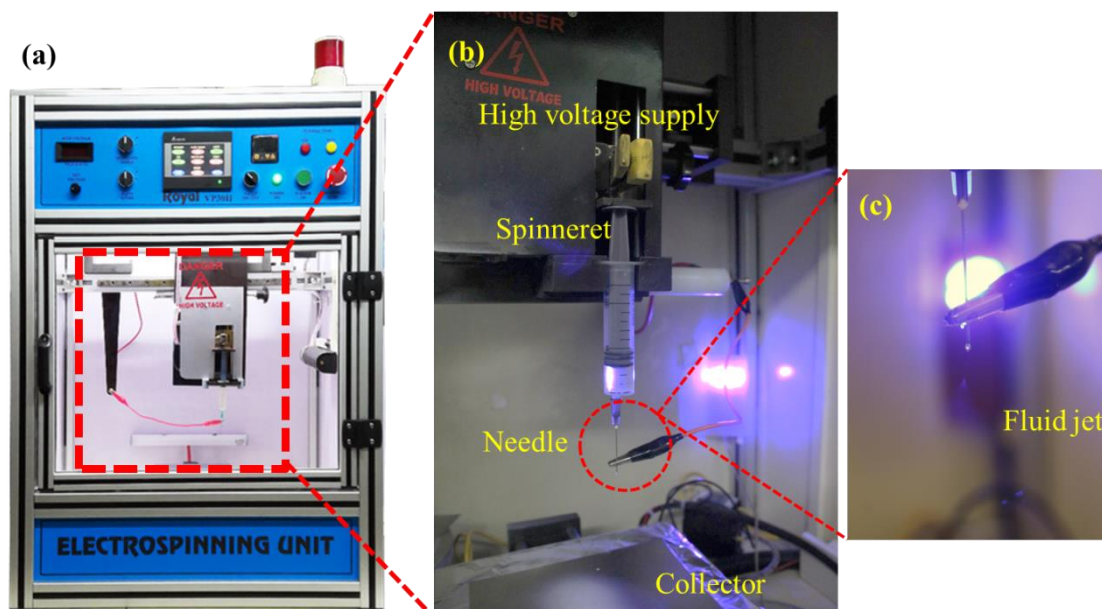
Figure 4.1.2: (a) Image of the Royal Vertical Electrospin set-up. (b) Different parts of the electrospin machine. (c) Image of fluid jet coming out of the end of the needle.

Electrospinning is an easy technique to produce uniform and continuous fiber from a polymer solution. An electrospinning device consists of three principal parts such as a spinneret, a high voltage power supply, and a collector (figure 4.1.2 (b)). The spinneret contains a syringe with a steel needle. A syringe pump drives the polymer solution through the open end of the steel needle at a constant rate. The high voltage source produces an electric field between the steel needle and the collector. When the electric field reaches a certain value, electrostatic force on the small drop formed at the end of the steel needle overcomes the surface tension of the liquid and a jet of the solution is ejected at a very high speed (figure 4.1.2 (c)) towards the direction of the collector which leads to quick drying of the solvent and thus fibers are produced. There are various parameters that determine the diameter of the fabricated fiber, like dielectric properties of the solution, surface charge density on the droplet, surface tension and viscosity of the solution, temperature, etc. By optimizing these parameters, the fiber diameter can be varied within a wide range of 50 nm to 1000

nm. For our present work, we have used vertical electrospin set-up made by Royal Enterprise, Chennai, Tamil Nadu. Figure 4.1.2 (a) shows the actual image of the set-up.

In the electrospinning process, the polymer solution was loaded in the 1 mL plastic syringe with a gauge needle attached to the end. A high DC voltage of 15 kV was applied between the needle and the collector steel plate, which was grounded and placed at a distance of 10 cm from the tip of the needle. A flow rate of 0.5 mL h^{-1} was maintained by a syringe pump. The whole electrospinning process was performed in air with a chamber temperature of 35 ^{o}C. The collector steel plate was placed on a plate heater at 60 ^{o}C. Relatively high plate temperature ensured the quick drying of the spun fiber, and thus agglomeration of the spun fiber was avoided. After the electrospinning process, the fiber mat was collected and dried in air at 150 ^{o}C and then exposed to H_2O_2. After that, the fibers were kept in a closed enclosure containing iodine vapor for 6 h for increased stabilization during the annealing process. Finally, the resulting fiber was annealed in a vacuum furnace at temperature 500 ^{o}C for 1 h resulting in the formation of MnO_2-GO composite. By this annealing process, PVA polymer was converted to carbonized fiber according to equation (4.1.1) [7]. This
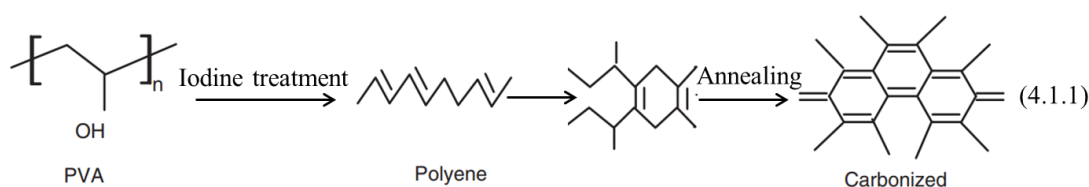
sample was designated as GM-1E, where the ratio of Mn^{2+} and GO is 5:1 by weight. Here 'E' signifies the electrospun sample. Similarly, the pristine MnO_2 fiber (designated as GM-0E) was fabricated with two other variations of MnO_2-GO composite having 5:2 (designated as GM-2E) and 5:3 (designated as GM-3E) ratios of Mn^{2+} and GO by weight. Another part of the electrospinning solution was spread dropwise on a steel plate and dried at 60 ^{o}C to form beads. Then these dropcasted beads were collected, dried, and annealed under the same conditions. Thus the disordered dropcasted samples were prepared and designated as GM-0D, GM-1D, GM-2D, and GM-3D (here D signifies dropcasted sample). The details of the samples, along with their respective synthesis technique, have been provided in the table-4.1.1. The schematic of the synthesis technique is depicted in Figure 4.1.1.

Table-4.1.1 Details of the different samples of MnO₂-GO.

Mn²⁺:GO	Electrospun Ordered Sample	Dropcasted Disordered Sample
5:0	GM-0E	GM-0D
5:1	GM-1E	GM-1D
5:2	GM-2E	GM-2D
5:3	GM-3E	GM-3D

4.2 Synthesis of ordered microfiber of MnO₂/Carbon by RJ-Spin method
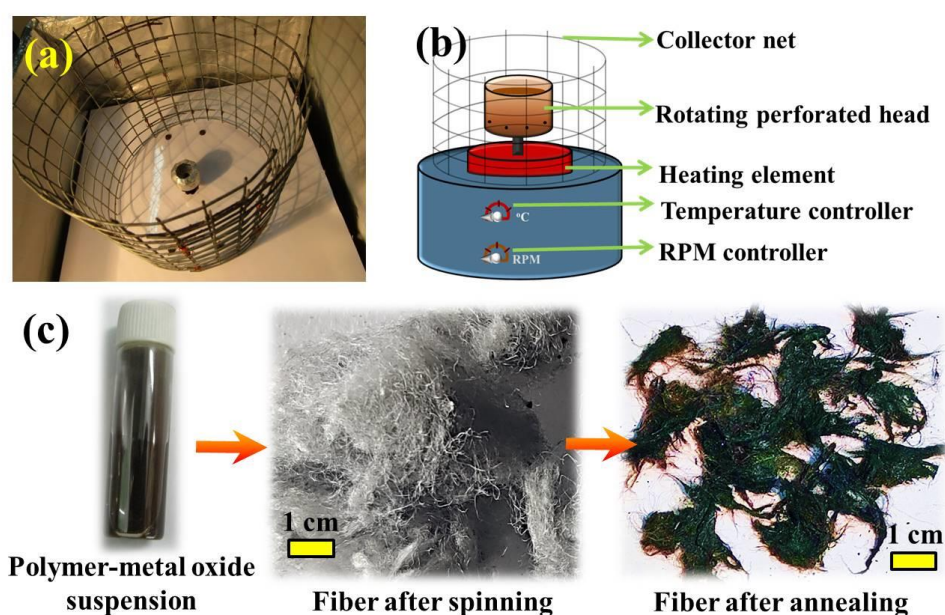
Figure 4.2.1: (a) Photo of the RJ-spin setup (b) Schematic of the same setup (c) Polymer-metal oxide solution at different stages of the synthesis.

Electrospin is one of the best methods for fiber fabrication. However, because of its very less yield capability (0.1-1.0 g h⁻¹), it is not suitable for mass production [8]. Hence, we have indigenously developed a Rotary-Jet Spin device (RJ-Spin) to speed up the fiber fabrication process. The device works similarly to a cotton candy machine. We had modified a commercial centrifuge machine (Remi-8C) which offers a maximum rpm of 6000 and is equipped with a very fine rpm controller. The rotating head of the centrifuge machine was replaced with a perforated aluminum container.

The cylindrical aluminum casing of a capacitor (4700 µF, 35 V) was found to be suitable for use as a rotating head. Very fine holes (~0.1 mm) were made in the wall of the cylindrical container using a hand drill. This perforated cylindrical container was mounted on the centrifuge machine very carefully while maintaining the rotational balance. A cylindrical net was used as the collector for fiber. The whole setup was placed inside a closed box. A heater was placed inside the box to maintain a relatively high surrounding temperature of 50-60 ^{o}C. A syringe pump was used to maintain a steady flow of the polymer solution in the container. A pipe attached to the syringe pump was brought over the rotating container, which supplied the polymer solution inside the container. Figure 4.2.1 (a) shows the indigenous RJ-spin arrangement without the heating element and the polymer supply system, and Figure 4.2.1 (b) shows the schematic of the setup. When the container rotates at very high rpm, the polymer solution inside it is forced through the small holes present in its side wall due to the action of centrifugal force. This stretches the polymer jet along the radial direction forming fibers that dry quickly because of the high surrounding temperature.

To synthesize MnO_2/Carbon-based microfiber using the RJ-Spin set up, initially, 1.5 g Manganese chloride ($MnCl_2$ (Merck India)) is added to 37 ml double distilled water to prepare an Mn^{2+} solution. Ammonium hydroxide (NH_4OH (Merck India)) is added to the solution to precipitate manganese hydroxide ($Mn(OH)_2$) according to the equation (4.2.1).

$$MnCl_2 + NH_4OH = Mn(OH)_2 + NH_4Cl \qquad\qquad (4.2.1)$$

Next, a small quantity of hydrogen peroxide (H_2O_2(Merck India)) is added to the $Mn(OH)_2$ suspension at an elevated temperature of 80 ^{o}C to prepare manganese dioxide suspension according to the equation (4.2.2) [9].

$$Mn(OH)_2 + H_2O_2 = MnO_2 + O_2 \qquad\qquad (4.2.2)$$

In this suspension 12 wt% Polyvinyl alcohol (PVA) powder is added to prepare the metal oxide polymer solution. This solution is fed to the perforated drum rotating at 4000 rpm at a constant rate of 10 mL h^{-1} using a syringe pump. Because of the action of the centrifugal force, the polymer solution is forced through the small holes and dries quickly to form a tiny strand of fibers in the chamber. The whole setup is

enclosed in a temperature-controlled chamber. The chamber temperature is kept fixed at 60 ^{o}C. The higher chamber temperature ensures quick drying of the fiber. The fiber is collected in a cylindrical net and annealed at 700 ^{o}C in an inert atmosphere for 1h, which is further used for different characterizations. By annealing the polymer-metal oxide fiber, the polymer matrix is converted to carbonaceous fiber, which supports the MnO_2. The different steps of the metal oxide-polymer solution have been shown in figure 4.2.1 (c). Here, we have omitted the use of GO while synthesizing the MnO_2/C fiber because it was seen that PVA/GO suspension was clogging the small holes in the container hampering the whole process. This clogging problem could have been avoided if a high rpm motor had been used.

4.3 Synthesis of $NiMn_2O_4$ via hydrothermal technique

The hydrothermal technique is an easy one-pot synthesis technique [10]. It incorporates water as the reaction medium under pressure greater than 1 bar and temperature greater than 100 ^{o}C. This synthesis technique is usually performed in a specially designed closed vessel capable of withstanding high pressure.
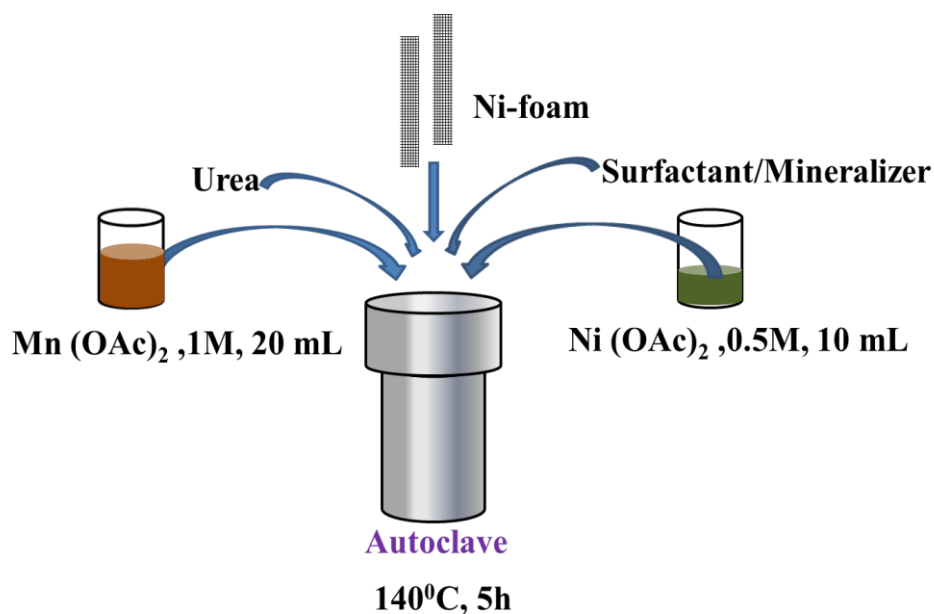
Figure 4.3.1: Scheme to synthesize $NiMn_2O_4$ with different morphologies.

Nickel acetate ($(CH_3COO)_2Ni.4H_2O$), manganese acetate ($(CH_3COO)_2Mn.4H_2O$), and urea ($CO(NH_2)_2$) were purchased from Merck. The different surfactants and mineralizer which were used to vary the morphology of the

composites were all obtained from Sigma Aldrich. These surfactants were cetyl trimethylammonium bromide (CTAB), sodium dodecyl sulfate (SDS), and glucose and the mineralizer was ammonium fluoride (NH_4F). Ni-foam was purchased from Gelon Energy, China. All these chemicals were of analytical grade and used without any further purification. Initially, 0.5 M 10 mL aqueous solution of nickel acetate and 1M 20 mL aqueous solution of manganese acetate were mixed using a magnetic stirrer. After proper mixing of these two solutions, 0.3 g urea was added to it, which was again stirred for 1 h. Here, urea acts as a carbonate ion source to form Ni-Mn-carbonate through the following reactions (4.3.1 to 4.3.5) [11]:

$$CO(NH_2)_2 + H_2O \rightarrow 2NH_3 + CO_2 \tag{4.3.1}$$

$$NH_3.H_2O \rightarrow NH_4^+ + OH^- \tag{4.3.2}$$

$$CO_2 + H_2O \rightarrow CO_3^{2-} + 2H^+ \tag{4.3.3}$$

$$Ni^{2+} + 2Mn^{2+} + 2OH^- \rightarrow NiMn_2(OH)_2 \tag{4.3.4}$$

$$NiMn_2(OH)_2 + CO_3^{2-} + nH_2O \rightarrow [NiMn_2(OH)_2](CO_3^{2-}).nH_2O \tag{4.3.5}$$

Upon heating, the complex bimetallic carbonate, the $NiMn_2O_4$, can be synthesized. Different surfactants and mineralizer were added separately with the mixture of nickel acetate and manganese acetate to prepare different variants of the $NiMn_2O_4$ composite. The addition of NH_4F as a mineralizer during the synthesis produces F^- ions, which form strong coordination with the Ni^{2+} and Mn^{2+} ions, and thus spherical particles of $NiMn_2O_4$ are obtained. On the other hand, the surfactants are able to produce different morphology based on their cationic or anionic nature. The mechanism of formation of different morphologies due to the addition of different chemicals has been discussed in detail in chapter 5 (section 5.3). The details of the sample designation and the added quantity of the different surfactants and mineralizer are given in table 4.3.1. After adding the surfactants or the mineralizer, the resultant solution was again stirred for 2 h. Next, the solution was transferred to a teflon coated steel container. Pieces of Ni-foam of size 0.5 cm x 3 cm were cut from the stock and were washed several times using a dilute aqueous solution of hydrochloric acid, water, and ethanol, respectively, to remove the oxide layers on the foam. After washing, these foams were dried at 70 ^{o}C. After adding these dried Ni-foams, the steel container was sealed tightly and heated at 180 ^{o}C for 6 h, and after heating, the

container was allowed to cool naturally. Nanoparticles coated Ni-foam was carefully removed from the container and washed in distilled water. These foams were annealed at 400 $^{\circ}$C for 1 h in the open air and used as working electrodes for the electrochemical measurements. The synthesis scheme is shown in figure 4.3.1. The residual composite was collected from the solution using a centrifuge and washed using d.i. water. This powder composite was also annealed at 400 $^{\circ}$C for 1 h.

Table 4.3.1: Details of the sample names and quantity of the chemical added to tune the morphology.

Sample Name	Chemical added to tune the morphology	Type of the chemical	Amount
NM1	NH_4F	Mineralizer	0.8 g
NM2	CTAB	Surfactant	0.8 g
NM3	SDS	Surfactant	0.8 g
NM4	Glucose	Surfactant	0.8 g

4.4 Synthesis of ordered microfiber of NiMn$_2$O$_4$ using RJ-Spin technique
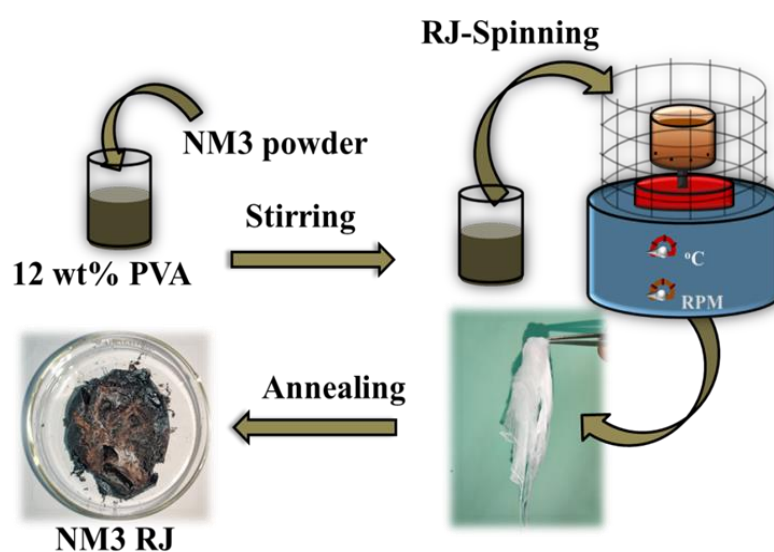
Figure 4.4.1: Synthesis scheme for microfiber of NiMn$_2$O$_4$

From the electrochemical measurement (Chapter 5, Section 5.3), we find that the $NiMn_2O_4$ prepared using SDS (NM3) offered the best charge storage performance. Hence, to fabricate the microfiber of $NiMn_2O_4$ we took pre-synthesized NM3 particles and ground it in a mortar. A fine powder was obtained, which was mixed with 12 wt% PVA polymer solution. This mixture of metal oxide and the polymer solution was magnetically stirred for 10 h. In a similar manner, as described in section 4.2, this polymer-metal oxide mixture was fed to the rotating perforated drum using a syringe pump at a rate of 8 ml h^{-1}. The polymer fiber embedded with the $NiMn_2O_4$ particles was obtained. After collecting the fiber, it was kept at an elevated temperature of 80 ^{o}C to remove excess moisture. The presence of excess moisture hampers the stability of the fiber during the annealing process. Next, the fibers are treated with iodine by keeping it in iodine vapor for 5 minutes. This iodine treatment prevents the fiber from breaking during the annealing process. Finally, the annealing was performed at 800 ^{o}C in an inert atmosphere for 3 h. The annealed fiber (named NM3RJ) was collected and used for further characterizations. Figure 4.4.1 depicts the synthesis scheme for NM3RJ.

4.5 References

[1] J. Xue, T. Wu, Y. Dai, and Y. Xia, Electrospinning and Electrospun Nanofibers: Methods, Materials, and Applications, *Chemical Reviews* 119 (2019) 5298-5415 doi: 10.1021/acs.chemrev.8b00593

[2] M. R. Badrossamay, H. A. McIlwee, J. A. Goss, and K. K. Parker, Nanofiber Assembly by Rotary Jet-Spinning, *Nano Letters* 10 (2010) 2257-2261 doi: 10.1021/nl101355x

[3] A. Ray, A. Roy, S. Saha, M. Ghosh, S.R. Chowdhury, T. Maiyalagan, S.K. Bhattacharya, S. Das, Electrochemical energy storage properties of Ni-Mn-Oxide electrodes for advance asymmetric supercapacitor application, *Langmuir*, 35 (2019) 8257–8267 doi:10.1021/acs.langmuir.9b00955.

[4] J. Xu, F. Lin, M. M. Doeff, W. Tong, A review of Ni-based layered oxides for rechargeable Li-ion batteries, *Journal of Materials Chemistry A*, 5 (2017) 874-901 doi: 10.1039/C6TA07991A

[5] W. Wei, X. Cui, W. Chen, D. G. Ivey, Manganese oxide-based materials as electrochemical supercapacitor electrodes. *Chemical society reviews*, 40 (2011) 1697-1721 doi: 10.1039/C0CS00127A

[6] D. A. Pethsangave, R. V. Khose, A. C. Chaskar, S. C. Jun, S. Some, Graphene derivative as a highly efficient nitrosonium source: a reusable catalyst for diazotization and coupling reaction, *ChemistrySelect*, 1 (2016) 6933–6940. doi:10.1002/slct.201601544

[7] U. Khair, A. Jalal, K. Uemura, & Y. Gotoh, Fabrication of carbon fibers from electrospun poly(vinyl alcohol) nanofibers. *Textile Research Journal*, 81 (2011) 659–672. https://doi.org/10.1177/0040517510385175

[8] O. O. Dosunmu, G. G. Chase, W. Kataphinan, D. H. Reneker, Electrospinning of polymer nanofibres from multiple jets on a porous tubular surface, *Nanotechnology*, 17 (2006) 1123 doi: 10.1088/0957-4484/17/4/046

[9] J. Petlicki, D. Palusova, T. G. M. van de Ven, Physicochemical Aspects of Catalytic Decomposition of Hydrogen Peroxide by Manganese Compounds, *Industrial & Engineering Chemistry Research,* 44 (2005) 2002-2010 doi: 10.1021/ie049595n

[10] S. Feng and R. Xu, New Materials in Hydrothermal Synthesis, *Accounts of Chemical Research*, 34 (2001) 239-247 doi: 10.1021/ar0000105

[11] X. L. Guo, X. Y. Liu, X. D. Hao, S. J. Zhu, F. Dong, Z. Q.Wen,Y. X. Zhang, Nickel-Manganese Layered Double Hydroxide Nanosheets Supported on Nickel Foam for High-performance Supercapacitor Electrode Materials, *Electrochimica Acta,* 194 (2016) 179–186 doi: 10.1016/j.electacta.2016.02.080

Originality Report for Chapter 4

(*Generated using Ithenticate Software excluding the first author publications of Mr. Samik Saha)

Chapter 4

ORIGINALITY REPORT

8%
SIMILARITY INDEX

PRIMARY SOURCES

1 Maziyar Sabet, Hassan Soleimani, Erfan Mohammadian, Seyednooroldin Hosseini. "The effect of graphene oxide on the mechanical, thermal characteristics and flame retardancy of polyurethane", Plastics, Rubber and Composites, 2020
Crossref
47 words — 2%

2 Paweł Nakielski, Chiara Rinoldi, Michał Pruchniewski, Sylwia Pawłowska et al. "Laser - Assisted Fabrication of Injectable Nanofibrous Cell Carriers", Small, 2021
Crossref
44 words — 2%

3 scholarworks.unist.ac.kr
Internet
34 words — 1%

4 Samik Saha, Sachindranath Das. "Nanomaterials in thin-film form for new-generation energy storage device applications", Elsevier BV, 2021
Crossref
29 words — 1%

5 Agnès Guigueno, Janie Dassa, Pascal Belin, Paul Louis Boquet. " Oversynthesis of a New Small RNA Suppresses Export Toxicity of DsbA'-PhoA Unfoldable Periplasmic Proteins ", Journal of Bacteriology, 2001
Crossref
10 words — < 1%

6 Min Liu, Nanping Deng, Jingge Ju, Lanlan Fan et al. "A Review: Electrospun Nanofiber Materials for
10 words — < 1%

Chapter 5

Results and Discussions

The previous chapter discusses the synthesis scheme of the different electrode materials. This chapter has discussed the results of compositional, structural, morphological, and electrochemical characterization of these samples in detail.

5.1 Ordered and Disordered sample of MnO₂-GO
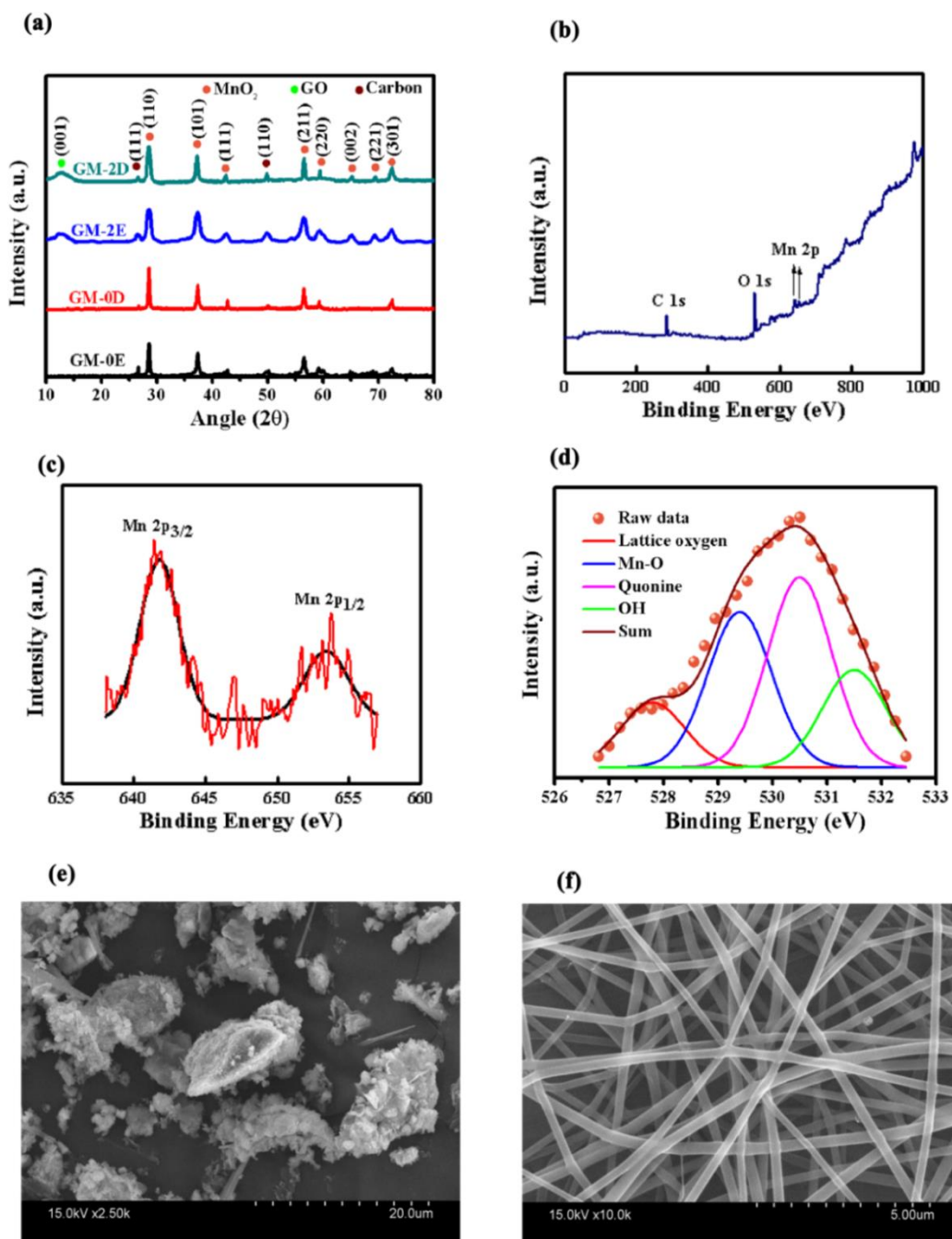
Figure 5.1.1: (a) XRD patterns of GM-0E and GM-2E(b) XPS survey spectrum of GM-2E. High resolution XPS data of (c) Mn 2p ₃/₂ and (d) O ₁ₛ of GM-2E. SEM images of (e) GM-2D and (f) GM-2E

The ordered and disordered samples of MnO_2-GO have been synthesized using electrospinning and dropcasting, respectively. Here, we discuss the various results of the different characterizations. Figure 5.1.1 (a) shows the powder XRD patterns of GM-0E, GM-0D, GM-2E, and GM-2D samples. The peaks at 28.7^0, 37.5^0, 42.8^0, 56.4^0, 59^0, 64.8^0, 69.1^0, 72.3^0, 75.9^0 are due to the tetragonal phase of MnO_2 (JCPDS 72-1984). The peaks at 26.6^0 and 49.5^0 are may be due to carbon (JCPDS 75-0444) which arises due to the thermal annealing of the PVA polymer. The GM-2E and GM-2D samples show the peaks of the tetragonal phase of MnO_2 with an additional broad peak nearly at $12^{0,}$ which corresponds to the graphene oxide, and a small hump near $20^{0,}$ which may be due to partially reduced GO [1]. The encapsulation of GO by PVA matrix may prevent GO from being totally reduced. These XRD patterns do not show any impurity peak suggesting a successful synthesis of pure MnO_2 and MnO_2-GO fiber.

The elemental analyses of GM-2E and GM-2D samples were performed by X-ray photoelectron spectroscopy (XPS). Figure 5.1.1 (b) shows the full survey spectrum of the GM-2E composite, which clearly indicates the presence of Mn, O, and C on the surface of the composite. Figure 5.1.1 (c) displays the high-resolution spectra of Mn 2p state of GM-2E, which can be deconvoluted into two different peaks, namely Mn $2p_{3/2}$ and Mn $2p_{1/2}$ at energy 642.1 eV and 653.9 eV, respectively. This suggests that the element Mn is in +4 valence state [2] in both these two composites. The energy separation of 11.8 eV is in excellent agreement with the literature. Figure 5.1.1 (d) represents the core level spectrum of O1s of GM-2E, which again can be deconvoluted into four distinct peaks. The peak at 527.9 eV is due to the lattice oxygen [3]. The peak at 529.4 eV represents Mn-O [4]. The peaks at 530.5 eV and 531.4 eV are due to the quinone groups and the O-H present in the GO [5].

The SEM image of the GM-2D (Figure 5.1.1 (e)) clearly shows the discreet cluster of the redox-active particles with negligible interconnection between them. Figure 5.1.1 (f) shows the uniform distribution of the electrospun fiber of the GM-2E sample having an average diameter of 260 nm. No bead formation was observed on the fiber. This fiber-like structure effectively connects the individual redox-active site resulting in superior electrochemical performance.
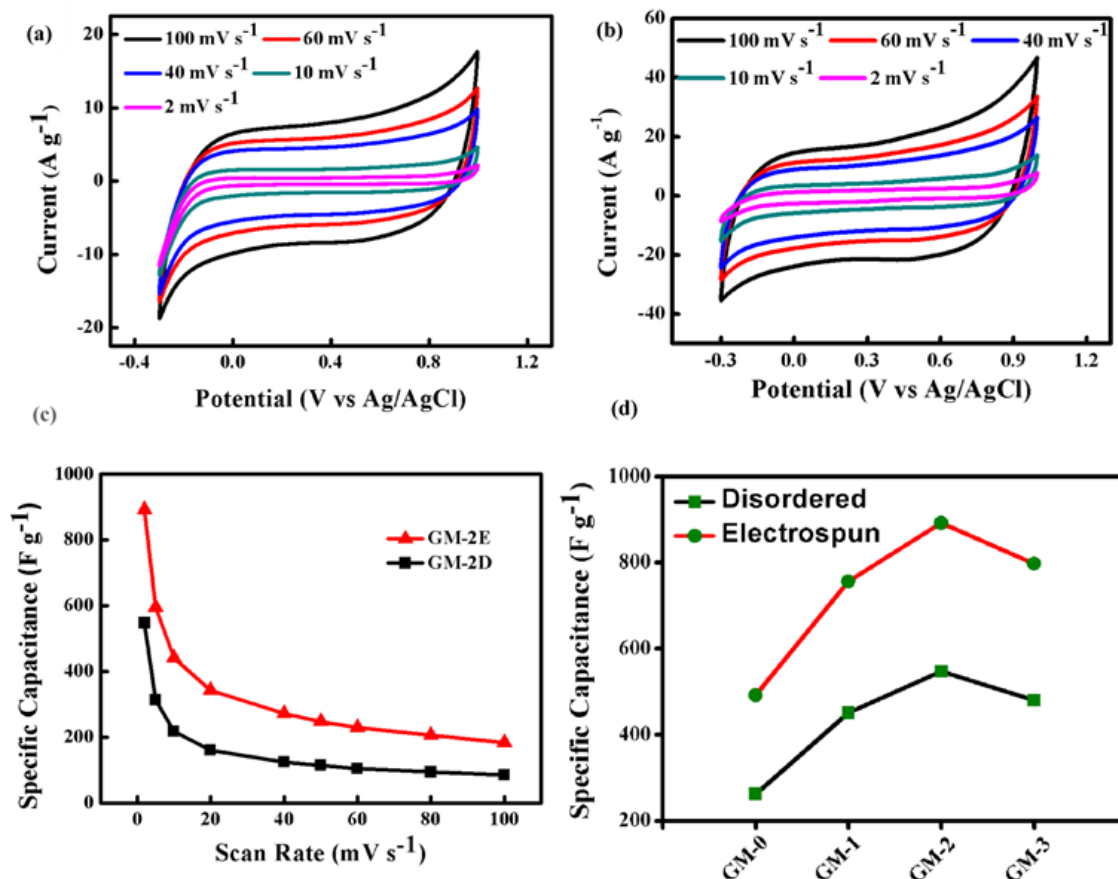
Figure 5.1.2: CV curves at different scan rates for (a) GM-2D and (b) GM-2E. (c) Specific capacitance vs. scan rate plot for the two samples. (d) Specific capacitance as obtained from the CV measurement for different samples.

Cyclic voltammetry (CV) has been performed in a three-electrode setup using aqueous 1M Na_2SO_4 solution as electrolyte within the potential range -0.3 V to 1 V. Results show that GM-2E and GM-2D demonstrate the highest specific capacitance among the respective groups (electrospun sample and dropcasted disordered sample). Thus the CV results at different scan rates are discussed for GM-2E and GM-2D samples, while the rest of the CV curves are shown in figure 5.1.3. Figures 5.1.2 (a) and 5.1.2 (b) show the CV curves for different scan rates for GM-2D and GM-2E, respectively. It is found that the electrospun sample (Figure 5.1.2 (b)) maintains its near rectangular shape down to the low scan rate of 2 mV s^{-1}. On the other hand, the disordered dropcasted sample deviates from its near rectangular shape at the boundary of the potential window at a low scan rate which suggests that the fiber-like ordered structure may participate in the redox reaction with the electrolyte within a wide potential window of 1.3V but the disordered sample cannot. A similar kind of trend is also observed for GM-0D, GM-0E, and GM-1D and GM-1E (Figure 5.1.3 (a)-(d)).
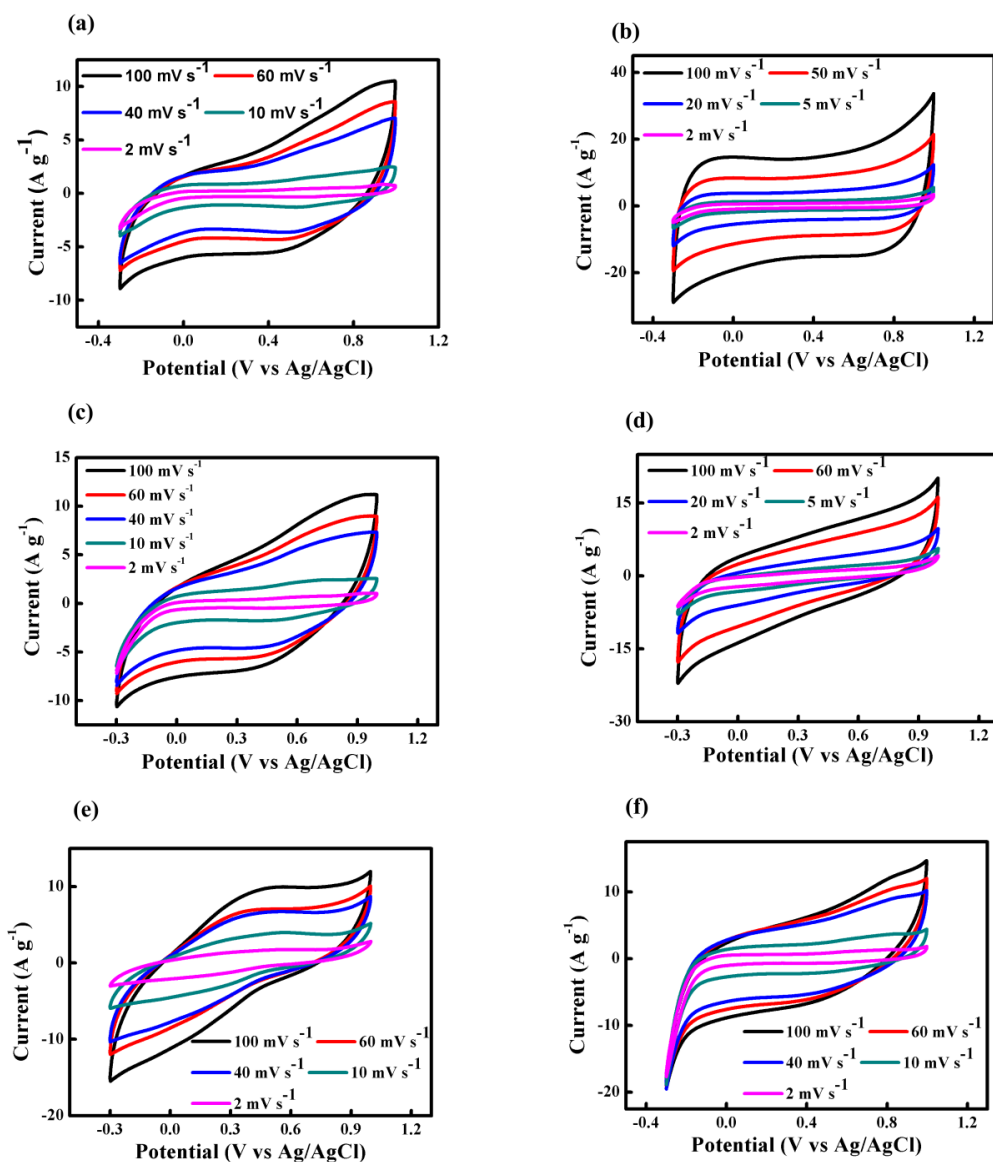
Figure 5.1.3: CV curves at different scan rates for (a) GM-0D (b) GM-0E (c) GM-1D (d) GM-1E (e) GM-3D (f) GM-3E

Figure 5.1.2 (c) shows the specific capacitance vs. scan rate plot for GM-2E and GM-2D. The specific capacitance value rises for both the samples with the decreasing scan rates. At a lower scan rate, the ions from the electrolyte get enough time to access both the inner and outer surface of the active material resulting in the accumulation of a large number of ions at the electrode, which effectively enhances the specific capacitance. We have observed with the increase of graphene oxide percentage, the specific capacitance rises for both disordered and ordered samples and attains a maximum value of 546.9 F g^{-1} for the sample GM-2D and 892.8 F g^{-1} for the sample GM-2E, both having Mn^{2+} and GO ratio 5:2. The addition of GO beyond this optimized amount slightly decreases the specific capacitance for both ordered and

disordered samples. Thus an opposite kind of behavior is observed for GM-3D and GM-3E (Figure 5.1.3 (e) and (f)), which is possibly because of the presence of an excessive amount of GO compared to MnO_2 in the sample [6]. Because of the encapsulation of the redox-active material MnO_2 by GO, the electrolyte cannot access MnO_2 nanoparticles, resulting in fewer redox reactions. Thus, the samples GM-3E and GM-3D show less specific capacitance, as shown in figure 5.1.2 (d). We can also see from figure 5.1.2 (d) that ordered electrospun samples always yield a higher specific capacitance value than the disordered counterpart.

Galvanostatic charge-discharge (GCD) is another useful tool to determine the performance of the electrode material. GCD of all samples was performed in the same setup using aqueous 1M Na_2SO_4 solution as electrolyte within the same window potential of -0.3V to 1V. Figure 5.1.4 (a) and 5.1.4 (b) represent the GCD curves at different current densities for GM-2D and GM-2E, respectively. All these discharge curves show three distinct regions (i) a small region of rapid discharge, (ii) a wide region of linear discharge, and (iii) a near exponential region of discharge at the tail. The small region of rapid discharge is mainly due to the internal resistance drop (I.R drop) of the electrode material. This drop in potential is mainly due to the weak electrical contact of the active material with the current collector and due to the intrinsic resistance of the electrolytes [7]. From figure 5.1.4 (a) and 5.1.4 (b), we can see that the dropcasted disordered sample GM-2D offers a higher I.R. drop compared to the electrospun ordered GM-2E sample, which again suggests that the electrospun sample offers much better electrical contact between the individual nanoparticles constituting the electrode. Using the equation (2.3.3), we get the specific capacitance values of 536.4 F g^{-1} for GM-2D and 863.0 F g^{-1} for GM-2E at the respective minimum current densities, which are very close to the values obtained from the CV.

Electrochemical Impedance Spectroscopy (EIS) is an important analytical technique to gain kinetic information of the redox processes which occur at the electrode-electrolyte surface at different time scales. The obtained EIS measurement data for GM-2D and GM-2E are plotted in figures 5.1.4 (c) and 5.1.4 (d) in the form of a Nyquist plot over a frequency range of 0.01 Hz to 100 kHz using an a.c. perturbation voltage of 10 mV. The high-frequency regions are shown in the inset of the respective Nyquist plots. The EIS data are fitted using Z-View software using an equivalent circuit which is shown in the inset of Figure 5.1.4 (c) and 5.1.4 (d). All the
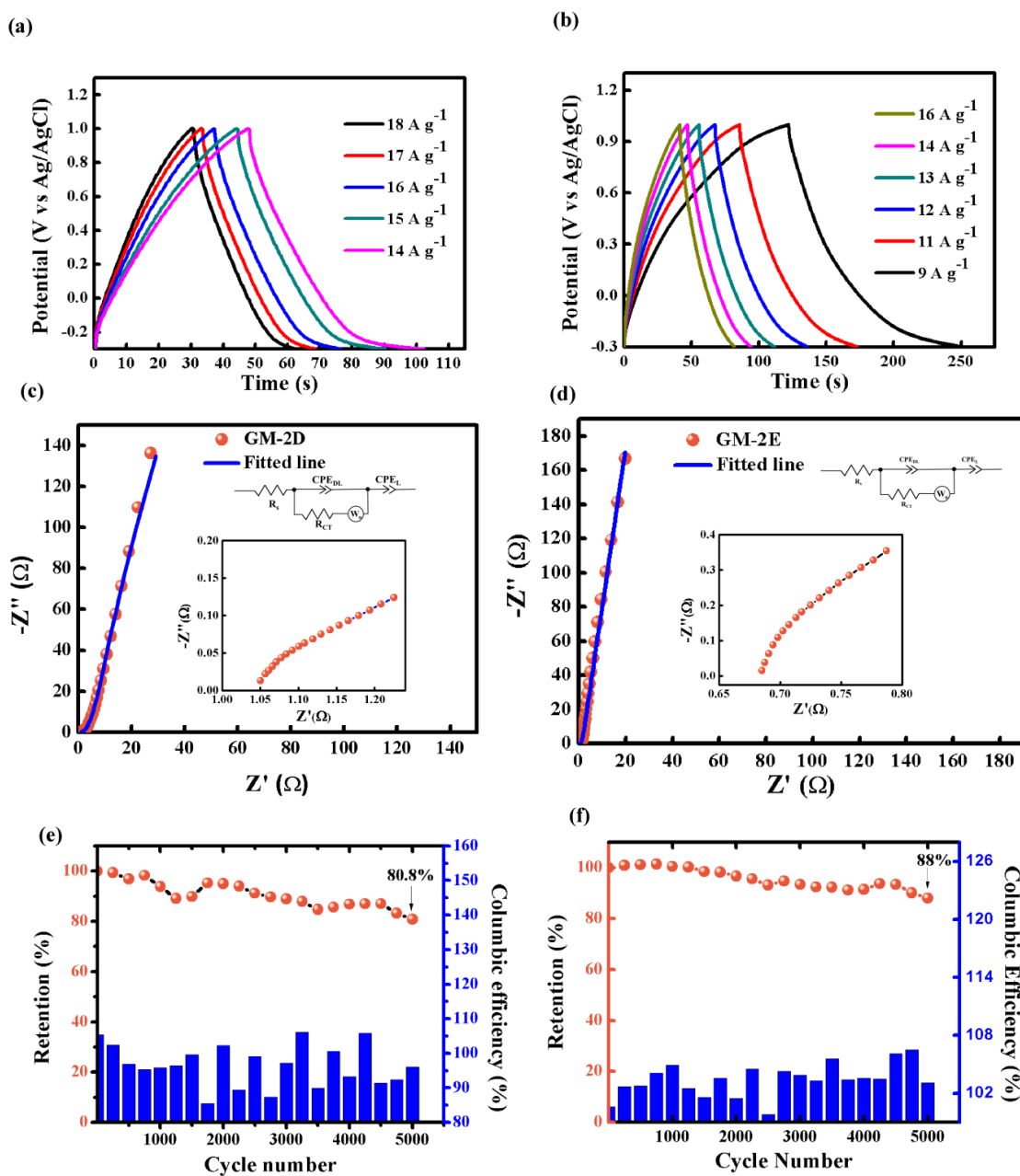
Figure 5.1.4: GCD curves at different current densities for (a) GM-2D and (b) GM-2E. Nyquist plot for (c) GM-2D (Inset: corresponding high frequency region and equivalent circuit used to fit the Nyquist plot) and (d) GM-2E (Inset: High frequency region for GM-2E and the same equivalent circuit used to fit the Nyquist plot). Cyclic stability analysis and columbic efficiency plots for (e) GM-2D and (f) GM-2E

calculated circuit parameters are presented in Table-5.1.1. Here R_s is the Equivalent Series Resistance (ESR), which generally occurs due to the combined resistance of the electrolyte and electrode [7]. From Table-5.1.1, it can be seen that the disordered bulk sample offers higher ESR compared to the ordered sample. This ESR is mainly

responsible for IR drop in the GCD profile. We have also seen from the GCD profiles that the ordered sample has a comparatively lower IR drop which has been verified using the equivalent circuit model. In the equivalent circuit, R_{CT} is the charge transfer resistance that determines the charge transfer rate from the electrode-electrolyte interface. The lower value of R_{CT} for GM-2E essentially suggests fast ion transport from the electrode surface. CPE_{DL} is the constant phase element arising due to the double layer effect at the interface of the electrode. This is

Table-5.1.1. Different parameters obtained from the fitting.

Sample	R_s (Ω)	R_{CT} (Ω)	CPE_{DL}	W_o	CPE_L
GM-2D	1.06	0.47	CPE_{DL}-Q = 0.001591 CPE_{DL}-n = 0.61948	W_{OR} = 1.08 W_{OT} = 0.2261 W_{OP} = 0.5716	CPE_L-Q = 0.027139 CPE_L-n = 0.58128
GM-2E	0.68	0.41	CPE_{DL}-Q = 0.069247 CPE_{DL}-n = 0.89134	W_{OR} = 1.01 W_{OT} = 0.6247 W_{OP} = 0.5279	CPE_L-Q = 0.068010 CPE_L-n = 0.91511

mainly because of the separation of ionic and/ or electronic charges at the interface. The higher value of CPE_{DL} for GM-2E suggests that the ordered sample stores more charges via electric double layer formation than the disordered sample [8]. W_o is the Warburg element which is due to the frequency-dependent diffusion. From table-5.1.1, we find that the value of Warburg resistance is less for the ordered sample, which suggests that the ion diffusion takes place much more easily compared to the dropcasted sample. CPE_L arises due to the charge storage via pseudocapacitive effect. In this case, also the electrospun ordered sample offers higher pseudocapacitance than the dropcasted disordered sample. This is because of the formation of a large number

of redox-active sites on the surface and inside the electrode material. Insets of figures 5.1.4 (c) and 5.1.4 (d) show the high-frequency region for the respective sample. We have also calculated the apparent diffusion coefficient (D_a) of the charge carriers for both these two samples from the diffusion-controlled regime of the Nyquist plot. We found that for GM-2D this regime extends from 0.2 Hz to 2 Hz, whereas for GM-2E the same extends from 1.7 Hz to 18 Hz. Following the procedure of S. K. Ujjain et al. [9-13] we found the value of apparent diffusion coefficient for GM-2D is 1.39 x 10^{-8} cm^2 s^{-1}, whereas for GM-2E the same value is 1.16 x 10^{-7} cm^2 s^{-1}. The higher value of diffusion coefficient for GM-2E again suggests that fiber-like porous structure enhances the charge diffusion process as well as electrochemical performances. In order to check the long-term stability, we performed 5000 GCD cycles for both GM-2D and GM-2E at the same current density of 30 A g^{-1}. Figures 5.1.4 (e) and 5.1.4 (f) show the variation of percentage retention of specific capacitance and columbic efficiency with the cycle number. The dropcasted sample GM-2D retains 80.8%, whereas GM-2E retains 88% of their respective capacitance after 5000 GCD cycles. This demonstrates that the fiber-like structure of the ordered sample provides extra structural support to the MnO$_2$-GO composite. This extra support prevents the large volumetric strain occurring during the repeated GCD cycles. The Columbic efficiency of a GCD cycle is defined as the ratio of the discharging time to charging time. Both
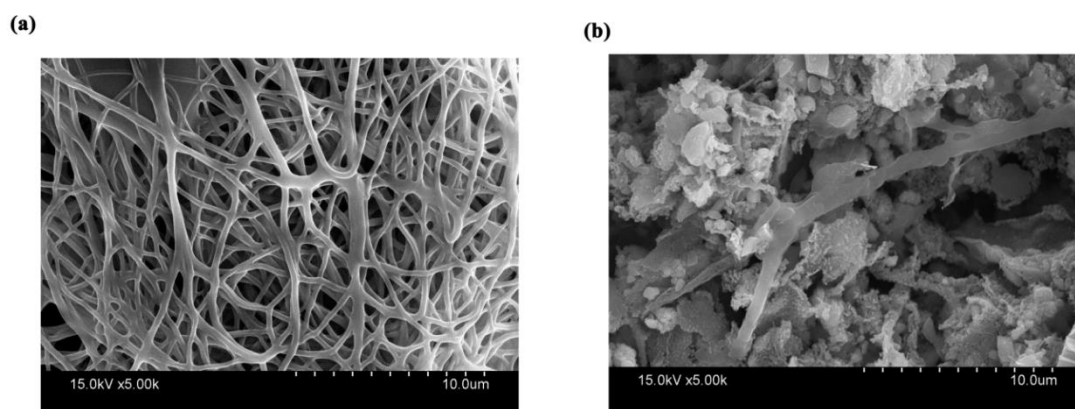
Figure 5.1.5: SEM image of (a) the electrode coated with GM-2E sample before electrochemical measurement (b) the same electrode after 5000 GCD cycles.

these two samples demonstrate columbic efficiency close to 100% over all the cycles. Figure 5.1.5 (a) and (b) show the SEM images of the GM-2E working electrode before and after the long-term stability test. It can be seen that fibers got almost destroyed after the 5000 GCD cycles. This could be the reason for the decrement of specific capacitance value after 5000 charge-discharge cycles.

We have already demonstrated the superiority of the ordered sample in the presence of an electrolyte medium. In order to further check the idea of good interconnectivity between the redox-active sites in the electrospun ordered sample compared to the disordered counterpart, we have performed the room temperature dielectric study on the samples to calculate the mobility (μ) and diffusion constant (D) of charge carriers. Though there is a difference in packing density of the pelleted sample with the sample used to test the electrochemical measurements, the values of the different parameters obtained from dielectric measurement actually support the idea of good connectivity between the individual nanoparticles. Figure 5.1.6 (a) shows the Cole-Cole plot of the two samples. Each Cole-Cole plot comprises a depressed semi-circle with a tilted spear. Such response can be modeled by a parallel combination of Constant Phase Element CPE_1 and a resistor (R) which are connected in series with another constant phase element CPE_2 (inset of Figure 5.1.6 (a)). Here
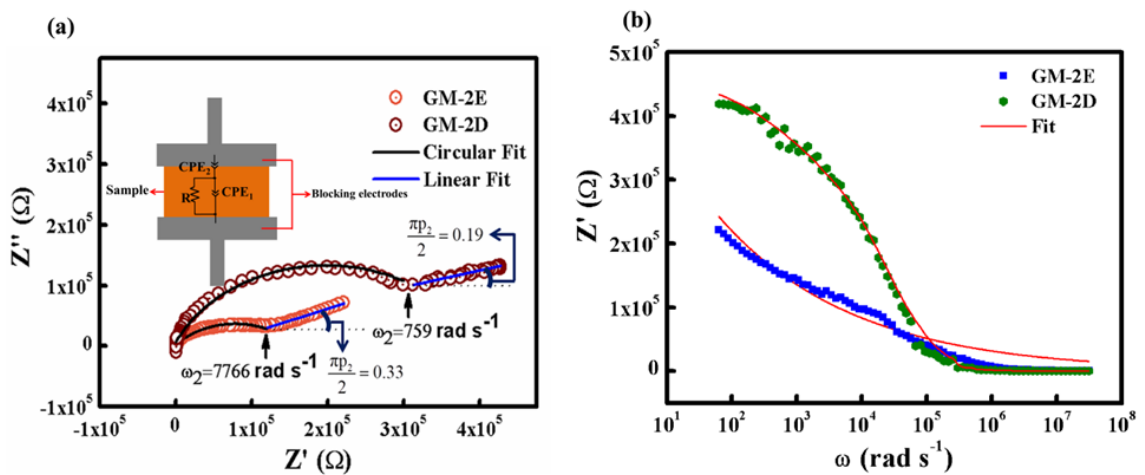
Figure 5.1.6: (a) Cole-Cole plot of the two samples at room temperature (inset: schematic of the dielectric measurement and the circuit element corresponding to complex impedance response) (b) Plot of $Z^{'}$ vs. ω for the two samples

CPE_1 is due to the bulk geometrical capacitance, and CPE_2 arises due to the establishment of an electric double layer at the interface of the blocking electrode and the sample. For individual CPE, real (Z') and the imaginary part (Z'') are given by,

$$Z' = \frac{k \cdot \cos\frac{\pi p}{2}}{\omega^p} \tag{5.1.1}$$

$$Z'' = \frac{k \cdot \sin \frac{\pi p}{2}}{\omega^{p}}$$

(5.1.2)

So the real and imaginary part for the equivalent circuit as shown in figure 5.1.5 (b) (inset) can be expressed by,

$$Z' = \frac{R + R^2 k_1^{-1} \omega^{P_1} \cos(\frac{\pi p_1}{2})}{1 + 2R k_1^{-1} \omega^{P_1} \cos(\frac{\pi p_1}{2}) + R^2 k_1^{-2} \omega^{2p_1}} + \frac{\cos(\frac{\pi p_2}{2})}{k_2^{-1} \omega^{P_2}}$$

(5.1.3)

$$Z'' = \frac{R + R^2 k_1^{-1} \omega^{P_1} \sin(\frac{\pi p_1}{2})}{1 + 2R k_1^{-1} \omega^{P_1} \cos(\frac{\pi p_1}{2}) + R^2 k_1^{-2} \omega^{2p_1}} + \frac{\sin(\frac{\pi p_2}{2})}{k_2^{-1} \omega^{P_2}}$$

(5.1.4)

where k_1^{-1} is the geometrical capacitance due to the bulk material and k_2^{-1} is the capacitance due to the electric double layer (EDL) developed at the electrode interface during the measurement, ω is the angular frequency, R is the material resistance of the material under investigation, which is equal to the length of the projection of the semi-circular arc on the Z' axis. p_1 is the ratio of the angle between (in radian) the real and imaginary impedance axes to the angle between (in radian) the diameter of the semicircle and the Z'' axis. p_2 is the parameter that controls the angle of leaning of the spear with respect to the Z' axis. p_1 and p_2 have values between 0 and 1 [14]. The mobility (μ) of the charge carrier at absolute temperature T can be determined from the Einstein-Nernst equation, which is given by,

$$eD = \mu K_B T$$

(5.1.5)

Here K_B is the Boltzmann constant. From the analysis of Bandara et al. [15] and Arof et al. [14] the diffusion coefficient of the material is given by,

(5.1.6)

$$D = \frac{(k_2 \varepsilon_r \varepsilon_0 A)^2}{\tau_2}$$

Here, ε_r is the relative permittivity of the material, and A is the area of the pelleted sample. ε_0 is the permittivity of the vacuum. τ_2 is equal to $1/\omega_2$, where ω_2 is the

angular frequency corresponding to the minimum of the imaginary part of the impedance spectra in figure 5.1.6 (a).

From equation (5.1.5) and (5.1.6) the mobility of charge carriers is given by,

$$\mu = \frac{e(k_2\varepsilon_r\varepsilon_0 A)^2}{k_b T \tau_2}$$

(5.1.7)

Equations (5.1.3) & (5.1.4) are used to fit the graph to evaluate the values of k_1 and k_2. One such fit of the Z' vs. ω is shown in figure 5.1.6 (b). Using the values of R, p_1 and p_2 obtained directly from the Cole-Cole plot of Figure 5.1.5 (a), we have evaluated the values of D and μ from the equations (5.1.6) and (5.1.7). These calculated values are enlisted in table-5.1.2 for the two different samples. Hence it can be concluded from the above study that because of the good interconnection between the nanoparticles, the ordered sample offers higher mobility and diffusion constant compared to the disordered sample having a negligible interconnection between the nanoparticles. The higher mobility, conductivity, and diffusivity of the ordered sample offer easy electron transport, which is beneficial for good electrochemical activity.

Table-5.1.2. Parameters obtained from the Nyquist plot and the fitting.

Values evaluated	GM-2D	GM-2E
Bulk resistance (R) (kΩ)	398.9	164
Conductivity (σ) (S cm^{-1})	6.9×10^{-5}	2.1×10^{-4}
p_1	0.74	0.53
p_2	0.12	0.21
k_2(F^{-1})	1.9×10^{5}	6.1×10^{5}
Diffusion Constant (D) (cm^{2}s^{-1})	1.4×10^{-12}	1.3×10^{-10}
Mobility (μ) (cm^{2}V^{-1}s)	5.4×10^{-11}	5.2×10^{-9}
Relative permittivity (ε_r)	4.9	4.9
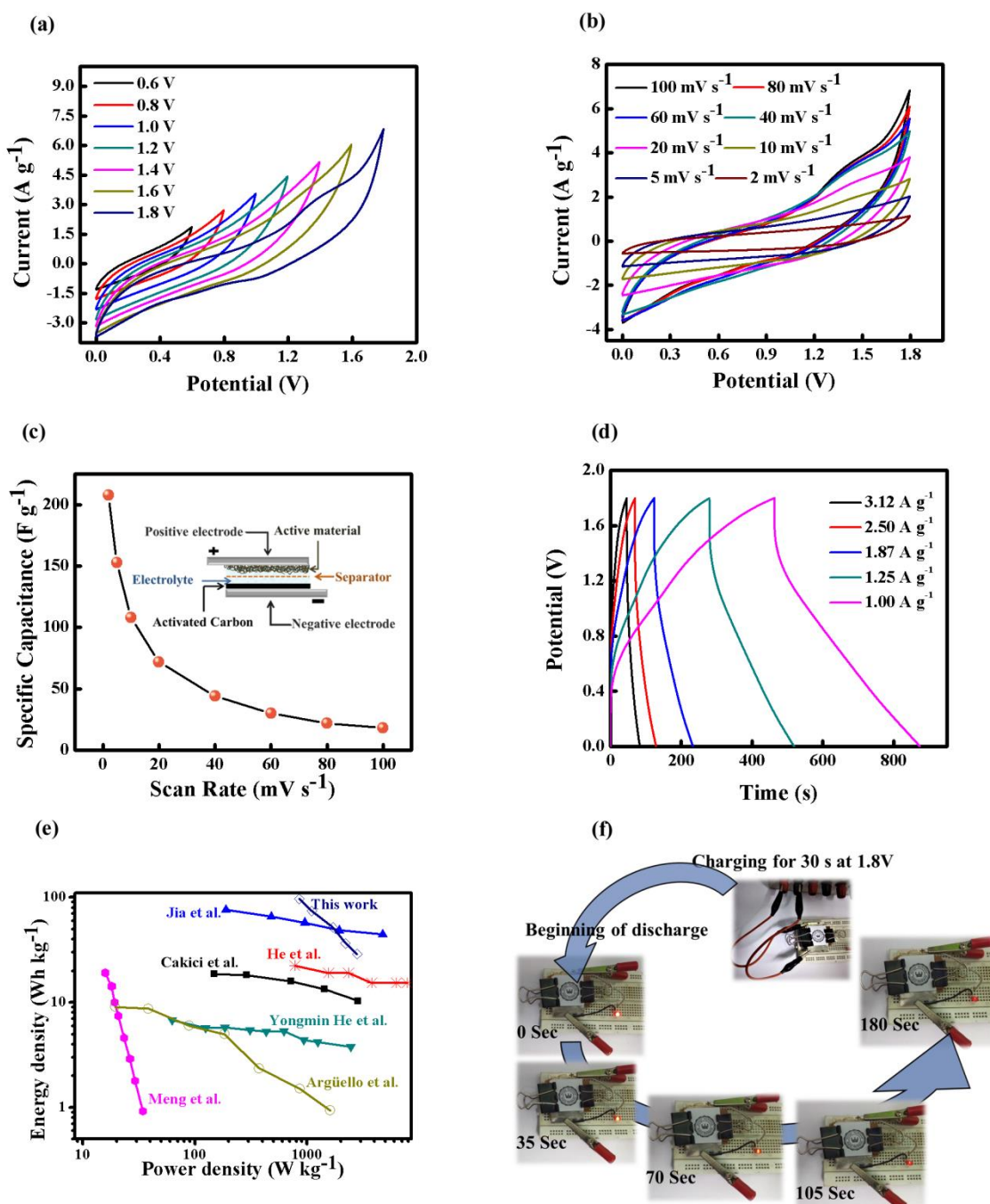
Figure 5.1.7: (a) CV curves at different potential windows at 100 mV s^{-1} scan rate (b) CV curves at different scan rates for 1.8V potential window(c) specific capacitance vs. scan rate plot for the device (inset) device schematic (d) GCD curves at different current densities (e) Ragone plot for the device along with some recent report for comparison (f) Charging state and discharging stages of the device at different time.

The device performance of the GM-2E sample has been demonstrated by assembling an asymmetric supercapacitor (ASC). A steel plate (2 cm x3 cm) coated with the ordered GM-2E sample is used as a positrode of the device, whereas an activated carbon-coated steel plate of similar dimensions is used for the negatrode. A filter paper (25 microns) soaked in a 1M aqueous Na_2SO_4 electrolyte acts as a separator. Inset of the Figure 5.1.7 (c) shows the schematic of the device. Figure 5.1.7 (a) shows the CV curves at different window potentials up to 1.8 V at a 100mV s^{-1} scan rate. Even on the higher side of the potential window, the CV curves maintain their near rectangular shape, which essentially suggests that the as-fabricated electrodes have high hydrogen and oxygen overpotential. Figure 5.1.7 (b) shows the CV curves at a 1.8 V wide potential window for different scan rates. Specific capacitance value calculated from the CV curves shows a maximum of 212 F g^{-1} at 2 mV s^{-1}, which decreases with the increasing scan rate (Figure 5.1.7 (c)). Figure 5.1.7 (d) shows the GCD curves of the ASC at different current densities. All the GCD curves show a near triangular profile with a small IR drop. The maximum specific capacitance value obtained at 1 A g^{-1} is 210 F g^{-1}, which is very close to the value obtained from the CV curves. The energy density (E) (Wh kg^{-1}) and power density (P) (W kg^{-1}) of the ASC can be calculated from the GCD curves at different current densities using the following equation (2.5.1) and equation (2.5.2) [16]. At the lowest current density of 1 A g^{-1}, the device offers a maximum energy density of 96.75 Wh kg^{-1} and a minimum power density of 0.85 kW kg^{-1}. As the current density is increased to 3.1 A g^{-1}, the energy density decreases to 28.8 Wh kg^{-1}, and power density maximizes to 2.8 kW kg^{-1}. This kind of behavior has been plotted as Ragone plot in figure 5.1.7 (e). We have also included results from some recent works [17-22] in the Ragone plot for the purpose of comparison. The fabricated device was connected to an external power supply and charged to 1.8 V for 30 s then it was connected to power a red LED. Because of the high energy density offered by the device, the LED remained on for more than 3 min. The charging state and the discharging states at different time durations have been shown in figure 5.1.7 (f). The EIS study of the device is shown as a Nyquist plot in figure 5.1.8 (a). The device offers comparatively low resistance over all frequencies. Inset of the Figure 5.1.8 (a) shows the circuit used to fit the experimentally obtained data. As previously discussed, R_s is the equivalent series resistance which in this case has a value of 0.17 Ω, and R_{ct} is the charge transfer resistance having a value of 4.04 Ω. These small
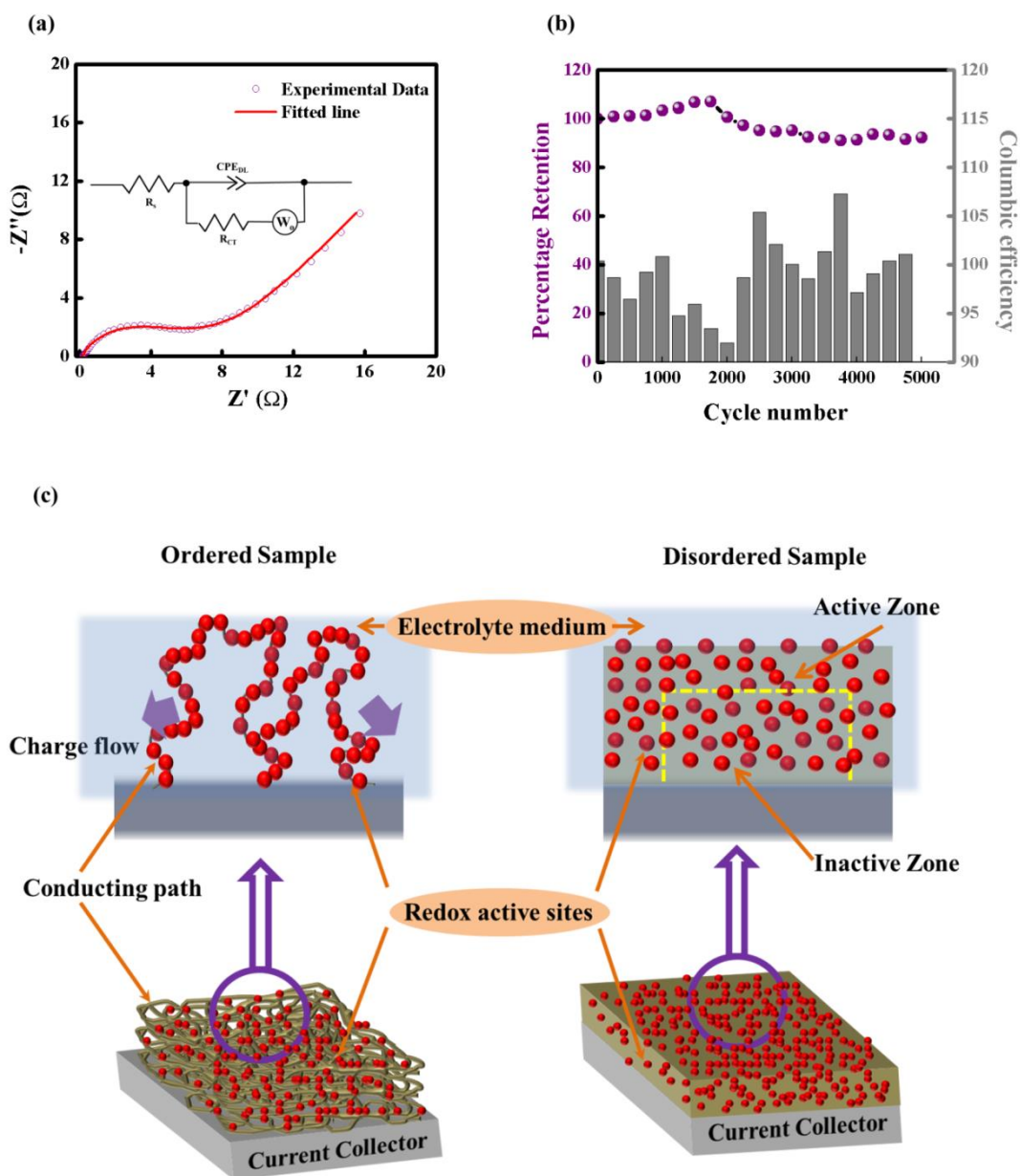
Figure 5.1.8: (a) Nyquist plot for the device (inset) circuit used to fit the data (b) Cyclic stability analysis and columbic efficiency plot for the device (c) Schematic of the electrodes coated with ordered electrospun and dropcasted disordered sample.

values of the resistances signify easy conduction of electrons and ions, which is beneficial for high power delivery. The long-term performance of the device was verified by performing 5000 GCD cycles at 3.1 A g^{-1} current density (Figure 5.1.8 (b)). Initially, up to the 1800th cycle, the specific capacitance rises, reaching a percentage retention value of 110%; after that, it decreases and reaches a value 93.3% after 5000 cycles, whereas columbic efficiency remains close to 100% with some minor variations over all the cycles. Figure 5.1.8 (c) shows the schematic of the

working electrodes coated with electrospun ordered sample and dropcasted disordered sample. During the electrospinning process, a well-defined conducting path connecting the nanoparticles has formed within the fiber. Thus electrons can easily reach the current collector following these paths, resulting in a small internal resistance of the electrode. Also, because of the fiber-like structure of the deposited material, the electrolyte can easily access the whole active material, which reduces the effect of dead mass and enhances the charge storage capacity. On the other hand, the disordered sample consists of nanoparticles that are less electrically connected to each other. This creates large potential barriers at different locations within the material for the electrons resulting in high electrode resistance. Three-dimensional accessibility of electrolyte is also reduced in the case of the dropcasted disordered sample. Only the active zone, which is the portion of the redox-active material close to the electrode-electrolyte interface, participates in the redox reaction with the electrolyte, but the redox-active nanoparticles belonging to the inactive zone cannot participate in the reaction and remain as a dead mass which also increases the resistance of the electrode. Thus from the electrochemical point of view, the electrospun ordered sample is a better candidate than the disordered sample for the electrodes of the supercapacitors.

5.2 Ordered microfiber of MnO₂/Carbon

Synthesis of MnO₂/Carbon microfiber by Rotary Jet-Spin method has been discussed in detail in the previous chapter. Here results of the different characterizations are discussed.
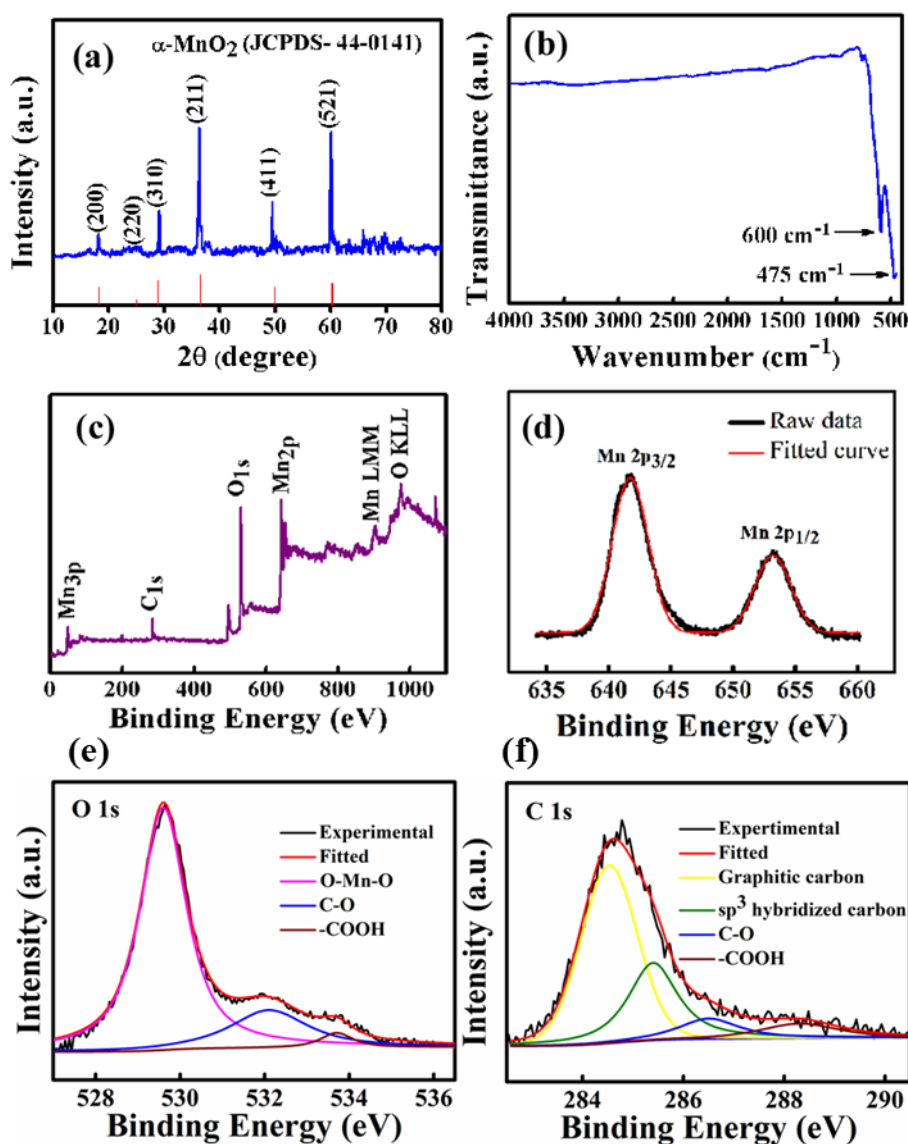
Figure 5.2.1: (a) XRD-pattern of the synthesized sample (b) FTIR spectrum of the sample (c) XPS survey scan of the sample. High resolution scan of (d) Mn 2p peak (e) O 1s (f) C 1s.

XRD of the powdered sample is performed using Rigaku Miniflex diffractometer with CuK$_\alpha$ radiation. XRD pattern of the sample (figure 5.2.1 (a)) shows the characteristic diffraction peak for single-phase α-MnO$_2$ (JCPDS-44-0141) [23]. The sharp peaks indicate good crystallinity of the sample. No other impurity peak indicates the successful synthesis of single-phase α-MnO$_2$.

Fourier transformed infrared (FT-IR) spectrum of the sample is presented in figure 5.2.1 (b). Two strong absorption peaks at 475 cm^{-1} and 600 cm^{-1} resemble the stretching vibration of O-Mn-O, indicating the presence of MnO_2 [24]. A small peak near 1000 cm^{-1} is may be due to the graphitic C-O vibration, which arises due to the presence of oxygenated functional groups on the carbonaceous fiber [25]. These groups may have formed during the annealing procedure due to the presence of small amount of oxygen in the vacuum furnace. A broad absorption peak near 3000 cm^{-1} corresponds to the stretching vibration of the H-O-H bond, suggesting the presence of a small amount of absorbed water in the sample.

Material composition on the sample surface is studied by X-ray photoelectron spectroscopy (XPS). Figure 5.2.1 (c) shows the survey scan of the sample, which shows the presence of Mn, O, and C on the sample. The presence of carbon is due to the formation of carbonaceous fiber resulting from the annealing of the polymer. The element Mn shows two photoelectric peaks, namely Mn 2p and Mn 3p, and one Auger peak at 902.6 eV (Mn LMM). Figure 5.2.1 (d) shows the high-resolution core-level spectrum of Mn 2p peak, which splits significantly due to spin-orbit interaction. The peak at 641.8 eV corresponds to Mn $2p_{3/2,}$ and the peak at 653.5 eV corresponds to Mn $2p_{1/2}$ with a separation of 11.7 eV between them, which suggests that Mn is in +4 oxidation state [26]. This separation value matches well with the existing literature. The deconvoluted spectra due to O 1s and C 1s are shown in figures 5.2.1 (e) and 5.2.1 (f), respectively. The O 1s spectrum can be deconvoluted into three peaks which are due to O-Mn-O (529.3 eV), C-O (532.4 eV), and –COOH (533.7 eV) groups. The deconvoluted C 1s spectrum shows the presence of graphitic carbon, sp^3 hybridized carbon, along with the C-O and –COOH bonds [27]. Thus XPS confirms the successful formation of MnO_2/Carbon fiber.

Figure 5.2.2 (a) and 5.2.2 (b) shows the field emission scanning electron microscopy ((FESEM (FEI Quanta FEG 200))) images of the fibrous sample before and after annealing, respectively. The annealed microfiber shows an average diameter of 5 μm. This fibrous nature of the sample effectively connects the individual redox-active sites and increases the electrolyte accessibility.

Energy dispersive X-ray spectroscopy (EDS) (figure 5.2.2 (c)) of the sample again confirms the presence of Mn and O on the sample with atomic percentage ratio
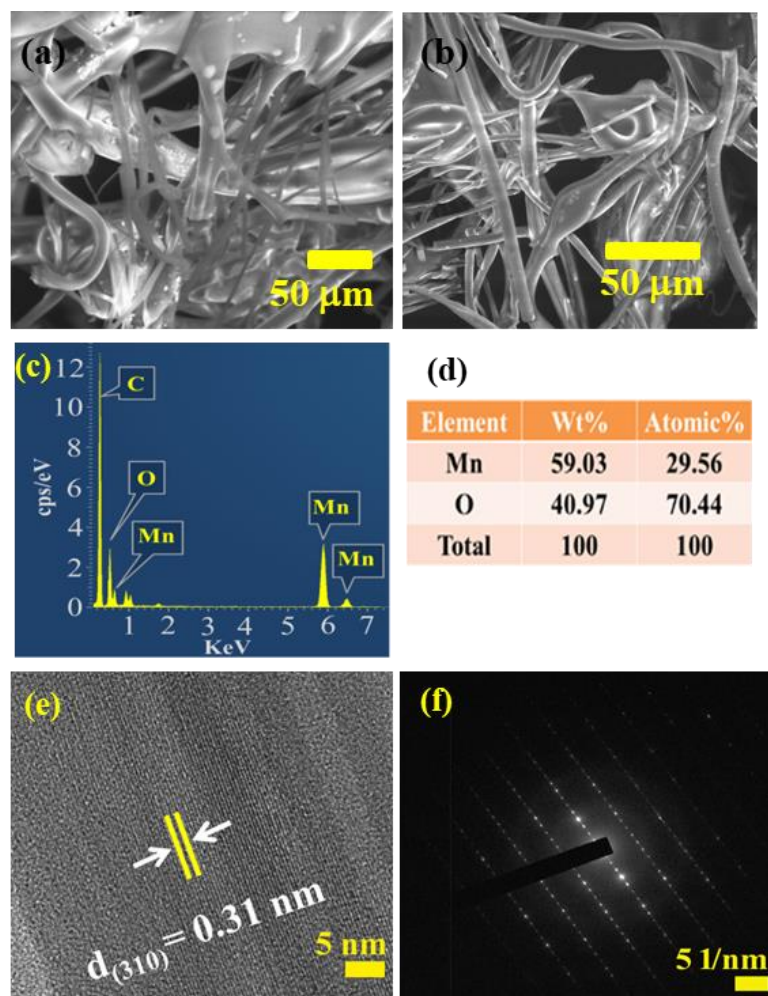
Figure 5.2.2: FESEM images of the fiber (a) before and (b) after annealing. (c) EDS spectroscopy of the fiber (d) Percentages of different elements as obtained from EDS (e) HRTEM image of the sample (f) SAED pattern of the sample

of Mn:O as 1:2.3 (as shown in figure 5.2.2 (d)), which closely resembles the atomic percentage ratio of that of the elements in MnO_2. The slightly higher value of the oxygen percentage is may be due to the additional oxygenated functional groups linked to the carbonized fiber as already concluded from XPS.

A lattice fringe spacing of 0.31 nm is obtained from the high-resolution transmission electron microscope (HRTEM) image of the sample (figure 5.2.2 (e)), which corresponds to the interplanar spacing of the (310) plane of α-MnO_2. Figure 5.2.2 (f) shows the selected area electron diffraction (SAED) pattern of the sample, which confirms the single-crystalline nature of the synthesized fiber [28].

After confirming the formation of single-phase MnO_2 fiber, the sample is investigated for electrochemical charge storage application. All the electrochemical

measurements are performed using CS131 (Corrtest, China) electrochemical workstation in a three-electrode setup. The counter and the reference electrode are platinum plate (1 cm x 1 cm) and Ag/AgCl in saturated KCl. 1M aqueous Na_2SO_4 is used as an electrolyte for all the electrochemical measurements. The fibrous sample is coated on a teflon coated graphite rod with a binder PVDF which acted as the
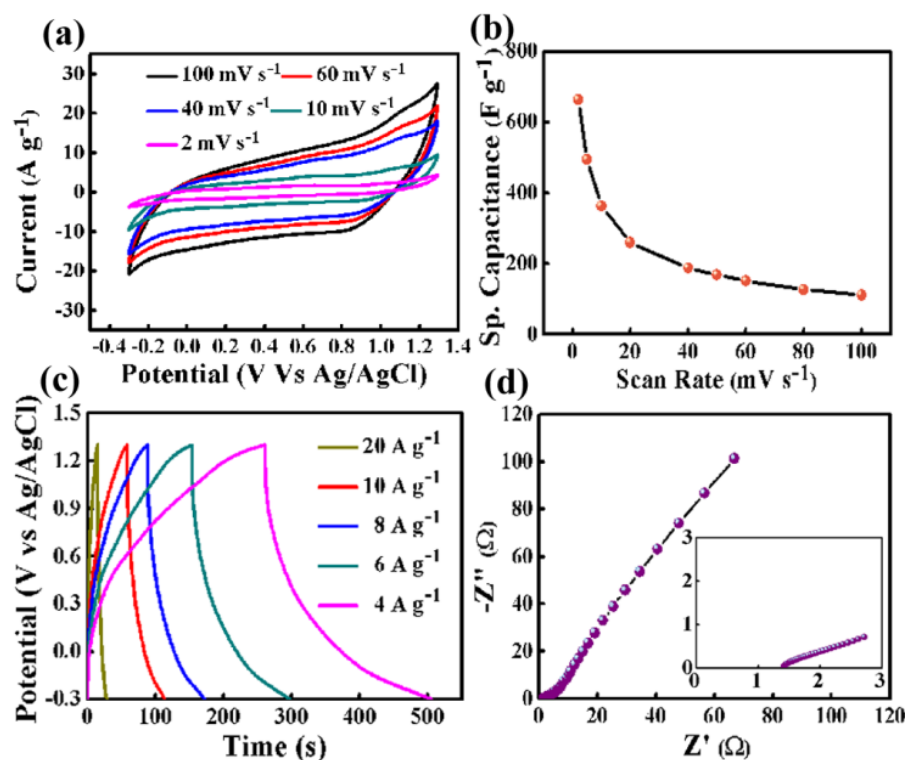
Figure 5.2.3: (a) CV plots at different scan rates (b) Specific capacitance vs. scan rate plot (c) GCD curves at different current densities (d) Impedance spectra for the sample (inset) the high frequency region for the impedance spectra.

working electrode. Figure 5.2.3 (a) shows the cyclic voltammetry (CV) curves within a potential window of -0.3 V to 1.3 V at different scan rates. The wide potential window allows the sample to store a large quantity of energy. The CV curves maintain their quasi-rectangular shape during all the potential sweeps at different scan rates. This suggests the microfiber can participate in the reversible redox reaction even at a very low scan rate. The specific capacitance (C_m) is calculated by using the equation (2.3.1). The highest specific capacitance of 663 F g^{-1} is obtained at the potential scan rate of 2 mV s^{-1}. Reduction in specific capacitance values can be seen with the increase in scan rate from the specific capacitance vs. scan rate plot in figure 5.2.3 (b). At a lower scan rate, the electrolyte ions can access a huge number of active sites. However, at a higher scan rate, because of the fast movement of the electrolyte ions, the specific capacitance is mainly dominated by the physical charge absorption

120

process on the surface of the electrode material. Figure 5.2.3 (c) shows the Galvanostatic charge discharge (GCD) profile of the sample at different current densities in the same aqueous 1M Na_2SO_4 electrolyte within the similar potential window of 1.6 V. The GCD curves deviate from the ideal triangular shape, which suggests that redox reaction contributes to the charge storing mechanism. A sharp fall can be observed in the GCD profile at the commencement of the discharge. This corresponds to the Ohomic drop due to the imperfect connection of the electrode material with the current collector (graphite rod) and due to the resistance of the electrolyte. The specific capacitances are calculated at different current densities using the equation (2.3.3). The maximum specific capacitance of 612 F g^{-1} is obtained at the lowest current density of 4 A g^{-1}. Electrochemical impedance spectroscopy of the material is performed under a similar three-electrode configuration with AC perturbation voltage of 10 mV within 0.01 Hz to 100 kHz. Figure 5.2.3 (d) shows the Nyquist spectrum of the sample. The high-frequency region has been shown in the inset of figure 5.2.3 (d), which intercepts the real axis at 1.4 Ω. This resistance is the series resistance R_s which arises mainly due to the imperfect connection of the electrode material with the current collector. The effect of R_s is observed in the GCD curves as ohmic drop. Considering only MnO_2, the ordered sample offers relatively low R_s.

A two-electrode device is fabricated using the MnO_2 microfiber as the positrode and activated carbon as the negatrode coated on steel current collector of dimension 2 cm x 3 cm. A Whatman filter paper (25 μm pore size) socked in 1M Na_2SO_4 is used as a separator. Figure 5.2.4 (a) shows the CV diagram for the device at 100 mV s^{-1} scan rate for different potential windows. The device can be operated at a higher potential window up to 1.8 V. However, to remain on the safer side, the whole electrochemical measurements for the device were carried out at a potential window of 1.6 V. Figure 5.2.4 (b) shows the CV diagrams for different scan rates at a potential window of 1.6 V. A highest specific capacitance of 135.6 F g^{-1} is obtained from the CV diagram at a scan rate of 2 mV s^{-1}. The variation of specific capacitance with scan rate has been demonstrated in figure 5.2.4 (c). The usual decrease of specific capacitance is observed with the increase in the scan rate. The quasi-triangular GCD profile of the device at various current densities is shown in figure 5.2.4 (d). A little IR drop at the beginning of the discharge is observed, which is
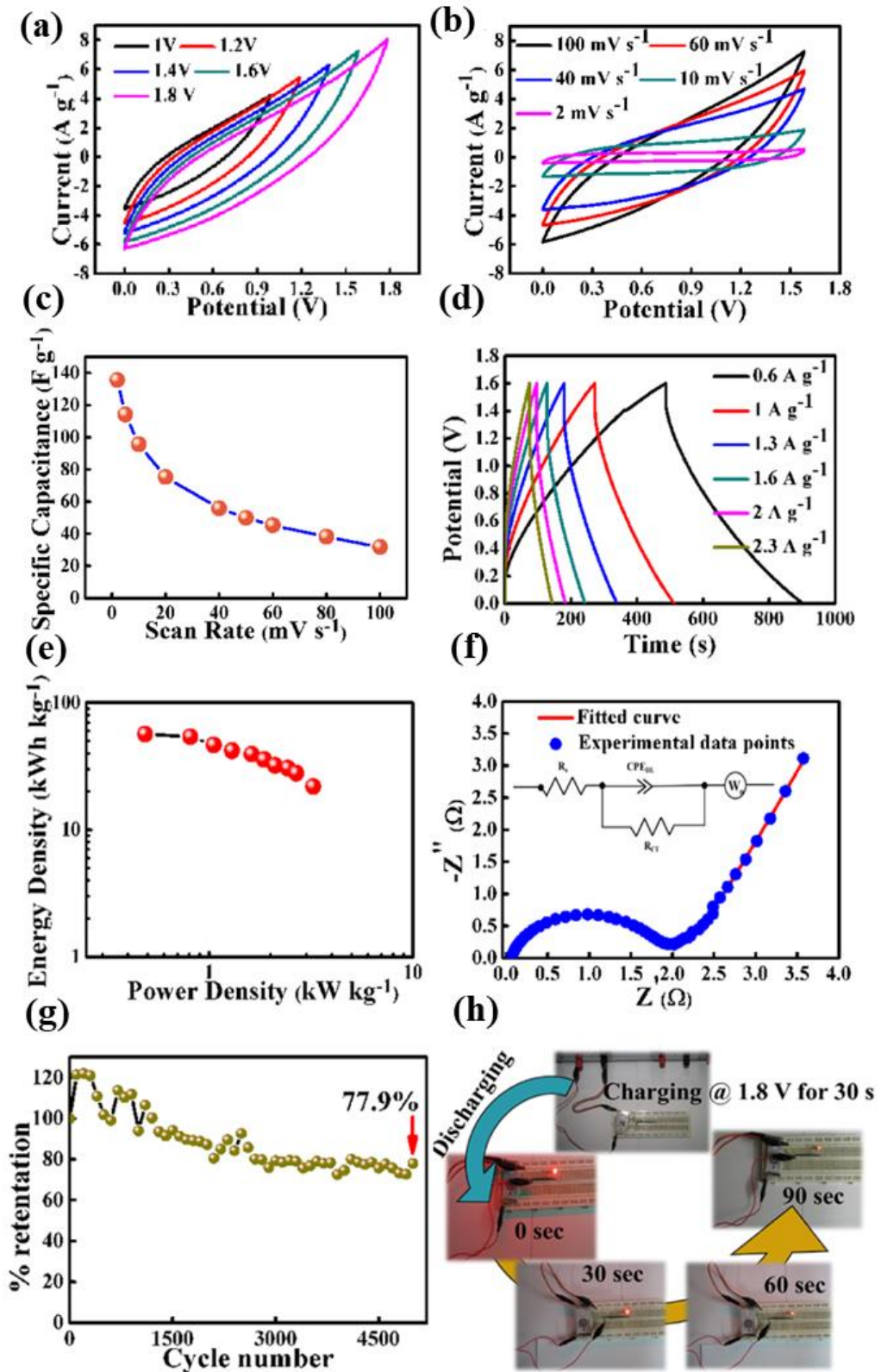
Figure 5.2.4: (a) CV plots at 100 mV s^{-1} for different potential windows (b) CV plots for 1.6 V potential window at different scan rates (c) Variation of specific capacitance with different scan rates (d) GCD plots at different current densities (e) Ragone plot (f) EIS Nyquist plot for the device (g) Long cyclic performance test for the device (h) State of device charging and discharging through LED

mainly due to the lack of proper contact of the microfiber with the current collector. Using the equation (2.3.3) specific capacitance of the device is also calculated at different current densities. A maximum specific capacitance of 110 F g^{-1} is obtained at a current density of 0.6 A g^{-1}. The specific energy and power density of the device were calculated at various current densities following equation (2.5.1) and equation (2.5.2). Figure 5.2.4 (e) shows the variation of energy density with power density (Ragone plot). The device demonstrates a peak power density of 3.2 kW kg^{-1} at a current density of 4 A g^{-1} and highest energy density of 56.7 Wh kg^{-1} at a current density of 0.6 A g^{-1}. The dynamic response of the device was obtained by performing the EIS at 0 V potential with ac perturbation potential of 10 mV within the frequency 0.01 Hz to 105 Hz. The figure 5.2.4 (f) shows the EIS of the device in terms of the Nyquist plot. The plot has been fitted using Zview software. The equivalent circuit has been shown in the inset of the figure 5.2.4 (f). The device offers low contact resistance of 0.06 Ω and low charge transfer resistance of 1.62 Ω. The cycling performance of the device is demonstrated by performing 5000 GCD cycles (figure 5.2.4 (g)), at the end of which, the device retained 77.9% of its initial capacitance. The device is used to power a red LED for more than 90 s after charging for only 30 s. Different states of charging and discharging have been shown in the figure 5.2.4 (h).

Thus RJ-spin can be used to fabricate metal oxide microfiber for application in the electrodes of future energy storage devices. Further, there are ample opportunities to utilize the technique to produce fiber of different metal-oxide and their composites with different carbonaceous materials. A detailed study of such a kind can improve the performance of the electrodes significantly. The scalability, production yield capability, and ease of synthesis could make the RJ-spin technique to be widely accepted in the industry.

5.3 Hydrothermally synthesized NiMn$_2$O$_4$

As concluded from the previous results and discussions, morphology plays a vital role in the overall charge storage performance of electrode material. Single metal oxides like MnO$_2$ offer relatively high resistance to current flow, which hampers the charge storage performance. Bimetal oxides, on the other hand, offer comparatively
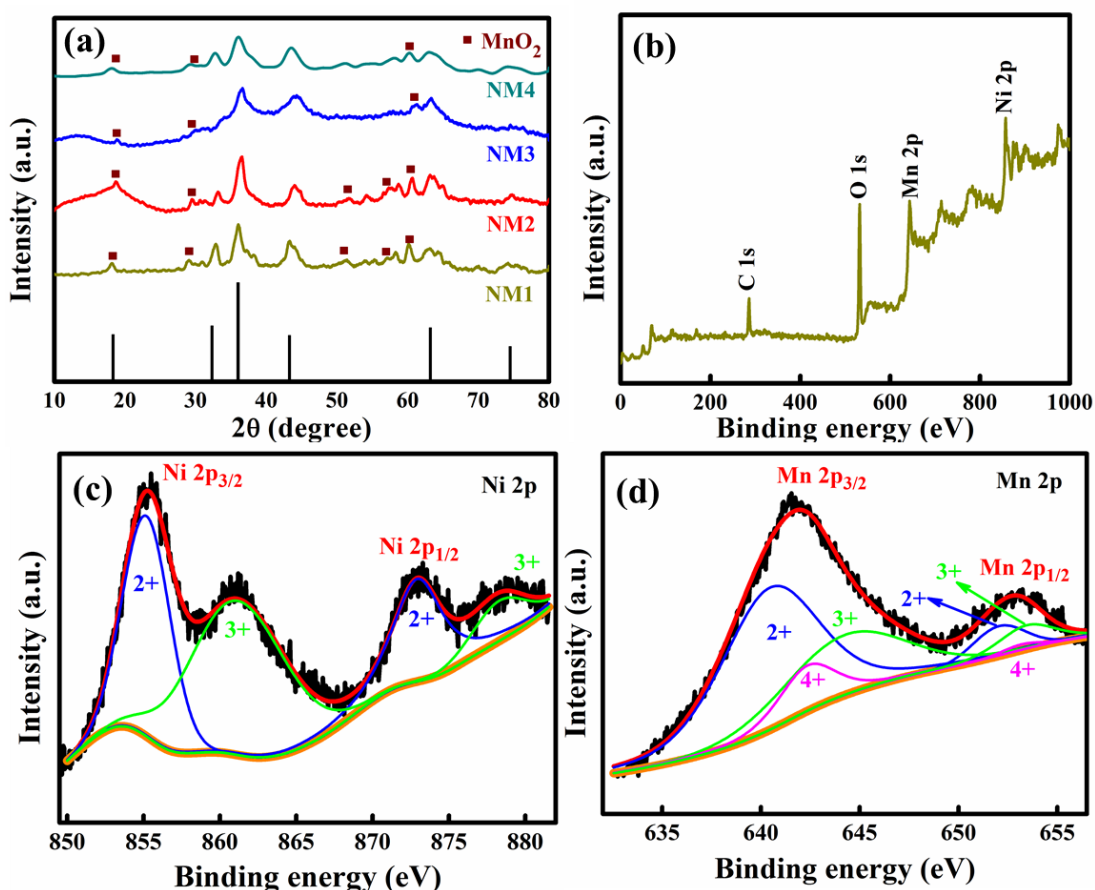
Figure 5.3.1: (a) XRD patterns of the samples. (b) XPS survey spectrum of the sample NM3. Core level XPS spectrum of (c) Ni 2p and (d) Mn 2p

good conductivity, and hence charge storage performance improves. In this section, we have discussed the results of different characterizations of the bimetallic oxide NiMn$_2$O$_4$. The synthesis of this material has already been discussed in the previous chapter. During the synthesis, we have utilized different surfactants to prepare morphologically different variants of NiMn$_2$O$_4$ to understand the effect of morphology on the electrochemical charge storage performance of this bimetallic oxide. Four different samples were prepared, the details of which are given in the previous chapter.

Figure 5.3.1 (a) shows the XRD patterns for all four samples all of which are nearly identical to each other. All the five highly intense peaks are found to match with the standard $NiMn_2O_4$ patterns (JCPDS no.71-0852). The diffraction peaks at 2θ = 18.3°, 36°, 43.25°, 63.2° and 74.5° correspond to the (1 1 1), (3 1 1), (4 0 0), (4 4 0) and (5 3 3) planes of $NiMn_2O_4$ [29-32]. The positions of all the diffraction peaks suggest that all the samples have the standard single-phase spinel structure of $NiMn_2O_4$ which belongs to the space group Fd-3m [33]. XRD of each sample also shows the presence of by-product phase α-MnO_2, which may have formed either at the time of increase of temperature or due to minor fluctuation of the temperature inside the reaction vessel during the reaction. The by-product phase has been indicated by a marker in figure 5.3.1 (a) according to the JCPDS no. 44-0141 [34]. However, the intensity of the XRD peaks due to the by-product phase is relatively weak compared to $NiMn_2O_4$, suggesting a little presence of α-MnO_2 in the sample.

X-ray photoelectron spectroscopy (XPS) is employed to find the surface elemental composition of the sample, which demonstrates the best electrochemical performance (NM3). Figure 5.3.1 (b) shows the survey spectrum of the NM3 sample. The presence of carbon, oxygen, manganese, and nickel can be seen from the survey. Figure 5.3.1 (c) shows the high-resolution core level scan of the Ni 2p peak, which splits into two peaks due to spin-orbit coupling. The peak at binding energy 854.9 eV corresponds to Ni $2p_{3/2}$, and the peak at binding energy 872.7 eV corresponds to Ni $2p_{1/2}$. Binding energy separation of 17.8 eV between these two peaks, along with the presence of two satellite peaks at 861.1 eV and 872.3 eV agree well with the literature [35]. The deconvoluted Ni 2p spectrum shows the presence of four peaks. Peaks at 855.2 eV and 872.6 eV can be consigned to the Ni^{2+} state, and peaks at 861.1 eV and 878.8 eV can be assigned to the Ni^{3+} state [36]. Figure 5.3.1 (d) shows the high-resolution Mn 2p spectrum having a spin-orbit doublet with binding energies of 653.4 eV (Mn $2p_{1/2}$) and 641.6 eV (Mn $2p_{3/2}$). Deconvolution of the Mn 2p spectrum resulted in six peaks. Among these, four peaks are relatively strong. The fitted peaks at 640.5 eV and 652.2 eV are linked to the Mn^{2+} state. The other two peaks at 644.4 eV and 653.4 eV can be attributed to the Mn^{3+} state. Two weak peaks at 642.4 eV and 653.5 eV are due to Mn^{4+} state, which arises due to the presence of a little amount of MnO_2 in the NM3 sample as confirmed by the XRD study [35, 37].
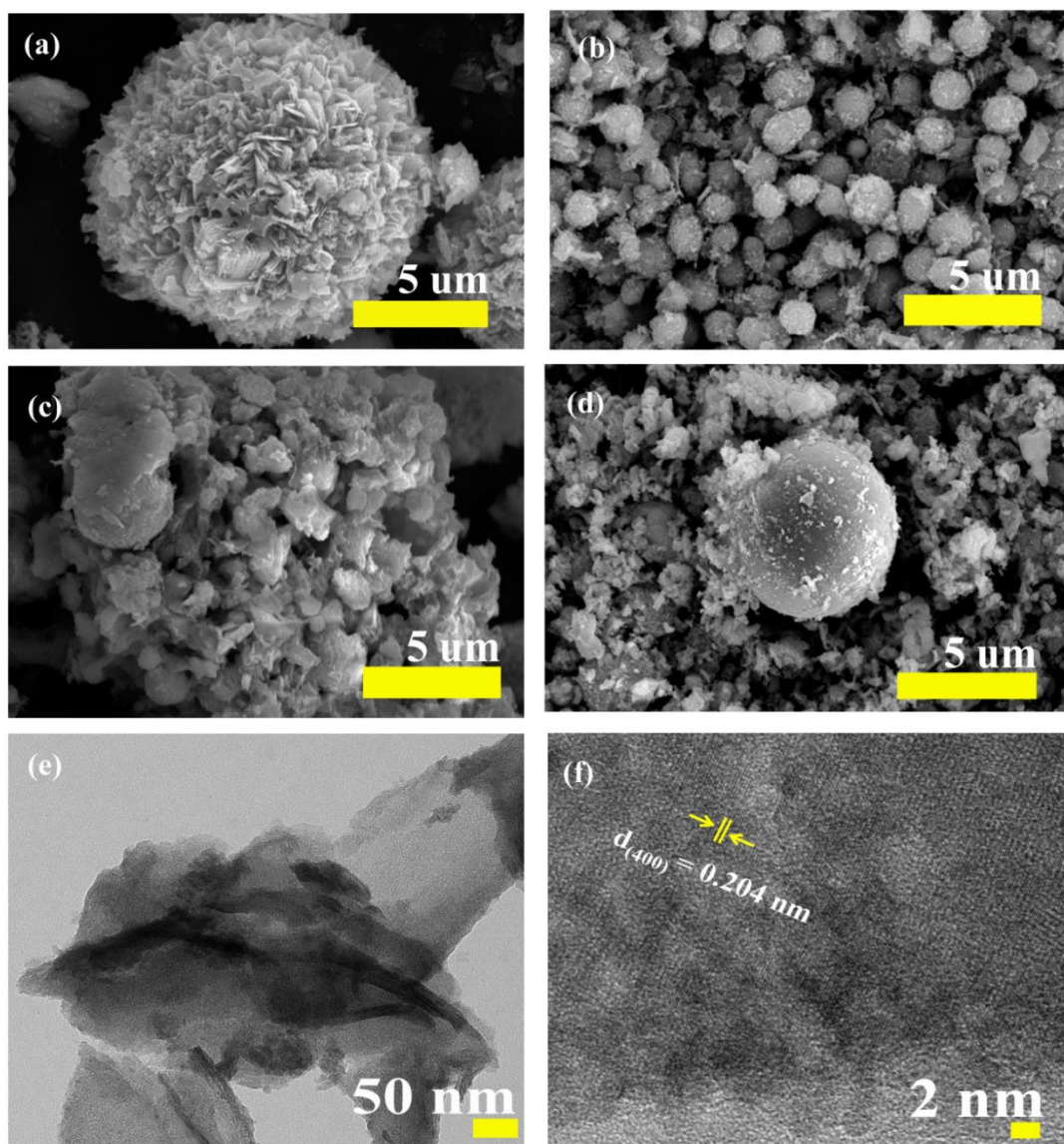
Figure 5.3.2: SEM images of (a) NM1 (b) NM2 (c) NM3 and (d) NM4. (e) TEM image of NM3 (f) HRTEM image of NM3

Figure 5.3.2 (a) shows the spherically shaped NM1 particles prepared using NH_4F as a mineralizer. The addition of NH_4F in the reaction medium results in the formation of F^- ions which form strong coordination with the Mn^{2+} and Ni^{2+} ions already present in the reaction mixture. Because of this coordination, the number of free ions to form the NiMn-oxide reduces, which in turn decreases the number of nuclei for the reaction. This results in the formation of a large NM1 microsphere [38]. Dissociation of NH_4F in the reaction medium results in the formation of HF acid. Due to the etching effect of HF, the microsphere of NM1 shows a rough surface [39]. Spherically shaped NM2 particles are shown in figure 5.3.2 (b). CTAB has been used in the synthesis of NM2, which acts as a cationic surfactant. CTAB concentration

chosen for the synthesis results in the formation of positively charged spherical micelles in the reaction medium. Due to the presence of long-chain and the cationic nature of the head group in CTAB, the ions cannot get close to each other. Hence, due to the repulsion between the positively charged micelles, the agglomeration of the ions is prevented. The ions get entrapped uniformly in the micelles so that after the reaction spherical nature of NM2 is obtained [40]. The small diameter of NM2 compared to the other variants of NM also reflects this repulsive interaction. Figure 5.3.2 (c) shows the interconnected morphology of the NM3, which has been synthesized using SDS. SDS is an anionic surfactant that forms negatively charged spherical micelles in the reaction medium. Because of the smaller size and the anionic nature of the micelles, the ions can get closer to each other. Thus due to the attraction between the micelles and the ions, large agglomeration can be formed, which results in an interconnected morphology [41]. This type of morphology effectively connects the different redox-active sites and thus demonstrates the best electrochemical charge storage performances. Figure 5.3.2 (d) shows the quasi-sphere of the NM4 sample synthesized through glucose-assisted hydrothermal reaction. Well disperse carbon spheres are formed due to the hydrothermal carbonization reaction of glucose [42]. The –OH and –CHO groups present on the carbon sphere results in the binding of Ni^{2+} and Mn^{2+} ions on the surface during the reaction. When the samples are annealed in open air the carbon escapes and spherical quasi-particles are formed [43]. Figure 5.3.2 (e) shows the TEM image of the NM3 sample, which clearly shows the interconnected nature of the sample. Figure 5.3.2 (f) shows the HRTEM image of the NM3 sample, which demonstrates the lattice fringe spacing of 0.204 nm, which corresponds to the (400) plane of $NiMn_2O_4$ [36, 44].

Nitrogen adsorption/desorption isotherms of the composites are shown in Figure 5.3.3. NLDFT method has been used to determine the pore size distribution of the individual composite. The inset of the individual plots shows the pore size distribution of the corresponding sample. The specific surface area and the pore width of the individual samples have been listed in Table 5.3.1. We have obtained a maximum specific surface area of 59.9 m^2 g^{-1} for sample NM3 and a minimum specific area of 10.6 m^2 g^{-1} for the sample NM4. The higher surface area of the composite allows a large number of active sites for the electrolyte ions to perform the redox reaction. This ensures rapid charge transfer at the electrode surface during the
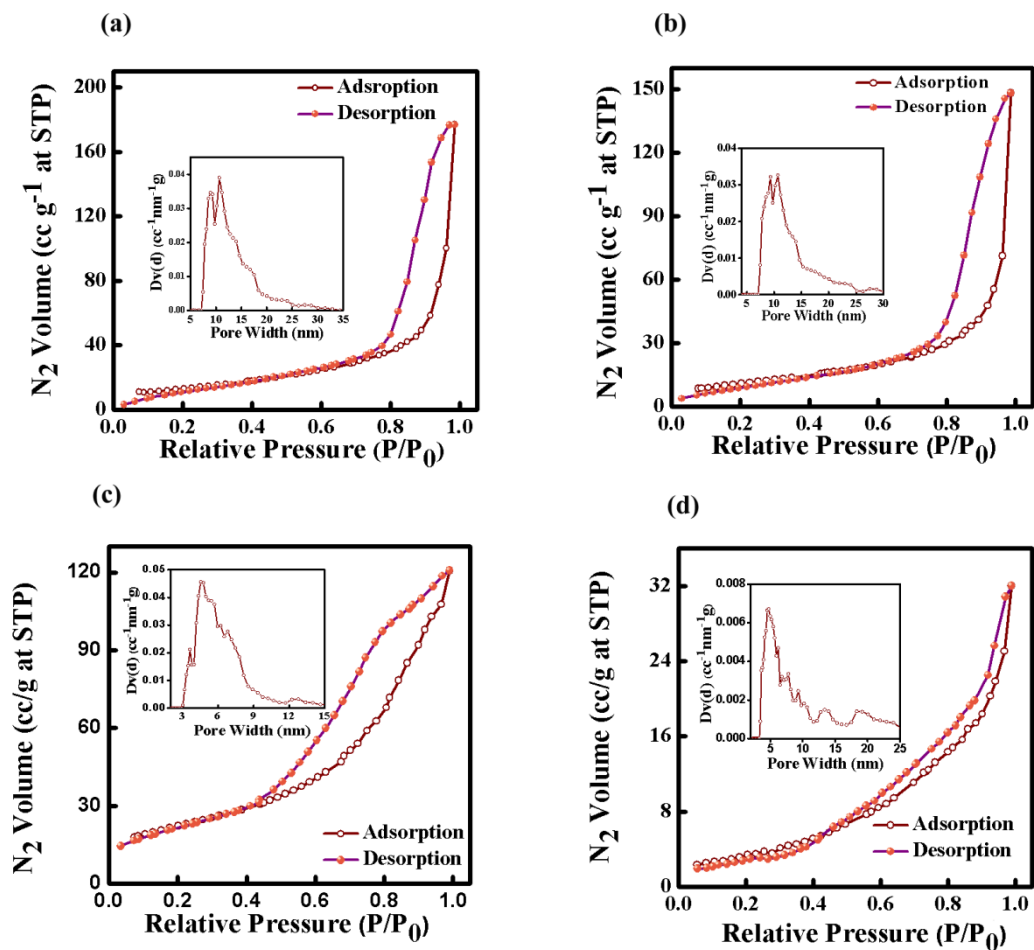
Figure 5.3.3: N$_2$ adsorption and desorption isotherms of (a) NM1 (b) NM2 (c) NM3 (4) NM4 with pore size distribution (Inset)

electrochemical process [45, 46]. For this reason, we have obtained maximum specific capacitance for the sample NM3 and minimum for NM4, which has further been discussed in the electrochemical analysis section.

Table 5.3.1: Parameters associated with BET for the different samples.

Sample name	Surface area (m^2 g^{-1})	Pore width (nm)
NM1	43.813	10.681
NM2	36.559	10.681
NM3	59.910	4.543
NM4	10.675	4.752
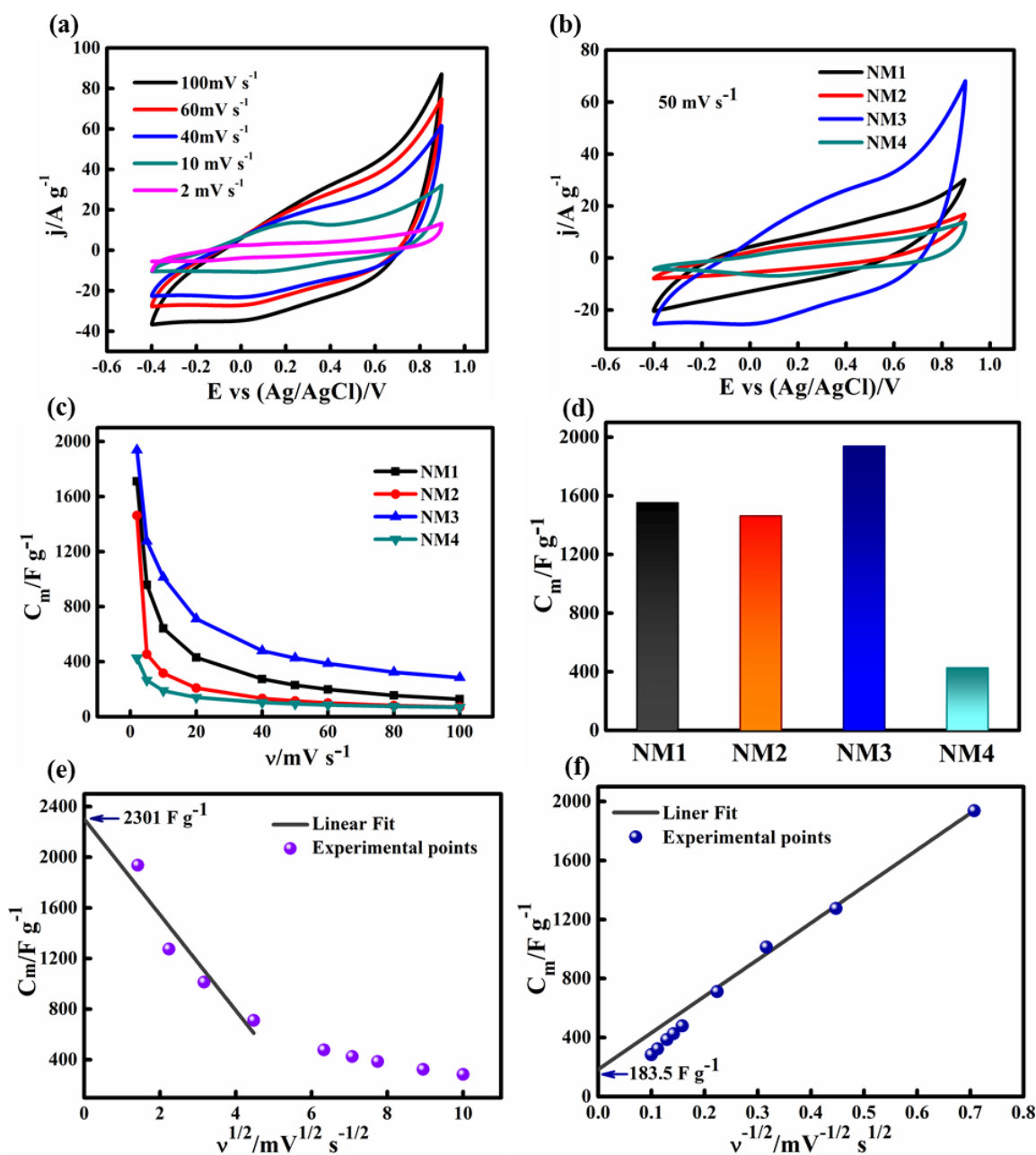
Figure 5.3.4: (a) CV curves at different scan rates for NM3, (b) comparison of CV curves at 50 mV s⁻¹ scan rate for the different samples, (c) specific capacitance vs. scan rate plot for the different samples, (d) bar diagram of maximum specific capacitance for the different samples obtained at 2 mV s⁻¹, (e) plot of specific capacitance vs. square root of scan rate for NM3 and (f) plot of specific capacitance vs. inverse square root of scan rate for NM3

Because of the higher specific surface area than the other composites and interconnected mesoporous structure, we have obtained the highest specific capacitance for the sample NM3 Figure 5.3.4 (a) shows the CV curves for the composite NM3 at different scan rates. The composite offers a window of 1.3 V. The

presence of redox waves along with the deviation from the ideal rectangular shape of the CV curves suggests that the storage mechanism is due to the combined contribution of the double-layer and Faradaic redox capacitances [47, 48]. In addition, there was no gas evolution observed at the electrode at the boundaries of sweep potential, suggesting that the sample possesses good stability in the wide potential window. Figure 5.3.b (b) shows the comparison of CV curves for different samples at 50 mV s^{-1} scan rate. The sample NM4 encloses the smallest area in the CV curve, whereas NM3 encloses the highest area. As the specific capacitance is proportional to the area enclosed thus, NM3 offers the highest specific capacitance, and NM4 shows the lowest specific capacitance. We have calculated the specific capacitance from the CV curves using equation (2.3.1). Figure 5.3.4 (c) shows the variation of specific capacitance with the scan rate for the different samples. It can be seen that the specific capacitance decreases with the increasing scan rate. The variation of specific capacitance with scan rates depends mainly on three processes: (a) charge transfer in the electrode, (b) ion diffusion in the electrolyte, and (c) surface adsorptions of the ions on the surface of the electrode materials [49]. At higher scan rates, all these processes become slow, and thus specific capacitance decreases. However, at lower scan rates, the ions get sufficient time to penetrate deep into the inner active sites. Thus, both the inner and outer active sites of the electrode material contribute to the total specific capacitance and hence specific capacitance reaches a maximum at a low scan rate and gradually decreases with the increasing scan rate. Figure 5.3.4 (d) shows the bar diagram of the maximum specific capacitance for different samples at 2 mV s^{-1}. NM3 offers the highest specific capacitance of 1937 F g^{-1}, and NM4 offers the lowest specific capacitance of 426 F g^{-1}. It is interesting to note that these variations of specific capacitance with the sample actually follow the BET surface area result (Table 5.3.1). Total specific capacitance offered by the electrode material can be written as a sum of two different contributions as expressed by equation (5.3.1) [50, 51]

$$C_T = C_{in} + C_{out} \hspace{4cm} (5.3.1)$$

Where C_T is the total specific capacitance, C_{in} is the specific capacitance due to the faradaic reaction, which mainly occurs in the inner side of the electrode, and C_{out} is the specific capacitance due to double layer contribution, which mainly occurs at the interface of the electrode and the electrolyte. At higher scan rates, the charge storage

depends mainly on the outer surface because of the shortage of time for the ion diffusion to happen inside the pores of the material. Thus C_{out} mainly involves the contribution due to the double layer mechanism. At very low scan rates ($v \rightarrow 0$), however, both faradic and double layer mechanisms contribute to the total charge capacity. Thus total capacitance can be obtained by extending the specific capacitance vs. $v^{\frac{1}{2}}$ curve to $v = 0$ as shown in Figure 5.3.4 (e). And the contribution due to the outer surface can be found out by extrapolating the plot of specific capacitance vs. $v^{-\frac{1}{2}}$ to $v \rightarrow \infty$ (i.e. $v^{-\frac{1}{2}} \rightarrow 0$) (Figure 5.3.4 (f)). We have obtained total specific capacitance $C_T = 2301$ F g^{-1} and specific capacitance due to the outer contribution C_{out} = 183.5 F g^{-1}. Hence, from equation (5.3.1), we have obtained the inner contribution to the capacitance C_{in} = 2117.5 F g^{-1}. The higher value of inner contribution to the specific capacitance suggests that the redox reaction plays a dominating role in storing the charges. Here it is worth mentioning that during the two linear fittings done in both figures 5.3.4 (e) and 5.3.4 (f) we have used the data for low scan rates only, and the higher scan rate region was avoided. This is because of the fact that at a higher scan rate, Ohmic drop becomes significant, which introduces nonlinearity in the respective plots [52].

Galvanostatic Charge Discharge (GCD) is another important tool to measure the electrochemical charge storage capability of the electrode material. Figure 5.3.5
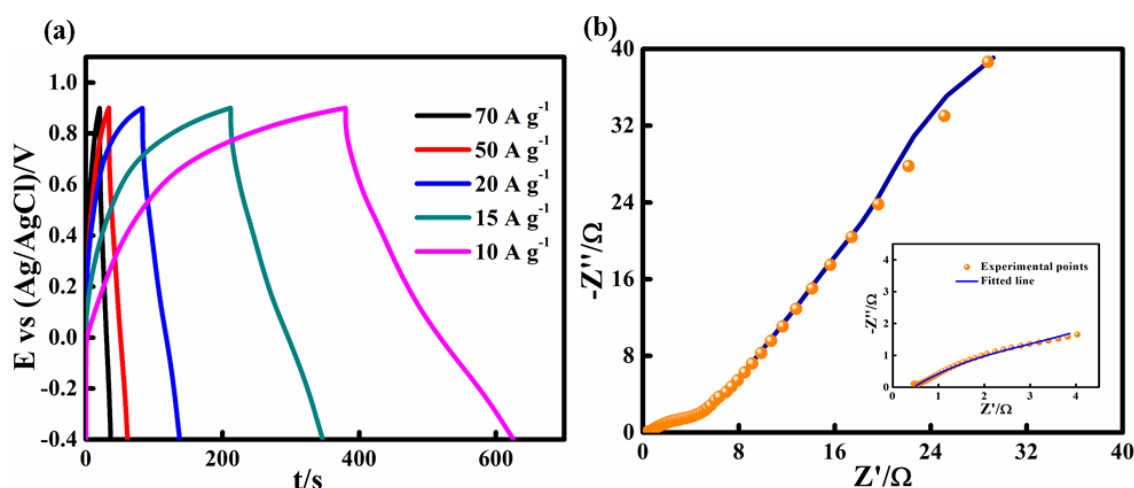

Figure 5.3.5: (a) Galvanostatic charge discharge curves at different current densities for NM3. (b) Electrochemical impedance spectroscopy of the NM3. Inset: the high frequency region of the impedance spectroscopy of the same composite along with the circuit used to fit the impedance spectroscopy data.

(a) shows the GCD profile for the NM3 electrode in 1 M Na_2SO_4 electrolyte within the same potential window as CV at different current densities. The GCD plot deviates significantly from the ideal triangular shape, which again suggests the domination of redox activity. $NiMn_2O_4$ offers large redox capacitance, which is believed to be due to the intercalation/de-intercalation of Na^+ ions from the electrolyte into the $NiMn_2O_4$ matrix as given in equation (5.3.2).

$$NiMn_2O_4 + Na^+ + e^- \leftrightarrow NaNiMn_2O_4 \tag{5.3.2}$$

Table 5.3.2: Comparison of specific capacitance with some reported results.

Serial No.	Electrode material	3-electrode specific capacitance	References
1	$NiMn_2O_4$	202 F g^{-1} @ 0.5 mA cm^{-2}	[50]
2	$NiMn_2O_4$ microsphere	768.9 F g^{-1} @ 1 A g^{-1}	[35]
3	$NiMn_2O_4$/rGO hydrogel	392.3 F g^{-1} @ 1A g^{-1}	[37]
4	$NiMn_2O_4$/rGO/PANI	757 F g^{-1} @ 1 A g^{-1}	[54]
5	$NiMn_2O_4$/C-sphere	470.7 @ 1 A g^{-1}	[55]
6	$NiMn_2O_4$ on Ni-foam	662.5 F g^{-1} @ 1 A g^{-1}	[56]
7	$NiMn_2O_4$ on 3D N_2 doped graphene	1308.2 F g^{-1} @ 1 A g^{-1}	[57]
8	MWCNT blended $NiMnO_3$/$NiMn_2O_4$	1347 F g^{-1} @ 5 A g^{-1}	[58]
9	$NiMn_2O_4$ @ CoS Core−Shell microspheres	1751 F g^{-1} @ 1 A g^{-1}	[59]
10	$NiMn_2O_4$ modified with SDS(NM3)	1937 F g^{-1} @ 2 mV s^{-1} and 1880 F g^{-1} @ 10 A g^{-1}	Present work

On the other hand, because of comparatively low specific surface area (~59.9 m^2 g^{-1}), NM3 cannot store a large quantity of charges via the double-layer formation. Thus redox activity dominates over the physical charge storage mechanism [50]. A very little IR drop can also be observed in the GCD plots at the high current density, proving little resistance and good capacitive properties. This IR drop is mainly due to the poor contact of the electrode material with the current collector and also because of the intrinsic resistance of the electrolyte [53]. We have obtained a specific capacitance value of 1880 F g^{-1} at the lowest current density of 10 A g^{-1} using

equation (2.3.3). In Table 5.3.2, we have compared the specific capacitance value of NM3 with $NiMn_2O_4$, and its different composite-based electrodes reported previously.

Electrochemical impedance spectroscopy (EIS) is a useful technique to obtain information about the charge transfer and electrolyte diffusion dynamics at the electrode-electrolyte interface. EIS was performed within 0.01 Hz to 100 kHz frequency range with an ac perturbation voltage of 10 mV. Figure 5.3.5 (b) shows the Nyquist plot of the NM3 sample. In the high-frequency region, a circular arc can be seen (Figure 5.3.5 (b) (inset)), the diameter of which determines the charge transfer resistance, which has the value of 5.1 Ω. The EIS data have been fitted using the equivalent circuit model using Z-view software. The equivalent circuit has been shown in the inset of Figure 5.3.5 (b). Here R_s is the total internal resistance which is mainly due to poor electrical contact between the electrode material and the current collector. From the fitting, we have obtained the value of R_s as 0.46 Ω. This low internal resistance suggests good power delivery.

A two-electrode asymmetric supercapacitor device has been fabricated using NM3 as the active material. Initially, 85% of the active material, 10% of activated carbon, and 5% of PVDF are well mixed, and then NMP is added to form a gel. A steel plate of dimension 2 cm x 3 cm has been coated with this gel. This plate works as the positrode of the device. A steel plate of similar dimensions coated with activated carbon only is used as the negatrode of the device. A filter paper (25 µm) is used as the separator, and 1M aqueous Na_2SO_4 is used as the electrolyte. Figure 5.3.6 (a) shows the schematic of the device. Figure 5.3.6 (b) represents the CV curves at different potential windows at 100 mV s^{-1} scan rate. No sharp water splitting current peak is observed over these different potential windows, which suggests that the device can be operated within 2 V potential window. This is mainly because of the fact that $NiMn_2O_4$ shows a high overpotential for oxygen evolution reaction [60]. The combination of this suitable positive electrode along with the activated carbon-based negative electrode increases the operating window of the device. However, to remain on the safer side, the whole device characterizations were performed at a 1.8 V window. Figure 5.3.6 (b) shows the CV curves within1.8 V potential window for different scan rates. The CV curves are nearly rectangular down to a low scan rate which suggests good supercapacitive behavior. Using equation (2.3.1), we have calculated the specific capacitance of the device, which shows the highest value of 270 F g^{-1} at 2 mV s^{-1} scan rate. Figure 5.3.6 (d) shows the specific capacitance *vs.*
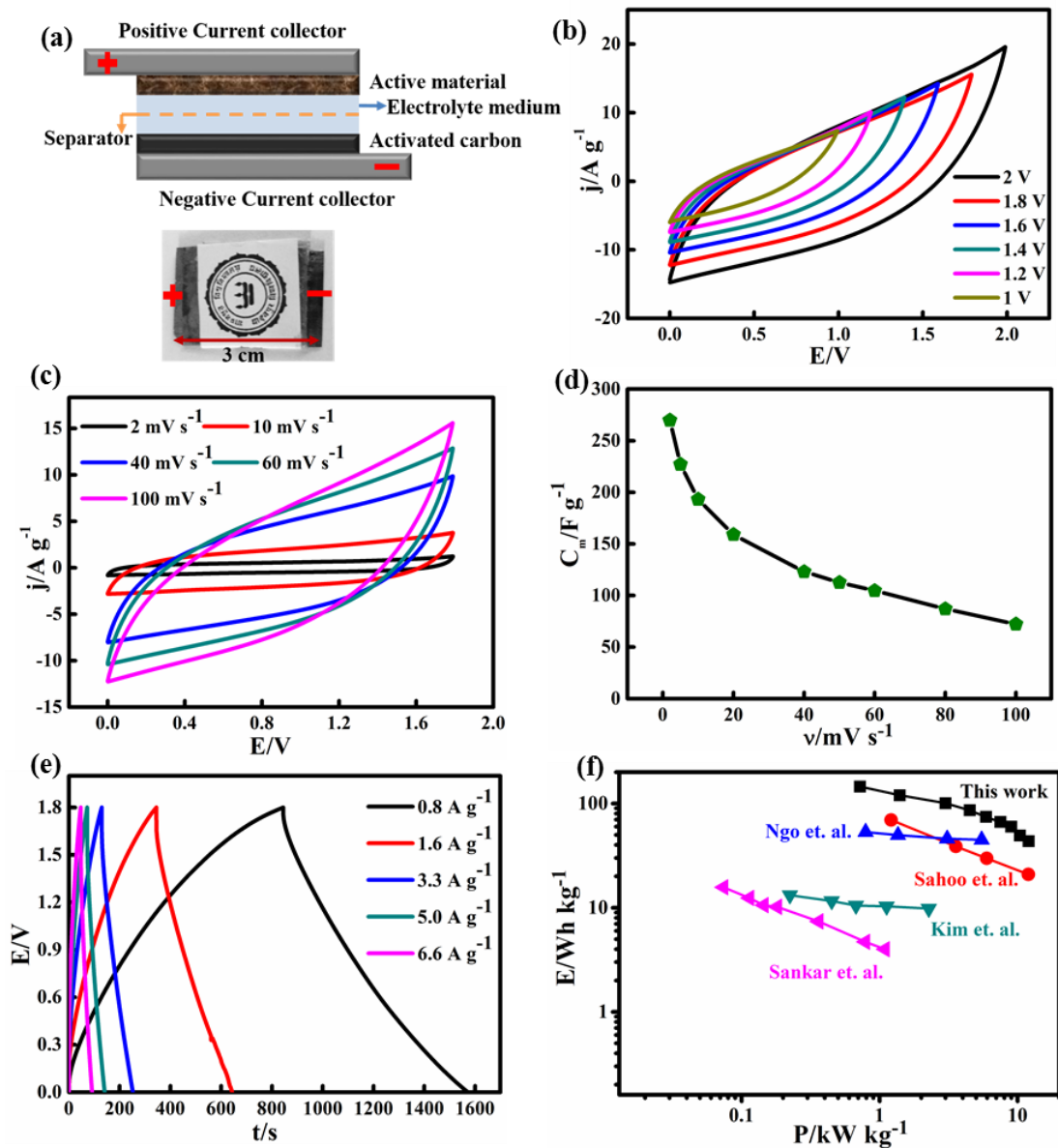
Figure 5.3.6: (a) Schematic of the device (inset: actual device). (b) CV at different window for the two electrode device at 100 mV s^{-1} scan rate. (c) CV at 1.8 V window for different scan rates (d) Specific capacitance vs. scan rates for the two electrode device. (e) GCD at different current densities for 1.8 V window. (f) Ragone plot for the device.

scan rate plot for the device. As can be seen from the figure that specific capacitance decreases with increasing scan rates which is mainly because of the fact that at a low scan rate the electrolyte ions can diffuse through the interior of the active material yielding higher value of specific capacitance. Figure 5.3.6 (e) shows the GCD profile of the device within 1.8 V potential window. The GCD curves show a nearly triangular shape with a very small I.R. drop. We have also calculated the specific capacitance from the GCD profile using equation (2.3.3). We have obtained a specific

134
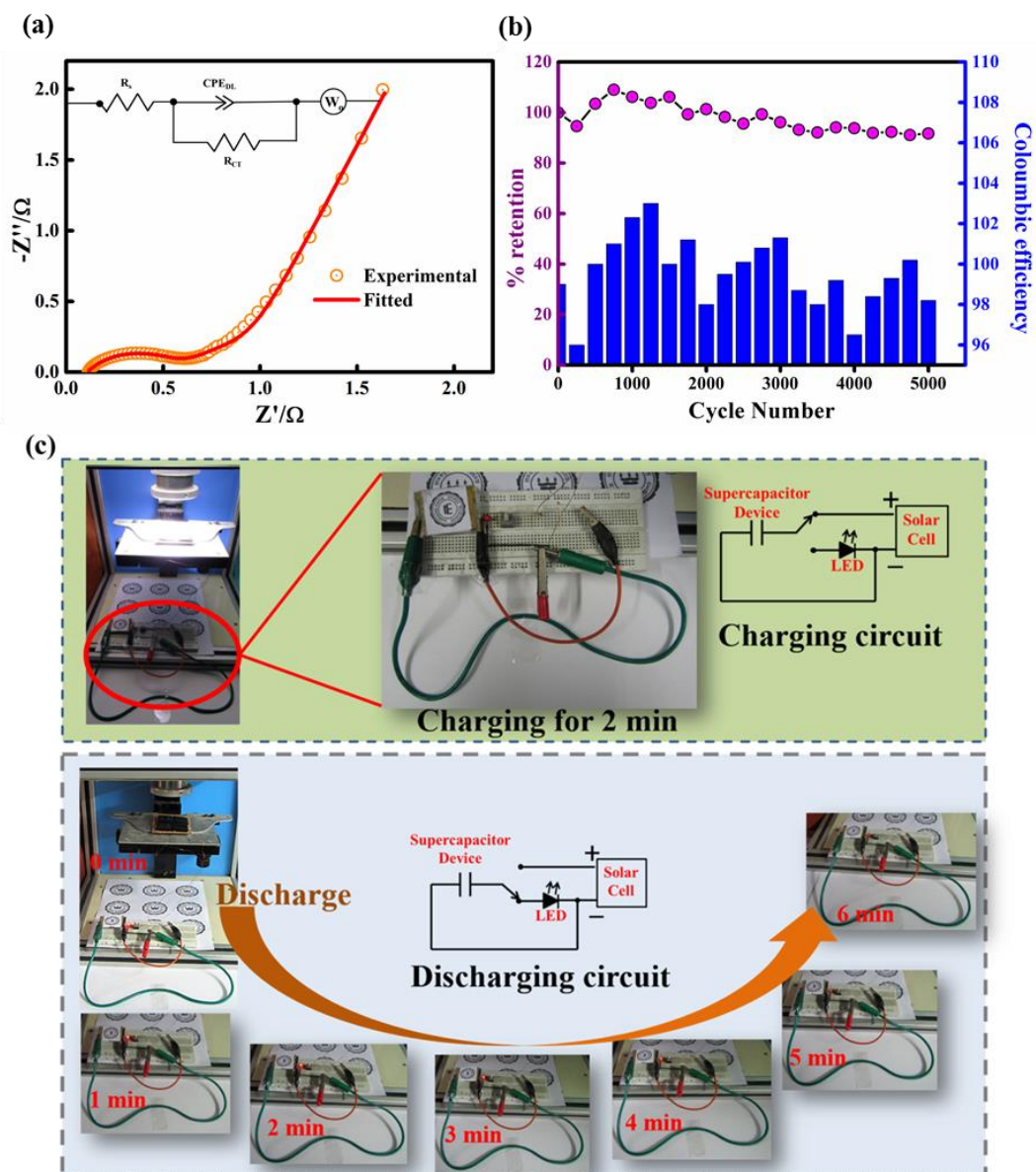
Figure 5.3.7: (a) Nyquist plot for the device (Inset: Circuit used to fit the data), (b) Cyclic stability analysis and plot of coulombic efficiency *vs.* number of cycles and (c) Different stages of charging and discharging of the device.

capacitance value of 293 F g^{-1} at the lowest current density of 0.8 A g^{-1} which is very close to the value obtained from the CV measurements. Using equations (2.5.1) and (2.5.2) we have calculated specific energy density and specific power density respectively at different current densities from the GCD data. Figure 5.3.6 (f) shows the energy density vs. power density plot or, more commonly, the Ragone plot along with the comparison with some recent results [37, 50, 54, 55]. The device shows a maximum energy density of 145.3 Wh kg^{-1} at the lowest current density of 0.8 A g^{-1}

135

and maximum power density of 12 kW kg^{-1} at the highest current density of 13.3 A g^{-1}. EIS was performed within the frequency range of 0.01 Hz to 100 kHz with an AC perturbation voltage of 10 mV to understand the charge dynamics of the device. Figure 8(a) shows the Nyquist plot for the device. The Nyquist plot has been fitted with Z-view software using the equivalent circuit shown in the inset of figure 5.3.7 (a). The device shows a contact resistance of 0.1 Ω and charge transfer resistance of 0.44 Ω. These low values of the resistances enable the device to store and deliver charges easily. Figure 5.3.7 (b) shows the cyclic performance of the device. The cyclic performance was studied by performing 5000 GCD cycles at 100 A g^{-1} current density. Initially, the specific capacitance decreases to 94% of the initial value then start to increase up to 750th cycle to a value of 109% of the initial value. Finally, after 800th cycle, the specific capacitance starts decreasing and reaches a value of 92% of the initial value after 5000 GCD cycles. The bar plot of figure 5.3.7 (b) shows the variation of coulombic efficiency with the cycle number. Nearly 100% efficiency was observed over all the cycles with some minor variations. Finally, the device was used to store charges from solar energy. Four commercially available solar panels (each having open circuit voltage 1.2 V and maximum power 68 mW at 1 sun intensity with AM 1.5 simulated solar radiation) were used for converting the solar energy into electrical energy. To meet the required charging voltage, two such panels were connected in series which were again connected in parallel with another series combination of two similar panels. This matrix of solar panels was placed under a solar simulator to charge the supercapacitor device. We charge the device for 2 min under 1 sun intensity and discharge the device through a red LED. The LED remains in on state for more than 6 min suggesting the high energy density of the device. Figure 5.3.7 (c) shows the different stages of the charging and discharging of the device.

5.4 Microfiber of $NiMn_2O_4$

In the previous section, we have seen that SDS-assisted hydrothermally synthesized $NiMn_2O_4$ (NM3) provides the best electrochemical performance compared to all the other samples. The high specific capacitance of this sample is mainly because of the higher surface area and interconnected morphology of the same. Previously, all the electrochemical measurements were performed using Ni-foam substrate, upon which the sample NM3 was deposited during the hydrothermal reaction. This is also a major factor behind the ultrahigh value of specific capacitance for this sample. Ni-foam substrate provides a conducting and porous backbone which enhances the specific capacitance value. However, Ni-foam is not a suitable substrate for commercial use as it is very fragile and tends to degrade in the electrolyte solution. Hence, we have utilized the RJ-Spinning technique to fabricate the fiber-like structure of the sample NM3 using an aqueous PVA polymer solution. Upon annealing in a vacuum, the PVA/NM3 polymer fiber converts to NM3/Carbon fiber (Named as NM3RJ). This Carbon backbone provides a morphologically ordered conducting path
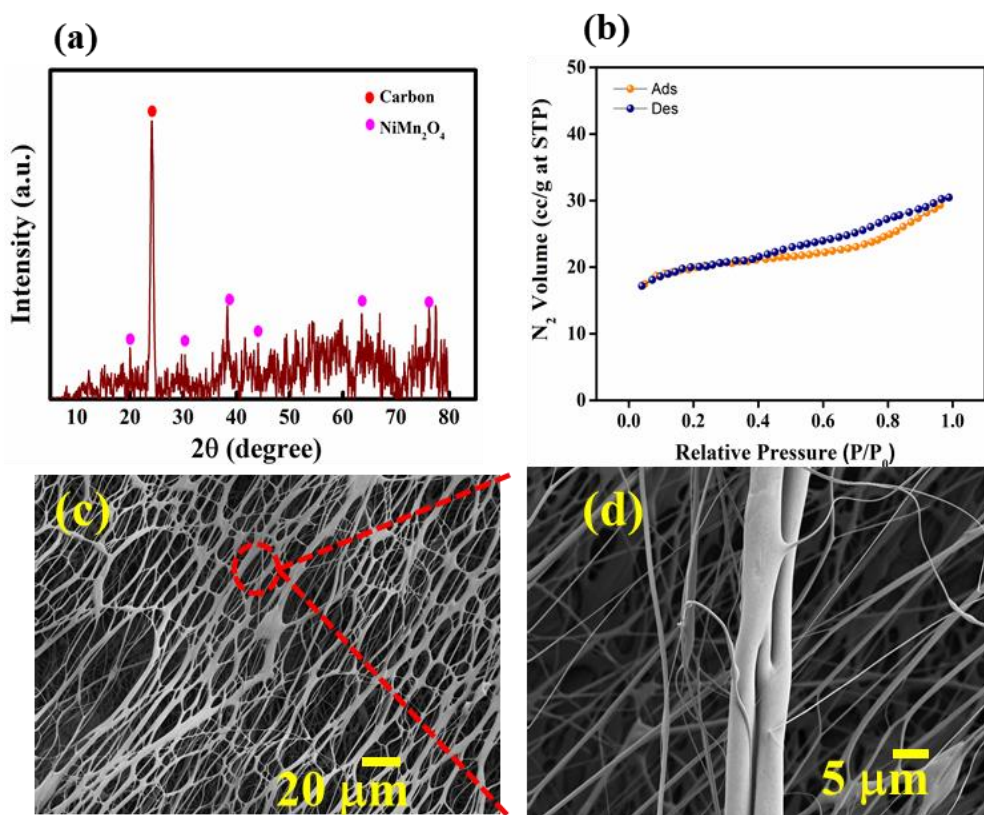
Figure 5.4.1: (a) XRD and (b) N_2 adsorption and desorption isotherms of NM3RJ, SEM images at (c) low and (d) high magnifications for the sample NM3RJ.

that can enhance the performance of the sample. The detailed synthesis scheme has been discussed in chapter 4. In this section, we will be discussing the results of different characterizations and compare its electrochemical storage performance with NM3 powder sample.

Figure 5.4.1 (a) shows the XRD pattern of the NM3RJ. All the highly intense peaks are found to match with the standard $NiMn_2O_4$ patterns (JCPDS no.71-0852) [29-32] and are very much similar to that obtained with NM3 in figure 5.3.1 (a). However, this XRD pattern includes a very intense peak at 24°. This intense peak is may be due to the (002) plane of the graphitic carbon [61]. Upon vacuum annealing the fiber, PVA converts to graphitic carbon, which forms the conductive backbone of the fiber. Figure 5.4.1 (b) displays the N_2 adsorption and desorption isotherms of NM3RJ. A specific surface area of 62.7 m^2 g^{-1} has been obtained for this fiber-type
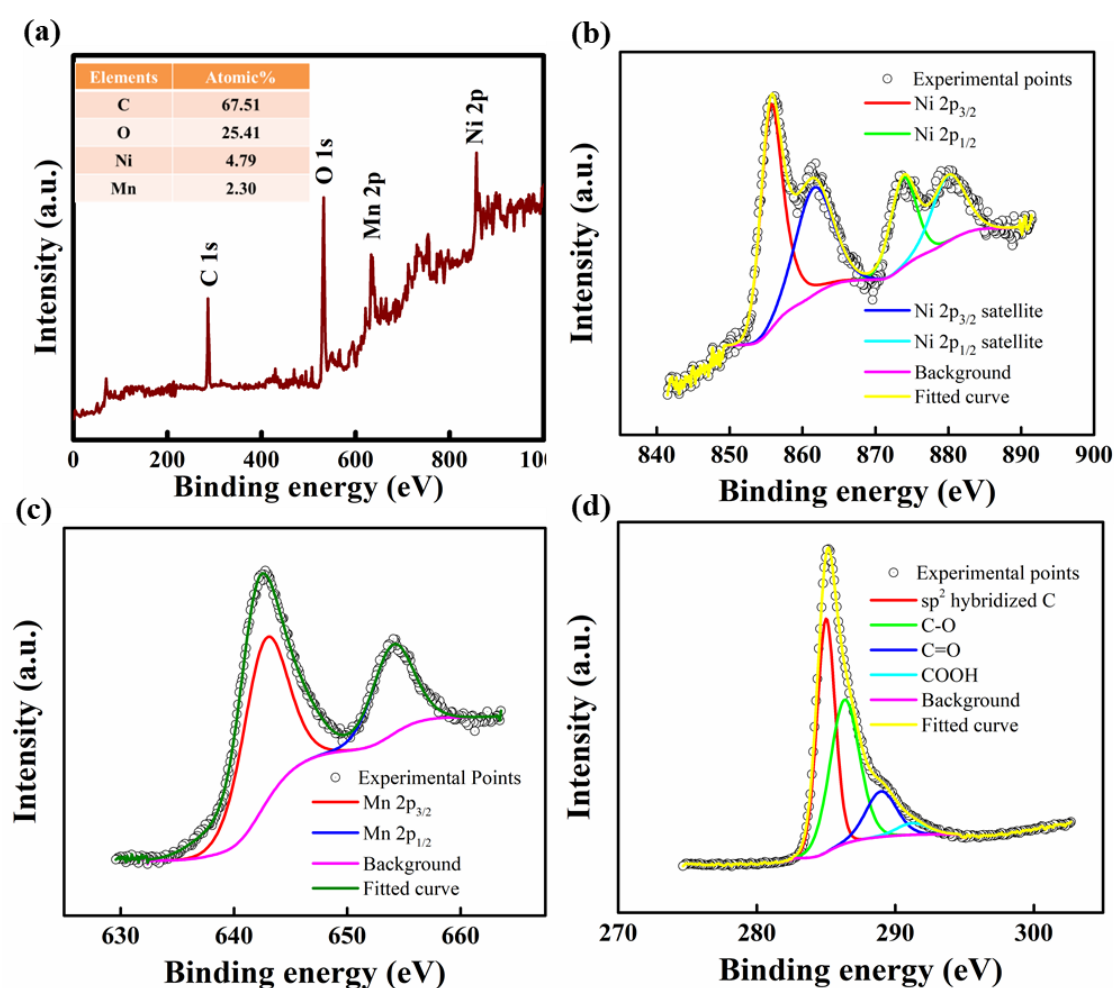
Figure 5.4.2: (a) XPS survey spectrum of NM3RJ. High resolution scans of (b) Ni 2p (c) Mn 2p (d) C 1s peaks

138

sample. Previously, we have obtained a specific surface area of 59.9 m^2 g^{-1} for the sample NM3 in powder form (Table 5.3.1). This suggests after fiber formation, the specific surface area of the sample increases. This enhancement of surface area improves the electrochemical charge storage performance for this fiber-like sample. SEM images at different magnifications of the NM3RJ sample has been demonstrated in figure 5.4.1 (c) and 5.4.1 (d). The images clearly reveal the fiber-like structure of the sample. Using ImageJ software, the average diameter for the fiber is estimated to be around 5 μm. The magnified SEM image of NM3RJ shows junctions of different fibers. This kind of morphology effectively connects the individual redox-active sites. Thus the overall resistance of the sample decreases. X-ray photoelectron spectroscopy (XPS) is employed to find the surface elemental composition of the NM3RJ sample. Figure 5.4.2 (a) shows the survey spectrum of the same, which demonstrates the presence of carbon, oxygen, manganese, and nickel. High-resolution scan of the Ni-peak has been shown in figure 5.4.2 (b), which shows four distinct peaks. The peaks at 855.5 eV and at 873.7 eV are assigned to Ni $2p_{3/2}$ and Ni $2p_{1/2}$ states, respectively. A binding energy difference ~18 eV between these two states confirms the presence of Ni^{2+} ions in the NM3RJ fiber [62]. The presence of additional shakeup peaks at 861.6 eV and at 880.1 eV can be observed. Figure 5.4.2 (c) shows the high-resolution scan for the Mn 2p peak. The doublet state of Mn 2p splits due to spin-orbit interaction. The peak at 642.5 eV is assigned to Mn $2p_{3/2}$, and the same at 654.1 eV is assigned to Mn $2p_{1/2}$ state. The binding energy separation of ~11.5 eV confirms the presence of Mn^{3+} ions in the sample. Both the survey spectrum and the high-resolution scan of the C 1s peak show a good presence of carbon in the sample. This carbon arises from the annealing of PVA polymer. Figure 5.4.2 (d) shows the high-resolution scan of the C 1s peak, which can be deconvoluted into several peaks. The peak at 285.1 eV corresponds to the sp^2 hybridized graphitic peak and is the most intense among all the peaks. This graphitic carbon is responsible for the good conductivity of the fibrous sample, the signature of which can also be seen from the XRD measurement. The peaks at 286.4 eV and at 289 eV correspond to C-O and C=O bonds present in the sample. These oxygen-containing groups result from incomplete carbonization of the polymer and somehow limit the conductivity of the sample [62, 63]. The atomic percentage ratios of the different atoms are shown in the inset of figure 5.4.2 (a). It can be seen that Ni: Mn is nearly1: 2 and thus follows the formula
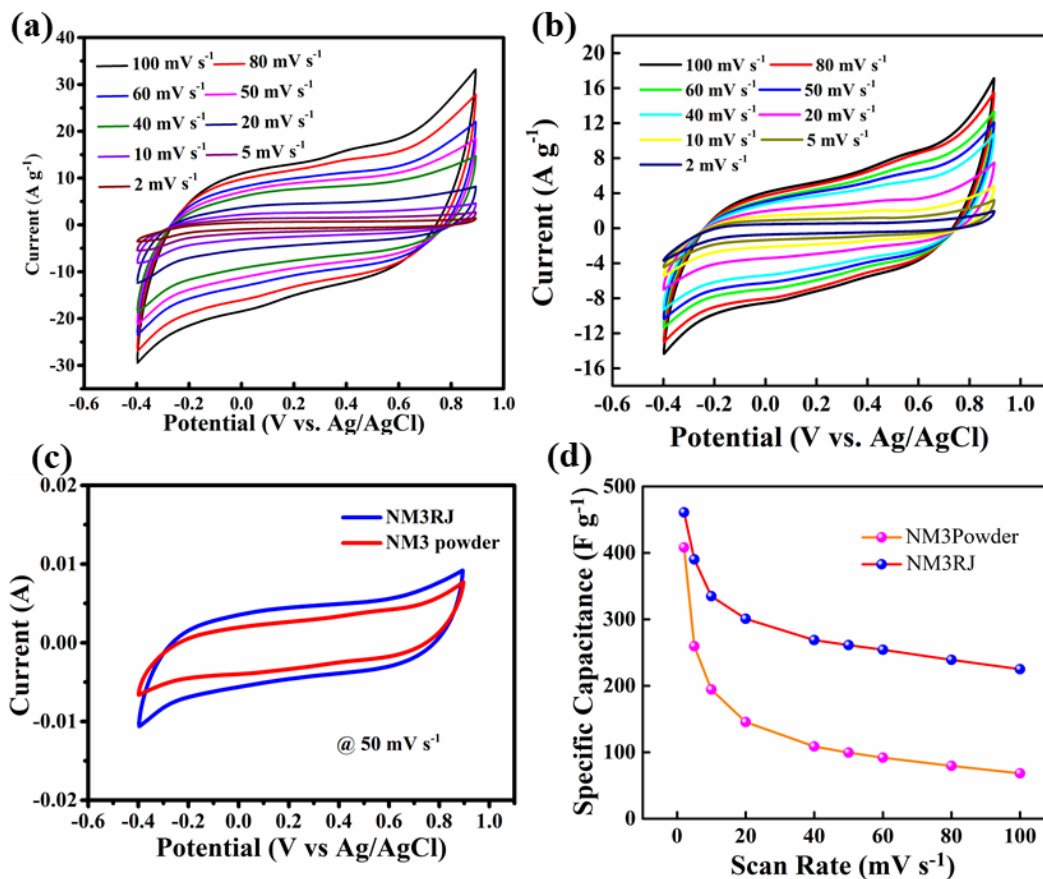
Figure 5.4.3: CV curves at different scan rates for the sample (a) NM3RJ and (b) NM3 Powder. (c) Comparison of CV curves for NM3RJ and NM3 powder at a fixed scan rate of 50 mV s^{-1}, (d) specific capacitance vs. scan rate plot for the sample NM3RJ and NM3 Powder.

for NiMn$_2$O$_4$. However, a large percentage of oxygen is due to the oxygen-containing functional groups, which arises due to incomplete carbonization.

Figure 5.4.3 (a) shows the CV curves at different scan rates for the NM3RJ sample. The CV was performed within a wide potential window of -0.4 V to 0.9 V (vs. Ag/AgCl in saturated KCl) using a 1 M aqueous Na$_2$SO$_4$ solution. The curves show typical pseudocapacitive nature having oxidation and reduction peaks. These peaks result from the transition of Mn^{3+}⇔ Mn^{4+} and Ni^{2+}⇔ Ni^{3+} [64-66]. Using equation (2.3.1), the specific capacitance for this sample has been calculated from these CV curves. The highest specific capacitance of 460 F g^{-1} was obtained at 2 mV s^{-1} scan rate. Figure 5.4.3 (b) shows the CV curves at different scan rates for the NM3 Powder sample within the same potential window of -0.4 V to 0.9 V. A highest specific capacitance of 405 F g^{-1} was obtained for the same.   Figure 5.4.3 (c) shows the comparison between the CV curves for NM3-powder and NM3RJ at a fixed scan

rate of 50 mV s^{-1} within the same potential window and same aqueous 1 M Na$_2$SO$_4$ electrolyte. It is worth mentioning; in the previous section (section 5.3) we have performed a similar CV measurement of NM3 sample deposited on Ni-foam. This results in a much higher current density and thus a very high specific capacitance value. However, when the same composite (NM3) was used as a powder form for the electrochemical measurement, it was seen that it offered relatively less current density, and thus a relatively smaller value of specific capacitance was obtained for the powder sample. On the other hand, a fiber-like structure was fabricated by synthesizing NM3RJ, which increases the specific surface area and conductivity. This results in superior electrochemical performance for the NM3RJ compared to the NM3 powder sample. This can be concluded from figure 5.4.3 (c). As the specific capacitance is proportional to the area enclosed by the CV curves, we can see that for a particular scan rate, NM3RJ encloses a higher CV area compared to that of the NM3 powder sample. Figure 5.4.3 (d) demonstrates the specific capacitance vs. scan rate plot for NM3RJ and NM3 Powder samples. The usual decrement of specific capacitance with increasing scan rate can be observed. At a higher scan rate, NM3RJ retains relatively high specific capacitance compared to both NM3 (on nickel foam) sample (figure 5.3.4 (c)) and NM3 Powder sample (figure 5.4.3 (d)). This is mainly because of the fiber-like morphology NM3RJ, which provides optimum porosity and allows easy access to the electrolyte ions, and can transport electrons effectively.

Total specific capacitance offered by the electrode material can be written as a sum of two different contributions as expressed by equation (5.4.1) [50, 51]

$$C_T = C_{in} + C_{out} \tag{5.4.1}$$

Where C_T is the total specific capacitance, C_{in} is the specific capacitance due to the faradaic reaction, which mainly occurs in the inner side of the electrode, and C_{out} is the specific capacitance due to double layer contribution, which mainly occurs at the interface of the electrode and the electrolyte. At higher scan rates, the charge storage depends mainly on the outer surface because of the shortage of time for the ion diffusion to happen inside the pores of the material. Thus C_{out} mainly involves the contribution due to the double layer mechanism. At very low scan rates ($v \rightarrow 0$), however, both faradic and double layer mechanisms contribute to the total charge capacity. Thus total capacitance can be obtained by extrapolating the specific
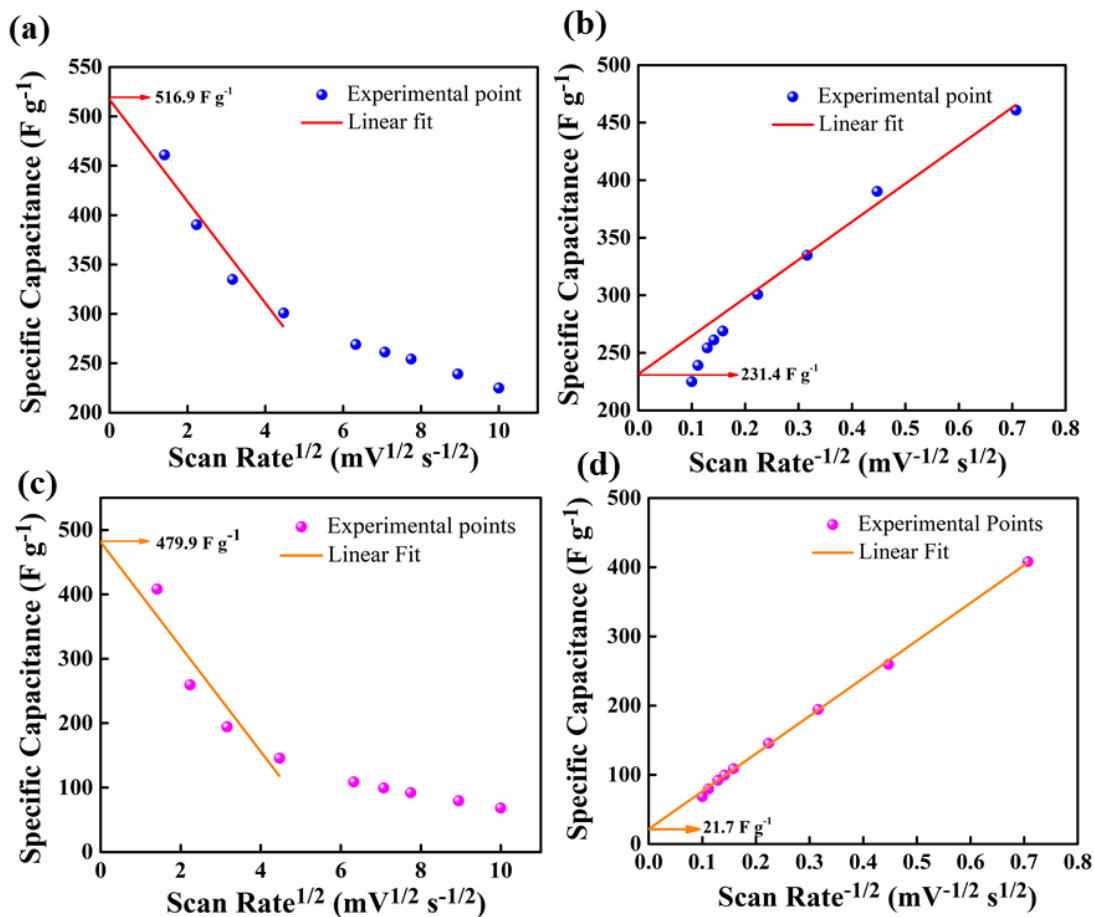
Figure 5.4.4: (a) Plot of specific capacitance vs. square root of scan rate for NM3RJ, (b) plot of specific capacitance vs. inverse square root of scan rate for NM3RJ, (c) Plot of specific capacitance vs. square root of scan rate for NM3 Powder, (d) plot of specific capacitance vs. inverse square root of scan rate for NM3 Powder.

capacitance vs. $v^{\frac{1}{2}}$ curve to $v=0$ as shown for the sample NM3RJ in Figure 5.4.4 (a) and for the sample NM3 Powder in figure 5.4.4 (c). And the contribution due to the outer surface can be found out by extrapolating the plot of specific capacitance vs.

$v^{-\frac{1}{2}}$ to $v \to \infty$ (i.e. $v^{-\frac{1}{2}} \to 0$) which has been plotted in figure 5.4.4 (b) for the sample NM3RJ and in figure 5.4.4 (d) for the sample NM3 Powder. We have obtained, for the NM3RJ sample, total specific capacitance C_T = 516.9 F g^{-1} and specific capacitance due to the outer contribution C_{out} = 231.4 F g^{-1}. Hence, from equation (5.4.1), we have obtained the inner contribution to the capacitance C_{in} = 285.5 F g^{-1}. The same values obtained for the sample NM3 Powder as C_T = 479.9 F g^{-1}, C_{out} = 21.7 F g^{-1}, and C_{in} = 458.2 F g^{-1}. The higher value of inner contribution to the specific capacitances for both these two samples suggests that the redox reaction plays a dominating role in storing the charges. However, it can be seen that the outer
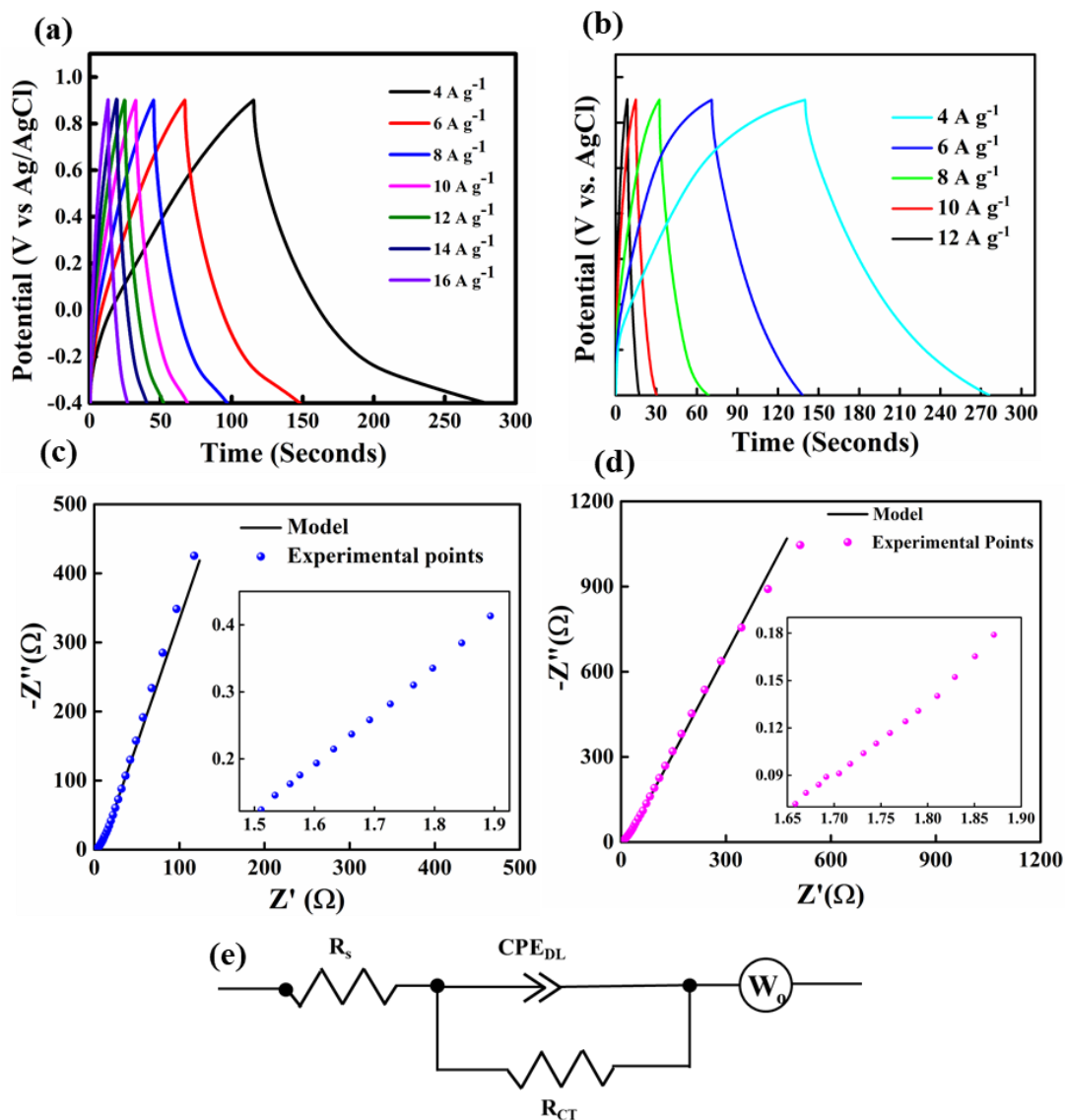
Figure 5.4.5: GCD plots at different current densities for the samples (a) NM3RJ and (b) NM3 powder. Nyquist plots for the samples (c) NM3RJ and (d) NM3 Powder, inset of both these two figures show the high frequency regions of the respective Nyquist plots. (e) Model circuit used to fit both these two Nyquist plots

contribution to the specific capacitance is much higher in NM3RJ than the NM3 Powder sample. This concludes that at high scan rates, the electrolyte ions can utilize maximum electrode material because of the optimum porosity of the ordered structure. Here it is worth mentioning that during the linear fitting done for both the samples, we have used the data for low scan rates only and the higher scan rate region was avoided. This is because of the fact that at higher scan rate Ohomic drop becomes significant which introduces nonlinearity in the respective plots [52]. Figure 5.4.5 (d) shows the GCD profiles for NM3RJ sample at different current densities. The GCD

curves show relatively low IR compared to NM3 powder sample (figure 5.4.5 (e)). This is because of the conducting network of the fiber which connects the individual redox active sites. Both these GCD plots show near triangular shape which is characteristic of the near rectangular CV profile as seen in figure 5.4.3 (a) and (b). Using equation 2.3.3 specific capacitances for both these two samples are calculated from the GCD data. A highest specific capacitance of 447 F g^{-1} and 408 F g^{-1} have been obtained at the lowest current density of 4 A g^{-1} for the NM3RJ and NM3 Powder samples, respectively. These values are very close to the value obtained from the CV curve. Figure 5.4.5 (c) and (d) display the EIS data in the form of Nyquist plot for both these two samples. The EIS has been performed at a frequency range 0.01 Hz-10^5 Hz using an AC perturbation signal having amplitude of 10 mV. The high frequency regions of the respective Nyquist plots have been shown in the inset of the figure 5.4.5 (c) and (d). These Nyquist plots are fitted using the model circuit as shown in figure 5.4.5 (e). Here R_s is the equivalent series resistance which includes the resistance due to improper contact with the graphite current collector, material resistance and electrolyte resistance. From circuit fitting we have obtained the R_s values as 1.51 Ω and 1.65 Ω for the samples NM3RJ and NM3 Powder. The lower value of Rs for NM3RJ suggests less material resistance and good contact with the current collector for the fibrous sample. In the equivalent circuit, CPE is the constant phase element. CPE is used in place of a capacitor in a model circuit to account the non-homogeneity in the system. CPE consists of two parts, CPE-T and CPE-P. If CPE-P equals 1 then the behaviour of the circuit element is identical to that of a capacitor. A CPE-P value between 0.9 and 1 signifies rough or porous surface. We have obtained a CPE-P value of 0.907 for the fibrous sample and 0.464 for the powder sample. This suggests, the fibrous sample offers a porous surface which is beneficial for charge storage. The R_{CT} in the equivalent circuit represents the charge transfer resistance. The NM3 powder sample offers a relatively high charge transfer resistance of 6.3 Ω compared to a relatively small value of 3.5 Ω for the sample NM3RJ. Thus the fiber-structure helps in efficient charge transport compared to the powder sample. Finally, the W_o is the Warburg impedance and arises due to diffusion of ions at low frequency. The powder sample offered a high Warburg resistance of 7.2 Ω compared to only 0.42 Ω for the fibrous sample. Thus the fiber morphology allows easy diffusion of ions.

5.5 References

[1] C. Fu, G. Zhao, H. Zhang, S. Li, Evaluation and characterization of reduced Graphene Oxide nanosheets as anode materials for Lithium-Ion batteries, *Int. J. Electrochem. Sci.* 8 (2013) 6269–6280.

[2] M. Zhang, Y. Liu, M. Hu, H. Wei, Y. Gao, Spiral wire-type stretchable all-solid-state supercapacitors based on MnO_2/graphene/Ni wires, *Electrochim. Acta.* 256 (2017) 44–51. doi:10.1016/j.electacta.2017.09.106.

[3] L. Armelao, D. Barreca, G. Bottaro, S. Gross, A. Gasparotto, C. Maragno, A. Zattin, L. Armelao, D. Barreca, G. Bottaro, S. Gross, Introduction to XPS studies of metal and metal-oxide nanosystems, *Surface Science Spectra.* 10 (2003) 137-142. doi: 10.1116/11.20050199.

[4] J.S. Lee, D.H. Shin, J. Jang, Polypyrrole-coated manganese dioxide with multiscale architectures for ultrahigh capacity energy storage, *Energy Environ. Sci.* 8 (2015) 3030–3039. doi:10.1039/c5ee02076j.

[5] B. Yu, X. Wang, X. Qian, W. Xing, H. Yang, L. Ma, Y. Lin, S. Jiang, L. Song, Y. Hu, S. Lo, Functionalized Graphene Oxide/phosphoramide oligomer hybrids flame retardant prepared via in situ polymerization for improving the fire safety of polypropylene, *RSC Adv.* 4 (2014) 31782–31794. doi:10.1039/c3ra45945d.

[6] A. Roy, A. Ray, S. Saha, S. Das, Investigation on energy storage and conversion properties of multifunctional PANI-MWCNT composite, *Int. J. Hydrogen Energy.* 43 (2018) 7128–7139. doi:10.1016/j.ijhydene.2018.02.153.

[7] M.S. Javed, S. Dai, M. Wang, D. Guo, L. Chen, X. Wang, C. Hu, Y. Xi, High performance solid state flexible supercapacitor based on molybdenum sulfide hierarchical nanospheres, *J. Power Sources.* 285 (2015) 63–69. doi:10.1016/j.jpowsour.2015.03.079.

[8] W. Wang, S. Guo, I. Lee, K. Ahmed, J. Zhong, Z. Favors, F. Zaera, M. Ozkan, C.S. Ozkan, Hydrous ruthenium oxide nanoparticles anchored to graphene and carbon nanotube hybrid foam for supercapacitors, *Sci. Rep.* 4 (2014) 9–14. doi:10.1038/srep04452.

[9] S.K. Ujjain, A. Das, G. Srivastava, P. Ahuja, M. Roy, A. Arya, M. Roy, Nanoceria based electrochemical sensor for hydrogen peroxide detection, *Biointerphases.* 9 (2014) 031011. doi:10.1116/1.4890473.

[10] S.K. Ujjain, G. Singh, R.K. Sharma, Co_3O_4@Reduced Graphene Oxide Nanoribbon for high performance Asymmetric Supercapacitor, *Electrochim. Acta.* 169 (2015) 276–282. doi:10.1016/j.electacta.2015.03.141.

[11] S.K. Ujjain, P. Ahuja, R.K. Sharma, Graphene nanoribbon wrapped cobalt manganite nanocubes for high performance all-solid-state flexible supercapacitors, *J. Mater. Chem. A.* 3 (2015) 9925-9931. doi:10.1039/c5ta00653h.

[12] P. Ahuja, S. Kumar, R. Kanojia, MnO_x/C nanocomposite : An insight on high-performance supercapacitor and non-enzymatic hydrogen peroxide detection, *Appl. Surf. Sci.* 404 (2017) 197–205. doi:10.1016/j.apsusc.2017.01.300.

[13] S. K. Ujjain, P. Ahuja, R. Bhatia, P. Attri, Printable multi-walled carbon nanotubes thin film for high performance all solid state flexible supercapacitors, *Materials Research Bulletin.* 83 (2016) 167–171. doi:10.1016/j.materresbull.2016.06.006.

[14] A. K. Arof, S. Amirudin, S. Z. Yusof, I. M. Noor, A method based on impedance spectroscopy to determine transport properties of polymer electrolytes, *Phys. Chem. Chem. Phys.* 16 (2014) 1856–1867. doi:10.1039/c3cp53830c.

[15] T.M.W.J. Bandara, M.A.K.L. Dissanayake, I. Albinsson, B.E. Mellander, Mobile charge carrier concentration and mobility of a polymer electrolyte containing PEO and Pr_4N^+ I^- using electrical and dielectric measurements, *Solid State Ionics.* 189 (2011) 63–68. doi:10.1016/j.ssi.2011.03.004.

[16] W. Yang, L. He, X. Tian, M. Yan, H. Yuan, X. Liao, J. Meng, Z. Hao, L. Mai, Carbon-MEMS-based alternating stacked MoS_2@rGO-CNT micro-supercapacitor with high capacitance and energy density, *Small.* 13 (2017) 1–8. doi:10.1002/smll.201700639.

[17] M. Cakici, K.R. Reddy, F. Alonso-Marroquin, Advanced electrochemical energy storage supercapacitors based on the flexible carbon fiber fabric-coated with uniform coral-like MnO_2 structured electrodes, *Chem. Eng. J.* 309 (2017) 151–158. doi:10.1016/j.cej.2016.10.012.

[18] W. He, C. Wang, F. Zhuge, X. Deng, X. Xu, T. Zhai, Flexible and high energy density asymmetrical supercapacitors based on core/shell conducting polymer nanowires/manganese dioxide nanoflakes, *Nano Energy*. 35 (2017) 242–250. doi:10.1016/j.nanoen.2017.03.045.

[19] H. Jia, Y. Cai, X. Zheng, J. Lin, H. Liang, J. Qi, J. Cao, J. Feng, W. Fei, Mesostructured Carbon Nanotube-on-MnO_2 nanosheet composite for high-performance supercapacitors, *ACS Appl. Mater*. Interfaces. 10 (2018) 38963–38969. doi:10.1021/acsami.8b14109.

[20] Y. He, W. Chen, X. Li, Z. Zhang, J. Fu, C. Zhao, E. Xie, Freestanding three-dimensional graphene/MnO_2 composite networks as ultralight and flexible supercapacitor electrodes, *ACS Nano*. 7 (2013) 174–182. doi:10.1021/nn304833s.

[21] X. Meng, L. Lu, C. Sun, Green synthesis of three-dimensional MnO_2/Graphene hydrogel composites as a high-performance electrode material for supercapacitors, *ACS Appl. Mater. Interfaces*. 10 (2018) 16474–16481. doi:10.1021/acsami.8b02354.

[22] J. A. Argüello, J. M. Rojo, R. Moreno, Electrophoretic deposition of manganese oxide and graphene nanoplatelets on graphite paper for the manufacture of supercapacitor electrodes, *Electrochim. Acta*. 294 (2019) 102–109. doi:10.1016/j.electacta.2018.10.091.

[23] Z. Y. Leong and H. Y. Yang, A Study of MnO$_2$ with Different Crystalline Forms for Pseudocapacitive Desalination, *ACS Appl. Mater. Interfaces.* 11 (2019) 13176. doi: 10.1021/acsami.8b20880

[24] D. Jaganyi, M. Altaf and I. Wekesa, Synthesis and characterization of whisker-shaped MnO$_2$ nanostructure at room temperature, *Appl Nanosci* 3 (2013) 329. doi: 10.1007/s13204-012-0135-3

[25] S. I. Senkevich, T. V. Druzhinina, I. M. Kharchenko, and Yu. G. Kryazhev, Thermal transformations of polyvinyl alcohol as a source for the preparation of carbon materials, *Solid Fuel Chemistry*, 1 (2007) 45. doi: 10.3103/S0361521907010107

[26] Z. Huang, Y. Song, D. Feng, Z. Sun, X. Sun, X. Liu, High Mass Loading MnO$_2$ with Hierarchical Nanostructures for Supercapacitors, *ACS Nano* 12 (2018) 3557. doi: 10.1021/acsnano.8b00621

[27] K. Laszlo , E. Tombacz , K. Josepovits, Effect of activation on the surface chemistry of carbons from polymer precursors, *Carbon* 39 (2001) 1217. doi: 10.1016/S0008-6223(00)00245-1

[28] D. Jampaiah, V.K. Velisoju, P. Venkataswamy, V.E. Coyle, A. Nafady, B.M. Reddy, S.K. Bhargava, Nanowire Morphology of Mono- and Bidoped α-MnO$_2$ Catalysts for Remarkable Enhancement in Soot Oxidation, *ACS Appl. Mater. Interfaces*, 9 (2017) 32652. doi:10.1021/acsami.7b07656.

[29] M. Islam, C. Catlow, Structural and electronic properties of NiMn$_2$O$_4$, *J. Phys. Chem. Solids,* 49 (1988) 119–123.

[30] P. Lisboa-Filho, M. Bahout, P. Barahona, C. Moure, O. Pen, Oxygen stoichiometry effects in spinel-type NiMn$_2$O$_4$-d samples, *Journal of Physics and Chemistry of Solids*, 66 (2005) 1206–1212. doi:10.1016/j.jpcs.2005.03.001.

[31] S. Asbrink, A. Waskowska, M. Drozd, E. Taliks, Physical properties and X-Ray diffraction of a NiMn$_2$O$_4$ single crystal below and above the ferrimagnetic transitation at T$_c$ = 145 K, *J. Phys. Chem Solids* 58 (1997) 725–729. doi: 10.1016/S0022-3697(96)00198-9

[32] J. M. A. Almeida, C. T. Meneses, A. S. De Menezes, R. F. Jardim, J. M. Sasaki, Synthesis and characterization of NiMn$_2$O$_4$ nanoparticles using gelatin as organic precursor, *Journal of Magnetism and Magnetic Materials* 320 (2008) 304. doi: 10.1016/j.jmmm.2008.02.062.

[33] A. Ray, A. Roy, M. Ghosh, J.A. Ramos-ramón, S. Saha, Study on charge storage mechanism in working electrodes fabricated by sol- gel derived spinel NiMn$_2$O$_4$ nanoparticles for supercapacitor application, *Appl. Surf. Sci*. 463 (2019) 513–525. doi: 10.1016/j.apsusc.2018.08.259.

[34] A. A. Hlaing and P. P. Win, The synthesis of α-MnO$_2$ nanorods using hydrothermal homogeneous precipitation, *Adv. Nat. Sci.: Nanosci. Nanotechnol*. 3 (2012) 025001. doi: 10.1088/2043-6262/3/2/025001

[35] Y. Sun, J. Zhang, X. Sun and N. Huang, High-performance spinel $NiMn_2O_4$ microspheres self-assembled with nanosheets by microwaveassisted synthesis for supercapacitors, *CrystEngComm*, 22 (2020) 1645-1652. doi: 10.1039/c9ce01623f

[36] W. Kang, Y. Tang, W. Li, X. Yang, H. Xue, Q. Yang, C. Lee, High interfacial storage capability of porous $NiMn_2O_4$/C hierarchical tremella-like nanostructures as the lithium ion battery anode, *Nanoscale* 7 (2015) 225–231. doi: 10.1039/c4nr04031g.

[37] Y. T. Ngo, L. Sui, W. Ahn, J. S. Chung, S. H. Hur, $NiMn_2O_4$ spinel binary nanostructure decorated on three-dimensional reduced graphene oxide hydrogel for bifunctional materials in non-enzymatic glucose sensor, *Nanoscale* , 9, (2017), 19318-19327. doi: 10.1039/c7nr07748c.

[38] H. Dua, Y. Wangb, H. Yuanb, L. Jiao, Facile synthesis and high capacitive performance of 3D hierarchical $Ni(OH)_2$ microspheres, *Electrochimica Acta*, 196 (2016) 84-91. doi: 10.1016/j.electacta.2016.02.190.

[39] L. Wang, H. Zhang, B. Wang, C. Shen, C. Zhang, Q. Hu, A. Zhou and B. Liu, Synthesis and electrochemical performance of $Ti_3C_2T_x$ with hydrothermal process, *Electron. Mater. Lett.*, 12 (2016) 702-710. doi: 10.1007/s13391-016-6088-z.

[40] M. S. Mastulia, N. S. Ansaria, M. A. Nawawia, A. M. Mahat, Effects of cationic surfactant in sol-gel synthesis of nano sized magnesium oxide, *APCBEE Procedia* 3 (2012) 93 – 98, doi: 10.1016/j.apcbee.2012.06.052.

[41] M. Darouie, S. Afshar, K. Zare & M. Monajjemi, Investigation of different factors towards synthesis of CuS spherical nanoparticles, *Journal of Experimental Nanoscience*, 8 (2013) 451-461. doi: 10.1080/17458080.2011.593563.

[42] X. Sun and Y. Li, Colloidal carbon spheres and their core/shell structures with noble-metal nanoparticles, *Angew. Chem.* 116 (2004) 607 –611. doi: 10.1002/ange.200352386.

[43] C-Y. Lee, S-J. Kim, I-S. Hwang, J-H. Lee, Glucose-mediated hydrothermal synthesis and gas sensing characteristics of WO_3 hollow microspheres, *Sensors and Actuators B,* 142 (2009) 236–242. doi: 10.1016/j.snb.2009.08.031.

[44] Y. Gawli, S. Badadhe, A. Basu, D. Guin, M. V Shelke, S. Ogale, Evaluation of n-type ternary metal oxide $NiMn_2O_4$ nanomaterial for humidity sensing, *Sensors Actuators B. Chem*, 191 (2014) 837–843. doi: 10.1016/j.snb.2013.10.071.

[45] L. Peng, Y. Liang, H. Dong, H. Hu, X. Zhao, Y. Cai, Y. Xiao, Super-hierarchical porous carbons derived from mixed biomass wastes by a stepwise removal strategy for high-performance supercapacitors, *J. Power Sources*. 377 (2018) 151–160. doi: 10.1016/j.jpowsour.2017.12.012.

[46] Y. Zhou, W. Jiang, S. Xuan, X. Gong, F. Ye, S. Wanga, Q. Fang, Asymmetric PSt-EA/Ni-Silicate hollow microsphere with a hierarchical porous shell, *J. Mater. Chem. B*, 1 (2013) 1414-1420. doi:10.1039/c2tb00508e.

[47] A. Roy, A. Ray, S. Saha, M. Ghosh, T. Das, B. Satpati, M. Nandi, S. Das, NiO-CNT composite for high performance supercapacitor electrode and oxygen evolution reaction, *Electrochim. Acta*. 283 (2018) 327–337. doi:10.1016/j.electacta.2018.06.154.

[48] C. Zequine, C. K. Ranaweera, Z. Wang, S. Singh, P. Tripathi, O. N. Srivastava, B. K. Gupta, K. Ramasamy, P. K. Kahol, P. R. Dvornic, R. K. Gupta, *Scientific Reports* 6 (2016) 31704. doi: 10.1038/srep31704.

[49] M. Li, M. Zhi, A. Manivannan, N. Wu, A reduced graphene oxide/Co_3O_4 composite for supercapacitor electrode , C. Xiang, *J. of Power Sources*. 226 (2013) 65-70 doi: 10.1016/j.jpowsour.2012.10.064

[50] K. V. Sankar, S. Surendran, K. Pandi, A. M. Allin, V. D. Nithya, Y. S. Lee, Studies on the electrochemical intercalation/de-intercalation mechanism of $NiMn_2O_4$ for high stable pseudocapacitor electrodes, *RSC Adv*. 5 (2015) 27649-27656. doi:10.1039/c5ra00407a.

[51] S. Ardizzone, G. Fregonara, S. Trasatti, "Inner" and "outer" active surface of RuO_2 electrodes, *Electrochim. Acta* 35 (1990) 263e267, doi: 10.1016/0013-4686(90)85068-X

[52] J. Duay, S. A. Sherrill, Z. Gui, E. Gillette, S. B. Lee, Self-limiting electrodeposition of hierarchical MnO_2 and $M(OH)_2/MnO_2$ nanofibril/nanowires: mechanism and supercapacitor properties, *ACS Nano*, 7, 2 (2013), 1200-1214. doi:10.1021/nn3056077.

[53] M. Sufyan, S. Dai, M. Wang, D. Guo, L. Chen, X. Wang, C. Hu, Y. Xi, High performance solid state flexible supercapacitor based on molybdenum sulfide hierarchical nanospheres, *Journal of Power Sources* 285 (2015) 63–69. doi: 10.1016/j.jpowsour.2015.03.079.

[54] S. Sahoo, S. Zhang, J. Shim, Porous ternary high performance supercapacitor electrode based on reduced graphene oxide, $NiMn_2O_4$, and polyaniline, *Electrochim. Acta*. 216 (2016) 386–396. doi: 10.1016/j.electacta.2016.09.030.

[55] M. R. Kim, M. Naidukalla, S. Kim, M. Kim, I. Kim, $NiMn_2O_4$ Nanosheet-decorated hierarchically porous polyaromatic carbon spheres for high-performance supercapacitors, *ChemElectroChem*, 4, (2017), 1214–1221. doi: 10.1002/celc.201700023.

[56] H. Wei, J. Wang, L. Yu, Y. Zhang, D. Hou, T. Li, Facile synthesis of $NiMn_2O_4$ nanosheet arrays grown on nickel foam as novel electrode materials for high-performance supercapacitors, *Ceramics International* 42 (2016) 14963–14969. doi: 10.1016/j.ceramint.2016.06.140

[57]   M. Zhang, Z. Song, H. Liu, T. Ma, Biomass-derived highly porous nitrogen-doped graphene orderly supported $NiMn_2O_4$ nanocrystals as efficient electrode materials for asymmetric supercapacitors, *Applied Surface Science* 507 (2020) 145065. doi:10.1016/j.apsusc.2019.145065

[58] S. Karmakar, D. Behera, Small polaron hopping conduction in $NiMnO_3/NiMn_2O_4$ nano-cotton and its emerging energy application with MWCNT, *Ceramics International* 45 (2019) 13052-13066. doi:10.1016/j.ceramint.2019.03.237

[59] N. Hu, L. Huang, W. Gong, and P. K. Shen, High-performance asymmetric supercapacitor based on hierarchical $NiMn_2O_4$@CoS core−shell microspheres and stereotaxically constricted graphene, *ACS Sustainable Chem. Eng*. 6 (2018) 16933−16940. doi: 10.1021/acssuschemeng.8b04265

[60] P. W. Menezes, A. Indra, O. Levy, K. Kailasam, V. Gutkin, J. Pfrommer and M. Driess, Using nickel manganese oxide catalysts for efficient water oxidation, *Chem. Commun*., 51 (2015) 5005-5008. doi: 10.1039/C4CC09671A.

[61] F. Y. Ban, S. R. Majid, N. M. Huang, H. N. Lim, Graphene Oxide and Its Electrochemical Performance, *Int. J. Electrochem. Sci.* 7 (2012) 4345.

[62] A. Umar, M. S. Akhtar, S. Ameen, M. Imran, R. Kumar, Y. Wang, A. A. Ibrahim, H. Albargi, M. Jalalah, M. A. Alsaiari, M.S. Al-Assiri, Colloidal synthesis of $NiMn_2O_4$ nanodisks decorated reduced graphene oxide for electrochemical applications, *Microchemical Journal*, 160 (2021) 105630. doi: 10.1016/j.microc.2020.105630

[63] M. Sandhiya, K. Subramani, M. Sathish, Augmenting the electrochemical performance of $NiMn_2O_4$ by doping of transition metal ions and compositing with rGO, *Journal of Colloid and Interface Science,* 598 (2021) 409–418. doi: 10.1016/j.jcis.2021.04.023.

[64] S. K. Cho, J. Chang, Electrochemically Identified Ultrathin Water-Oxidation Catalyst in Neutral PH Solution Containing Ni^{2+} and Its Combination with Photoelectrode. *ACS Omega,*2 (2017) 432-442. doi: 10.1021/acsomega.6b00448

[65] S. Maiti, A. Pramanik, T. Dhawa, M. Sreemany, S. Mahanty, Bi-Metal Organic Framework Derived Nickel Manganese Oxide Spinel for Lithium-Ion Battery Anode. *Mater. Sci. Eng., B*. 229 (2018) 27-36. doi: 10.1016/j.mseb.2017.12.018

[66] M. Y. Arsent'ev, N. Y. Koval'ko, A. V. Shmigel', P. A. Tikhonov, M. V. Kalinina, $NiMn_2O_4$ Spinel as a Material for Supercapacitors with a Pseudocapacity Effect. *Glass Phys. Chem.* 43 (2017) 376-379. doi: 10.1134/S1087659617040022

Originality Report for Chapter 5

(*Generated using Ithenticate Software excluding the first author publications of Mr. Samik Saha)

Chapter 5

ORIGINALITY REPORT

12%
SIMILARITY INDEX

PRIMARY SOURCES

1	pubs.rsc.org Internet	182 words — 1%
2	link.springer.com Internet	65 words — 1%
3	Zhongbing Wang, Zihao Zhu, Chunlei Zhang, Chengqiao Xu, Chunnian Chen. "Facile synthesis of reduced graphene oxide/NiMn2O4 nanorods hybrid materials for high-performance supercapacitors", Electrochimica Acta, 2017 Crossref	60 words — < 1%
4	akita-pu.repo.nii.ac.jp Internet	59 words — < 1%
5	ro.uow.edu.au Internet	53 words — < 1%
6	gyan.iitg.ac.in Internet	46 words — < 1%
7	iopscience.iop.org Internet	41 words — < 1%
8	hdl.handle.net Internet	37 words — < 1%

Chapter 6
Conclusion and Scope

6.1 Conclusion

In this thesis work, we have studied the effect of particle morphology of different metal oxide-based samples on their electrochemical charge storage performance. For this purpose, at first, we have chosen a single metal oxide, MnO_2, because of its well-known pseudocapacitive charge storage performance. However, MnO_2 degrades over time after repeated charge-discharge cycles because of the large volumetric strain suffered during the repeated electrochemical process. To stabilize the sample against this strain, we added graphene oxide to make a composite of MnO_2-Graphene oxide (MnO_2-GO). We have optimized the GO quantity for the best performance. It was seen that for a 5:2 loading of MnO_2 and GO (by weight), the specific capacitance of the sample maximizes, and further increase in the GO percentage slightly reduces the specific capacitance value. Further, we studied the effect of sample morphology on electrochemical performance. For this purpose, we have prepared ordered and disordered samples of MnO_2-GO. Ordered samples were prepared using the electrospinning technique, which resulted in a fiber-like morphology, and the disordered samples were prepared using the dropcasting method. Due to the good connection between the individual nanoparticles, the ordered electrospun samples demonstrate good electrochemical performances compared to the dropcasted samples. We obtained a maximum specific capacitance of 892.8 F g^{-1} for the ordered sample, whereas the disordered sample with the same MnO_2 and GO ratio offers 546.9 F g^{-1}. A correlation between the electrochemical performances and dielectric behaviors of the ordered and disordered samples was made by performing a room temperature impedance spectroscopy study which reveals that the ordered sample offers higher charge mobility, diffusivity, and conductivity. Finally, we have assembled an asymmetric supercapacitor using the GM-2E sample as an active material. The device showed a maximum power density of 2.8 kW kg^{-1} at a current density of 3.1 A g^{-1} and a maximum energy density of 96.75 Wh kg^{-1} at a current density of 1 A g^{-1}. The device retained 93.3% of its initial capacitance after 5000 GCD cycles performed at 3 A g^{-1}. The excellent electrochemical behavior and long-term stability make the electrospun ordered GM-2E sample a useful electrode material for future energy storage devices.

However, electrospinning is a slow process, which makes it unsuitable for large-scale production. Hence, we devised an apparatus that can produce similar fiber samples in much larger quantities. The apparatus works similar to the cotton candy machine and is known as rotary jet spin system. We have prepared MnO_2 microfiber using a rotary jet spin assembly in this next work. As confirmed by the FESEM measurement, after annealing the jet spun sample, we obtained microfiber of MnO_2 having an average diameter of 5 μm. This MnO_2 microfiber has been investigated for application in supercapacitor electrodes. The microfiber offers excellent electrochemical properties because of the ordered and well-connected morphology. The highest specific capacitance of 663 F g^{-1} is obtained at the lowest scan rate of 2 mV s^{-1}. A two-electrode asymmetric supercapacitor device is fabricated using the microfiber sample as positrode and activated carbon as the negatrode. The device offers a high specific capacitance of 135.6 F g^{-1} along with excellent charge storage capability. Thus rotary jet spin can be used to fabricate metal oxide microfiber for application in the electrodes of future energy storage devices. Further, there are ample opportunities to utilize the technique to produce fiber of different metal-oxide and their composites with different carbonaceous materials. The scalability, production yield capability, and ease of synthesis could make the rotary jet spin technique to be widely accepted in the industry.

The main disadvantage of single metal oxides is their high resistivity. On the other hand, bimetallic oxides show relatively less resistivity alongside the presence of multiple valency states, making them suitable for supercapacitor electrodes. Hence, in the next work we have chosen a bimetallic oxide of nickel and manganese. Nickel oxides are well-known battery-type material; on the other hand, manganese oxides are popular pseudocapacitive material. Thus electrode made of a combination of both these two oxides should demonstrate high energy density and high power density. We have synthesized $NiMn_2O_4$ through a hydrothermal technique using different surfactants and mineralizers. We found the addition of these chemicals results in different morphology of the $NiMn_2O_4$ with different surface areas and particle sizes. The addition of sodium dodecyl sulfate (SDS) during the synthesis maximizes the surface area, and hence better electrochemical performance was obtained with this variant of $NiMn_2O_4$ coated on Ni-foam. This sample offered a three-electrode specific capacitance of 1937 F g^{-1} at 2 mV s^{-1}. The same material was used to fabricate a two-

electrode device that shows a specific capacitance of 270 F g^{-1} at 2 mV s^{-1} with the maximum power density of 12 kW kg^{-1} and maximum energy density 145.3 Wh kg^{-1}. Finally, the device was used to harness solar energy using commercially available solar cells. The overall performance of the two-electrode device actually suggests its usability as a future energy storage device.

The sample NiMn$_2$O$_4$ coated on Ni-foam (NM3) shows an ultrahigh-specific capacitance. The reason behind this ultrahigh value is the superior connectivity of the sample with the Ni-foam substrate. Here Ni-foam both acts as a current collector and connects the individual redox-active sites of NiMn$_2$O$_4$ electrically. The porous structure of Ni-foam also enhances electrolyte accessibility. But, Ni-foam is not a suitable alternative for commercial use as it is very fragile and degrades in the electrolyte solution. Hence, we again used the rotary jet spin technique to fabricate the fiber of the previously synthesized NiMn$_2$O$_4$ (NM3) in an attempt to increase the connectivity between the redox-active sites through fiber-like morphology. SEM measurement shows the fiber-like structure having an average diameter of 5 μm. Because of this fiber-like morphology, the rotary jet synthesized sample (NM3RJ) showed high specific surface area compared to the powder NM3 sample. We also compared its electrochemical performance with the powder NiMn$_2$O$_4$ sample. As the powder NiMn$_2$O$_4$ (NM3 powder) do not have good interconnection within its redox-active sites, it offered relatively less current density at a fixed scan rate compared to the rotary jet-assisted synthesized sample of NiMn$_2$O$_4$ (NM3RJ). NM3RJ offered a high specific capacitance of 460 F g^{-1} at 2 mV s^{-1}, as confirmed from both CV and GCD measurements.

Thus it can be concluded that the morphology of the electrode material plays a vital role in determining the overall charge storage performance. Morphology, which offers high surface area, good inter-particle electronic connectivity, good electrolyte accessibility, should demonstrate excellent electrochemical charge storage performance. The high surface area of the electrode material enhances the charge storage capability via the EDLC mechanism. Good inter-particle connectivity enhances the charge transport rate and thus increases the power density. Good electrolyte accessibility reduces the effect of dead mass on the electrode, and the whole active material coated on an electrode can be utilized for charge storage.

6.2 Scope for future research

Transition metal-oxide-based electrode materials offer high energy density and high power density. However, because of high internal resistance and lack of long-term stability, they are not yet been used commercially. Modification of the material morphology can address a few of these problems. This thesis work explores the effect of the morphology of the supercapacitor electrode material on its charge storage performance. Below listed are a few among many improvements which may address the problems of transition metal-oxide based electrodes.

1. Investigation of morphologically ordered tri-metal oxides and beyond for supercapacitor electrode.
2. Effect of other different types of morphologies on the electrochemical performance of particular electrode material. In this regard, the development of a proper theoretical framework is necessary along with the experimental work.
3. More research on the improvement of the rotary-jet spin device is required to be able to fabricate nanofiber with good uniformity. As we know, decreasing the fiber's dimension will enhance the surface area.
4. The rotary-jet spin device can be utilized to work with different types of polymer solutions having different viscoelastic properties. Thus the effect of different polymers on the fiber geometry can be studied along with the electrochemical performance.
5. The device fabrication technique has to be improved. In this regard, proper choice of electrolyte, current collector, and separator is very much necessary. Also, the high self-discharge rate of supercapacitor has to be suppressed by using a proper methodology.

The field of supercapacitor research is very vast and always evolving. With the investments of billions of dollars in research, it seems that the future of supercapacitors is very bright.

Originality Report for Chapter 6

(*Generated using Ithenticate Software excluding the first author publications of Mr. Samik Saha)

Chapter 6

ORIGINALITY REPORT

10%
SIMILARITY INDEX

PRIMARY SOURCES

1	pubs.rsc.org Internet	62 words — 4%
2	www.science.gov Internet	25 words — 2%
3	iopscience.iop.org Internet	24 words — 2%
4	Nitin Choudhary, Chao Li, Julian Moore, Narasimha Nagaiah, Lei Zhai, Yeonwoong Jung, Jayan Thomas. "Asymmetric Supercapacitor Electrodes and Devices", Advanced Materials, 2017 Crossref	18 words — 1%
5	Kabir O. Oyedotun, Farshad Barzegar, Abdulmajid A. Mirghni, Abubakar A. Khaleed, Tshifhiwa M. Masikhwa, Ncholu Manyala. "Examination of High-Porosity Activated Carbon Obtained from Dehydration of White Sugar for Electrochemical Capacitor Applications", ACS Sustainable Chemistry & Engineering, 2018 Crossref	9 words — 1%
6	"Nanocarbon-Based Materials for Asymmetric Supercapacitors", Nanocarbons for Advanced Energy Storage, 2015. Crossref	8 words — 1%

THANK YOU